Summer 8-31-2020

Design and Synthesis of Fluorescent Silica Nanoparticle Conjugates for Metal Ion Sensing Applications

Hank Deuermeyer
hank.deuermeyer@gmail.com

Design and Synthesis of Fluorescent Silica Nanoparticle Conjugates for Metal Ion Sensing Applications

A thesis presented to the faculty of the Department of Chemistry at the University of San Francisco in partial fulfillment of the requirements for a degree of

Master of Science in Chemistry

Written by

Hank Deuermeyer
Bachelor of Science in Chemistry, ACS Accredited,
Bachelor of Science in Biotechnology
Saint Cloud State University, Saint Cloud, MN

August 2020

Design and Synthesis of Fluorescent Silica Nanoparticle Conjugates for Metal Ion Sensing Applications

Thesis written by

Hank Deuermeyer

This thesis is written under the guidance of the Faculty Advisor Committee, approved by all its members, and has been accepted in partial of the requirements for a degree of

Master of Science in Chemistry
from the
University of San Francisco

Thesis Committee

Lawrence D. Margerum, Ph.D.
Research Advisor

Ryan West, Ph.D.
Assistant Professor

Janet Yang, Ph.D.
Assistant Professor

Marcelo Camperi, Ph.D.
Dean, College of Arts and Sciences

Acknowledgments

I would like to acknowledge first and foremost Dr. Lawrence Margerum for his guidance and patience throughout my time at USF. His support through not only research but also teaching has led me to become a better chemist, teacher, and person.

I would also like to not only acknowledge but thank wholeheartedly, Dr. Janet Yang. My continued siege on her office hours was not only allowed but welcomed. Without her friendship, advice, and literal instrumental support, such as the ultracentrifuge, I would not have been able to expand and expedite my project or grow into the chemist that I am today. I am forever thankful.

Many thanks to Deidre for always answering my pedantic and often redundant questions. She was always willing to help me and anyone else that asked. For that, I am grateful, Deidre.

Jeff Oda, I had a blast working for you! From helping with closed biotech companies to cleaning rotary pumps, a million thanks for letting me tag along and help out. Truly a great person to work with and I cannot emphasize enough, the lengths he has helped me while at USF.

Thank you Andy for helping me with instrumentation and keeping me on my toes. I will miss your jokes and witty banter in the halls. I hope my MN addition to your magnet collection was a good one.

And to all my friends, Yasmin, Maddy, Denny, David, Mike, Stephen, Dakota, Peter, Whit, Alicia, Adam, Ben, Erica, Lucas, Sasha, Erin, and Aubrey. Without you all, I would not have become a better chemist or person. I am going to miss going to Lucky to buy some chicken tens for lunch, having our coffee hours, West World discussions, and watching Rick and Morty on our lunch breaks. I am going to miss teaching/ tutoring chemistry and watching seeing the light bulb come on (“*p = -log!” -Sasha*). I am going to miss being a goof ball with all of you. But what I will miss most of all are the things I’m going to miss out on. You have made my life in SF unforgettable and I will cherish my experiences with every one of you. A special thanks to Peter and Dakota. Without your help with making nanoparticles and helping with amine assays, this project would not have progressed as far as it did!

I cannot thank my aforementioned mentors, colleagues, and friends enough for the support and dedication that I received while at USF. Thank you all for making my two and a half years in San Francisco phenomenal!

Table of Contents

Abstract

A novel series of fluorescent nanoparticle conjugates were designed and synthesized for the selective turn-off sensing of low concentrations of Cu^{2+} ion (nM-μM) in 2:1 ethanol:10 mM HEPES (pH 7). Silica nanoparticles (~250 nm) were modified with heterobifunctional polyethylene glycol (PEG) linkers and a third generation PAMAM dendron to function as chelator for Cu^{2+} ions. The organic dye fluorescein isothiocyanate (FITC) was subsequently conjugated to the dendron to act as a fluorescent sensitizer for the nanoparticle that is quenched upon the binding of Cu^{2+}. Fluorescent nanoparticle conjugates using third and fourth generation PAMAM dendrimers (SNP-G_3-FITC and SNP-G_4-FITC) were synthesized for comparison. The dendron conjugate (SNP-PEG_8-G_{3S}-FITC) was determined to have a higher dynamic range (0.10-1.99 μM Cu^{2+}) than the dendrimer counterparts (0.02 -0.30 μM Cu^{2+}). A follow- up series of sensors were designed and synthesized using FITC-conjugated silica nanoparticles for use in characterization of the surface using Fluorescence Resonance Energy Transfer (FRET). These conjugates provide examples of an attractive modular framework for other fluorescent nanoparticles to be synthesized and tailored to analytes of interest. Silica nanoparticle conjugates can be readily synthesized using known reactions, easily isolated from reaction solutions, and they remain undetectable in fluorescent experiments.

Chapter 1. Introduction

The two main foci of this project were nanoparticle conjugation via selective syntheses and the application of these conjugates to sense analytes using steady-state fluorescence methods. In order to put this project into context, a number of key topics must be reviewed that will then be referred to in successive chapters. The goal of this chapter is to cover, generally, the necessary topics and is not an exhaustive overview of any particular topic. The design of this introduction is to provide the reader with enough information to continue reading uninterrupted, however, the reader is implored to peruse the reference material for a deeper understanding. Each topic will begin broadly to provide the reader with an overview and scope that will narrow to the applicable areas of the topic. The first topic to be explored is the field of nanotechnology. What is nanotechnology? Why is it important and how might the development of nanotechnology improve everyday life?

Nanotechnology

Nanotechnology, the manipulation of matter in a range of 1-100 nanometers in at least one dimension, is understandably a broad topic that is a multifaceted area of study that requires the understanding of multiple disciplines.[1] Nanotechnology is the coalescence of physics, chemistry, engineering, material science, and biology. The prefix "nano" refers to 10^{-9}, or one billionth of something, so one nanometer (nm) is one billionth of a meter. Materials on the nm scale are considered nanomaterials and are produced or characterized via nanotechnology. Particles on this "nano" scale are then defined as nanoparticles (NP).[1] Relative sizes of atoms and molecules up to the size of everyday objects are shown in Figure 1.1. Take note of the size differences between the objects, such as the diameter of a baseball (~1 x 10^8 nm) and the thickness of a piece of paper (~1 x 10^5). The orders of magnitude difference between a baseball and a piece of paper is the same difference as between a piece of paper and a virus (~1 x 10^2 nm).

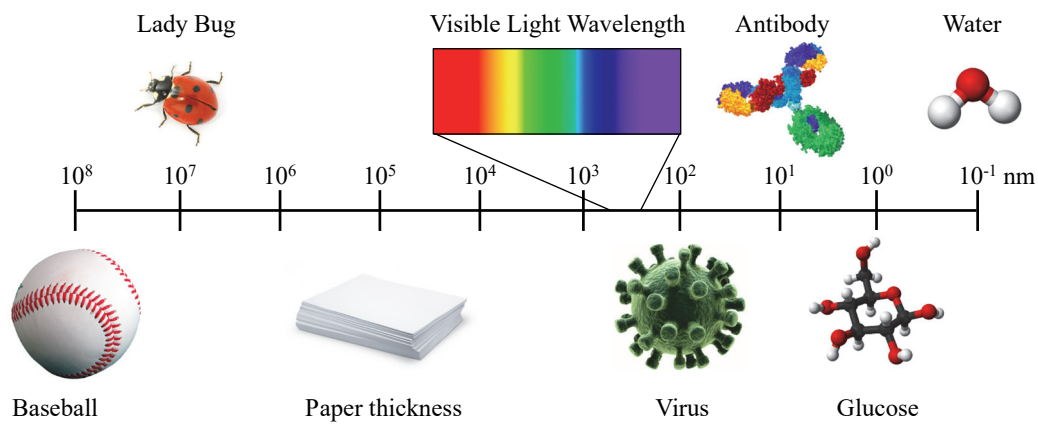

Figure 1.1 Comparisons of object size in nm, where 1-1000 nm is the range for nanotechnology.

Since nanomaterials are found between the atomic and macroscopic, the properties exhibited by nanomaterials are novel and are relative to the scale.[2] These materials have proven difficult to fabricate, and characterization methods have been limited until recently, when improvements have been made in accuracy and precision.[1] Such improvements have led to the coalescence of two approaches for fabricating nanomaterials: either the top-down or bottom-up approach.[1]

The top-down approach is currently the primary source of nanotechnology in the form of the semiconductor industry.[1] This approach uses lithography, mechanical printing, and milling methods to reduce a macroscopic material down to the nanoscale.[3] Reproducibility, control, precision, and established techniques are the hallmarks of top-down approaches.[3] However, in order to push the limits of top-down techniques, as in lithography for example, new components must be fabricated which allow for shorter wavelengths of light to be used without damaging the lithographic lenses. However, this too has its limitations. Top-down methods tend to be more sensitive to defects, expensive, and wasteful when compared to bottom-up.[3]

The bottom-up approach to nanotechnology employs a building up methodology and the application of molecular or atomic thin-films, which is simpler, faster, and more cost effective than the top-down approaches mentioned earlier. Selected thin-film techniques include vapor deposition, molecular self-assembly, and sol-gel processes.[4] As compared to top-down, bottom-up exhibits a wider range of opportunities for the fabrication of functional nanomaterials using chemical synthesis, which builds up from the atomic or molecular scale. This approach was, until recently, limited to simple structures[3], however, more and more complex structures are published every year.[5] The pursuit of nanotechnology development, through multidisciplinary collaboration and with the aid of initiatives and grants, will expand the field and allow for more complexity in bottom-up approaches.

Nanotechnology is highly multidisciplinary and has applications in the aforementioned fields as well as others such as medicine, agriculture, transportation, and textiles.[3] Due to the interdisciplinary nature of nanotechnology, the National Nanotechnology Initiative (NNI) has built a diverse group of 20 departments and independent agencies, including the NIH, NSF, and DOE, all working under the following shared philosophy:

> "*A future in which the ability to understand and control matter at the nanoscale leads to a revolution in technology and industry that benefits society.*"

This group of agencies has identified and defined areas of research and development in which to focus, which are called Nanotechnology Signature Initiatives (NSIs). The NSIs consist of the following areas:[6]

1. Nanotechnology for Solar Energy Collection and Conversion
2. Nanoelectronics for 2020 and Beyond
3. Sustainable Nanomanufacturing
4. Nanotechnology Knowledge Infrastructure
5. Nanotechnology for Sensors and Sensors for Nanotechnology: Improving and Protecting Health, Safety, and the Environment

Two of the five NSIs are included as foci within this project: Sustainable Nanomanufacturing and Nanotechnology for Sensors and Sensors for Nanotechnology. The fifth NSI, Nanotechnology for Sensors and Sensors for Nanotechnology, was the primary focus of this project. This initiative is further refined into two main areas of research and development: (1) the development and promotion of new technologies that employ nanomaterials to overcome technical barriers associated with conventional sensors and (2) the development of methods and devices to detect and identify engineered materials throughout their life cycles to assess the potential impact on human and environmental health. This project was geared more towards the first in the form of bioconjugate techniques to overcome technical barriers in conventional sensors such as harsh or cumbersome synthetic routes, limited modularity and sensor library expansion, as well as sensitivity and selectivity towards analytes. Specifically, nanotechnology in the form of nanoparticles and

their subsequent coatings in a bottom-up approach were used as chemical sensors and were modular in design. This design could be applied to other analytes in future endeavors based on literary precedents.[6] However, before expanding upon the design of sensors, a knowledge of sensor terminology and characteristics as well as background on the chemicals and compounds utilized should be reviewed.

The nanomanufacturing NSI was considered to be a secondary focus and is defined in terms of sustainability or the capability of the nanomaterial to be scaled-up, cost effective, reliable, and have a responsible production.[6] Responsible production of a reliable nanomaterial was accomplished through green syntheses of a novel nanoparticle sensors.

Sensor Terminology and Characteristics

The basic requirement for a sensor is for an external stimulus to change the functionality output.[1] Sensors are similar to detectors in that both "detect" an analyte but sensors differ by providing quantitative information whereas detectors simply provide binary information on the presence or absence of an analyte.[1] Sensors can be further categorized as static versus dynamic. Static sensors measure steady states, that is, systems that have reached equilibrium and are no longer changing by a detectable amount at the time of the measurement. Dynamic sensors, however, take real-time measurements that are transient, such as rates. The sensors in this thesis are static, and the following definitions are measurable characteristics of static sensors: accuracy, precision, error, resolution, selectivity, sensitivity, dynamic range, drift, stability, and response time.[1] (Each characteristic has been defined in a manner to allow the reader to quickly reference back and has provided applicable experimental context.)

Accuracy: The degree to which the sensor response conforms to a true value. Accuracy assessments are performed by using a known standardized analyte or comparing the new sensor to a standard method, such as a 1000 ppm copper standard from NIST or using atomic absorption (AA) spectroscopy, respectively. Using both the standard and the AA together provides a method comparison for accuracy.

Precision: The degree to which a sensor response is refined to a singular value that is represented by the number of digits given. High precision results in the individual measurements closely conforming to the mean. Assessing the precision of sensors can be performed through repeated measurements of the same type (e.g. same concentration of analyte, repeated trials).

Error: The difference between the true value and the value measured by the sensor. Error is associated with the accuracy and precision of the sensor and can be extracted from the data gathered to determine accuracy and precision.

Noise: A random fluctuation in sensor response while the concentration of analyte remains constant. This can be a result of external or internal sources. External noise arises from temperature fluctuations and ambient light interference, among others. Internal noise can be further categorized into the following types: electric, shot, generation-recombination, and pink

noise. Internal sources of noise can result from fluctuations of the sensor at the molecular-level and results of the baseline noise in a system cannot be avoided. Since the noise descends from the system, information about the system can be derived if the noise can be accurately measured.[7]

Resolution: Resolution represents the smallest significant change in sensor response to a change in analyte concentration that can be measured. This value is limited to the noise of the sensor.

Sensitivity: The ability of a sensor to have an incremental change of output in response to the incremental change in analyte concentration. Sensitivity assessments may be performed by adding sequentially increasing amounts of analyte to the sensor and measuring the response. If the sensor response is incrementally changed by this sequential addition, the sensor is said to be sensitive to the added analyte.

Dynamic range: The range in which the sensor is sensitive to the analyte. The lower limit of the dynamic range is dependent on the resolution of the sensor, whereas the upper limits are defined as the concentration in which added analyte will no longer change the response of the sensor.

Selectivity: The ability of a sensor to be sensitive to a single analyte in the presence of other analytes. Selectivity is assessed via an artificial combination of possible interfering analytes or by using a real, environmental sample that has an unknown concentration of unknown numbers of analyte types. This is a measure of the sensors viability in the field and selectivity measurements should be carried out in the order of the artificial combination followed by the environmental sample in which the sensor is to be applied.

Stability: The ability of a sensor to produce the same response to the same analyte over a period of time.

Drift: The gradual change in the response of a sensor to an analyte while the analyte concentration remains constant. Drift can be attributed to instability in the sensor or the sensor environment (e.g. contamination).

Response time: The time duration in which the response of the sensor stabilizes.

Sensors are categorized by their optical, thermal, electrical, vibrational, and chemical responses.[1] As an example, chemical sensors measure and quantify the analyte (element or compound) the sensor was designed to sense via some chemical transformation.

An example of chemical sensors are dye indicators, such as phenolphthalein (Figure 1.2), which is used in acid-base titrations to monitor large changes in concentration of H^+. Acidic solutions with

phenolphthalein added remain colorless until added base causes full deprotonation of the acid, and the pink color appears when the pH reaches 8.2 or higher. The spirolactum located at the center of the molecule breaks once the molecule becomes deprotonated, which then induces the color change from colorless to pink.[8]

Phenolphthalein alone is considered to be a detector, but upon the addition of thymol blue, methyl red, and bromothymol blue, the dye becomes part of a sensor for pH. The combination of these dyes is termed as a "universal indicator" and allows for the determination of relative pH in a solution via color change within a few pH units.[9] For the more accurate and precise determination of pH, one uses a pH probe that employs electrochemical sensing. Both the pH probe and the universal indicator have a similar dynamic range (pH = 0 - 14) but the probe has better sensitivity and resolution with significantly less noise and error than the use of dye indicators.[10]

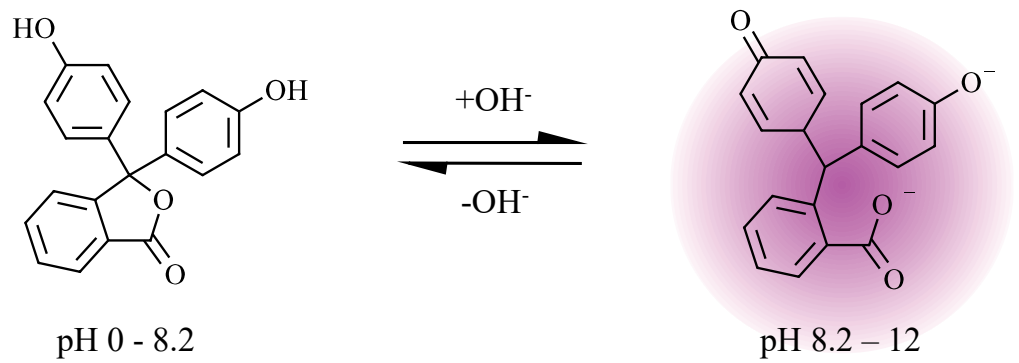

Figure 1.2 Color change of phenolphthalein between the protonated (colorless) and the deprotonated form (pink).

For pH determination, the analyte of interest is H^+, which has enormous importance in both biology and chemistry. Metal ions are also important and can be detection through a variety of methods including spectroscopy.

Spectroscopy

Using light, spectroscopists can perturb atoms and molecules of interest to gain a wealth of knowledge. Spectroscopy can be subdivided into multiple types based on the energy of the light. Use of gamma rays can provide information about the nucleus, whereas microwave spectroscopies provides information on molecular rotations.[11] Most spectroscopic techniques require the initial absorption of incident light, including UV-vis, Fourier Transform Infrared (FTIR), and microwave spectroscopies. Other techniques, like fluorimetry, measure effects after light absorption. The main spectroscopic sensing technique of this thesis is molecular fluorescence. In order to adequately describe fluorescence from excited states, one needs to understand absorption theory from ground states. The following sections will start with general molecular absorption and then lead to the connection between molecule and spectra (absorption, excitation, and emission).

Molecular Absorption Theory

The simplest interaction between light and matter is the absorption of one photon by one molecule. The general Equation 1.1 shows a molecule, M, absorbing a photon. The energy from the photon (hv)

produces an excited molecule, M*. This absorption occurs in the range of 10^{-15} seconds (s) and, depending on the energy of the incident photon, a certain excited state will be populated. The three types of excited states are electronic, vibrational, rotational, or some combination of the three.[12]

$$M + h\upsilon \rightarrow M^* \qquad where\ E = h\nu = \frac{hc}{\lambda} \qquad \text{Equation 1.1}$$

Absorption of low energy, infrared light produces vibrational excited states, while absorption of visible and ultraviolet light produces electronically excited states. Molecular identity, types of bonds within the molecule, as well as phase (gas, liquid, or solid) dictate absorption characteristics. A more in-depth explanation of an electronically excited state using molecular orbital theory is the promotion of an electron from the HOMO to the LUMO of a molecule upon absorption of an ultraviolet or visible photon.[11]

The electronic transition of a promoted electron within a molecular orbital diagram is usually simplified to an absorption diagram where the HOMO is denoted as S_0 and the LUMO is S_1 (Figure 1.3).[13] The horizontal lines show the relative energies of the various states. The thick black lines show singlet electronic state energies (S_n) coinciding with the vibrational ground state (ν_0), and the thin black lines denote the vibrational states within that particular electronic state.[13] Absorption of an infrared photon of an adequate energy by the molecule will promote an electron from the ground state to higher vibrational states (ν_{0+n}), which results in a vibrationally excited molecule (green arrows in Figure 1.3). Absorption of visible light (red arrows in Figure 1.3) results in the promotion of an electron to the first electronic state ($S_0 \rightarrow S_1$), producing an electronically excited molecule. Higher energy, visible light may promote the electron to higher vibrational states than ν_0 in S_1, thereby producing an electronically and vibrationally excited molecule. Increasing the energy of incident light even further produces an electronically excited molecule in the S_2 singlet state (LUMO +1) shown in Figure 1.3 as blue arrows.[14] As stated previously, the identity of the molecule (bonds/elements) generally dictate the wavelengths that absorb. The energy gap between the HOMO (S_0) and LUMO (S_1) within the molecular orbital diagram contracts and expands based on bonding and will absorb lower and higher energy light, respectively. The neat and quantized transitions above are descriptions of a single molecule M being excited by $h\upsilon$ to M* without other interacting molecules. Absorption spectroscopies, however deal with large populations of molecules, typically within some medium.

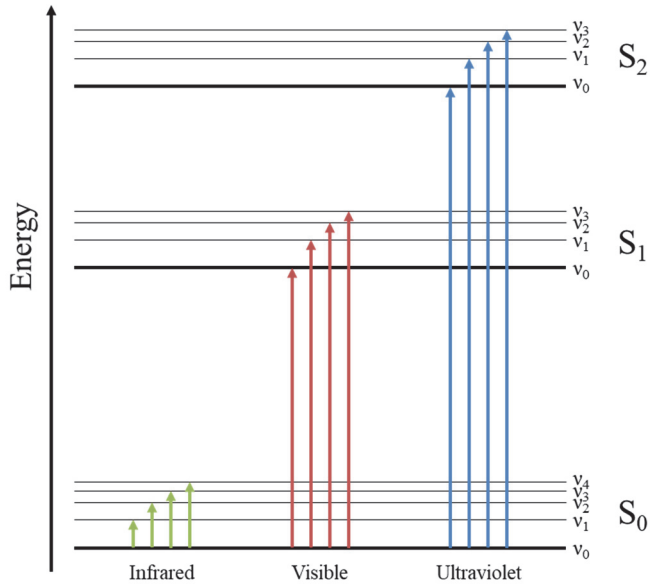

Figure 1.3 Jablonski diagram depicting the transitions of ground state electrons being promoted into excited states by infrared (green), visible (red), and ultraviolet (blue) light. S_n denotes the electronic states whereas v_n denotes the vibrational states of each electronic state. *Reprinted from Lakowicz*.[13]

In large populations of molecules, a blending of states occurs.[14] This blending results in a population distribution, called a band, around the most probable state. Depending on the complexity, symmetry, and environment of the molecules being perturbed, distinct distributions of the electronic, vibrational, and rotational bands can be observed.[14] An excellent example is the highly symmetric compound, benzene. Figure 1.4 shows the two electronic states of benzene (S_2 and S_1) dissolved in methanol as well as the refined vibrational bands within S_1. The absorption spectrum of benzene vapor (Figure 1.4 right, blue) shows the rotational bands that are within the vibrational bands. *Note: The diagram in* Figure 1.3 *does not show the rotational states within each vibrational state to reduce the complexity of the figure but one can imagine multiple rotational energy states within each individual vibrational state.* Solvent interactions can broaden band widths and remove rotational fine structure (benzene in methanol) or even remove vibrational fine structure (benzene in water), where only a single peak is shown for S_1. Navigating back to the molecular side of absorption, once the absorption of light occurs, the molecule is left in an excited state. There are many ways in which an excited state (S_1) can return to the ground state (S_0). This is generally called the deactivation of excited states.

Excited states can undergo deactivation through a variety of competing processes, each of which contribute a relative magnitude dependent on the rate constant of the process.[15] The deactivation of excited states can be divided into two categories: (1) non-radiative decay (fast) and (2) radiative decay (slow). Non-radiative decay is the deactivation of an excited state without emitting a photon, whereas radiative decay emits a photon.

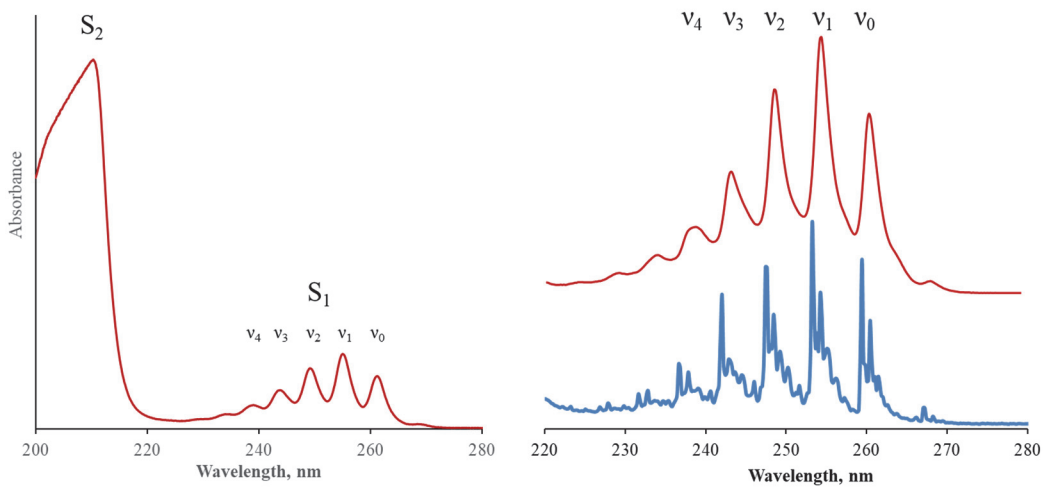

Figure 1.4 Full absorption spectrum of benzene (left) dissolved in methanol showing the two electronic excited states S_2 and S_1. Truncation of the full spectrum showing the vibrational states of S_1 (right) in dissolved in methanol (red) and provides a comparison for the refined rotational bands within the vibrational bands in the absorption spectrum of benzene vapor (blue).[16] *Spectra were taken from the author's undergraduate course work.*

Since the collision rate of molecules in solution is on the order of 10^{-12} s, the time frame of vibrational deactivation is on the order of picoseconds and is the fastest of the deactivation processes.[15] Typically, the incident photon must have more energy than required to promote the electron to the ν_0 of the S_1, and thus the electron is promoted into a higher vibrational state (ν_{0+n}) within the S_1. A vibrational deactivation (Figure 1.5, red dashed line) of the excited state (ν_{0+n}) occurs, and the vibrational state is lowered to ν_0 of the S_1.[15] An electronically excited state can be deactivated by dissipating the excess energy to the surrounding molecules through intramolecular vibrations.[14] This is called internal conversion. The internal conversion between S_2 and S_1 shown in Figure 1.5 occurs on the order of 10^{-12} s, however, the internal conversion deactivation from S_1 to S_0 is a much larger energy gap and proceeds approximately 1000 times slower (10^{-9} s, ns).

Processes that compete with the internal conversion (non-radiative) deactivation of an S_1 excited state are fluorescence (radiative) and intersystem crossing (non-radiative). Both processes progress on the order of nanoseconds (10^{-9} s).[14] Fluorescence is a radiative deactivation where a photon of lower energy than the excitation photon is emitted, returning the S_1 excited state to S_0. Intersystem crossing creates a lower energy excited triplet state T_1 (one electron spin flipped).The spin flip is induced by an adequately strong magnetic field; however, the magnetic component of light is too weak to induce a spin flip, and therefore spin-orbit coupling accounts for the change.[14] Most non-linear, organic molecules have low directional orbital momentum so that spin-orbit coupling is weak, however, with the introduction of heavy atoms (bromine and iodine), stronger spin-obit coupling is achieved, leading to a higher probability of intersystem crossing.[14] The newly created triplet state can then undergo radiative decay through the process of phosphorescence, which is on the order of 10^{-2} s.[14]

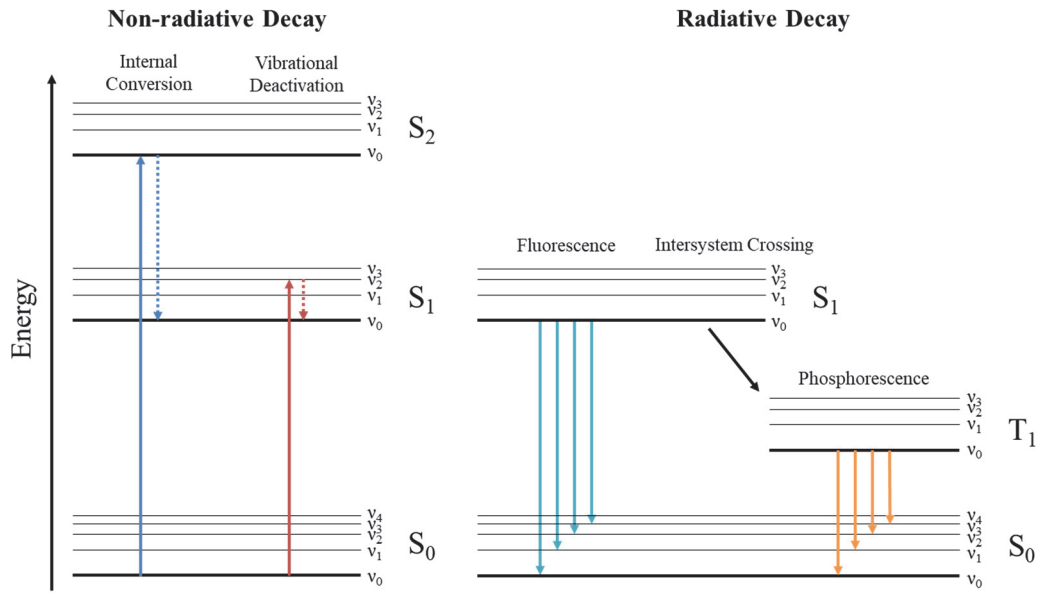

Figure 1.5 Jablonski diagrams showing the types of non-radiative decay (left) and radiative decay (right). Excitation to S_2 (blue) decays (dotted blue) to S_1 through internal conversion. Excitation to ν_2 of the S_1 state decays to the lowest vibrational state (ν_0) of S_1 through vibrational deactivation. *Reprinted from Lakowicz.*[13]

Emission of light through fluorescence and phosphorescence may be inhibited through a variety of mechanisms by a number of atoms and molecules. These processes, generally known as quenching, tend to provide a faster and lower energy route to deactivation through vibrational relaxation. Quenching will be covered in more detail in Chapter 3.

Fluorescence Theory

A molecule that has absorbed a photon (Equation 1.2) can undergo fluorescence and emit a photon, as shown in the following equation:

$$M^* \rightarrow M + h\upsilon \qquad \text{Equation 1.2}$$

which is the opposite of Equation 1.1. Fluorescence emission is the transition from the S_1 to S_0 (vibrational deactivation occurs on the order of 10^3 times faster, is from a thermally equilibrated state (S_1)[13] and therefore, as stated by Kasha's rule, emission is *only observed from the lowest excited state of any multiplicity* (vibrational manifold, $\nu = 0$)).[17] Yet, the excitation and subsequent emission from a molecule is not 100% efficient. As discussed earlier, non-radiative processes, such as internal conversions, compete as a route for deactivation. The measure of how efficient a fluorophore absorbs and emits light is called quantum yield.

Quantum yield and fluorescence lifetimes are intrinsic characteristics of a fluorophore within a particular medium and is a measure of efficiency to emit a photon after absorbance. A fluorophore with 100% efficiency or a quantum yield of 1 will emit one photon for every photon absorbed. Fluorophores with quantum yields that approach 1 display the brightest emissions. Quantum yields are calculated using the following equation:[13]

$$Q = \Gamma/(\Gamma + k_{nr}) \qquad \text{Equation 1.3}$$

where Γ is the emission rate of the fluorophore of the fluorophore and K_{nr} is all possible non-radiative decay processes clustered into one rate constant. The quantum yield of a fluorophore approaches 1 when $k_{nr} < \Gamma$, however, when the competing process of non-radiative decay approaches Γ ($k_{nr} = \Gamma$) the quantum yield approaches 0.5. If non-radiative decay becomes the primary mode of excitation deactivation, the quantum yield approaches 0. The lifetime is the average length of time that the fluorophore spends in the excited state and thusly becomes the time frame in which the environment can interact with the fluorophore. These two concepts are described with a simplified Jablonski diagram (Figure 1.6).[13]

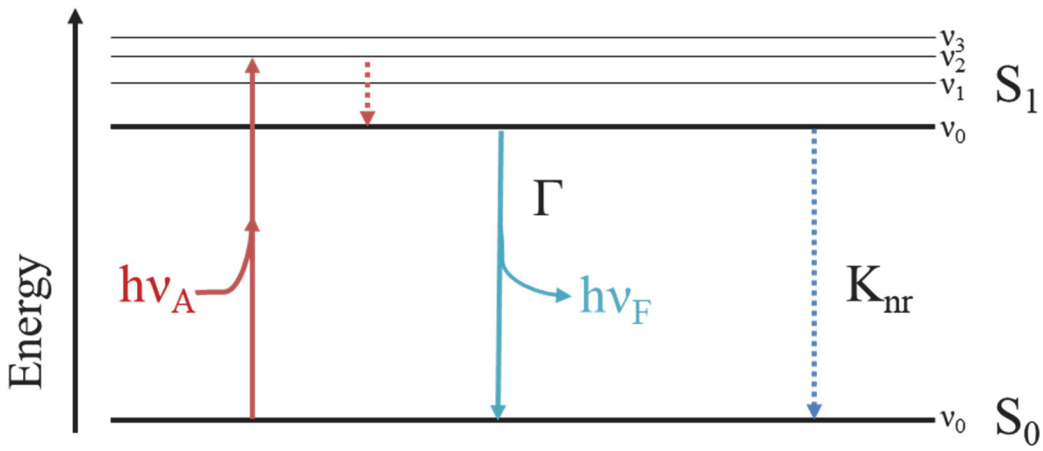

Figure 1.6 A simplified Jablonski diagram illustrating the competitive processes between Γ and K_{nr} after the absorption of a photon (hν) and the vibrational relaxation (red dotted arrow) to ν_0 of S_0.[13]

Molecular Excitation and Emission Spectra

Fluorescence excitation and emission spectra measure the distribution of large populations of emitted photons from excited molecules.[14] Emission spectra are largely independent from the wavelength of excitation. However, the intensity of the emission spectra is dependent on the excitation intensities. Selecting the wavelength that results in the highest excitation (EX 1, Figure 1.7) results in the highest emission intensity (EM 1, Figure 1.7). As shown in Figure 1.7, the emission spectra are red shifted (bathochromic) compared to the excitation, which means wavelengths of emitted light are longer and lower in energy than the excitation wavelengths. This is difference in wavelength between the excitation and emission maxima is called the Stokes shift. [10] This difference is variable depending on dye and environment.

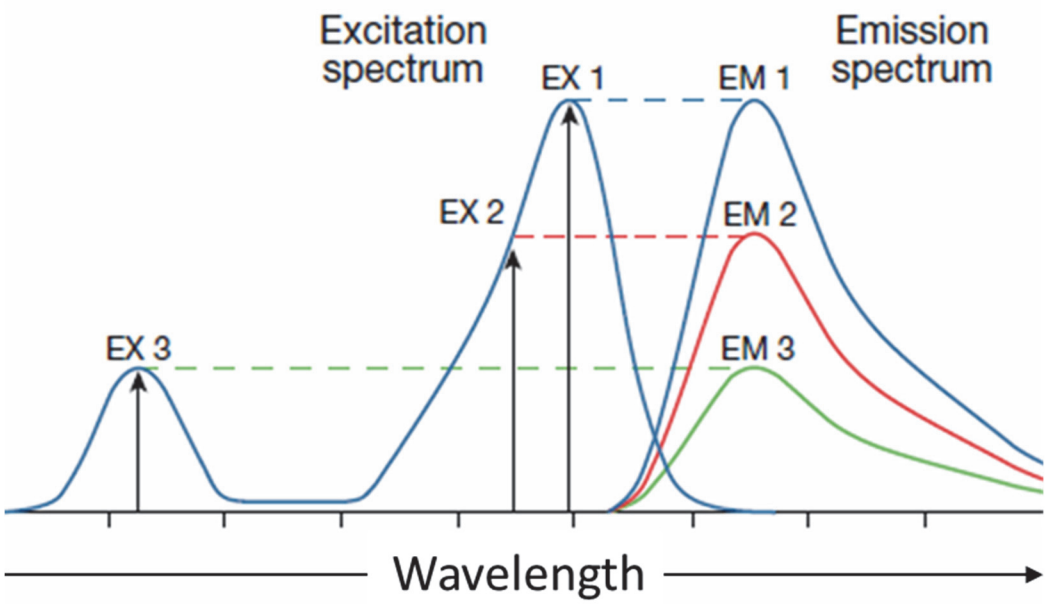

Figure 1.7 Excitation spectrum of a fluorophore and three resulting emission spectra (EM 1, EM 2, and EM 3) from the three excitation wavelengths EX 3, EX 2, or EX 1. The wavelength of emission does not change with the change of excitation wavelength but does change the amplitude or intensity of the emission spectrum. *Figure reprinted from The Molecular Probes Handbook.*[18]

At room temperature, a large population of states are accessible within the vibrational modes of S_1 as described by a Boltzmann distribution. This distribution leads to multiple S_0-S_1 promotions and broadening of the excitation/absorption band.[14] Similarly, transitions from the lowest vibrational state (ν_0) of S_1 to different vibrational energy states (ν_{0+n}) within S_0 give rise to band broadening in the emission spectra.[14] Band broadening is also found in substituted aromatic molecules. The most probable transition from S_1 to vibrational mode of the S_0 results in the most intense band and is a direct correlation to the number of molecules undergoing such a transition.[14]

Solvent and Environmental Effects

As mentioned earlier, deactivation of an excited state can occur through vibration of the fluorophore via molecular interaction between the excited molecule and the solvent. Therefore, solvent and the local environment of the fluorophore have profound effects on the emission of a fluorophore.[13] Solvent polarity and hydrogen bonding can change the quantum yield and emission spectrum of a fluorophore. Quantifying the effects of solvent polarity and hydrogen bonding have been thought of as some of the most challenging topics in fluorescence spectroscopy, and therefore a qualitative discussion will be sufficient here.[13,19] A fluorophore in a more polar solvent will result in a lower emission intensity than a fluorophore in a less polar solvent (Figure 1.8a), which then results in a redshift in the emission spectrum a process called solvatochromic shift.[13]

Absorbing a photon of light (Figure 1.8b, $h\nu_A$), by a ground state molecule M, induces a transition dipole moment within the absorbing molecule that redistributes the electron density of the molecule in the direction of the oscillating electric vector of the light wave.[13] This redistribution of electrons then polarizes the solvent molecules and causes the reorganization of the solvent molecules about the absorbing molecule. This allows for the dissipation of energy via photoinduced charge transfer from the excited molecule M^* to the solvent molecules.[19] The excited molecule emits, and the solvent molecules reorganize (relax) back to the ground state.[13]

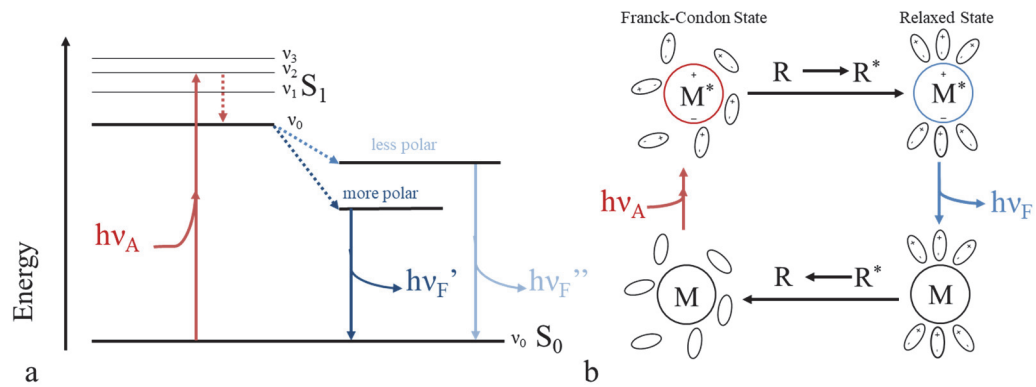

Figure 1.8 Jablonski diagram (a) showing the dependence of solvent relaxation on solvent polarity. The higher the polarity, the more energy is removed from the excited molecule causing a redshift in the emission spectrum.[13] A general depiction (b) of a ground state molecule, M, surrounded by solvent molecules, absorbing light to become excited (M^*), then emitting light to return to the ground state.

Depending on the fluorophore, this solvent relaxation process can drastically alter the emission. The dye 1-anilino-8-naphthalene sulfonic acid (ANS), shown in Figure 1.9a, is a well-known *polarity probe* due to the minimal emission in aqueous environments.[19] By measuring the emission of ANS in different solvents (Figure 1.9b), Barghouthi et al. reported a decrease in emission intensity and a redshift of ANS emission wavelength as solvent polarity increased.[20]

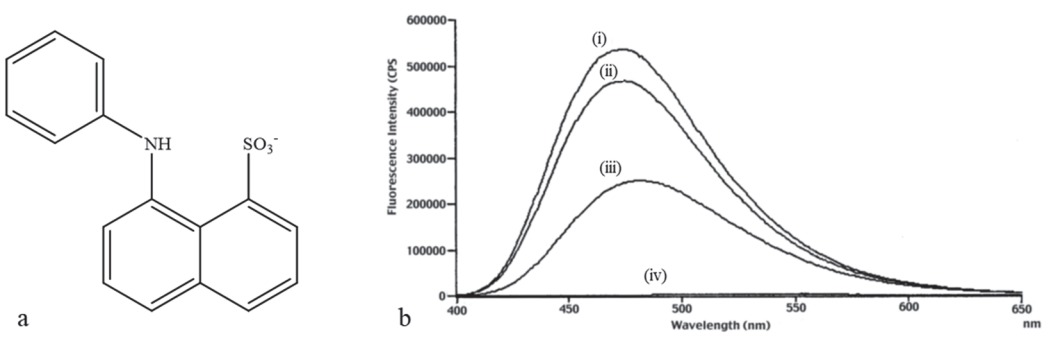

Figure 1.9 The fluorescent dye (a) 1-anilino-8-naphthalene sulfonic acid is known to be susceptible to changes in fluorescence (b) due to solvent polarity. Similar concentrations of ANS were dissolved in (i) butanol, (ii) ethanol, (iii) methanol, (iv) and water by Barghouthi et al. demonstrating that the emission intensity decreases as the polarity of the solvent increases. Reprinted (b) from Barghouthi et al.[20]

The quantum yield of ANS changes in different solvent mixtures of dioxane: water and ethanol: water (Figure 1.10). In other work, 0.2% ethanol in cyclohexane caused a significant change in ANS emission, and increasing the ethanol concentration to 3% changed the emission to a nearly identical emission spectrum of pure ethanol.[21] This was explained by hydrogen bonding interactions between ethanol and the ANS dye since macroscopic properties such as polarity and viscosity were not significantly changed.[19]

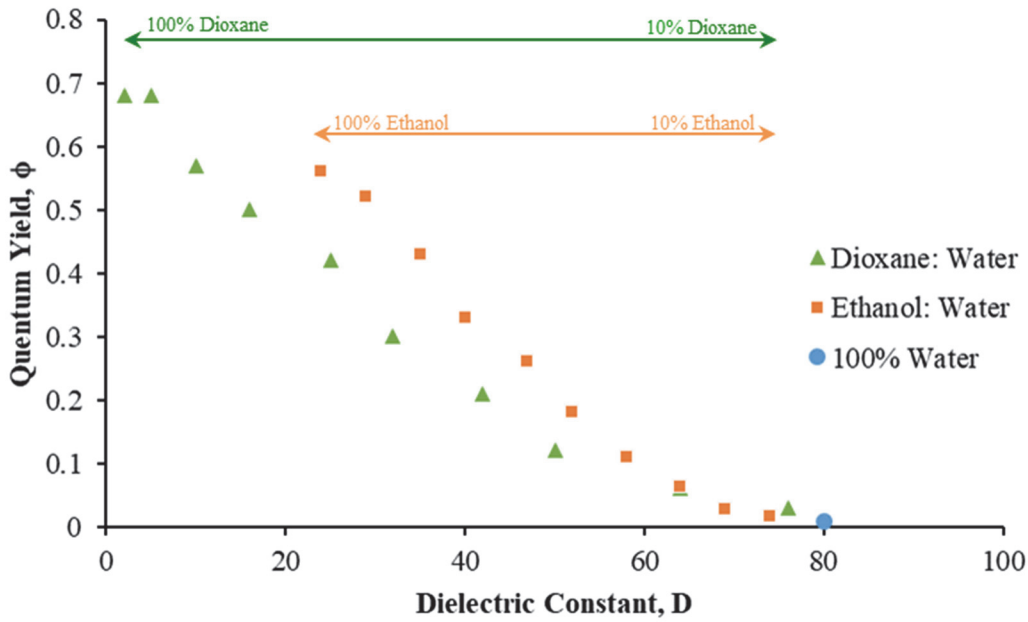

Figure 1.10 ANS in dioxane (▲) and ethanol (■) solvent mixtures with water showing the inverse relationship between dielectric constant of the solvent with the quantum yield of ANS.[21]

The polarity dependence of ANS emission has been exploited in various sensing applications for biological systems. ANS remains nearly entirely non-fluorescent until intercalated into hydrophobic regions of proteins and membranes, thereby providing a wealth of knowledge relating to cellular structures.[19] By understanding the fluorescence characteristics of a dye, such as the quenching of ANS in aqueous environments, one can design sensors with certain fluorophores that exploit desired fluorescent characteristics in order to sense environments or analytes of interest.

Fluorescent Chemical Sensors

Chemical sensing via fluorescence spectroscopy has provided various fields such as chemistry, biology, and environmental sciences a simple and fast means to identify and quantify metal ions, as well as other analytes, with incredible sensitivity and selectivity.[22] Fluorescent chemical sensors can also be tuned to a particular analyte of interest by changing the components of the sensor and are mostly a two to three component design: a fluorophore, a recognition site, and sometimes a scaffold (i.e. an anchor point). The fluorescence characteristics of the fluorophore must change in the presence of the analyte. Changes in fluorescence characteristics can either be static (do not change with time) or dynamic (changes with time). Static or steady state processes can be fluorogenic (turn-on), attenuation (turn-off), or result in a shift in fluorescence excitation/emission maxima. Dynamic sensing in fluorescence uses time-resolved changes such as fluorescence anisotropy or lifetime measurements of the fluorophore for analysis.[13] Dynamic measurements of fluorescence tend to be difficult to conduct and replicate and will not be addressed in this thesis. Static measurements in fluorescence tend to be either charge or energy transfer mechanisms.[13] The proximity of the fluorophore and quenching moiety is varied in the presence of the analyte. Turn off sensors rely on the analyte to bring the quencher within a sufficient distance to quench. Turn on sensors rely on analytes to remove quenchers from quenching distance of the fluorophore. The following section describes a few options for fluorophores as well as more in-depth examples of these fluorophores being used in chemical sensors.

Fluorophores

There are thousands of fluorescent probes available from commercial sources.[13] There are three fluorophore classes for routine fluorescence sensing: quantum dots[23,24], coordination complexes[25], and organic dyes.[26,27] The fluorescence theory provided above is for the molecular fluorescence of organic dyes utilized in this thesis. Some important parameters when choosing fluorophores for particular applications are: tunability, absorption, quantum yield, lifetime, full width at half-maximum (FWHM), conjugation, photodegredation, and Stokes shift. The following section compares and contrasts the three fluorophore classes.

Quantum dots (QDs) are semiconductor nanoparticles that range from 1-10 nm in diameter. Upon the absorption of light, excitons are produced, and light is emitted due to the subsequent recombination of the electron and hole.[24] Emission wavelengths of chemically similar quantum dots are dependent on the size of the particle. In general, as the particle increases in size, the wavelength of the emitted light also increases. As an example, the emission of cadmium selenide quantum dots excited with 365 nm light ranges from blue to red with the diameters of ~ 3, 3.8, and 4.3 nm for green, yellow, and orange emission, respectively.[24] QDs can be further tuned by synthesizing core/shell quantum dots, which can extend the emission range from 450 - 650 nm to 380 - 2000 nm. QDs exhibit longer lifetimes (Table 1.1), single peak mission spectra with a FWHM between 25-35 nm, and higher resistance to photo- and chemical degradation, compared to other fluorophores (e.g. organic dyes).[24] Longer lifetimes and narrow FWHM reduces the interference from autofluorescencing samples such as biological samples, and the lack of degradation ensures adequate emission intensities to obtain sequential measurements or continued exposure.[24]

Coordination compounds can also be used as fluorophores with transition metals and even lanthanides. Lanthanides are sometimes inherently fluorescent, however, absorption of photons tend to be low, and the eventual emissions tend to be long-lived.[28] By adding organic sensitizer chelates, lanthanides become far more useful in fluorescence applications.[28]

These organic sensitizer chelates are chromophores that transfer the absorbed energy from the photon to the lanthanide, which then emits via ligand to metal charge transfer (LMCT). Lanthanide coordination compounds emit single or multiple narrow (< 10 nm FWHM) peaks that can span both visible and NIR.[28] For applications in biology, lanthanide coordination compounds are extremely useful since the lifetimes are far longer (millisecond) than the inherent autofluorescence (nanoseconds) of autofluorescing samples.[13,28] Transition metal coordination compounds can be tuned similarly to the lanthanide complexes, extending emissions to the NIR, by changing the electronic properties of the ligands associated with the metal.[29] Large Stokes shifts and long lifetimes also make transition metal coordination compounds primary candidates for sensing in autofluorescing samples.[29]

Organic dye compounds emit intense but brief visible light (Table 1.1), which interferes with autofluorescing samples. Organic fluorophores can also be tuned through syntheses but have slightly larger absorption coefficients (Table 1.1). Under constant or repeated illumination, organic fluorophore will photodegrade especially in solution.[13] FWHM and Stokes shifts can vary dramatically in organic dyes. As an example, the fluorescein dye FITC has a FWHM of about 40 nm and a Stokes shift of less than 20 nm whereas 1, 8 ANS has a FWHM of 90 nm and a Stokes shift of 105 nm[13]. Caution must be taken when conjugating dyes, as changes in structure can alter fluorescent properties (refer to the *Organic Dyes for Sensing Applications* section).

Table 1.1 Comparison of Photoluminescent Characteristics between Fluorophore Classes[14,15,24]

Fluorophore Class	ε_{Max}, M^{-1} cm^{-1}	Quantum Yield	Lifetimes, s	Orbitals Involved
Quantum dots	10^5-10^7 (very strong)-	0.1 -0.9	> 10^{-9}	-
Organic dyes	$10^{3.7}$-10^5 (strong)		≤ 10^{-9}	π orbitals
Coordination compounds				
π-electron ligands	$10^{2.7}$-$10^{3.7}$ (medium)	0.1 -0.9	10^{-9} - 10^{-3}	π orbitals (LMCT, MLCT)
non π-electron ligands	<100 (weak)	-	-	d and f orbitals

These three classes of fluorophores (quantum dots, coordination compounds, and organic dyes) have been used in sensing of different analytes in a variety of configurations. In order for a fluorescent sensor to sense, however, an interaction between the fluorophore and the analyte must occur. For dynamic sensing, collisions tend to be the main factor in sensing, but for static sensing, binding or recognition sites are required. Electrostatic interactions and chelation of analytes ensure a static interaction between analyte and sensor during the absorption and emission of photons.

Recognition Sites and Chelation

Terms like chelation and guest-host interactions are often used to describe similar phenomenon in different contexts, although distinct differences are apparent. Chelation, in coordination chemistry, refers to molecules that coordinate with metal ions at two or more atoms through donation of electrons (Lewis bases).[30] *Guest-host* is a term typically used in supramolecular chemistry where the analyte is an entire molecule.[30] Typically, guest-host interactions include hydrogen-bonding, electrostatic, or hydrophobic/hydrophilic interactions, whereas chelation results in much stronger coordinate covalent bonds. However, chelation may be used to describe guest-host interactions.[30] Recognition or binding sites for the analyte of interest are important aspects of sensors and can be designed by understanding chelation and guest-host interactions. The structure and composition of the binding site dictates how the analyte interacts with the chemical sensor. These interactions include the selective sensing of an analyte and any inhibitory or competitive sensing of interfering analytes. Effects from interfering molecules are minimized though molecular specificity for the analyte of interest.

Typically, chelators are organic molecules that are rich in nitrogen, phosphorous, oxygen, and sulfur to serve as donors of electron density (Lewis bases) to metals (Lewis acids). The organic backbone typically consists of C-C and C-N single bonds, which provides free rotation along the bond axis and allows the molecule to wrap and twist around metal ions forming 5 or 6 member motifs.[30] Chelator shapes are quite diverse and include linear, branched, and cyclic, among others, due to this rotational freedom through sigma bonds. The denticity or number of donor sites is defined by the number of Lewis bases forming bonds to the metal ion. Increased denticity increases the stability of the chelate-metal interactions and leads to a more stable coordination compound.[30] The size of the chelate ring also plays a role in stability. The chelate ring refers to the number of atoms from one Lewis donor to the other, plus the metal atom. Saturated five -membered and unsaturated six-membered chelate rings are considered the most stable for the first row of transition metals, whereas saturated four-membered rings are sterically strained. The stabilizing "chelate effect" significantly decreases as the ring size increases beyond six.[30] An excellent example of chelation is ethylenediamine tetraacetic acid (EDTA, Figure 1.11) a well-known and broad range chelator of metal cations. EDTA has two tertiary amines and four carboxylic arms that can wrap around and engulf the cation. The Lewis bases of EDTA provide excellent orbital overlap in cations with d-orbitals creating five 5-membered chelate rings around the cation.[30]

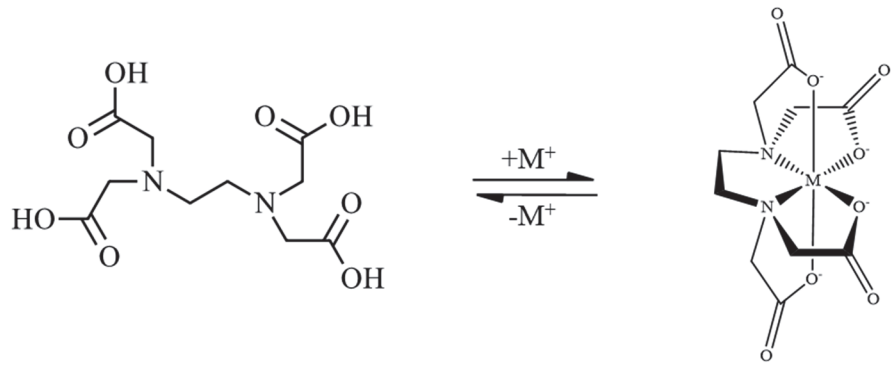

Figure 1.11 The EDTA chelation (denticity = 6) of a cation M^+

The relative stability of chelate-metal complexes comes from comparing the formation constants (K_{form}) at a given pH. The formation of a chelated metal (M^{n+}) with chelate (L) and the equilibration expression are shown in Equation 1.4 and Equation 1.5, where the brackets denote concentrations. As Equation 1.5 shows, the higher the $[ML^+]$, the higher the value of the K_{form}. Therefore, high formation constants lead to more product or chelated metal ions.

$$M^+ + L \leftrightarrow ML^+ \qquad \text{Equation 1.4}$$

$$K_{form} = \frac{[ML^+]}{[M^+][L]} \qquad \text{Equation 1.5}$$

A qualitative approach to describe and approximate large formation constants for chelates prior to experimentation is to use Hard-Soft Acid-Base (HSAB) theory. HSAB states that hard acids and hard bases, as well as soft acids and soft base, form more stable compounds than hard and soft compounds. Hard acids and bases are described as nonpolarizable whereas soft acids and bases are polarizable.[31] Examples of hard and soft acids and bases are provided in

Table 1.2. This table can be used qualitatively to predict possible ligands (bases) for certain metal ions (acids). A more quantitative description of HSAB theory can be found in Miessler et al.[31]

The HSAB theory of acids and bases does not always translate perfectly to the world of chelators. This is likely due to the denticity and organic backbone of the chelator which can increase the probability of an acid interacting with a base outside the respective class of acid.

Table 1.2 Examples of Hard Soft Acids and Bases abridged from Miessler et al.[31]

	Hard	**Borderline**	**Soft**
Bases	F^-, Cl^-	Br^-	I^-, H^-
	H_2O, OH^- O_2^-		H_2S, SH^- S^{2-}
	ROH, R_2O, CH_3COO^-		RSH, RS^-, R_2S, SCN^-
	NO_3^-, NH_3, RNH_2	$C_6H_5NH_2$, C_5H_5N, N_3^-	PR_3, C_6H_6, CN^-
Acids	H^+, Na^+, K^+		
	Mg^+, Ca^{2+}		
	Al^{3+}, Cr^{3+}, Mn^{2+}, Fe^{3+}, Co^{3+}	Fe^{2+}, Co^{2+}, Ni^{2+}, Cu^{2+}, Zn^{2+}	Cu^+, Ag^+, Au^+, Cd^{2+}, Hg^{2+}, Pd^{2+}, Pt^{2+}
	M^{4+} or higher		M^0

A predicted outcome using HSAB and Table 1.3 would be that EDTA, which is rich in hard and borderline bases, is best for hard and borderline acids. The experimentally determined formation constants for EDTA, formation constants for EDTA under high pH (deprotonated $EDTA^{4-}$), are provided in Table 1.3 and show that EDTA is a very strong borderline base due to relatively large K_{form} across all three categories. *Note: Most texts are not clear on the protonation state of the chelate and normally use the fully deprotonated state. At lower pH formation constants may be smaller due to the competition of H^+ and M^+ for the carboxylic acids of EDTA. Such cases report conditional constants, K.* Although not an explicit tool for predicting chelation of certain metals, HSAB is considered a rough starting point when designing sensors.

Table 1.3 Formation Constants for $EDTA^{4-}$ Complexes[10]

Hard		**Borderline**		**Soft**	
Acid	**log K_{form}**	**Acid**	**log K_{form}**	**Acid**	**log K_{form}**
Mg^{2+}	8.69	Fe^{2+}	14.33	Ag^{+}	7.32
Ca^{2+}	10.7	Co^{2+}	16.31	Cd^{2+}	16.46
Mn^{2+}	13.79	Zn^{2+}	16.5	Hg^{2+}	21.8
Al^{3+}	16.13	Ni^{2+}	18.62		
Fe^{3+}	25.1	Cu^{2+}	18.8		

Scaffolds

A scaffold is defined as a point for anchoring chelates or fluorophores. Scaffolds can vary in size and composition and may provide other functions such as inherent fluorescent (quantum dots), chelation properties (dendrimers), or both (proteins and DNA). In fluorescent sensors, scaffold compositions that are transparent to the wavelength of exciting and emitted light are preferred to reduce inherent sensor interference. As with fluorophores, there are nearly an infinite number of scaffolds that can be used and covering each one would be impractical. Silica-based scaffolds will be the focus here to test the hypothesis that changing the size of the scaffold will change properties of the sensor.

Silica scaffolds are quite common for visible fluorescence applications.[32-35] Glass slides and mesoporous silica can be physically dipped into reagents to apply chelates and fluorophores.[32] Even macroscopic (100- 1000 μM) particles such as controlled pore glass are readily isolated from reaction solutions via filtration. Still considered a nanotechnology, fluorescent thin films on the surface of bulky solids provide opportunities to accomplish solid state sensing via fluorimetry. Displacement assays utilize scaffolds to tether indicators until an analyte displaces the indicator, which can then be sensed in the bulk solution. Macroscopic scaffolds, however, introduce scattering effects when applied to fluorescence sensing. Nanoparticles from 10 -200 nm are a viable option when choosing a scaffold that reduces scattering during sensing. While the scattering issue of larger scaffolds can be addressed, nanoparticles themselves pose processing difficulties during chelation and fluorophore attachment as well as clean isolation and uniform dispersibility.[36] The processing issues identified in this work with modified nanoparticles will be discussed further in later chapters (Chapter 2 Synthesis, Separation, and Characterization, Past Synthetic Procedures: The Literature and the Margerum Group).

Examples of Fluorescent Sensing

A few examples of the three classes of fluorescent sensors are shown in Figure 1.12, and the following paragraphs outline how each sensor works. Additional information on sensing characteristics such as sensitivity, selectivity, dynamic range, and applications is included.

A surface modified CdTe quantum dot (Figure 1.12a), ionically couples to a modified gold nanoparticle and quenches the quantum dot via Förster Resonance Energy Transfer (FRET) mechanism.[37] Upon the addition of lead ions, the carboxylic acids on the surface of the gold nanoparticle chelated the lead, removed the nanoparticle from the quantum dot, thereby turned the fluorescence of the quantum dot on.[23] The structure of the sensor was a quantum dot used as both the fluorophore and a scaffold due to the conjugated amine groups on the surface. The amine groups were used as recognition sites (chelates) for the colloidal gold-carboxylic acid conjugate, and the carboxylic acid groups were recognition ligands for the lead to bind. Wang et al. tested a variety of other multivalent cations to determine the selectivity of the sensor. Cobalt, cadmium, copper, silver, lead, zinc, mercury, and iron (II/III) were tested with and without the addition of lead. Silver and iron were the only ions to show interference, which was circumvented using counter ions such as chloride and fluoride to precipitate silver or iron, respectively, in real samples.[37] Wang et al. found the detection limit of the quantum dot sensor at 30 ppb Pb(II) (0.14 μM) with a linear dynamic range of 0.22 – 4.51 ppm (1.1 – 22 μM). This type of sensor was applied to environmental water remediation testing and biological samples, such as blood in lead poisoning. Actual sample testing was not performed, but the study mimicked sample environments to showed feasibility.

Another example of a fluorescent sensor was a lanthanide complex sensor with sensitizer (Figure 1.12b), which uses carboxylic acids to chelate terbium ion (Tb^{3+}) while the (2-pyridylmethyl) ethylenediamines chelate any free zinc ion (Zn^{2+}). The pyridine substituents absorb photons and, zinc chelation, the absorbed photon induced an electron transfer from zinc to terbium. Upon photo-induced electron transfer (PET) from the zinc to the terbium, the terbium then emitted a photon and turns the sensor on (Figure 1.12b).[38] In this example, the sensing fluorophore was a lanthanide chelated by the diethylenetriaminepentaacetic acid (DPTA)-bisamide group (similar in structure to ETDA). The N,N-bis(2-pyridylmethyl)ethylamine (PMEA) groups were used to chelate Zn^{2+} and act as sensitizers for the zinc ion to absorb the photon. The scaffold was the DPTA and the chelated lanthanide (terbium ion). Hanaoka et. al. reported that the sensor had a 1:1 response and was sensitive to zinc at 100 μM, even in the presence of other ions. Other divalent cations that were tested included calcium, magnesium, copper, iron, nickel, cobalt, and manganese that were added separately as well as mixed with zinc ion to show the selectivity of the sensor for zinc.[38] Hanaoka et. al suggest that the chelated lanthanide metal ion sensor could be applied to biological samples.[38] Like the quantum dot example, actual biological samples were not tested.

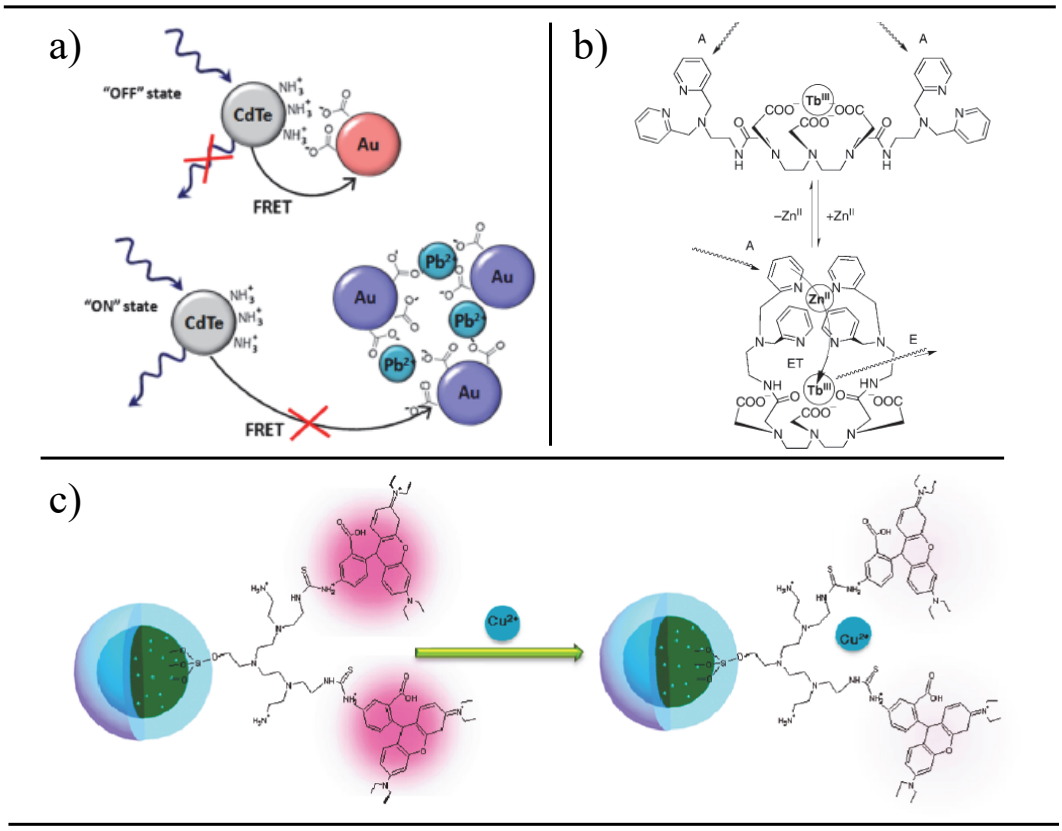

Figure 1.12 Examples of metal ion sensors that use (a) quantum dots[37], (b) lanthanide complexes[38], and (c) organic dyes.[27]

The final class in Figure 1.12 used *organic dyes* to sense metals. A double dye system was used where the dye buried in the nanoparticle was a reference dye and the external dye was used to sense copper. The reference dye (fluorescein) was incorporated into the silica nanoparticle in a so-called dye doped nanoparticle. A sufficiently thick shell of silica followed by a polymer (PEI) coating was used to anchor a rhodamine dye on the outside that limited reference-sensing dye interactions. Such ratiometric sensors avoid energy transfers, such as FRET, between the fluorophores, but isolate the reference fluorophore while the sensing rhodamine emission changes with analyte concentration. The inherently fluorescent scaffold was the fluorescein doped silica nanoparticle as well as the PEI polymer. The polymer also had chelation properties when copper was introduced which allowed the copper to interact and quench the sensing dye, rhodamine. The rhodamine dye was quenched (lowered emission intensity) upon the chelation of copper ion by the PEI polymer in the concentration range of 100-1000 nanomolar (nM) Cu(II). Zong et al. tested a number of other cations like zinc, aluminum, cobalt, nickel, silver, mercury, lead, and, cadmium to show the selectivity of the response from the sensor with copper only. As in other studies, suggested applications were water remediation and testing of biological samples. However, this study demonstrated the viability of the nanoparticle copper sensor in real samples that included industrial wastewater and the imaging of intercellular copper in HeLa cell proliferation assays.[27]

In these first three examples, the sensor was dissolved (Figure 1.12b) or suspended (Figure 1.12a and Figure 1.12b) in solution. The next example is a macroscopic solid that utilizes mesoporous silica-immobilized rhodamine coated on a glass substrate for the sensing of mercury.[39] The proposed mechanism of sensing shows an opening of the spirolactam ring within the rhodamine dye in the presence of mercury,

which then turns on the fluorescence (similar to pH sensor phenolphthalein upon protonation, Figure 1.12). The mesoporous silica was considered a scaffold for the rhodamine fluorophore (Figure 1.13).

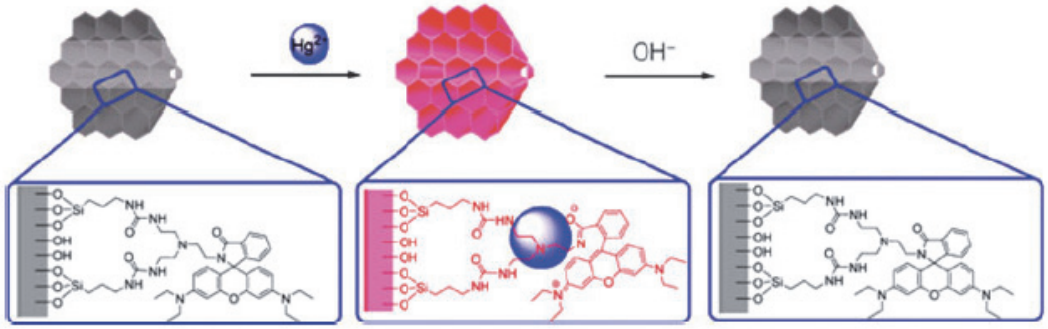

Figure 1.13 Addition of mercury turns on the fluorescence of rhodamine, and the addition of a basic solution removes the mercury and allows the sensor to be reused. Reprinted from Lee et al. [39]

The rhodamine coated mesoporous silica was used to coat the glass substrate by merely drying to the surface of the glass, which was yet another scaffold (Figure 1.14).[39] The tethering group 3-(triethoxysilyl) propylisocyanate along with the spirolactum ring of the rhodamine was used as the chelate for the mercury ion (Figure 1.13). The rhodamine coated mesoporous silica was also used independently of the glass substrate as a sensor in solution.

Lee et al. did not report the limits of their sensors. Single additions of 2.25 mM Hg(II) were added to the mesoporous suspensions and to the substrates (Figure 1.14). The addition of hydroxide ion at 0.005 M elicited a third decrease in emission intensity, and an increase to 0.5 M OH^- resulted in a two-thirds decrease in total intensity.

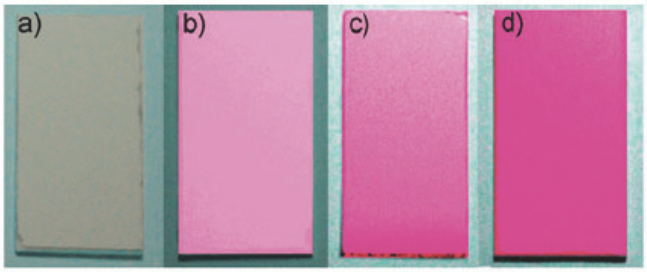

Figure 1.14 The glass substrates shown without (a) and with the presence of (b) 1.0 x 10^{-5}, (c) 1.0 x 10^{-4}, and (d) 1.0 x 10^{-3} M Hg^{2+}. Reprinted from Lee et al.[39]

The addition of Zn^{2+}, Pb^{2+}, and Cu^{2+} resulted in 12%, 12%, and 50% increase in emission as observed with mercury, respectively.[39] Interestingly, the original authors performed similar work a few years later (not shown) with a shorter, tris(2-aminoethyl)amine tether to attach the rhodamine 6G directly to a glass substrate. This resulted in a specificity to lead using a similar spirolactum ring opening mechanism.[40] The detection limit of this lead selective sensor was 10^{-4} M Pb(II). A wide range of ions were tested at this concentration (Li^+, Na^+, K^+, Mg^{2+}, Fe^{2+}, Fe^{3+}, Co^{2+}, Cu^{2+}, Ag^+, Zn^{2+}, Cd^{2+}, Hg^{2+}, etc) and resulted in an average of 6x lower fluorescence, indicating selectivity for lead.[40]

The examples given above provide a glimpse into the world of fluorescent chemical sensors. By using nanotechnology through bottom-up techniques via chemical syntheses, sensors can be created and tuned for specific sensing at a wide range of concentrations. Currently, the field of fluorescent chemical sensors is still in its infancy where most sensors are made and tested against a battery of analytes to

determine responses and sensitivities. Eventually, a sensor may be designed via chemical synthesis with a particular analyte in mind.

Low Concentration Analytes of Interest

The following sections are meant to provide guidance as to the level of importance and impact of certain chemicals and compounds in different contexts. The chemicals are found at low concentrations (nM-μM) in aqueous environments and are broken down into three groups, which include biologically essential metals, hazardous metals, and non-metals. These sections should provide some bearing for application of the sensing materials presented in this thesis as well as future project goals to create new materials aimed for different chemicals of interest that will expand the modular design library of such sensors.

Biologically Essential Metal Ions

In general, transition metals ions are required for the function of many cellular processes. Without the necessary concentrations of these ions, cellular processes may shut down, leading to adverse effects. Metal ions that are considered biologically essential are those that are required for an organism to assume normal function. These ions include several oxidation states of copper, zinc, iron , manganese, cobalt, or molybdenum.[41] Different organisms require different ions to continue normal life processes, and thus examples will be given to compare the variety of biological needs. This section will focus on humans and the respective diseases and disorders that arise from a surplus or deficiency of two metals ions.[41]

A conserved trait among the animal kingdom is the use of a circulatory system to transport biologically important compounds throughout the organism. Blood components between organisms, however, can differ drastically. For example, humans and the majority of vertebrates use hemoglobin for oxygen transport, which employs an iron ion within a porphyrin cofactor and a histidine residue to bind oxygen for transport. This iron active site within the heme group is the reason that blood is red. In contrast, spiders and crustaceans, as well as some mollusks, octopuses, and squids, employ a copper cluster bound by histidine residues to transport oxygen within the protein hemocyanin and, as the name suggests, the blood is a blue or cyan colored.[42]

While copper is not at the center of oxygen transporters in humans, copper is generally used for single electron redox chemistry in a variety of other proteins.[43] One such protein, ceruloplasmin, converts ferrous iron to ferric iron (Fe^{2+} to Fe^{3+}) and contains up to 70% of the copper (Cu^{2+}) in blood serum,[43] of which concentrations in the average adult human ranges from 17 to 27 μM.[44] Deficiencies in copper can lead to a number of negative consequences within the body. Table 1.4 provides a breakdown of average copper concentrations in human organs measured in autopsies.[45]

Table 1.4 Copper concentrations in Human Organs

Organ	Concentration, μM	n=
Liver	54.6	79
Brain	52.2	43
Heart	51.3	5
Kidney	33.8	76
Lung	30.1	27
Spleen	19.4	3

Menkes disease, a genetic disorder that affects the copper transporter within cell membranes mostly found in the large intestine, leads to dietary copper deficiencies due to malabsorption. Lack of copper can wreak havoc in other areas of the body, such as the brain, where the thinning of atrial walls caused by copper deficiencies can lead to fatal aneurisms.[43] Another genetic disorder called Wilson disease is characterized by the overabundance of copper. Normal absorption of copper in the intestines is displayed in patients with Wilson disease; however, the cause of the disease is the reduced function of copper excretion. Without proper excretion, copper accumulates, leading to liver toxicity and neurological symptoms such as depression, schizophrenia, speech impediments, and tremors.[43] Regulation of copper levels within the brain is incredibly important, as shown by the severe symptoms of Menkes and Wilson disease. Copper has also been linked to the development of other neurological diseases in patients not affected by Menkes or Wilson disease. These diseases include Parkinson's, Creutzfeldt-Jacob, and Alzheimer's disease.[43] A hallmark of Alzheimer's is the aggregation of proteins called β-amyloid, which leads to plaques within the brain that in part cause dementia. Low copper concentrations within the brain have been reported in Alzheimer's patients, whereas elevated copper levels were shown to inhibit amyloid accumulation in mice with a genetic predisposition for amyloid plaque formation.[43] Zinc was also reported to be linked to Alzheimer's, however the overabundance of zinc within the brain is thought to aid in amyloid plaque formation.[46]

Zinc, the second most abundant transition metal in most organisms, is important in the regulation of gene expression in humans, since 50% of all transcription regulatory proteins contain zinc active sties.[47] In humans, zinc can be found in concentrations of 140 μM in whole blood samples.[48] Zinc was also found to be active during insulin secretion from the pancreas, and free zinc ion is released upon the oxidative stress of cells. Additionally, excess intracellular zinc is a contributing factor in neurological disorders such as epilepsy and Alzheimers disease.[47] Studying the inter- and intracellular concentrations of zinc could provide new insight into the disease. Maret et al. propose that fluorescent chelating agents hold the greatest promise for zinc ion studies in biological environments.[46] However, more robust studies must be done on the interactions of fluorescent dyes with various analytes to ensure that the sensing characteristics of the dye reflect the sensing of the target analyte and not of interfering contaminants. Current monitoring of metal ions in certain fields of cell biology rely on molecular dye systems that are found to have varying sensitivities to non-analyte metals, thereby resulting in modified protocols to adjust for false signal changes.[26] Studying dye-metal characteristics could lead to more sensitive and selective sensing as well as to the development of techniques for studying metal ions *in vitro.* The use of fluorescence for the sensing of ions could be applied toward measurement of copper levels and subsequent diagnosis of Menkes or Wilson disease.

Patients with an excess or deficiency of biologically essential metals can experience a range of diseases. Competition of those essential metals with other metals and ions can also lead to disease. Metals and ions that inhibit normal function of proteins within cells by replacing the essential metals are considered hazardous and responses to those hazardous metals, much like the biologically essential metals, vary with concentration.

Hazardous Metals and Metal Ions

Hazardous metals produce a toxic response at concentrations that interrupt the normal biological processes of an organism. Hazardous metals, such as mercury, can bio-accumulate within the organism through its life, presenting symptoms later on as well as passing the hazardous metal through the food chain to other organisms.[49] Sources of hazardous metals include mining, industrial uses, and improper recycling

and storage of the metals that eventually leech into the environment through waterways.[49] The Agency for Toxic Substances and Disease Registry (ATSDR), a federal public health agency of the U.S. Department of Health and Human Services, protects communities from the potentially harmful effects from exposure to natural and synthetic hazardous materials.[50] Under the Superfund Amendments and Reauthorization Act (SARA), the ATSDR and the Environmental Protection Agency (EPA) are required to create a priority list of hazardous materials that are commonly found at facilities listed on the National Priorities List (NPL) and pose a significant threat to human health. The priority list of hazardous materials is not, however, a listed in order of the most toxic substances but prioritized based on a combination of the frequency, toxicity, and potential for human exposure at NPL sites. The complete and current Substance Priorities List (SPL) can be found on the ATSDR website along with the description of the scoring system and is updated every two years.[50] The EPA also publishes a list of hazardous chemicals that provides contamination level data.

The EPA also limits the amount of certain contaminants in drinking water. The National Primary Drinking Water Regulations (NPDWR) are designed to be legally enforceable primary standards and treatment techniques that are applicable to public water systems and limit the levels of contaminants in drinking water. The NPDWR provides Maximum Contaminant Levels (MCL) for each of the contaminants and potential health concerns as well as potential contamination sources. The MCL are in concentrations of parts-per-million (ppm, mg/L) and, although low, concentrations that exceed the MCL may cause significant health effects. Table 1.5 shows the ATSDR rank, MCL, and potential health effects of selected hazardous contaminants that were considered relevant to this project.

Furthermore, the EPA issued the Lead and Copper Rule on June 7, 1991, which has a primary objective of minimizing lead and copper levels in drinking water through water treatment to prohibit corrosion of lead and copper containing plumbing (Table 1.5).[51] The Action Level (AL) for lead and copper are 0.015 mg/L (72 nM) and 1.3 mg/L (20 μM) respectively. If lead and copper levels meet or exceed the ALs, then one or more of the following actions must be performed: source water monitoring and source water treatment, corrosion control treatment, or service line replacement.[51]

Table 1.5 Selected Ions from ATSDR Substance Priority List and the NPDWR

Name	ATSDR 2017 Rank	National Primary Drinking Water Regulations	
		MCL* (mg/L)	Potential Health Effects from Long-Term Exposure Above the MCL
Arsenic	1	0.010	Skin damage or problems with circulatory systems, and may have increased risk of getting cancer
Lead	2	0.015	Infants and children: Delays in physical or mental development; children could show slight deficits in attention span and learning abilities Adults: Kidney problems; high blood pressure
Mercury	3	0.002	Kidney damage
Cadmium	7	0.005	Kidney damage
Cyanide	35	0.2	Nerve damage or thyroid problems
Cobalt	51	NA	NA
Nickel	57	NA	NA
Zinc	75	NA	NA
Chromium	78	0.1	Allergic dermatitis
Copper	118	1.3	Short term exposure: Gastrointestinal distress Long term exposure: Liver or kidney damage
Silver	225	NA	NA

* Maximum Contaminant Level (MCL) - The highest level of a contaminant that is allowed in drinking water. MCLs are set as close to MCLGs as feasible using the best available treatment technology and taking cost into consideration. MCLs are enforceable standards.

Non-metals Requiring Detection

As with metals, the non-metal compounds of interest within this work have biological importance, such as phosphates (PO_4^{3-}). Phosphates are ubiquitous in animal cells and are involved in a variety of processes such as pH buffering, energy transference, membrane synthesis, and cell signaling. By monitoring the levels of free phosphate, these cellular processes can also be monitored.[52] Other non-metal ions can cause detrimental effects to personal and environmental health, such as cyanide (CN^-). The MCL of CN^- is 0.2 mg/L (4.1 μM) for drinking water set by the EPA, and upon exposure of levels higher than the MCL, cyanide has adverse effects to the central nervous system as well as other areas that have a high metabolic demand for oxygen, such as the lungs.[53] Cyanide primarily affects cellular function through the binding of metals within metalloenzymes, such as the copper center of cytochrome c oxidase, which then prevents cells and tissue from using oxygen.[53] This leads to systemic histotoxic hypoxia and can eventually lead to death. Detection of anions are often more difficult to detect than cations, however, anion-induced changes to the fluorescence characteristics of certain dyes allow for the detection of these ions at low concentrations.[54]

Other non-metal compounds are listed in the ATSDR, such as aromatic compounds, which include trinitrotoluene (TNT), polychlorinated biphenols (PCBs), dichlorodiphenyltrichloroethane (DDT), and polyaromatic hydrocarbons (PAHCs). Although these compounds all have detrimental effects to both the environment and personal health, many of these compounds are intrinsically fluorescent. Thus, the sensing of these compounds via a fluorescent chemical sensor is a challenging endeavor that will require selectivity between mixtures of aromatics that cannot be discerned through fluorescence spectroscopy alone.

Designing an Ideal Sensor

When designing a sensor, several considerations regarding the scaffold, chelator, and fluorescent probe must be made to ensure the effectiveness of the sensor. The scaffold must not interfere with the measurement of signal. The chelator should follow the principles of coordination chemistry such as preferred donors, ligand field geometries, and hard-soft acid-base concepts and must not attenuate or influence the fluorescence signal. The chelator and fluorophore together must be selective to a specific ion, especially when in competition with high concentrations of other ions with similar charges.

Nanoparticles as Scaffolds

Suspended nanoparticles in solution provide an easily isolated conjugate, unlike their dissolved molecular sensor counterparts, and have limited spectroscopic interference as compared to macroscopic scaffolds. Nanoparticles also provide a vastly larger surface area for the same amount of material as a macroscopic scaffold. To further clarify, imagine a spherical particle the size of a regulation sized baseball. The surface area of this macroparticle is about 1.68×10^{16} nm^2 with a volume of about 2.04×10^{23} nm^3. The ratio of surface area to volume for this macroparticle would be 8×10^{-7}. Now, if we use the same amount of material to create 200 nm spherical particles, the ratio increases to 0.030, which is a 375,000x increase in surface area for the same mass. This would allow for an increase of surface area for surface modifications for sensing applications. Surface modifications alter not only the sensing capabilities of the particles, but also the chemistry and the stability of the particle in solution.

Colloids are insoluble particles that are dispersed in a suspension media or more specifically a homogenous distribution of particles throughout the suspension medium. Stable colloids are characterized by the resistance of particle precipitation within the suspension medium. Colloidal stability remains an important aspect in the world of colloids, and is especially important to consider when developing a sensor.

Without adequate dispersion, problems with detection and sensitivity may arise, especially when measurements rely on the absorption and emission of photons within a cuvette. The following colloidal stability argument is based on electrostatic stabilization in an aqueous environment. A more mathematically rigorous argument, as well as other arguments, such as steric stabilization and the perturbation-attraction theorem, are available in the text *Structured Fluids Polymers, Colloids, Surfactants.*[55,56]

Induced-dipole interactions are common in condensed phases and exist regardless of electrical charges. Particles that have a net electrical charge that is neutral are more prone to aggregation due to the particle being more polarizable from another neutrally charged particle.[55] The net polarization from particle to particle results in the attractive forces that agglomerate particles. Polarization still occurs when the net electrical charge is not neutral (positive or negative), however, the net electrical charge overcomes the induced dipole. Therefore, the attractive forces from induced dipoles is overcome by the Coulombic repulsion between particles.[55] Additionally, to remain in suspension, particles require enough thermal energy to overcome the gravitational force on the particle. As the particle grows in size, the required thermal energy to prevent gravitational precipitation (settling) also grows. By increasing the Coulombic repulsion, particles are less likely to aggregate and then less likely to be overcome by gravitational forces, which then leads to a more stable colloid. There is an upper limit on particle size that is dependent on the colloid system (suspension media and particle composition). Conversely, particles that are too small are not adequately surrounded by solvent molecules and will agglomerate upon contact with another particle due to induced-dipole forces. This is due to small particles being too small to have enough surface charge.

Particle sizes can range from nanometers to microns, and the ability to obtain indefinite suspension of the particle in a fluid depends on the size of the particle. Thus, factors such as composition, size, concentration, and surface charge of the nanoparticles need to be taken into account to select viable routes to create a sensor from a nanoparticle scaffold.[56] *Note that there are other properties such as shape that may need to be addressed for applications outside of the aims of this thesis.* There are an almost infinite number of available nanoparticle compositions that vary in properties. The easiest distinction between particle compositions is the organic and inorganic divide.

Some of the more common organic nanoparticles are polymer based and include polystyrene, poly(strene/acrylate) copolymer, poly(methylmethacrylate), and poly(hydroxyethylmethacrylate.[56] These organic nanoparticles remain transparent in the visible spectrum when suspended in a colloid, however, aromatic side chains in the polystyrene polymers can interfere with excitation and emission of fluorophores, while the ether linkages in the acrylate nanoparticles provides sites for chelation of metal ions.[56] Organic nanoparticles are also considered nanoplastics, and use of organic nanoparticles may add to the already problematic micro/nanoplastic problem in the environment.[57] Other organic nanoparticles made from biodegradable polymers such as poly-(D,L-lactide-co-glycolide) are readily available and have been used in areas such as drug delivery.[58] These nanoparticles also have a large number of ether linkages that can be offered for metal ion chelation. A disadvantage to organic nanoparticles is susceptibility to degradation in organic solvents during synthesis.

Inorganic nanoparticles include metals, metal chalcogenides, and main group oxides. Some inorganic nanoparticles such as gold remain inert and have been used for sensing applications in the past.[37,59] Iron oxide nanoparticles are extremely convenient to functionalize and use, with rapid isolation of the nanoparticles from reaction solutions via magnetic properties of the nanoparticles. However, both of these nanoparticles are opaque and can interfere with fluorescence by absorbing or scattering light. Metal sensing has been achieved with magnetic nanoparticles, although via Ion Coupled Plasma Optical Emission Spectroscopy (ICP-OES).[60] As discussed in a previous section, quantum dots (an inorganic nanoparticle)

can be used for a scaffold as well as a fluorophore, however the composition and size can make the use of the quantum dot an unfavorable option. Current materials used for quantum dots tend to be toxic (cadmium or lead chalcogenides), which would be counterproductive to the green chemistry goal, whereas sizes of quantum dots (1-10 nm) vary with color but ultimately small nanoparticles pose a challenge for surface coatings when colloidal stability is important. Coatings involving silanes or the other, more challenging surface coatings[61], can remedy toxic effects, however, the interference with fluorescent measurements is a hindrance with the metal and metal chalcogenides nanoparticles.

Silica: An Ideal Scaffold

An inexpensive, visibly transparent material that is readily synthesized and functionalized is silica (SiO_2). Silica nanoparticle syntheses have been extensively studied, and the variables that control nanoparticle size have been determined. Silica is essentially inert and found in the environment as sand or in life such as in the shells of diatoms.[62] Silica is also readily imbued with internal dyes during synthesis[15,63], which may offer interesting sensing characteristics such as ratiometric sensing. For these reasons, silica nanoparticles were chosen to be the scaffold for this thesis. Alumina would also make a seemingly viable option for a scaffold; however, alumina nanoparticle studies are not used as ubiquitously as silica, which could pose downstream problems in sensor development.

Silica nanoparticles are typically synthesized via the bottom-up process call the Stöber method (more detail in the following section Synthesis of Silica Nanoparticles). Here, the size is controlled by volume-to-volume ratios between water and ammonia during the polymerization of the tetraethylorthosilicate into SiO_2. The stability of dispersed silica nanoparticles in water is dependent on the surface of the nanoparticle.[64] Surface charge and the ability to form hydrogen bonds allow silica nanoparticles to remain suspended indefinitely. The outermost layer of a silica nanoparticle is primarily silanol (Si-OH) groups[64] that readily accept and donate hydrogen bonds. This allows for layers of water molecules to non-covalently coat the nanoparticle (hydration layers). At low pH the bare silica surface is considered to have an overall neutral charge. The pH at which the surface charge is neutral is called the isoelectric point (IEP) and occurs at pH 3.4.[64] Upon lowering the pH, surface charge becomes more negative as the silanol group becomes deprotonated and reaches a maximum negative charge at pH 7. An overall negative charge repels other nanoparticles, which leads to fewer agglomerations and a more stable colloid.

Surface coatings with silanes or other conjugates are best when the surface charge is not changed during the synthesis.[36] Addition of inert groups, such as methyl groups, while conjugating active groups (amines) were found to be necessary to ensure colloidal stability.[65]

The surface of the nanoparticle is affected by the composition of the outermost layer or coating and the size of the nanoparticle. In fact, the size of a spherical particle determines the curvature of the particle surface that can greatly affect the pK_a and therefore the charge of conjugated molecules.[66] As described in Wang et al., as nanoparticle size increases, the curvature decreases and the distance between charged head-groups decreases. Electrostatic repulsion increases and shifts the equilibrium of protonation/deprotonation towards the uncharged species. Wang et al. concluded the pK_a of a head group on a nanoparticle should lie between that of a free species and that of a monolayer on a flat surface.[66] In the case of 11-mercaptoundecanoic acid (MUA), a drastic range between free ($pK_a = 4.8$) and bound on a flat surface ($pK_a = 10$) could pose a potential issue when using a general pK_a table when designing nanoparticles and their respective coatings.[66]

Surface Coatings of Nanoparticles

Coating the surface of a nanoparticle is a useful method to change the surface characteristics and functionality. The goal of surface coatings is to achieve desirable characteristics such as increased dispersibility, the addition of binding sites, or variation of the optical properties of the material. As described earlier, Zong et al. used a combination of a polymer and dye to functionalize the surface of a nanoparticle to bind and sense an analyte.[27] By changing the polymer and dye of these particles, a wide variety of sensors can be synthesized and tested without changing the nanoparticle core. This idea that modification to the surface results in changes to the functionality of the particle can be applied to other particles as well.

As described in the previous section, silica is an inexpensive and versatile scaffold material that can be modified to make a variety of scaffold types. A wide variety of surfaces can be created through reacting the surface of silica nanoparticles with silanes. Silanes are reactive silicon containing molecules that can be divided into two types that are based on the surfaces that are created: inert and reactive (coupling agents). *Note: A multitude of silane options for surface coatings are available through Gelest.*[67] Both inert and reactive silanes are useful for coatings for sensor synthesis. An inert silane, such as trimethoxymethylsilane (MTMS), is used as a spacer between reactive silanes like aminopropyl-triethoxysilane (APTES). An MTMS spacer can decrease steric interference between APTES groups on the surface of the particle. The reactive group then provides a tether to add additional functionality to a surface.

Due to the difficulty of maintaining a stable colloid of silica nanoparticles in non-aqueous solvents, bioconjugate techniques are used to ensure non-specific reactions and coagulation are minimized. *Note: Bioconjugate techniques are considered organic, but the technique uses a subset of reactive groups on the molecule of interest to react at specific functional groups in non-traditional solvents used in organic synthesis.* A bioconjugate is the linking (-conjugate) of a molecule(?) to a biomacromolecule (bio-) substrate to add functionality.[56] This may include adding a fluorescent dye to a protein for microscopy studies or the tethering of two proteins to increase the efficiency of enzymatic catalysis. *Note that throughout the remainder of the thesis, nanoparticles that differ in functionality or other characteristics are referred to as conjugates. Also, when discussing the fluorescence of molecules, the term conjugation will appear and refers to the altering of single and double bonds in organic molecules.*

The reactive groups for the conjugating agents are made by traditional organic synthetic methods, are commercially available, and most react readily in aqueous environments.[56] An incredibly helpful text written by Greg T. Hermanson ,*Bioconjugate Techniques,* outlines these techniques to help plan a synthetic route to the conjugate of interest.[56] Hermanson provides a number of general reaction protocols to provide insightful direction in troubleshooting and adapting the process to the conjugate of interest. With only a few dozen different reactive groups, an almost infinite number of conjugates can be created that differ in structure and functionality.[56] Table 1.6 shows a selected collection of reactive groups for amine and thiol functional groups that are most relevant to this thesis.

Note: A more exhaustive list is provided in Greg T. Hermanson's Bioconjugate Techniques. These functional groups are added to a molecule or macromolecule to provide a selective yet easy route to functionalize a surface or molecule. Armed with a functional group table (Table 1.6) and knowledge of the molecule to be conjugated, any number of conjugates with specific functions and applications can be designed. Examples of some molecules to be conjugated, along with functions of the molecule are provided in Table 1.7. Commonly bioconjugated molecules are commericially and come with the reactive groups attached.

Table 1.6 Selected reactive groups on conjugating agents for common starting functional groups

Surface Functional Group	Reactive Group	Bond Formed
Amine, Carboxylic acid	Imidazole	Amide, Ester
Amine	Acyl azide	Amide
	N-Hydroxysuccinimide (NHS)	Amide
	Iscothiocynate (ITC)	Isothiourea
Thiol	Maleimide	Thioether
	Aziridine	Thioether
	Pyridyl disulfide	Disulfide

Fluorescent dyes such as fluorescein are available with a variety of conjugating reactive groups, which include isothiocynate (FITC), a group that reacts with primary amines. This method of fluorescent labeling is used often in cell biology experiments to label protein residues such as glycine and lysine.[56] Polyethylene glycol (PEG) is a commonly employed conjugating agent, used to increase the solubility of pharmaceuticals or to stave off immunogenic responses. PEG comes with mono- or bifunctionality (reactive groups).[56] Bifunctional PEG can be homo- or heterofunctional, which can give rise to selective conjugation of two entities with two different available functional groups. This approach is described in Chapter 2, in the case of NHS-PEG_x-Malemide. PEG can also be controlled synthetically to contain a variety of lengths (x = 2, 4, 8, 12, 24 units) to vary the distances between the tethered entities.[56]

Table 1.7 Selected molecules used in bioconjugation by functionalizing with reactive groups[56]

Molecule	Function
Fluorescein	Fluorescent label
Polyethylene glycol (PEG)	Enhances water solubility, reduction of immunogenicity, extends stability and half-life
Terpyridine	Tridentate ligand for most transition metals
Immunoglobulins	High affinity and selectivity towards antigens
Dendrimer	Drug carriers, enhanced detection sensitivities, metal chelation, multivalent bioconjugation scaffold

Dendrimers, as with synthetic PEG polymers, can also vary in sizes, though the globular-like polymers differ in generation (n = 0-10 at intervals of 0.5). These dendrimeric polymers can be used in metal chelation due to the large number of available functional groups within the polymer that can act as chelation sites. The end groups of the dendrimers increase with increasing generation and can be used to tether the dendrimer to a surface or add fluorescent labels.

Use of Polyamine Dendrimers for surface coatings: An Overview

Dendrimers are a generic class of synthetically produced macromolecules that have a core with branching arms that, through careful syntheses, lead to controlled molecular mass and size. They are considerably different from linear polymers. Polyamine dendrimers are a subclass where the terminal branching arms terminate in primary amines, although many external surface groups are possible.[68,69] Linear polymers are considered a 1→1 polymer, which means the polymer does not branch after the addition of each new monomer. Dendrimers typically have a 1→2 fractal branching pattern (sometimes 1→3) leading to a doubling (or tripling) of each end group with every addition of monomers.[70] Addition of monomers

increases the generation of the dendrimer. An example of a 1→2 dendrimer is shown in Figure 1.15 where a single arm branches into two on every arm, therefore a dendrimer with 4 end groups would grow to 8 end groups after the addition of monomers. The two approaches of dendrimer synthesis are the divergent or convergent approach (Figure 1.16). As described by the names, the divergent method uses a core (atom or molecule) to then build up the dendrimer from all sides thereby diverging from the core. The convergent method, however, builds up the branches first and then links the branches together, or converging, to form the core. Each synthetic method has strengths and weaknesses depending on certain synthetic goals. At first glance, divergent and convergent approaches appear quite similar, however, emphasis on the core type can instill the distinction. A larger polyaromatic core that is insoluble in most solvents, such as a perylene anhydride, is best incorporated via the convergent method.[71] This allows for any issues in insolubility to be addressed after the branched arms of the dendrimer have been formed.

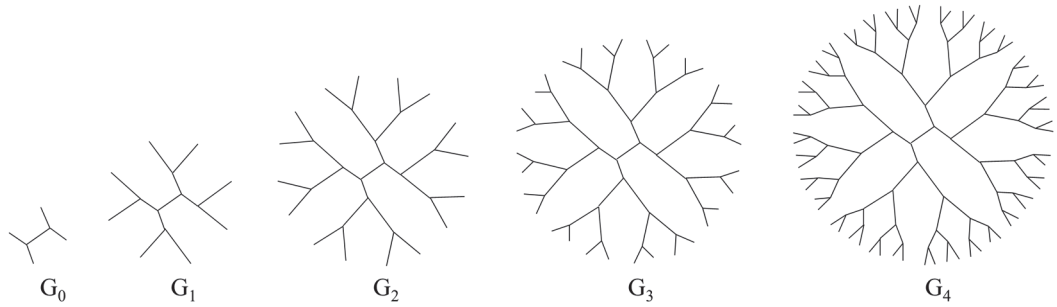

Figure 1.15. Line structure depiction of dendrimers showing relative size increases and branching as dendrimer generation increases from generation 0 (G_0) to generation 4 (G_4). *Note. In this illustration, the lengths of the lines are not representative of bond lengths, molecules were drawn for clarity, and shapes as drawn are not representative of the shapes of dendrimers in solution.*

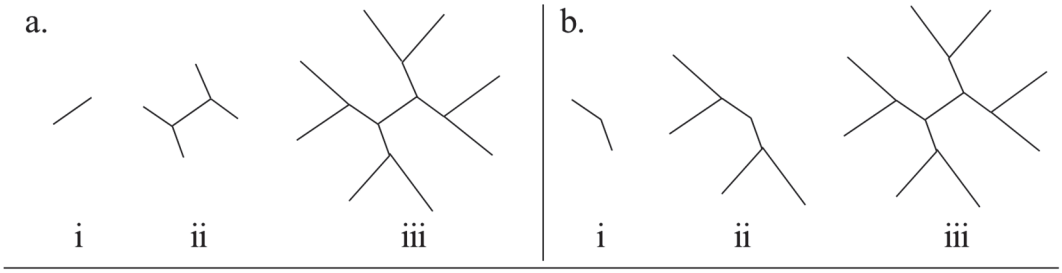

Figure 1.16. Line structure depiction of dendrimer synthetic approaches of a G_1 dendrimer where the divergent (a) approach starts with the core (ai) and continues to build out towards the periphery (aii-iii). The convergent (b) approach starts with a branching portion of the dendrimer (bi) and is built towards the periphery (bii) that is then followed by the linking of the branches to form the core (biii).

The syntheses of linear polymers produce a range of molar masses, whereas the synthesis of dendrimeric polymers can be regulated. This control arises from the successive addition of two distinct monomers in an iterative process where a monomer ends in a multiple bond site, such as a nitrogen, leading to branching.[68] Dendrimers have also shown enhanced solubilities when compared to linear polymer counter parts of similar mass[72], likely due to the regular branching and built-in three dimensional confirmation. Linear polymers adopt random coiling confirmations, whereas the dendrimer adopts a regular, globular shape.[69] As shown in Figure 1.15 and Figure 1.16, early generation dendrimers appear flat

and disc shaped, however, upon increasing the generation, dendrimers tend to become more globular in each progressive generation and reach a limit on accessibility to end groups and the interior. For some dendrimers, like PAMAM, theoretical calculations put the generation cap at 10 or 4096 end groups. Dendrimers are not rigid and can adopt dynamic shapes that include oblate spheres that can drastically flatten when in the presence of a flat surface[73] or change density with changes to salt concentrations, growing more dense and compact as concentrations increase.[74] The dynamic conformational changes of the dendrimer in different environments depends not only on the environment but also the type of dendrimer.

Dendrimers, much like other polymers, come in a wide variety of polymer types that are defined by composition. The main components (core, internal branching, and end groups) can be mixed and matched to create an almost unlimited number of combinations that allows for the tuning of the polymer properties. Examples of some covalent based dendrimers are provided in Figure 1.17. Surface or end groups can dictate the charge of the dendrimer at physiologic pH. Amine surface groups are protonated at neutral and acidic pH, resulting in an overall positive charge on the dendrimer. Alcohol and azide groups tend to be neutral whereas phosphate, sulfonate, and carboxylic acid groups result in an overall negative charge (especially at neutral to high pH). The internal branching and the core create internal pockets between the branches thereby creating a nanoenvironment. These pockets are perfect for small molecules and ions to fit and bind. An example is a dendrimer composed of a hydrophobic core and branches with hydrophilic end groups. This dendrimers would form unimolecular micelles that could envelop small, hydrophobic molecules.[74] These so-called guest-host properties allow for dendrimers to be useful in a broad range of applications.

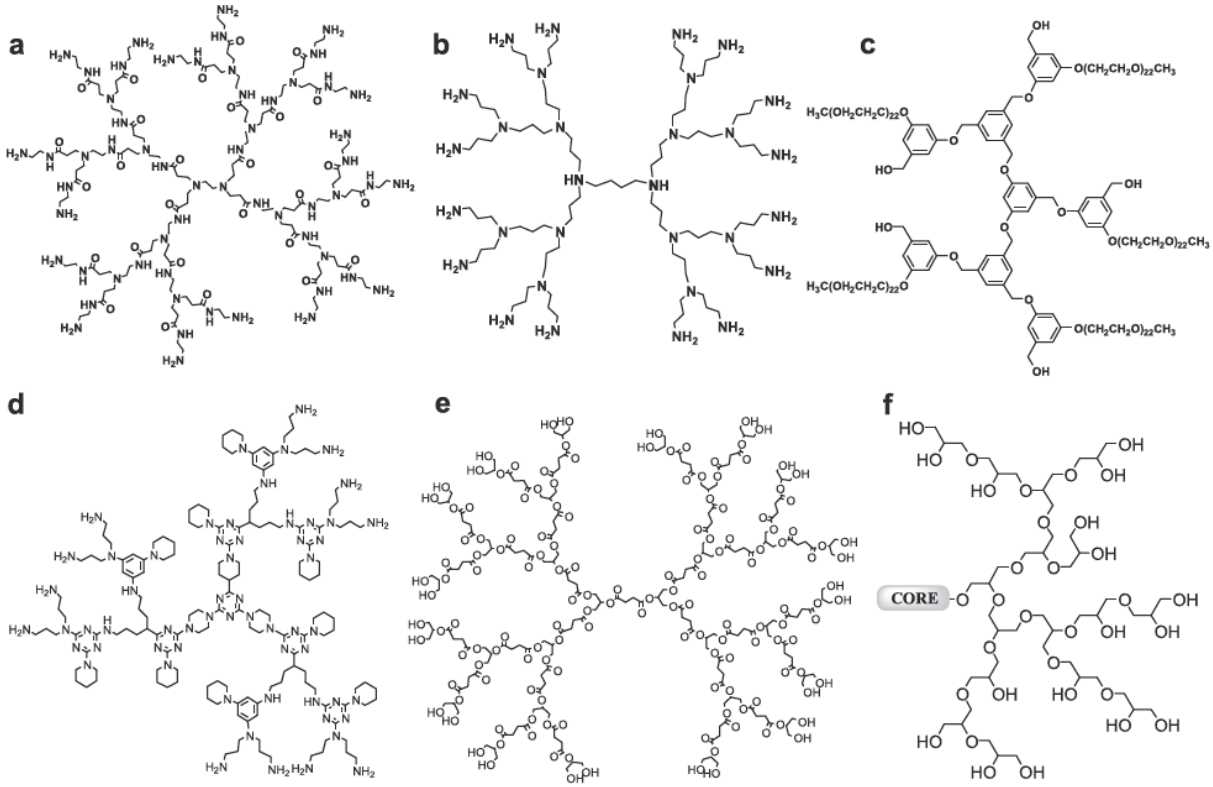

Figure 1.17 Examples of commonly used dendrimers. (a) G_2 poly(propylene imine) (PPI), (b) G_1 polyamidoamine (PAMAM), (c) G_1 polyester, (d) G_2 polyglycerol dendrimer, (e) G_2 triazine based dendrimer, and (f) G_1 poly(glycerol-succinic acid) dendrimer. Reprinted from Khandare et. al.,[75] which was originally modified and reprinted from Calderon et al.[76]

The guest-host properties make dendrimers an interesting polymer with applications in drug delivery,[74,75,76] catalysis,[74,77,78] and sensing.[79,80] In drug delivery, drug molecules can 'absorb' into the dendrimer as a guest and be administered to the body. Upon localization to the target site, the dendrimer can then deliver the payload via some stimuli (pH, enzymatic, or light).[76] This method enhances solubility for drugs with poor drug solubility as well as bioavailability without the need to change the structure of the drug.[76] As with drug delivery, dendrimers offer many sites for catalysis. Dendrimers may contain catalytic sites within the core, between the branches arms, or on the periphery of the molecule.[74] Benefits of placing the catalytic site within the dendrimer include increased selectivity from use of the branched arms as steric hindrances, as with biological enzymes, which lead to Henri Brunner coining the word *dendrizymes*.[81] Centralized catalytic cores can limit reaction rate or the overall yield by being too sterically hindering.[74,82] Peripheral sites provide more sites for catalytic groups, which allow for faster reaction rates but may limit selectivity. Catalytic sites can range from something as innocuous as an alkoxide focal point buried within a poly(arylether) dendrimer, which was used in the initialization of ring opening anionic polymerization of ε-caprolactone,[83] to internalized porphyrin rings used in shape and size selective epoxidation catalysts with manganese at the core.[84] Dendrimers without any additional functionalization may catalyze reactions, as in the generation 4 polyamidoamine (PAMAM) dendrimers in the aminolysis of p-nitrophenyl acetate.[85] Dendrimers can be functionalized with the help of chelated metals such as zinc (II) bound at the periphery of poly(propylene imine) dendrimers for use in the ester hydrolysis of p-nitrophenyl picolinate.[72] As with drug delivery and the binding of zinc ions in the PPI dendrimers, dendrimers in general have also been used in the sensing of various molecules and ions by using these guest-host properties.

Dendrimers have been employed in a variety of sensing methods that include electrochemical,[86-88] gravimetric,[89] and fluorescence detection[79,90] among others.[91] These detection platforms can achieve micromolar to attomolar detection limits for a variety of analytes. Some examples of the analytes include DNA, [87,92,93] explosives,[94,95] or metal ions.[79,80,96,97] Zong et al. (Figure 1.12) and Gerrans et al. have shown that the application of polyethylene imine (PEI) dendrons[27] as well as PAMAM dendrimers[79], respectively, could be used as chelators for copper ions in fluorescent chemical sensors. These fluorescent sensors relied on the copper chelation within the dendrimer/dendron in order to sense the copper. Other sensors can be designed with the same dendrimers based on the chelation properties of PEI or PAMAM. There is an abundance of literature precedents for a variety of transition metal ions that can bind to the surface and within PAMAM dendrimers (Table 1.8).

Table 1.8 PAMAM dendrimers shown to bind metal ions

Ion	PAMAM Dendrimer		Reference
	Generation	Terminal end	
Hg^{2+}	0.0	Amine	98
Pb^{2+}	1.0, 1.5, 4.0	Amine and Carboxyl	99
Cd^{2+}	2.0	Hydroxyl	100
Cr^{3+}	4.0	Hydroxyl	101
Mn^{2+}	3.5, 5.5, 7.5	Carboxyl	102
Co^{2+}	4.0	Amine	96
$Fe^{2+/3+}$	4.0	Hydroxyl	103
	4.0	Hydroxyl	104
Ni^{2+}	4.0	Hydroxyl	103
	0.0	Amine	98
Zn^{2+}	2.0	Hydroxyl	100
Cu^{2+}	4.0	Amine	105
	3.0-5.0	Amine	106
	3.0, 5.0, 7.0	Amine	107
	2.0-4.0	Hydroxyl	108
	0.0	Amine	98
Ag^{+}	2.0-6.0	Amine	109
	0.0	Amine	98
Au^{3+}	4.0	Amine	110
Pd^{2+}	4.0	Amine and Hydroxyl	111
	4.0	Amine	112
	4.0	Hydroxyl	113
	4.0	Hydroxyl	114
Pt^{2+}	4.0	Amine and Hydroxyl	111
	4.0	Amine	112

PAMAM dendrimers are chelators of metal ions due to the primary and tertiary amines (Lewis bases) throughout the molecule (Figure 1.18). The PAMAM dendrimers are commercially available with amine, carboxyl, and hydroxyl terminal groups. These end groups can be easily functionalized with fluorescent dyes, chelates, or merely changing functional groups. By adding fluorescent dyes, the metal ion may attenuate the dye upon chelation, thereby creating a metal sensor. By changing the end groups to other chelates such as terpyridine or different end groups, like xanthate,[97] the chelation properties of the PAMAM dendrimer can change. PAMAM dendrimers have also been shown to increase binding capacity for metal ions when immobilized on substrates, such as alumina.[103]

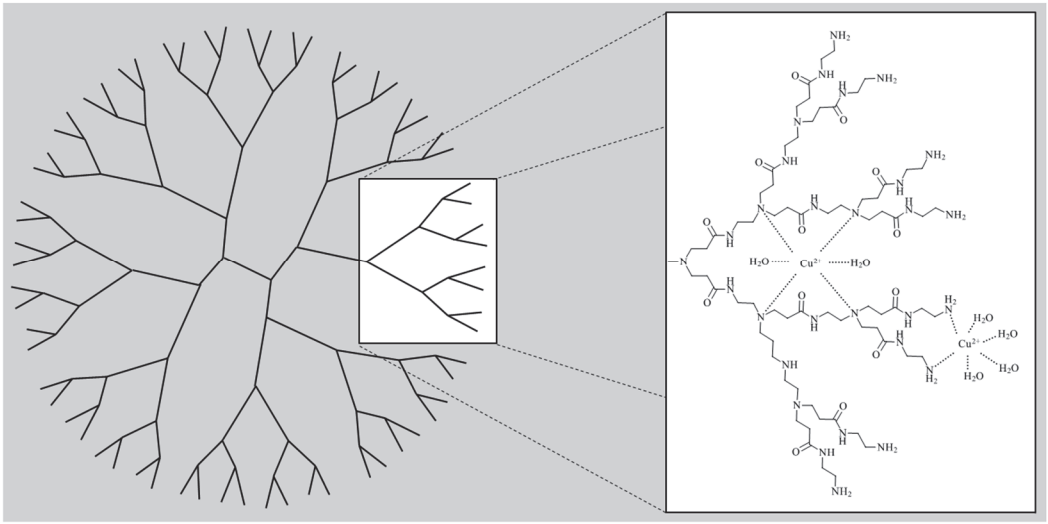

Figure 1.18 G_4 PAMAM dendrimer chelation of copper (II) ions in aqueous solution, adapted from Ottaviani[107] and Diallo.[115]

PAMAM dendrimers are better than simple, single molecule chelators due to the number of chelation sites per dendrimer. Furthermore, versatile end groups aid in chelation and help the dendrimer or the dendrimer conjugate (nanoparticle) remain in solution.[75] The regular shape of dendrimers should provide more reliable chelation sites when introduced to new environments or when conjugated to materials. However, PAMAM dendrimers are not without drawbacks. Dendrimers tend to be cost prohibitive and susceptible to degradation under ambient conditions, through retro-Michael addition, which could limit shelf life.[75]

Organic Dyes for Sensing Applications

The following section is serves as a general guide for fluorescent organic dyes and provides the reader with a starting point in sensor design based on specific analytes. The reader is encouraged to explore references such as Molecular Probes Handbook[26], Principles of Fluorescence Spectroscopy[13], Molecular Fluorescence Principles and Applications[19], and Bioconjugate Techniques[56] texts as well as the primary literature.

Currently, fluorescent organic dyes used as ion sensors or molecular probes in cell biology are analogs of the BODIPY, coumarin, napthalimide, cyanine, fluorescein, rhodamine, or the indo and fura dyes (Figure 1.19).[18] Fluorescent organic dyes are stabilized via conjugation of p-orbitals through alternating double bonds that results in the delocalization of electrons across the molecule.[13] Functional groups can be added or changed through synthetic processes in order to change the electronic properties of the conjugated system of the dye. These functional groups may include chelates for metal ions, which modulate the fluorescence character of the dye.[116] *Note: An excellent source that describes substituent effects on emission character is Molecular Fluorescence Principles and Applications by Bernard Valeur.*[19]

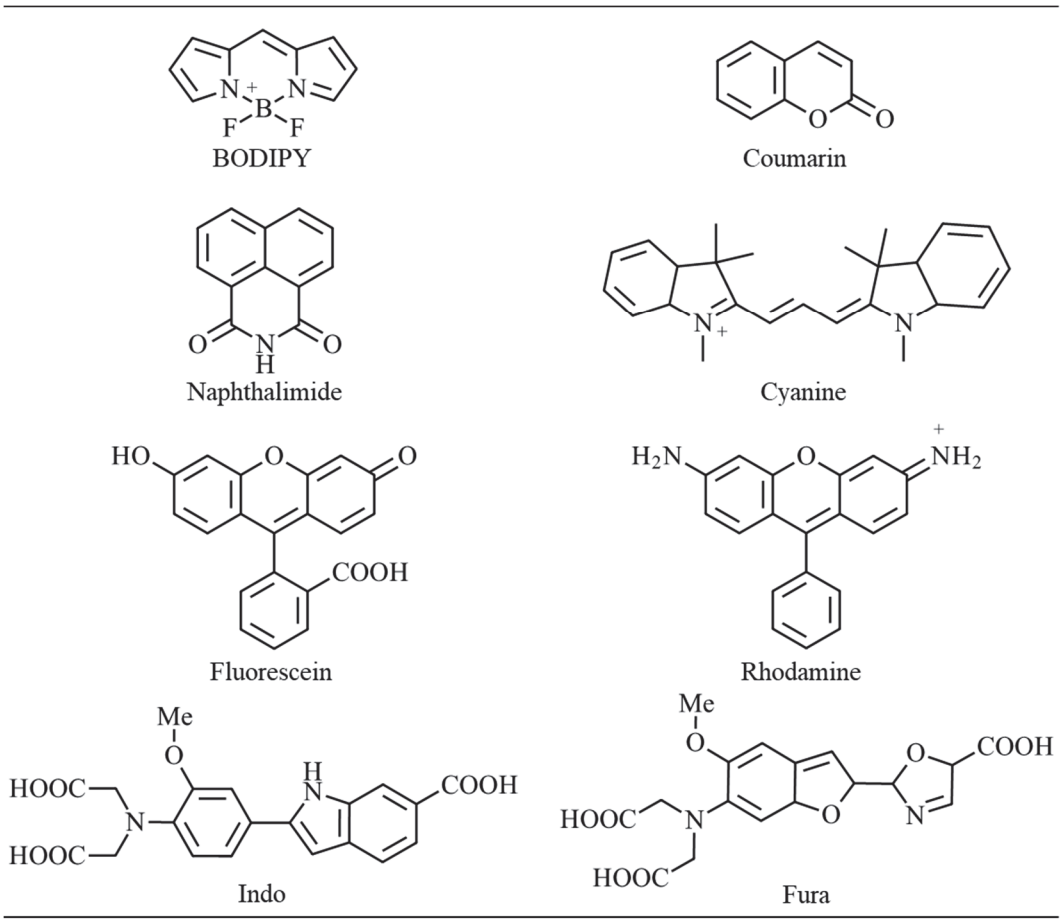

Figure 1.19 Common fluorescent probes (dyes) that are routinely used as building blocks to design and tune analogues for certain fluorescence characteristics and metal ion sensing.

Fluorescein and rhodamine analogs differ by only three functional groups and are among the most commonly used dyes in protein labeling due to high absorptivity, quantum yield, and water solubility.[117] Fluorescein has a number of potential drawbacks such as a high rate of photobleaching, broad emission that limits multicolor applications, and the tendency to quench when conjugated onto biopolymers at high concentrations.[117] Also, the excitation and emission maximums of fluorescein shifts drastically with changes in pH (Figure 1.20), which may become problematic depending on application.[18] However, the changes in absorbance and emission intensity of fluorescein with respect to pH have been exploited to create fluorescent pH sensors to monitor a diverse range of physiological processes such as apoptosis, cell proliferation, and ion transport.[118] Upon protonation, the electron density from the conjugated xanthene core (red in Figure 1.22) is removed, which then lowers the absorbance of incident photons, thereby lowering emission intensity.[118] Rhodamine analogs, however, are not affected by changes in pH and are also among the most photostable dyes.[117]

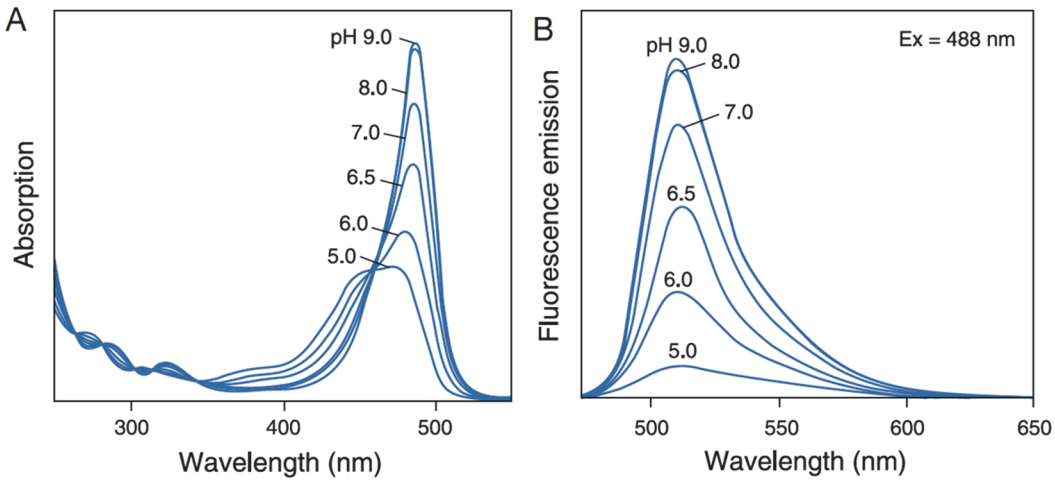

Figure 1.20 Absorption (A) and emission (B) intensity of fluorescein dye changes drastically when the pH changes from 5.0 - 9.0. Reprinted from the Molecular Probes Handbook.[117]

Effect of Substituents Changes on Dye Fluorescence

Substituent changes to fluorescein can change the fluorescent character of the dye. Fluorescein absorbs and emits maximally at 500 nm and 522 nm, respectively, with a quantum yield of 0.92.[18,119] By altering the hydrogens on fluorescein to chlorine, as shown in Figure 1.21, the emission wavelength shifts 18 nm with an increased quantum yield to 0.96 (tetrachlorofluoroscien).[119] Heavier halogens (Br and I) yield far more drastic results. Substitution with bromine forms the dye eosin Y, which has a quantum yield of 0.68 and emission maximum at 547 nm. Erythrosine B is the product of substituting iodine which gives a dismal quantum yield of 0.14 and the most red-shifted spectrum, an emission maximum of 551 nm.[119] Traditionally, these fluorescein analogs are used for cell stains in histology[120] or used as phosphorescent probes[18] due to the increase intersystem crossing of the excited molecule (as described in the *Spectroscopy* section). Metal ion sensing, however, has gone largely unexplored.

Addition of substituents containing atoms with lone pairs can result in photoinduced electron transfer (PET) quenching of fluorescein, thereby lowering the quantum yield of the dye. The quantum yield for fluorescein is nearly 1, however, with the addition of R_1 in the Mercury Sensor 1 (MS1) of Figure 1.22, the quantum yield plummets to 0.04 due to a PET quenching from the lone pair of the aniline nitrogen.[121] Nolan et al. showed a 5-fold increase in emission intensity with the addition 1 equivalent of mercury (1 μM) due to the mercury accepting the lone pairs from the aniline while chelated.[121] The chelators in Zinc Sensor 1 (ZS1) were the exact same chelators (N,N-bis(2-pyridylmethyl)ethylamine, PMEA) in the lathanide example described earlier in the *Recognition Sites and Chelation* section. A similar mechanism was reported by Burdette et al., where the addition of the PMEA substituents resulted in a lowering of quantum yield in ZS1 to 0.25 but, upon chelating zinc, increased to 0.92.[122] The detection limit of ZS1 was determined to be 0.172 nM.

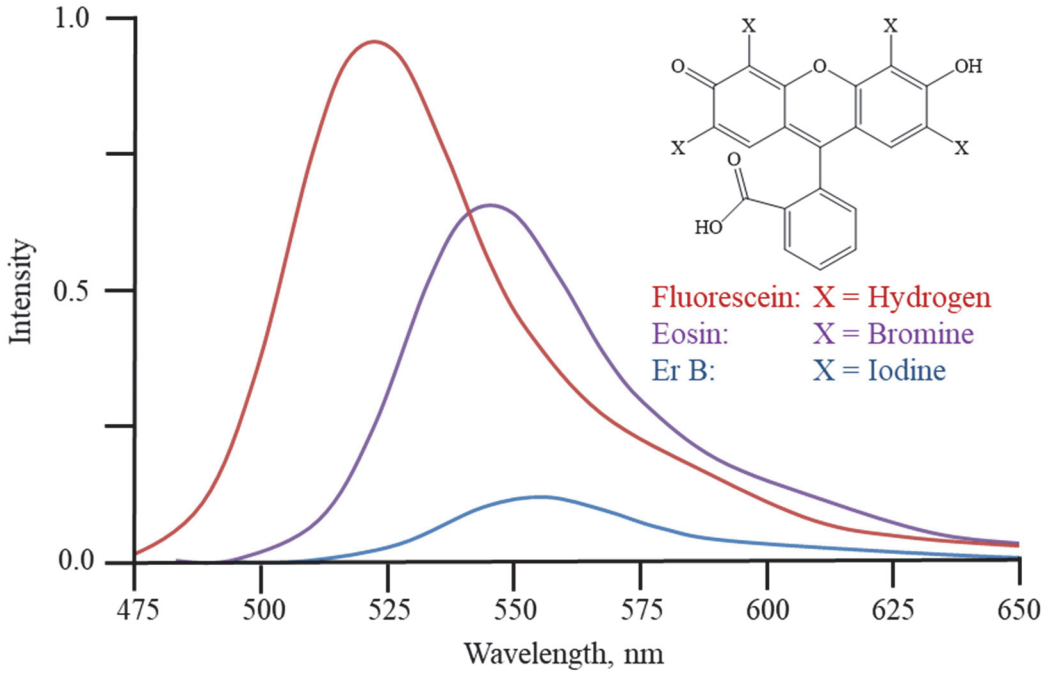

Figure 1.21 Comparison of emission spectra between fluorescein, eosin Y and erythrosin B (ErB) showing the decrease in intensity, as well as a emission maximum shifts as X becomes heavier. Figure reprinted from Principles of Fluorescence Spectroscopy, Solvent: Ethanol.[13]

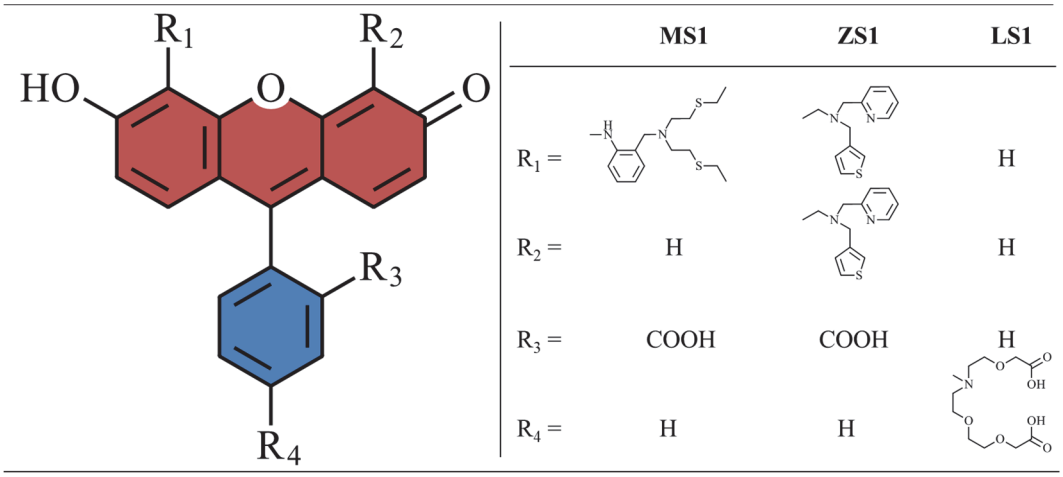

Figure 1.22 General fluorescein molecule (left) illustrating the two aromatic regions of the molecule, which are the xanthene (red) and the benzyl (blue) regions, and some areas to add substituents (R-groups). The substituents added (right) can change the selectivity of the fluorescein analog to mercury[116,121], zinc[122,123], or lead.[124]

A substituent substitution to the R_4 position with a crown ether-like chelate again PET quenches the fluorescein dye until, in this case, lead was chelated. Response to lead was detected at concentrations as low as 5 μM and showed selectivity over 14 other ions when those ions were at ~27 times the concentration of lead (2 mM and 75 μM, respectively).[124]Armed with the knowledge that a chelate containing a nitrogen will PET quench the dye, fluorogenic sensors can be synthesized, tested, and modified to tune sensors for particular applications.

Effect of Changes to Dye Core on Dye Fluorescence

The previous examples outlined in Figure 1.21 and Figure 1.22 show how the addition of heavy atom and chelate substituents can be used to exploit a change in the fluorescent character (quantum yield and emission wavelength) of a dye. The following examples of fluorescein analogs have added substituents, but the cause for the change in fluorescent character (emission wavelength) was the modification of the xanthene fluorescent core (Figure 1.23). By removing and replacing the oxygen with a dimethyl carbon (a so-called carbofluorescein), the excitation and emission wavelengths red shifted to 544 and 567 nm, respectively, while the quantum yield decreases to 0.62.[125] The quantum yield decreases to 0.048 with the addition of the tetrathia-azaheptadecane (TAHD) chelate due to PET quenching. The effect of the morpholine and the TAHD substituents on the emission wavelength was not determined, although red shifting was thought to occur from the original dimethyl carbon fluorescein. The trifluoromethyl substituent was thought to increase optical brightness by increasing steric bulk that decreases rotational motion between the xanthene and benzyl regions, thereby minimizing non-radiative decay (black arrow, Figure 1.23).[126] Addition of these substituents create the *Copper Carbo Fluor 1* (CCF1) of Jia et al. (Figure 1.23a) where the quantum yield increases from 0.048 to 0.30 upon the binding of copper (Table 1.9).[127]

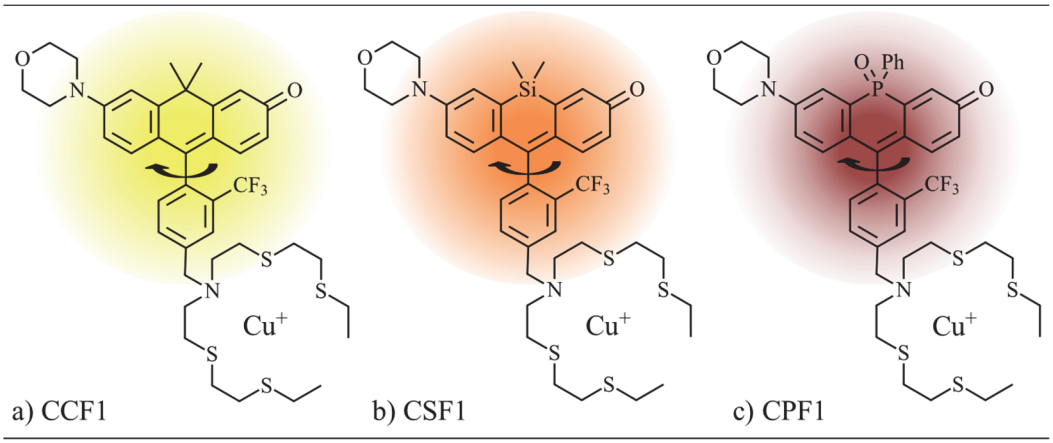

Figure 1.23 The Chang group changed the emission color of the fluorescein analog shown above by changing the oxygen within the xanthene core to $C(CH_3)_2$ (a), $Si(CH_3)_2$ (b), and POPh (c), which changes the emission maximums to 608 (yellow), 638 (orange), and 679 nm (red) respectively.[127]

Table 1.9 Abridged spectral properties of copper probes upon binding copper from Jia et al.[127]

	CCF1 + Cu → CCF1-Cu		CSF1 + Cu → CSF1-Cu		CPF1 + Cu → CPF1-Cu	
Φ =	0.048	0.30	0.0041	0.053	0.00018	0.0020
λ_{ex} (nm) =	516	580	568	616	569	654
λ_{em} (nm) =	608	608	638	639	679	680

Further substitution of the xanthene core with silicon (CSF1) and phosphorous (CPF1) redshifts the emission of the fluorescein analog (Figure 1.23b and c).[127] An increase in quantum yield upon binding of copper was also seen in CSF1 and CPF1 although significantly lower than the CCF1 analog. The substitution of the oxygen in the xanthene core would seem to have a similar effect on the emission character of the dye. A study by Jia et al. claim that the use of Tetrakis(acetonitrile)copper(I) hexafluorophosphate

($[Cu(MeCN)_4]PF_6$) as a copper (I) source remains copper (I) in aqueous solution is questionable due to the limited solubility and stability of $[Cu(MeCN)_4]PF_6$ in aqueous environments.[128] Use of copper (II) sulfate as a Cu^{2+} source was thought to be sufficient to test selectivity of copper (I) against copper (II), however, this author remains skeptical of the copper species reported in the study. The authors also claimed limited increase in fluorescence emission in copper (II) but decided copper (II) was being reduced by the sulfur chelate, which then increased the fluorescence.

Aside from the source of copper, the authors show a dynamic range of 0.2 - 1.0 μM copper in an aqueous solution of 1 μM sensor (1:1 copper: sensor). Selectivity was demonstrated by adding 2 mM excess of some cations (Na^+, K^+, Mg^{2+}, Ca^{2+}, and Zn^{2+}) and 50 mM of others (Mn^{2+}, Fe^{2+}, Co^{2+}, Ni^{2+}, and Cu^{2+}).[127] Although quantum yield is important in sensing, changes in response can make a poor emitting fluorophore a fantastic sensor as seen in the case of CPF1, where the quantum yield increased from 0.00018 to a dismal 0.0020. Despite this, CPF1 showed a measurable change (11x increase) at low concentrations of copper even in the presence of other ions.

Jia et al., as well as the other examples, have demonstrated that substituent changes made to parent fluorophores (Figure 1.23) can result in changes in fluorescent character that can then be exploited for sensing purposes. The design of fluorophores can often be an entire thesis project alone. Thus, the purchase of readily available and widely used fluorophores such as fluorescein isothiocynate (FITC) and rhodamine isothiocynate (RITC) were thought to be the most efficient way forward for this thesis. As the following section and chapters will describe, just a few types of scaffolds, chelates, and fluorophores can produce a wide variety of fluorescent sensors. Furthermore, an important aspect of a project is to understand the context of its inception, and the following section will outline the work conducted previous to this one.

Recent History of the Margerum Group

Research in the Margerum group has primarily focused on the bottom-up approach in fabrication of materials by adding thin layers of polymer to silica. This work has progressed from macroscopic materials, such as controlled pore glass (CPG) beads, towards the micro and nanoscopic scale in the form of nanoparticles. The following descriptions are from past student theses and were chosen due to their accessibility online through the repository at the University of San Francisco, should the reader wish to read on.

Chang Liu (*Surface Tethered PAMAM Dendrimers On Controlled Pore Glass as Color Release Sensors for Phosphates*) used CDI chemistry to bind three different generations of PAMAM dendrimer (3.0, 4.0, and 5.0) to CPG beads.[129] The PAMAM dendrimer was anchored and used as a multivalent bioconjugation scaffold using CDI chemistry to attach the copper (II) chelators, amino-functionalized Terpyridine (A-terpy) or N,N bis(carboxymethyl)-L-lysine (NTA) ligands. Chang used a packed column of modified beads with flowing copper (II) solutions to obtain binding breakthrough data, which indicates the amount of copper that binds to the coatings versus volume added. By changing the generation and the end groups, the data showed the following:

1. As the generation of dendrimer increases, the binding capacity of copper increases
2. The binding capacities of the three end group types were in the following order amine > NTA > Carboxylic acid (through CDI intermediate hydrolysis) > terpy
3. However, through acid digestion, the NTA and terpy ligand coatings showed stronger binding for copper ions (resisted releasing copper during rinsing)

Next, Chang developed an indicator displacement assay for phosphate ions. Chelating dyes added to the dendrimer bound Cu(II) were 6,7-dihydroxy-4-methylcoumarin (DHMC) and bromopyrogallol red (BPR), which are coumarin and fluorescein analogs, respectively. The PAMAM modified CPG with metal dye complex were packed into a flow column (CPG-G_n-terpy-Cu-dye or CPG- G_n-NTA-Cu-dye; n = 3.0, 4.0, and 5.0) and the outflow was monitored via a fluorimeter (either continuous or batch modes). Upon addition of phosphate ion, the dye was displaced from the surface bound Cu-dye complex. Chang tested other biologically relevant phosphate containing ions such as ADP, ATP, and pyrophosphate and determined that phosphate was the only ion that could displace the indicator dyes.

Justin Dancer performed similar work in his 2014 thesis *Glass Foundation Chemosensor Synthesis and Functionality Analysis* by testing similar CPG materials with other biologically relevant molecules.[130] Using the amino acids L-histidine (H), L-leucine (L), L-alanine (A), and the neurotransmitter dopamine, Dancer examined the displacement of pyrocatechol violet (PV), a phenolphthalein analog, from CPG-G_n-terpy-Cu (n = 3.0 and 4.0) and CPG-TESPSA-G_3-NTA-Cu conjugates (TESPA is a silane linker used to increase the distance between CPG surface and the dendrimer). The displacement for these materials was monitored via UV-vis spectrophotometry. The generation 3 (n = 3.0) material resulted in a displacement trend as follows: L > H > dopamine > A, where A ≅ 0 absorbance units. Alternatively, the generation 4 results did not follow the same trend, which was as follows: H > dopamine > L > A. The NTA conjugate that used generation 3 dendrimer resulted in an absorbance trend of dopamine > H > L > A. Dancer's CPG materials for the use in IDA detection was not very selective for the amino acids and neurotransmitter that were tested, however, the IDA could be used as a general detection method for these molecules.

In Jonathan J. Liu's 2015 thesis, *Terpyridine Functionalized Dye-Doped Silica Nanoparticles (DDSN) for Detection of Metal Ions,* the use of silica nanoparticle scaffolds rather than CPG first appears. Liu's approach was to modify the IDA method to a turn-off and turn-on Quenching Displacement Assay (QDA). In general, QDA methods use a covalently bound dye surrounded by metal ion chelates. Upon chelation, the chelate-metal complex quenches the nearby dye, thereby turning the sensor off (turn-off). Addition of an anion that removes or hinders the quenching of the dye by the chelate-metal complex allowed the dye to turn back on (turn-on). Liu's work focused on the first portion of the QDA, the quenching of the dye through metal chelation. He showed that upon the addition of metal ions to silica nanoparticles (SNP) coated in a terpy chelate and a dye (FITC or RITC), the dyes would quench in a metal dependent manner. Liu concluded that the SNP-terpy-RITC conjugate was selective for cobalt (II) and copper (II) with some quenching with nickel (II), zinc (II), and iron (III), whereas lead (II) showed no signs of quenching. The quenching of nickel, zinc, and iron were 5x less efficient or more at quenching than the cobalt or copper (all metal concentration were tested at 0-3.0 μM). The SNP-terpy-FITC conjugate showed similar selectivity in metal ions where copper and cobalt were quenched with similar efficiency whereas lead, nickel, zinc, and iron were 3x less efficient or more than the cobalt or copper (all metal concentration were tested at 0-3.0 μM). The lack of selectivity for different metal ions was not considered a problem in this study. Not only has terpy been known to be a general chelator for numerous transitional,[131] alkali, and alkaline metals as well as metalloids,[132] but the QDA depends on the interaction of an anion with the metal ion. This broad spectrum of metal ion chelation holds promise for future work on this project. One hypothesis is that the differences in chelated metal ions would lead to differences in anion turn-on sensing. Using a different chelator, Alicia Luhrs performed similar work and produced a functioning QDA.

Alicia Luhrs completed her 2016 thesis on *Dendrimer Modified Silica Nanoparticles as Fluorescent Chemosensors for the Detection of Copper and Cyanide Ions.*[133] The bulk of the work was on SNP-G_n-RITC (n = 1.0, 3.0-5.0 generation of PAMAM dendrimers). There was high turn-off selectivity for

copper only at 0-20 μM when testing a battery of metal ions (Cu^{2+}, Zn^{2+}, Ni^{2+}, Ag^{+}, Cd^{2+}, Pd^{2+}, Co^{2+}, and Fe^{3+}). Upon addition of anions to the copper quenched SNP-G_n-RITC materials, only cyanide and ethylenediaminetetraacetic acid (EDTA) were able to restore (turn-on) the fluorescence. The other ions included azide and phosphate. Luhrs also showed that copper quenching efficiency increased as dendrimer generation increased up to 4.0, which then decreased in the 5.0-generation. There were similar results for both copper and cyanide/EDTA sensitivity and efficiency when changing the surface dye from RITC to FITC on the SNP-G_4 materials. Further studies with the SNP-G_4-RITC conjugate revealed the ability to use the nanoparticle sensor for the sensing of the aromatic 8-Anilino-1-naphthalenesulfonic acid (ANS) molecule via Förster Resonance Energy Transfer.

During the transition from CPG materials to nanoparticle materials, the overall goal of these projects shifted from Indicator Displacement Assays (IDA) towards Quenching Displacement Assays (QDA). In subsequent projects the metals became the focus for sensing to use as standalone sensor if selective or to become a QDA if the dye was quenched from a broad range of metals. During this transition, the dyes were covalently bound to the nanoparticles through bioconjugate techniques. In IDA, the dye-chelator needed to bind strongly enough to prevent leeching during washes, yet labile enough to be displaced, which can be difficult to achieve. In contrast, in QDA, the dye is fixed and the ion becomes labile. Additionally, changes to synthetic steps and characterization of these materials were required in attempts to develop more viable sensors, especially those with nanoparticle scaffolds.

The following chapters will describe some of the challenges that were discovered in the transition from CPG materials to nanoparticles and the synthetics steps taken to address those issues. The materials generated from those steps were then tested and compared to determine the sensing capabilities with respect to each other and to that of Luhrs' work.

References

1 Kalantar-zadeh, K. & Fry, B. *Nanotechnology-Enabled Sensors*. (Springer, 2008).
2 Shriver, D., Weller, M., Overton, T., Armstrong, F. & Rourke, J. *Inorganic Chemistry*. 6th edn, (W. H. Freeman, 2014).
3 Steed, J. W. & Gale, P. A. *Supramolecular Chemistry: From Molecules to Nanomaterials*. (Wiley, 2012).
4 Khanna, V. K. *Integrated Nanoelectronics Nanoscale* (Springer, 2016).
5 Van Noorden, R. & Castelvecchi, D. World's tiniest machines win chemistry Nobel. *Nature* **538**, 152-153, doi:10.1038/nature.2016.20734 (2016).
6 Kalil, T. & Bruce, A. (ed Executive Office of the President) (Subcommittee on Nanoscale Science, Engineering, and Technology Committee on Technology, National Science and Technology Council, 2016).
7 West, R. M. The Chalkboard: Fluctuation Analysis. *The Electrochemical Society Interface* **26**, 49-51, doi:10.1149/2.F02174if (2017).
8 Wade, L. G. *Organic Chemistry*. 8th edn, (Pearson, 2012).
9 Richardson, F. R. Universal indicator for pH 1-13. *Journal of Chemical Education* **33**, 517, doi:10.1021/ed033p517 (1956).
10 Skoog, D. A., West, D. M., Holler, F. J. & Crouch, S. R. *Fundamentals of Analytical Chemistry*. Eighth edn, (Thomson Brooks and Cole, 2004).
11 Skoog, D. A., Holler, F. J. & Crouch, S. R. *Principles of Instrumental Analysis*. 6th edn, (Thomson Brooks/Cole 2007).
12 Laidler, K. J., Meiser, J. H. & Sanctuary, B. C. in *Physical Chemistry* Ch. 13, (Houghton Mifflin Company, 2003).
13 Lakowicz, J. R. *Principles of Fluorescence Spectroscopy*. 3rd edn, (Springer, 2006).
14 Steiner, U. E. in *Photodynamic therapy: From theory to application* (ed Mahmoud H. Abdel-Kader) Ch. 2, (Springer, 2014).
15 Balzani, V., Ceroni, P. & Juris, A. *Photochemistry and Photophysics: Concepts, Research, Applications*. (Wiley-VCH, 2014).
16 Hollas, M. *Basic Atomic and Molecular Spectroscopy*. (The Royal Society of Chemistry, 2002).

17 Kasha, M. Characterization of electronic transitions in complex molecules. *Discussions of the Faraday Society* **9**, 14, doi:10.1039/df9500900014 (1950).
18 Johnson, I. & Spence, M. T. Z. in *The Molecular Probes Handbook: A Guide to Fluorescent Probes and Labeling Technologies* Ch. 1, (Life Technologies, 2010).
19 Valeur, B. *Molecular Fluorescence Principles and Applications*. (WILEY-VCH, 2001).
20 Barghouthi, S. A., Perrault, J. & Holmes, L. H. Effect of Solvents on the Fluorescence Emission Spectra of 1-Anilino-8-Naphthalene Sulfonic Acid: A Physical Chemistry Experiment. *The Chemical Educator* **3**, 1-10, doi:10.1007/s00897980254a (1998).
21 Brand, L., Seliskar, C. J. & Turner, D. C. in *Probes of Strucuture and Function of Macromolecules and Membranes* Vol. 1 Probes and Membrane Function (eds Britton Chance, Chuan-Pu Lee, & J. Kent Blasie) 17-31 (Academic Press, 1971).
22 Jeong, Y. & Yoon, J. Recent progress on fluorescent chemosensors for metal ions. *Inorganica Chimica Acta* **381**, 2-14, doi:10.1016/j.ica.2011.09.011 (2012).
23 Vazquez-Gonzalez, M. & Carrillo-Carrion, C. Analytical strategies based on quantum dots for heavy metal ions detection. *J Biomed Opt* **19**, 101503, doi:10.1117/1.JBO.19.10.101503 (2014).
24 Petryayeva, E., Algar, W. R. & Medintz, I. L. Quantum Dots in Bioanalysis: A Review of Applications Across Various Platforms for Fluorescence Spectroscopy and Imaging. *Applied Spectroscopy* **67** (2013).
25 Que, E. L., Domaille, D. W. & Chang, C. J. Metals in neurobiology: probing their chemistry and biology with molecular imaging. *Chem Rev* **108**, 1517-1549, doi:10.1021/cr078203u (2008).
26 Johnson, I. & Spence, M. T. Z. in *The Molecular Probes Handbook: A Guide to Fluorescent Probes and Labeling Technologies* Ch. 19 (Life Technologies, 2010).
27 Zong, C., Ai, K., Zhang, G., Li, H. & Lu, L. Dual-emission fluorescent silica nanoparticle-based probe for ultrasensitive detection of Cu2+. *Analytical Chemistry* **83**, 3126-3132, doi:10.1021/ac2001324 (2011).
28 Li, M. & Selvin, P. R. Luminescent Polyaminocarboxylate Chelates of Terbium and Europium: The Effect of Chelate Structure. *Journal of the American Chemical Society* **117**, 8132-8138, doi:10.1021/ja00136a010 (1995).
29 Yeung, M. C.-L. & Yam, V. W.-W. in *Luminescent and Photoactive Transition Metal Complexes as Biomolecular Probes and Cellular Reagents* (ed Kenneth Kam-Wing Lo) (Springer, 2015).
30 Lawrence, G. A. *Introduction to Coordination Chemistry*. (John Wiley and Sons Ltd, 2010).
31 Miessler, G. L., Fischer, P. J. & Tarr, D. A. *Inorganic Chemistry*. Fifth edn, (Pearson 2014).
32 Kim, H. N., Lee, M. H., Kim, H. J., Kim, J. S. & Yoon, J. A new trend in rhodamine-based chemosensors: application of spirolactam ring-opening to sensing ions. *Chem Soc Rev* **37**, 1465-1472, doi:10.1039/b802497a (2008).
33 Korzeniowska, B., Nooney, R., Wencel, D. & McDonagh, C. Silica nanoparticles for cell imaging and intracellular sensing. *Nanotechnology* **24**, 442002, doi:10.1088/0957-4484/24/44/442002 (2013).
34 Knopp, D., Tang, D. & Niessner, R. Review: bioanalytical applications of biomolecule-functionalized nanometer-sized doped silica particles. *Anal Chim Acta* **647**, 14-30, doi:10.1016/j.aca.2009.05.037 (2009).
35 Wang, L., Zhao, W. & Tan, W. Bioconjugated silica nanoparticles: Development and applications. *Nano Research* **1**, 99-115, doi:10.1007/s12274-008-8018-3 (2008).
36 Moore, C. J. *et al.* Controlling colloidal stability of silica nanoparticles during bioconjugation reactions with proteins and improving their longer-term stability, handling and storage. *Journal of Materials Chemistry B* **3**, 2043-2055, doi:10.1039/c4tb01915f (2015).
37 Wang, X. & Guo, X. Ultrasensitive Pb2+ detection based on fluorescence resonance energy transfer (FRET) between quantum dots and gold nanoparticles. *Analyst* **134**, 1348-1354, doi:10.1039/b822744f (2009).
38 Hanaoka, K., Kikuchi, K., Kojima, H., Urano, Y. & Nagano, T. Selective detection of zinc ions with novel luminescent lanthanide probes. *Angew Chem Int Ed Engl* **42**, 2996-2999, doi:10.1002/anie.200351122 (2003).
39 Lee, M. H., Lee, S. J., Jung, J. H., Lim, H. & Kim, J. S. Luminophore-immobilized mesoporous silica for selective Hg2+ sensing. *Tetrahedron* **63**, 12087–12092, doi:10.1016/j.tet.2007.08.113 (2007).
40 Ju, H., Lee, M. H., Kim, J., Kim, J. S. & Kim, J. Rhodamine-based chemosensing monolayers on glass as a facile fluorescent "turn-on" sensing film for selective detection of Pb2+. *Talanta* **83**, 1359-1363, doi:10.1016/j.talanta.2010.11.016 (2011).
41 Maret, W. The Metals in the Biological Periodic System of the Elements: Concepts and Conjectures. *Int J Mol Sci* **17**, doi:10.3390/ijms17010066 (2016).
42 Terwilliger, N. B. Functional adaptations of oxygen-transport proteins. *J Exp Biol* **201**, 1085-1098 (1998).

43 Cater, M. A. & Mercer, J. F. B. in *Molecular Biology of Metal Homeostasis and Detoxification From Microbes to Man* (eds Markus J. Tamás & Enrico Martinoia) (Springer, 2006).
44 Versieck, J. & Cornelis, R. Normal levels of trace elements in human blood plasma or serum. *Analytica Chimica Acta* **116**, 217-254, doi:10.1016/s0003-2670(01)95205-5 (1980).
45 Lech, T. & Sadlik, J. K. Copper concentration in body tissues and fluids in normal subjects of southern Poland. *Biol Trace Elem Res* **118**, 10-15, doi:10.1007/s12011-007-0014-z (2007).
46 Maret, W. & Li, Y. Coordination dynamics of zinc in proteins. *Chem Rev* **109**, 4682-4707, doi:10.1021/cr800556u (2009).
47 Vallee, B. L. & Falchuk, K. H. The biochemical basis of zinc physiology. *Physiol Rev* **73**, 79-118, doi:10.1152/physrev.1993.73.1.79 (1993).
48 Folin, M., Contiero, E. & Maria Vaselli, G. Zinc content of normal human serum and its correlation with some hematic parameters. *Biometals* **7**, 75-79, doi:10.1007/bf00205198 (1994).
49 Jaishankar, M., Tseten, T., Anbalagan, N., Mathew, B. B. & Beeregowda, K. N. Toxicity, mechanism and health effects of some heavy metals. *Interdiscip Toxicol* **7**, 60-72, doi:10.2478/intox-2014-0009 (2014).
50 CDC. ATSDR's Substance Priority List. *Agency for Toxic Substances and Disease Registry* (2017).
51 EPA. in *National Primary Drinking Water Regulations for Lead and Copper: Short-Term Regulatory Revisions and Clarifications* 57781-57820 (Office of the Federal Register, National Archives and Records Administration, 2008).
52 Venditto, V. J. & Szoka, F. C., Jr. Cancer nanomedicines: so many papers and so few drugs! *Adv Drug Deliv Rev* **65**, 80-88, doi:10.1016/j.addr.2012.09.038 (2013).
53 ATSDR. *Toxicological Profile for Cyanide* (ed U.S. Department of Health and Human Services) (Agency for Toxic Substances and Disease Registry, Atlanta, GA, 2006).
54 Paredes, J. M. *et al.* Real-time phosphate sensing in living cells using fluorescence lifetime imaging microscopy (FLIM). *J Phys Chem B* **117**, 8143-8149, doi:10.1021/jp405041c (2013).
55 Witten, T. & Pincus, P. in *Structured Fluids Polymers, Colloids, Surfactants* Ch. 5, 113-150 (Oxford University Press, 2004).
56 Hermanson, G. T. *Bioconjugate Techniques*. 3rd edn, (Academic Press, 2013).
57 da Costa, J. P., Santos, P. S. M., Duarte, A. C. & Rocha-Santos, T. (Nano)plastics in the environment - Sources, fates and effects. *Sci Total Environ* **566-567**, 15-26, doi:10.1016/j.scitotenv.2016.05.041 (2016).
58 Nah, J.-W., Jeong, Y.-D. & Koh, J.-J. Drug release from nanoparticles of Poly(DL-lactide-co-glycolide). *Korean Journal of Chemical Engineering* **17**, 230-236, doi:10.1007/bf02707148 (2000).
59 Saha, K., Agasti, S. S., Kim, C., Li, X. & Rotello, V. M. Gold nanoparticles in chemical and biological sensing. *Chem Rev* **112**, 2739-2779, doi:10.1021/cr2001178 (2012).
60 Mashhadizadeh, M. H. & Karami, Z. Solid phase extraction of trace amounts of Ag, Cd, Cu, and Zn in environmental samples using magnetic nanoparticles coated by 3-(trimethoxysilyl)-1-propantiol and modified with 2-amino-5-mercapto-1,3,4-thiadiazole and their determination by ICP-OES. *J Hazard Mater* **190**, 1023-1029, doi:10.1016/j.jhazmat.2011.04.051 (2011).
61 Jana, N. R., Earhart, C. & Ying, J. Y. Synthesis of Water-Soluble and Functionalized Nanoparticles by Silica Coating. *Chemistry of Materials* **19**, 5074-5082, doi:10.1021/cm071368z (2007).
62 Raven, P. H., Johnson, G. B., Losos, J., Singer, S. & Mason, K. in *Biology* Ch. 29, (McGraw Hill, 2008).
63 Montalti, M., Prodi, L., Rampazzo, E. & Zaccheroni, N. Dye-doped silica nanoparticles as luminescent organized systems for nanomedicine. *Chem Soc Rev* **43**, 4243-4268, doi:10.1039/c3cs60433k (2014).
64 Metin, C. O., Lake, L. W., Miranda, C. R. & Nguyen, Q. P. Stability of aqueous silica nanoparticle dispersions. *Journal of Nanoparticle Research* **13**, 839-850, doi:10.1007/s11051-010-0085-1 (2010).
65 Bagwe, R. P., Hilliard, L. R. & Tan, W. Surface modification of silica nanoparticles to reduce aggregation and nonspecific binding. *Langmuir* **22**, 4357-4362, doi:10.1021/la052797j (2006).
66 Wang, D. *et al.* How and why nanoparticle's curvature regulates the apparent pKa of the coating ligands. *Journal of the American Chemical Society* **133**, 2192-2197, doi:10.1021/ja108154a (2011).
67 Arkles, B., Maddox, A., Singh, M., Zazyczny, J. & Matisons, J. Silane Coupling Agents Connecting Across Boundaries. (2014).
68 Abbasi, E. *et al.* Dendrimers: synthesis, applications, and properties. *Nanoscale Res Lett* **9**, 247, doi:10.1186/1556-276X-9-247 (2014).
69 Zeng, F. & Zimmerman, S. C. Dendrimers in Supramolecular Chemistry: From Molecular Recognition to Self-Assembly. *Chemical Reviews* **97**, 1681-1712, doi:10.1021/cr9603892 (1997).

70 Newkome, G. R. & Shreiner, C. D. Poly(amidoamine), polypropylenimine, and related dendrimers and dendrons possessing different 1→2 branching motifs: An overview of the divergent procedures. *Polymer* **49**, 1-173, doi:10.1016/j.polymer.2007.10.021 (2008).

71 Liu, K., Xu, Z. & Yin, M. Perylenediimide-cored dendrimers and their bioimaging and gene delivery applications. *Progress in Polymer Science* **46**, 25-54, doi:10.1016/j.progpolymsci.2014.11.005 (2015).

72 Bosman, A. W. Dendrimers in action: structure, dynamics and functionalization of poly(propylene imine) dendrimers. *Technische Universiteit Eindhoven*, doi:10.6100/IR523548 (1999).

73 Mecke, A., Lee, I., Baker, J. R., Jr., Holl, M. M. & Orr, B. G. Deformability of poly(amidoamine) dendrimers. *Eur Phys J E Soft Matter* **14**, 7-16, doi:10.1140/epje/i2003-10087-5 (2004).

74 Bosman, A. W., Janssen, H. M. & Meijer, E. W. About Dendrimers: Structure, Physical Properties, and Applications. *Chemical Reviews* **99**, 1665-1688, doi:10.1021/cr970069y (1999).

75 Khandare, J., Calderon, M., Dagia, N. M. & Haag, R. Multifunctional dendritic polymers in nanomedicine: opportunities and challenges. *Chem Soc Rev* **41**, 2824-2848, doi:10.1039/c1cs15242d (2012).

76 Calderon, M., Quadir, M. A., Strumia, M. & Haag, R. Functional dendritic polymer architectures as stimuli-responsive nanocarriers. *Biochimie* **92**, 1242-1251, doi:10.1016/j.biochi.2010.02.017 (2010).

77 Antebi, S., Arya, P., Manzer, L. E. & Alper, H. Carbonylation Reactions of Iodoarenes with PAMAM Dendrimer-Palladium Catalysts Immobilized on Silica. *The Journal of Organic Chemistry* **67**, 6623-6631, doi:10.1021/jo020271n (2002).

78 Astruc, D. & Chardac, F. Dendritic Catalysts and Dendrimers in Catalysis. *Chemical Reviews* **101**, 2991-3024, doi:10.1021/cr010323t (2001).

79 Gerrans, K., Luhrs, A., Feider, C. & Margerum, L. D. Silica nanoparticles functionalized with polyamidoamine (PAMAM) dendrimers as platforms for photoluminescence (PL) sensing of copper and cyanide ions. *J Colloid Interface Sci* **470**, 276-283, doi:10.1016/j.jcis.2016.03.004 (2016).

80 Dodangeh, M., Gharanjig, K. & Arami, M. A novel Ag(+) cation sensor based on polyamidoamine dendrimer modified with 1,8-naphthalimide derivatives. *Spectrochim Acta A Mol Biomol Spectrosc* **154**, 207-214, doi:10.1016/j.saa.2015.09.031 (2016).

81 Brunner, H. Dendrizymes: Expanded ligands for enantioselective catalysis. *Journal of Organometallic Chemistry* **500**, 39-46, doi:10.1016/0022-328x(95)00507-m (1995).

82 Twyman, L. J., King, A. S. H. & Martin, I. K. Catalysis inside dendrimers. *Chemical Society Reviews* **31**, 69-82, doi:10.1039/b107812g (2002).

83 Gitsov, I., Ivanova, P. T. & Fréchet, J. M. J. Dendrimers as macroinitiators for anionic ring-opening polymerization. Polymerization of ε-caprolactone. *Macromolecular Rapid Communications* **15**, 387-393, doi:10.1002/marc.1994.030150501 (1994).

84 Bhyrappa, P., Young, J. K., Moore, J. S. & Suslick, K. S. Dendrimer-Metalloporphyrins: Synthesis and Catalysis. *Journal of the American Chemical Society* **118**, 5708-5711, doi:10.1021/ja953474k (1996).

85 Martin, I. K. & Twyman, L. J. Acceleration of an aminolysis reaction using a PAMAM dendrimer with 64 terminal amine groups. *Tetrahedron Letters* **42**, 1123-1126, doi:10.1016/s0040-4039(00)02203-6 (2001).

86 Yoon, H. C. & Kim, H.-S. Multilayered Assembly of Dendrimers with Enzymes on Gold: Thickness-Controlled Biosensing Interface. *Analytical Chemistry* **72**, 922-926, doi:10.1021/ac991299a (2000).

87 Zhu, N., Gu, Y., Chang, Z., He, P. & Fang, Y. PAMAM Dendrimers-Based DNA Biosensors for Electrochemical Detection of DNA Hybridization. *Electroanalysis* **18**, 2107-2114, doi:10.1002/elan.200603589 (2006).

88 Siqueira, J. R. *et al.* Layer-by-Layer Assembly of Carbon Nanotubes Incorporated in Light-Addressable Potentiometric Sensors. *The Journal of Physical Chemistry C* **113**, 14765-14770, doi:10.1021/jp904777t (2009).

89 Lubczyk, D. *et al.* Simple and sensitive online detection of triacetone triperoxide explosive. *Sensors and Actuators B: Chemical* **143**, 561-566, doi:10.1016/j.snb.2009.09.061 (2010).

90 Lard, M. *et al.* Fluorescence resonance energy transfer between phenanthrene and PAMAM dendrimers. *Phys Chem Chem Phys* **12**, 9285-9291, doi:10.1039/b924522g (2010).

91 Satija, J., Sai, V. V. R. & Mukherji, S. Dendrimers in biosensors: Concept and applications. *Journal of Materials Chemistry* **21**, 14367, doi:10.1039/c1jm10527b (2011).

92 Mark, S. S., Sandhyarani, N., Zhu, C., Campagnolo, C. & Batt, C. A. Dendrimer-functionalized self-assembled monolayers as a surface plasmon resonance sensor surface. *Langmuir* **20**, 6808-6817, doi:10.1021/la0495276 (2004).

93 Benters, R. DNA microarrays with PAMAM dendritic linker systems. *Nucleic Acids Research* **30**, 10e-10, doi:10.1093/nar/30.2.e10 (2002).

94 Olley, D. A. *et al.* Explosive Sensing with Fluorescent Dendrimers: The Role of Collisional Quenching†. *Chemistry of Materials* **23**, 789-794, doi:10.1021/cm1020355 (2011).

95 Singh, P. *et al.* Dendrimer modified biochip for detection of 2,4,6 trinitrotoluene on SPR immunosensor: Fabrication and advantages. *Sensors and Actuators B: Chemical* **137**, 403-409, doi:10.1016/j.snb.2008.12.027 (2009).

96 Balzani, V. *et al.* Dendrimers as fluorescent sensors with signal amplification. *Chemical Communications*, 853-854, doi:10.1039/b002116o (2000).

97 Ilaiyaraja, P., Kumar Singha Deb, A., Ponraju, D. & Venkatraman, B. Xanthate functionalized PAMAM dendrimer (XFPD) chelating ligand for treatment of radioactive liquid wastes. *Journal of Environmental Chemical Engineering* **3**, 1047-1054, doi:10.1016/j.jece.2015.03.013 (2015).

98 Krot, K. A., de Namor, A. F. D., Aguilar-Cornejo, A. & Nolan, K. B. Speciation, stability constants and structures of complexes of copper(II), nickel(II), silver(I) and mercury(II) with PAMAM dendrimer and related tetraamide ligands. *Inorganica Chimica Acta* **358**, 3497-3505, doi:10.1016/j.ica.2005.05.001 (2005).

99 Xu, Y. & Zhao, D. Removal of Lead from Contaminated Soils Using Poly(amidoamine) Dendrimers. *Industrial & Engineering Chemistry Research* **45**, 1758-1765, doi:10.1021/ie050618n (2006).

100 Nepomnyashchii, A. B. *et al.* Cyclic voltammetry studies of Cd2+ and Zn2+ complexation with hydroxyl-terminated polyamidoamine generation 2 dendrimer at a mercury microelectrode. *Journal of Electroanalytical Chemistry* **621**, 286-296, doi:10.1016/j.jelechem.2008.01.025 (2008).

101 Barakat, M. A. *et al.* Remediation of Cu(II), Ni(II), and Cr(III) ions from simulated wastewater by dendrimer/titania composites. *J Environ Manage* **117**, 50-57, doi:10.1016/j.jenvman.2012.12.025 (2013).

102 Ottaviani, M. F., Montalti, F., Romanelli, M., Turro, N. J. & Tomalia, D. A. Characterization of Starburst Dendrimers by EPR. 4. Mn(II) as a Probe of Interphase Properties. *The Journal of Physical Chemistry* **100**, 11033-11042, doi:10.1021/jp953261h (1996).

103 Castillo, V. A., Barakat, M. A., Ramadan, M. H., Woodcock, H. L. & Kuhn, J. N. Metal ion remediation by polyamidoamine dendrimers: a comparison of metal ion, oxidation state, and titania immobilization. *International Journal of Environmental Science and Technology* **11**, 1497-1502, doi:10.1007/s13762-013-0346-5 (2013).

104 Mankbadi, M. R., Barakat, M. A., Ramadan, M. H., Woodcock, H. L. & Kuhn, J. N. Iron chelation by polyamidoamine dendrimers: a second-order kinetic model for metal-amine complexation. *J Phys Chem B* **115**, 13534-13540, doi:10.1021/jp208546a (2011).

105 Tran, M. L., Gahan, L. R. & Gentle, I. R. Structural Studies of Copper(II)−Amine Terminated Dendrimer Complexes by EXAFS. *The Journal of Physical Chemistry B* **108**, 20130-20136, doi:10.1021/jp037569h (2004).

106 Diallo, M. S., Christie, S., Swaminathan, P., Johnson, J. H. & Goddard, W. A. Dendrimer Enhanced Ultrafiltration. 1. Recovery of Cu(II) from Aqueous Solutions Using PAMAM Dendrimers with Ethylene Diamine Core and Terminal NH2Groups. *Environmental Science & Technology* **39**, 1366-1377, doi:10.1021/es048961r (2005).

107 Ottaviani, M. F., Montalti, F., Turro, N. J. & Tomalia, D. A. Characterization of Starburst Dendrimers by the EPR Technique. Copper(II) Ions Binding Full-Generation Dendrimers. *The Journal of Physical Chemistry B* **101**, 158-166, doi:10.1021/jp962857h (1997).

108 Zhou, L., Russell, D. H., Zhao, M. & Crooks, R. M. Characterization of Poly(amidoamine) Dendrimers and Their Complexes with Cu2+by Matrix-Assisted Laser Desorption Ionization Mass Spectrometry. *Macromolecules* **34**, 3567-3573, doi:10.1021/ma001782j (2001).

109 Ottaviani, M. F., Valluzzi, R. & Balogh, L. Internal Structure of Silver−Poly(amidoamine) Dendrimer Complexes and Nanocomposites. *Macromolecules* **35**, 5105-5115, doi:10.1021/ma010492f (2002).

110 Knecht, M. R., Garcia-Martinez, J. C. & Crooks, R. M. Hydrophobic dendrimers as templates for au nanoparticles. *Langmuir* **21**, 11981-11986, doi:10.1021/la051475c (2005).

111 Crooks, R. M., Zhao, M., Sun, L., Chechik, V. & Yeung, L. K. Dendrimer-Encapsulated Metal Nanoparticles: Synthesis, Characterization, and Applications to Catalysis. *Accounts of Chemical Research* **34**, 181-190, doi:10.1021/ar000110a (2001).

112 Ye, H., Scott, R. W. J. & Crooks, R. M. Synthesis, Characterization, and Surface Immobilization of Platinum and Palladium Nanoparticles Encapsulated within Amine-Terminated Poly(amidoamine) Dendrimers. *Langmuir* **20**, 2915-2920, doi:10.1021/la0361060 (2004).

113 Oh, S. K., Niu, Y. & Crooks, R. M. Size-selective catalytic activity of Pd nanoparticles encapsulated within end-group functionalized dendrimers. *Langmuir* **21**, 10209-10213, doi:10.1021/la050524i (2005).

114 Gomez, M. V., Guerra, J., Velders, A. H. & Crooks, R. M. NMR characterization of fourth-generation PAMAM dendrimers in the presence and absence of palladium dendrimer-encapsulated nanoparticles. *J Am Chem Soc* **131**, 341-350, doi:10.1021/ja807488d (2009).
115 Diallo, M. S. *et al.* Dendritic Chelating Agents. 1. Cu(II) Binding to Ethylene Diamine Core Poly(amidoamine) Dendrimers in Aqueous Solutions. *Langmuir* **20**, 2640-2651, doi:10.1021/la036108k (2004).
116 Domaille, D. W., Que, E. L. & Chang, C. J. Synthetic fluorescent sensors for studying the cell biology of metals. *Nat Chem Biol* **4**, 168-175, doi:10.1038/nchembio.69 (2008).
117 Johnson, I. & Spence, M. T. Z. in *The Molecular Probes Handbook: A Guide to Fluorescent Probes and Labeling Technologies* Ch. 1, (Life Technologies, 2010).
118 Johnson, I. & Spence, M. T. Z. in *The Molecular Probes Handbook: A Guide to Fluorescent Probes and Labeling Technologies* Ch. 20, (Life Technologies, 2010).
119 Zhang, X. F., Zhang, J. & Liu, L. Fluorescence properties of twenty fluorescein derivatives: lifetime, quantum yield, absorption and emission spectra. *J Fluoresc* **24**, 819-826, doi:10.1007/s10895-014-1356-5 (2014).
120 *Comprehensive Cytopathology*. 3rd edn, (Saunders Elsevier, 2008).
121 Nolan, E. M. & Lippard, S. J. A "turn-on" fluorescent sensor for the selective detection of mercuric ion in aqueous media. *J Am Chem Soc* **125**, 14270-14271, doi:10.1021/ja037995g (2003).
122 Burdette, S. C., Walkup, G. K., Spingler, B., Tsien, R. Y. & Lippard, S. J. Fluorescent Sensors for Zn2+ Based on a Fluorescein Platform: Synthesis, Properties and Intracellular Distribution. *Journal of American Chemical Society* **123**, 7831–7841, doi:10.1021/ja0100591 (2001).
123 Nolan, E. M. *et al.* Zinspy sensors with enhanced dynamic range for imaging neuronal cell zinc uptake and mobilization. *J Am Chem Soc* **128**, 15517-15528, doi:10.1021/ja065759a (2006).
124 He, Q., Miller, E. W., Wong, A. P. & Chang, C. J. A selective fluorescent sensor for detecting lead in living cells. *J Am Chem Soc* **128**, 9316-9317, doi:10.1021/ja063029x (2006).
125 Grimm, J. B. *et al.* Carbofluoresceins and carborhodamines as scaffolds for high-contrast fluorogenic probes. *ACS Chem Biol* **8**, 1303-1310, doi:10.1021/cb4000822 (2013).
126 Dodani, S. C. *et al.* Copper is an endogenous modulator of neural circuit spontaneous activity. *Proc Natl Acad Sci U S A* **111**, 16280-16285, doi:10.1073/pnas.1409796111 (2014).
127 Jia, S., Ramos-Torres, K. M., Kolemen, S., Ackerman, C. M. & Chang, C. J. Tuning the Color Palette of Fluorescent Copper Sensors through Systematic Heteroatom Substitution at Rhodol Cores. *ACS Chem Biol*, doi:10.1021/acschembio.7b00748 (2017).
128 Kubas, G. J., Monzyk, B. & Crumblis, A. L. Tetrakis(Acetonitrile)Copper(1+) Hexafluorophosphate(1-). 68-70, doi:10.1002/9780470132593.ch15 (1990).
129 Liu, C. *Surface Tethered PAMAM Dendrimers On Controlled Pore Glass As Color Release Sensors For Phosphates* Master's Thesis thesis, Univeristy of San Francisco (2013).
130 Dancer, J. *Glass Foundation Chemosensor Synthesis and Functionality Analysis* Master's Thesis thesis, University of San Francisco (2014).
131 Barquín, M., Cancela, J., González Garmendia, M. J., Quintanilla, J. & Amador, U. Coordination compounds of 4,2′ -6′ ,4″ -terpyridine, [MCl2(4,2′ -6′ ,4″ -terpyridine)], M = Mn(II), Co(II), Ni(II), Cu(II) or Zn(II). Crystal structure of catena-poly [(dichlorozinc)-μ-(4,2′ -6′ ,4″ -terpyridine)]. *Polyhedron* **17**, 2373-2378, doi:10.1016/s0277-5387(97)00420-8 (1998).
132 Constable, E. C. The Coordination Chemistry of 2,2′ :6′ ,2″ -Terpyridine and Higher Oligopyridines. **30**, 69-121, doi:10.1016/s0898-8838(08)60240-8 (1986).
133 Luhrs, A. *Dendrimer Modified Silica Nanoparticles as Fluorescent Chemosensors for the Detection of Copper and Cyanide Ions*, University of San Francisco, (2016).

Chapter 2. Synthesis, Separation, and Characterization

Introduction

As indicated by the title, the following sections outline the synthetic, separation, and characterization of nanoparticles that have undergone surface conjugation. These nanoparticles were then used/test for the sensing of analytes (Chapter 3). This chapter begins with an outline of the synthetic procedures of previous projects within the Margerum group followed by general mechanisms, with reaction schemes and figures to clarify reactions for the synthesis of colloidal silica nanoparticles (SNP). Other conjugation methods, however, are far too expansive to cover in a thesis, and for that the reader is directed to the Bioconjugate Techniques text.[1] The chapter continues with a comparison of general separation and characterization techniques used to isolate and to ensure successful synthesis of nanoparticle conjugates. The chapter will then describe the specifics of each synthesis and provide diagrams to show a 'cored' view (e.g. Figure 2.1) of the assumed surface of the SNP conjugate. This cored view is considered to be the 'ideal' version of the material and the reader should take note that this is likely unrealistic, however, current characterization methods cannot refine surface structures to refute the presented view.[2]

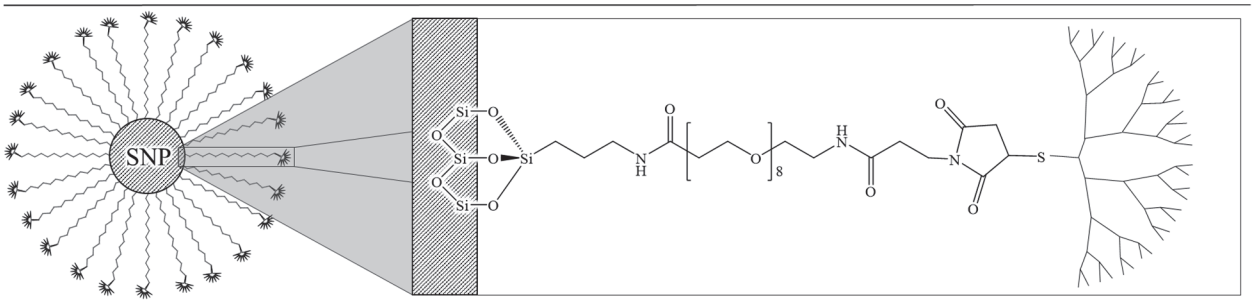

Figure 2.1 Cored view of the conjugated surface of a silica nanoparticle with a silane, heterobifunctional PEG, and cystamine dendron. *Note that the nanoparticles are spherical, considerably larger than the conjugated coating, and that this view is not to scale. Similar figures will be used to illustrate steps in syntheses in this chapter and to aid in clarification as to which conjugated material is being addressed later in the thesis.*

Past Synthetic Procedures: The Literature and the Margerum Group

Currently, the literature lacks adequate requirements for the dispersion of SNPs before, during, and after a synthesis. This is especially apparent in articles that describe the applications of SNP conjugates and provide the bare minimum for synthetic procedures (e.g. time, temperature, molar equivalents, and headspace atmosphere).[2] Conjugation alters the surface chemistry of the particles, altering the stability of the colloid as a whole.[2] Colloid stability is a factor that is often overlooked but can pose downstream difficulties especially with the repeatability of both dispersion stability and adequate functionalization. Furthermore, major problems for applied nanoparticle conjugation studies are (1) lack of nanoparticle conjugation robustness and reproducibility, (2) use of expensive or specialized reagents, and (3) inadequate protocols for handling and use.[2,3,4]

Past research in the Margerum group evolved from conjugating G_0-G_5 PAMAM dendrimers from the surface of controlled pore glass beads (visible) to 22 nm diameter silica nanoparticles through the use of carboxydiimidazole (CDI) chemistry. The role of the silica within the sensor drastically changed from a non-dispersed scaffold that merely chelated analytes to a dispersed scaffold where the sensing took place on the surface of the nanoparticle. This difference is deceivingly inconspicuous, but by attempting to covalently attach the sensing molecule to the scaffold, the group entered the world of colloids.

A major goal of this project was to address the nanoparticle agglomerations occurring during conjugation reactions (that became apparent in previous projects) by identifying which aspects of the synthetic route could lead to agglomerations. Three major synthetic ideas were thought to be sources of the agglomerations and instability of past colloids. The first was using solvents that are incompatible with silica nanoparticles; the second was the use of non-specific conjugation; and the third was the size of the particles.

The Margerum group used commercially produced silica nanoparticles, called LUDOX® AS30, which were a bare, hydroxyl terminated SNP that measures 22 nm in diameter. The first step was the silanization of the surface with (3-aminopropyl) triethoxysilane (APTES) in a 1:1:1.6 H_2O: acetic acid: ethanol solution.[5] Problems with agglomerations could arise immediately due to the instability of silica nanoparticles in a low pH solution, in which the protonation of the hydroxyl groups lowers the surface charge of the particles and reduces repulsion.[6] Use of amino silanes, such as APTES, also leads to more hydrophobic particles than the bare silica, and a possible option for replacement is an epoxy silane.[7] If the colloid is not well dispersed, the nanoparticles may be too concentrated (localized or in general) leading to increased collisions, which can lead to an agglomeration. If agglomerated or a collision occurs during the silanization of the surface, the silane may covalently attach the two interacting particles. This idea of cross-linking nanoparticles through a silane is far more likely to occur with smaller nanoparticles. To avoid crosslinking of small nanoparticles, mono-alkosysilanes are considered a better option than the tri-alkoxysilane APTES.[6] Crosslinking, however, was not limited to the first conjugation of the total synthesis. Organic solvents were used in downstream conjugation reactions.

The use of organic solvents was a viable option for conjugation of large silica substrates, such as glass slides or even controlled pore class, for two reasons: (1) the number of substrates were low (1 or a few thousand per gram respectively), and (2) the relative mass per substrate was high thereby making chances for agglomeration nearly non-existent since the covalent bonding of a few conjugation molecules would easily break. Therefore, approaches to surface modification in non-aqueous solvents were performed successfully without incident. Once the dimensions of the silica shrink to the nanoscale, the dimensions of the SNP begin to approach the same scale of the conjugating molecules allowing for mistaken covalent agglomeration through conjugation. Organic solvents, however, are very poor for the colloidal stability of silica. As in the case of low pH causing colloidal instability, lack of polarity in organic solvents such as dioxane[8] will ultimately lead to the nanoparticles agglomerating during synthetic procedures. Traditionally, surface functionalization to silica surfaces has been performed in non-aqueous solvents to ensure full surface coverage with water sensitive reagents.[9]

The group's previous syntheses used a zero-length crosslinker, called carbonyldiimidazole (CDI), that reacts readily with primary amines on both ends to achieve a monolayer of PAMAM dendrimer on the surface of each SNP. CDI requires non-aqueous solvents due to the linker hydrolyzing before reaction can occur with primary amines[1]; however, SNPs are only stable in aqueous solvents (due to the inherent charges on the surface of the nanoparticle). Solvent polarity is therefore crucial to ensure that a charged passive layer surrounds the nanoparticle so that similarly charged particles repel in solution. In contrast, in non-polar solvents, this repulsion does not exist, and even in aprotic, polar solvents the interaction between particles can overcome the surface charge on the nanoparticles and allow agglomerations to occur.[6] Additionally, SNPs that had an amine surface were reacted with CDI, rinsed of remaining unreacted CDI, and then dendrimer was added to the newly activated SNP.[5] Molar excess of CDI was used to attempt complete conversion of amines into CDI-activated groups but incomplete conversion of amines may have led to SNP-SNP agglomerations through unreacted amine sites on the SNPs. Similarly, SNP-dendrimer-SNP could arise if the dispersion is too concentrated and not enough dendrimers are available to coat each

nanoparticle. Improper dispersion of SNPs may also cause undesired agglomerations to form. Again, size may play a role in the conjugation of dendrimers on the nanoparticle. Since the larger generation dendrimers (G_3 – G_5) start to approach the size of the smaller nanoparticles, and can be thought of as amine coated nanoparticles as well. This in turn increases the concentration of *total particles* and can lead to more agglomerations. The mere size of nanoparticles alone can cause agglomerations.

Due to the curvature on small nanoparticles (<60 nm), the silanols (Si-O-H) are isolated and do not hydrogen bond to surrounding silanols.[10] In larger particles (>60 nm), the silanol groups hydrogen bond, which results in a polarization of the O-H bond and allows protonated silanol groups to hydrogen bond with the surrounding water and repulse other nanoparticles. This polarized bond and hydrogen bonded water is also thought to increase the reactivity of surface silanols with silanes on the surface of the nanoparticle.[10] In other words, larger silica nanoparticles have sites that are more reactive and are more stable once dispersed, which would allow for better conjugation reactions.

Attempts were made to circumvent the creation of irreversible agglomerations (coagulations) by using more dilute syntheses in more polar, aprotic solvents and by ensuring dispersion of the colloidal suspension before adding reactants. Particle size was increased at least 10 fold (~250 nm) in order to achieve an order of magnitude (or larger) size difference between dendrimer and SNP. Additionally, a completely water based synthesis was designed to remove organic solvents.[1] The following synthetic procedures outline the general reaction descriptions and mechanisms of the previous non-aqueous methods. This is followed by the newly designed method in the bottom approach of the SNP conjugate material. Procedures provided later in the chapter are not considered robust, struggle with reproducibility, and use expensive reagents. The hope of this project was to provide a systematic process with the purpose to steer the reader toward a more favorable direction for nanoparticle conjugation.

Synthesis of Silica Nanoparticles

Silica nanoparticles have been the subject of a variety of research applications that range from food additives,[11] biomaterials,[1] and sensing[12] due to the versatility of the material. Synthetic procedures allow for the tuning of nanoparticle size, shape and surface conjugation for function while remaining relatively non-toxic.[13] Today, most syntheses of monodispersed silica nanoparticles can be traced back to a single set of syntheses published in 1968 where Werner Stöber, Arthur Fink, and Ernest Bohn made spherical particles with diameters of 50 nm to 2 μm. This was accomplished through the hydrolysis of alkyl silicates (alkylsilane) and condensation of the silicic acid in solutions of ammonium hydroxide and various alcohols (methanol, ethanol, n-propanol, and n-butanol).[14] Prior to syntheses, the alkyl silicate used was distilled in order to ensure regular spherical nanoparticles with relatively narrow size distributions.[14] Stöber et al. described the formation of nanoparticles was observed within the first 10 min due to an increased opalescence of the solution which finally turned turbid within 15 min.[14] Samples were taken throughout the 120 min synthesis and a scanning electron microscope (SEM) was used to show the reaction reached a uniform size within 15 min.

SNPs were found to be the smallest and fastest forming in methanol. As the alcohol increased in size from (methanol to ethanol, etc.) the size of the particles also increased, the formation was slowed, and the size distribution was larger in the larger alcohols.[14] Similar results were observed when the alkyl ester on the silicates were increased (methyl to ethyl, etc). The concentration of water and ammonia was varied and increasing concentrations of both, saturated and 6 M respectively, resulted in the increase of particle size. Increased water concentration was also determined to increase condensation rate, whereas the absence of ammonia resulted in irregular shapes of particles. Ammonia was thus concluded to be influential in the

morphology of the nanoparticles.[14] The predictive control of nanoparticle size via synthetic methodology was determined to be a 30% margin of error in size prediction and the geometric size distribution was below 1.10. This pioneering work has been dubbed the Stöber method, and despite some variations over the years, the main components of the synthesis remain intact and are in continued use today, earning an incredible 717 citations in 2016 alone and on par to match in 2017.

Mechanisms for the Stöber method start with agreement on the hydrolysis and condensation steps (Scheme 2.1), but the growth of the nanoparticle up to sizes larger than a few nanometers continues to be debated. The initial steps of SNP synthesis begin with the hydrolysis of the alkyl silicate monomers followed by the subsequent condensation into oligomeric precursors that continue to grow into small seed nucleations (Scheme 2.1). The small seed nanoparticles are approximately 2.3 nm at this step, which is where the two proposed mechanisms diverge. The first attributes the increased growth in nanoparticle size to monomer additions.[15,16] This idea takes a more traditional approach to the growth of solid structures from solutions in general. However, the formation of silica structures was later shown to be far more dynamic[17] and include the association of small nanoparticles that then collapse to give rise to larger particles.[18],[19] As the particles collapse the unreacted Si-OH groups react producing water and fill the interstices, which produces particles that are solid (not mesoporous).[17]

Scheme 2.1 General mechanism of silica nanoparticle formation from an alkylsilicate precursor

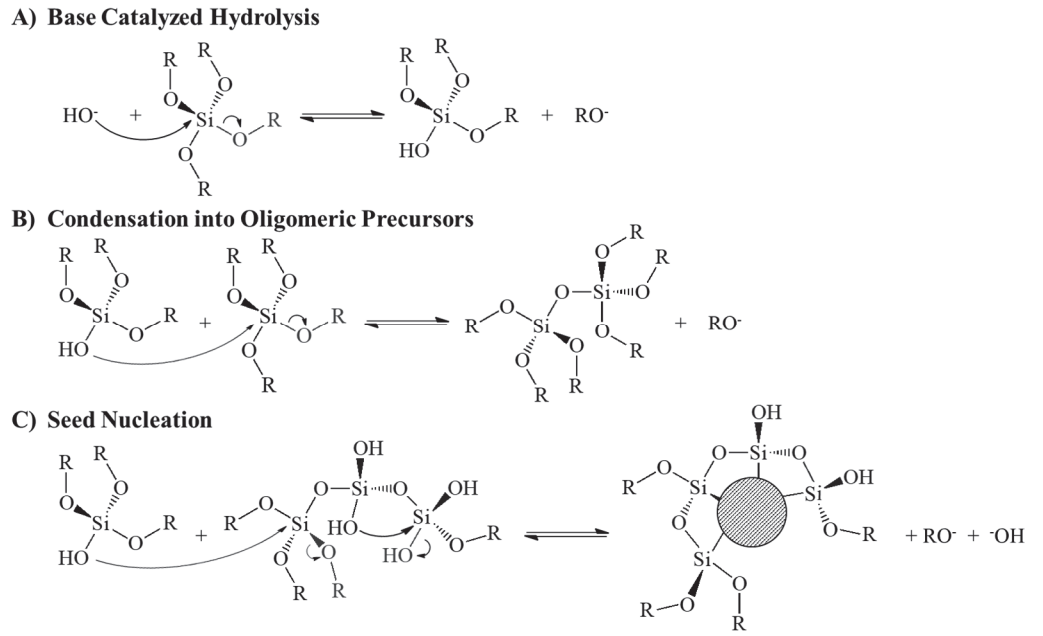

Regardless of the mechanism, there is a consensus on the importance of water and ammonia concentrations to the final size.[15,16,18,20] Zhang et. al. showed that, upon predilution of the alkyl silicate (tetraethylorthosilicate, TEOS) in ethanol prior to synthesis, the resulting monodispersed silica nanoparticle ranged from 150 nm ± 5% to 1 μm ± 1%.[21] This predilution removed the need for distillation of the alkyl silicate before the synthesis but also narrowed the size distribution to 1-5% instead of the 30% shown in the original Stöber method. Zhang et al. also showed that the diameters of smaller nanoparticles could be increased with sequential additions of the diluted alkyl silicates and even determined an equation to determine the final SNP size if the number of particle seeds remains constant.[21] The equation,

$$d = d_o(V/V_o)^{1/3}$$ Equation 2.1

shows that nanoparticles of a larger diameter (d) can be made with the average of the seed diameter (d_o) multiplied by the cube root of the ratio between the total volume (V) of alkyl silicate, and the volume (V_o) of the alkyl silicate used to produce the seeds. Soto-Cantu et al. extended the work of Zhang et al. by showing the size of the nanoparticles could be designed in a general synthesis with the variation of water: TEOS weight ratios and concluded that the increase of this ratio increased the size of the nanoparticles.[22] Soto-Cantu provided a method of calculating the sizes based on other synthetic compositions to formulate predictions, however, the predictions were 2-3x larger than the actual SNP sizes. Soto-Cantu also ensured that the conservation of the ratios yielded similar results in size after increasing syntheses to gram scaled quantities.[22] With the ability to finely tune these materials to a desirable size range, comparisons between sizes for certain applications was possible.

As stated in the previous chapter, the application desired in the work described here was to use the nanoparticle as a scaffold to build a chemical sensor. The sensor was to be small enough to remain dispersed in solution during syntheses and fluorescence measurements but large enough to be easily isolated from reactants after syntheses. Iijima et al. established that the particles size significantly affected the surface silanol structure of silica nanoparticles, which then affected the stability of the colloid as well as the reactivity of the surface.[10] Larger particles (200 nm) were said to have a less drastic surface curvature, which then allowed for more hydrogen bonding between adjacent surface silanols and water molecules (Figure 2.2).

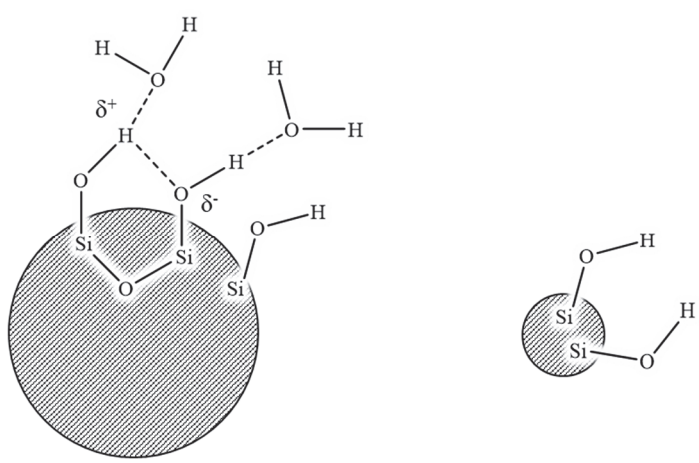

Figure 2.2 Larger particles (>30 nm, left) have surface silanols that hydrogen bond with adjacent silanols resulting in the polarization (δ^+, δ^-) of the surface, resulting in a high hydration and therefore water layer formation. Smaller nanoparticles (<10 nm, right) have isolated silanols that do not result in the formation of a stable hydration layer. Reprinted from Kamiya et al.

Gram scale quantities of large, bare SNPs are required to perform 10-100 mg scale conjugation syntheses that can then be compared since the mass of the SNP scaffold essentially remains constant. Addition of surface conjugates to small nanoparticles (1 - 10 nm) could alter the overall mass and could drastically change the surface chemistry of the particles. The size of the nanoparticles as well as suspension

media within a colloid are considered to be important aspect of colloidal stability. Colloids created and used in non-polar solvents are most stable with long alkyl coatings, however, when using polar solvents, charged surfaces or surfaces that can take part in hydrogen bonding are preferred.

As stated above, particles in previous graduate student projects were considered to be too small for the desired conjugation steps and, after numerous failed attempts to ensure colloidal stability with the dendrimer conjugations, the nanoparticle size was increased from ~20 nm to 250 nm. The size increase allows for a nanoparticle conjugate that can endure conjugations of large polymers, such as dendrimers, while remaining in solution as well as being easily isolated post-conjugation.

Surface Chemistry and Conjugations

Silanizations[1]

Reactions involving silanes, monomeric silicon-based molecules that contain four other substituents, are typically called silane-coupling reactions. Silanes with carbon, hydrogen, and oxygen directly attached to the silicon are considered to be organosilanes. Silane coupling reactions, sometimes referred to as silanization, are used in a variety of applications that include the functionalization of organic molecules as a protecting group[1] or covalently bonding inorganic substrates (or surfaces) with organic molecules.[1] The organic group on the silane may be a long chain hydrocarbon that provides the substrate with hydrophobic character or may end in reactive groups that permit downstream reactions. The general structure of a triethoxy organosilane (Scheme 2.2) consists of only a single organic chain, typically alkyl with some R-group, and three hydrolyzable groups (tryethoxy). The hydrolyzable groups may consist of a number of groups such as hydrogen (silicon hydride), a halogen (silicon halide), an alcohol group (silanol), or alkoxy groups (typically methoxy- or ethoxysilanes). Silanol groups undergo spontaneous hydrogen bonding in solution at room temperature whereas the alkoxysilanes are relatively stable and unreactive to the hydroxyide groups at room temperature and thus, increased temperatures are required.

Scheme 2.2 Generalized silanization of the SNP surface

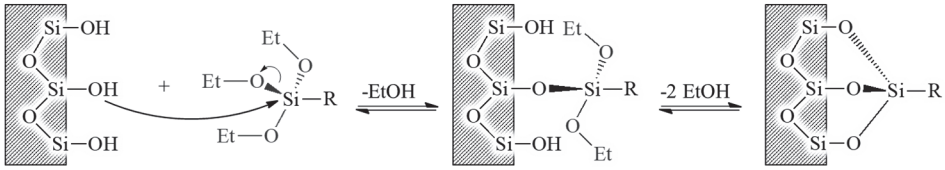

The most common type of organosilane for surface functionalization is the alkoxy silanes whose alkoxy groups undergo hydrolysis to form a reactive silanol intermediate that subsequently couples to the substrate (Scheme 2.2). In aqueous solutions, the silanol intermediates begin to hydrogen bond which inevitably leads to silanol condensation and polymerization leading to the synthesis of silane polymers.[1] This silane polymer then hydrogen bonds to the surface, undergoes another condensation reaction, and the final surface functionalization is completed.[1] A more in-depth scheme can be found in the Silane Coupling Chapter (Chapter 13) in Hermanson's Bioconjugate Techniques.[1] Although monolayer deposition is assumed and shown in figures, monolayers do not occur. Gelest, a prominent silane supplier, reports that deposition of silanes in 0.25% aqueous solutions result in layers approximately three to five silanes thick.[9] Non-aqueous environments are more likely to produce monolayers due to lack of hydrogen bonding and subsequent polymerization of the alkoxysilanes with each other prior to condensation on the surface of the substrate. The condensation, however, introduces water into the reaction, and to ensure a continuous

monolayer the removal of water is critical.[9] Silane coupling reactions can be carried out in aqueous solution, non-aqueous organic solvent, a combination of aqueous and organic solvent, and even vapor phase. The reaction conditions are usually dictated by the nature of the substrate undergoing the silanization. Size effects, such as the differences between nanomaterials and macromaterials as well as differences in material composition will dictate the optimal synthetic route approach.

A wide variety of inorganic surfaces can undergo passivation or functionalization with organosilanes that include silica, quartz, and other glasses as well as oxides of aluminum, copper, tin, titanium, iron, chromium, zirconium, nickel, and zinc metals in order of efficiency and stability.[1] To ensure stable silanization, the surface must be cleaned (similar to the cleaning of glass) with (5% HCl) or piranha (25% sulfuric acid solution with 15% hydrogen peroxide) solutions. This results in a high density of hydroxyl functional groups for the silanes to bond, which then allows for higher density of silanization.

Once the silane binds to the surface of the substrate, further conjugation can occur with the functional group of the silane. This reactive group is typically an amine, hydroxyl, aldehyde, epoxy, carboxylate, thiol, and sometimes alkyl groups (hydrophobic interactions or used as a spacer between other silanes). Amine and alkyl silanes are the primary focus of this thesis and the remainder of the reactive groups will no longer be discussed, however the reader is directed to the Bioconjugate Techniques text and chemical suppliers such as Gelest for other conjugation options. The organosilane 3-Aminopropyltriethoxysilane (APTES) is a common silane-coupling agent especially in the functionalization of silica nanoparticles[1] and was used in conjunction with trimethoxymethylsilane (MTMS), which was used as a spacer. The differences in the alkoxy groups (ethoxy and methoxy respectively) are apparent in the reactivity and deposition of the organosilane. The methoxy group does not require water for hydrolysis and can undergo hydrolysis and subsequent polymerization in non-aqueous solvents. The ethoxy requires water and is typically performed in ethanol water mixtures (5% water) with acetic acid to lower the pH (4.5-5.5) that results in a layer of three to five silanes thick.[9] Due to the inherent differences in reactivity, a 1:1 molar ratio of methoxy:ethoxy would likely result in the incorporation of more methoxy silanes than ethoxy on the surface. The surface of the silica nanoparticle was functionalized with amine groups that were spaced using methyl groups. This provide adequate space for reactions on the surface (remove steric hindrance), the amine group can then be functionalized further. There are a wide variety of amine reactive groups using on conjugation reactions; however, only carboxylate, NHS-ester, and isothiocynate reactions will be considered here.

As discussed, alkoxysilanes not only react with the surface of inorganic substrates, such as silica, but permits further functionalization which classifies these silanes as bifunctional linkers in the sense that they link two distinctly different molecules or macromolecules together. The linking of molecules for distinctly new properties from the separate components opens the materials to new applications, which is at the heart of bioconjugation.

Carbonyldiimidazole Reactions[1]

The zero-length crosslinker N, N'-carbonyldiimidazole uses two acylimidazole leaving groups for coupling reactions (Figure 2.3). A nucleophile, such as a primary amine on the surface of a nanoparticle, attacks the carbonyl carbon and thereby releases an imidazole leaving group. The remaining imidazole group, called an imidazole carbamate, is considered an active intermediate and was assumed to be left intact for further conjugation with another nucleophile such as another primary amine. This reactive group is sometimes referred to an activated functional group, in this case an activated amine. CDI may also be used for the activation of hydroxyl groups, however, through a different mechanism, of which can lead to side

reactions that produce active carbonates between adjacent hydroxide groups. Interestingly, the carbonate group remains reactive towards amines to create carbamate linkages. Although highly reactive, CDI chemistry has synthetic limitations in appropriate solvents.

Dry, non-aqueous solvents are required to achieve an adequate yield. Even in the presence of small amounts of water, CDI almost immediately hydrolyzes into imidazole and carbon dioxide from the nucleophilic attack from water. Solvents are suitable with a water content of less than 0.1%. Suitable solvents for CDI chemistry include THF, DMF, and DMSO. Upon addition of water to these solvents in the presence of CDI, bubbles of CO_2 can be seen, and if an excess of CDI is quenched with water, heat will evolve.[23] The imidazole carbamate (activated group) has a half-life of hours in aqueous environments, and the conjugate can be moved to aqueous solutions after the initial CDI activation.[1] CDI, however, can undergo side reactions with hydroxyl groups and subsequent amine groups creating a stable urethane linkage or with carboxylic acids creating ester bonds.[1]

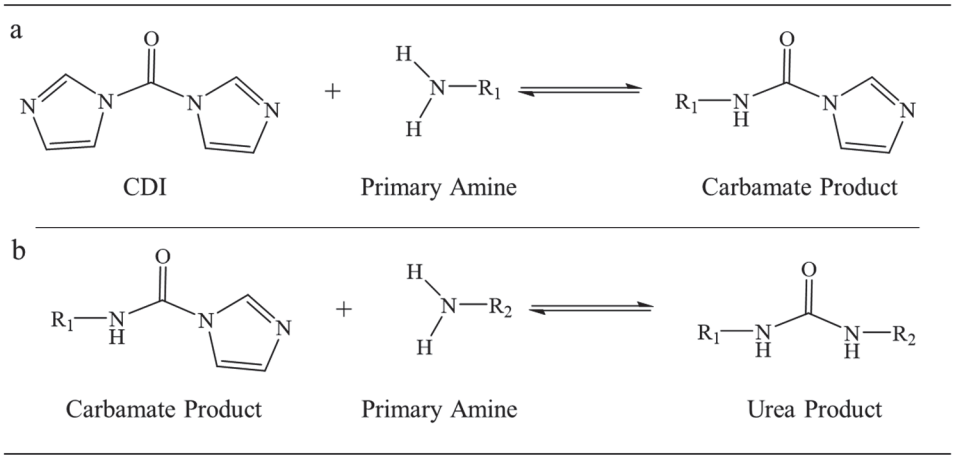

Figure 2.3 General reaction of carbonyldiimidazole (CDI) with two different primary amines where (a) the first primary amine (H_2N-R_1) is completely converted to the carbamate product and (b) a second primary amine (H_2N-R_2) is introduced.[1]

NHS-ester Reactions[1]

Reactions with primary amines are not limited to CDI conjugation. The N-hydroxysuccinimide ester (NHS-ester) reacts with primary (Figure 2.4) and secondary amines to produce stable amide and imide bonds respectively. The reaction is similar to that of the CDI, where the amine nucleophilically attacks the carbonyl on the activated ester thereby creating an amide bond and disrupting the ester bond. As with CDI, the NHS-ester hydrolyzes in water but with a half-life of hours (physiologic pH) instead of minutes. The more water-soluble and water stable sulfo-NHS-ester can be used in place of the NHS-ester with the similar specificity as the NHS-ester. Both NHS-esters and the sulfo-NHS-ester react with sulfhydryl and hydroxyl groups; however, the resulting thioester and esters are not stable and degrade in aqueous solutions and in the presence of amines.

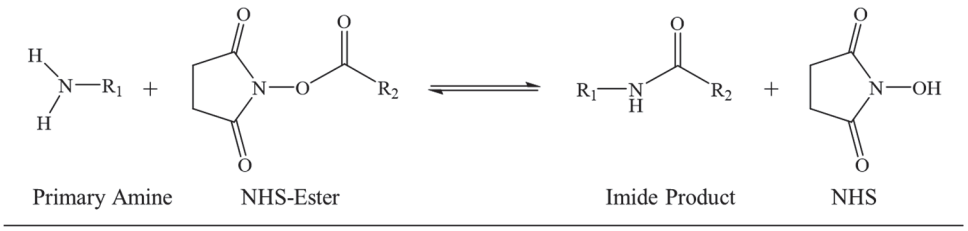

Figure 2.4 General reaction of NHS-ester with a primary amine

Isothiocynate (NCS) Reactions

Unlike the CDI and NHS-ester reactive groups, isothiocynates do not contain a leaving group when reacting with a primary amine (Figure 2.5). The primary amine nucleophilically attacks the carbon on the thioketone of the NCS group creating a thiourea linkage. Similar to the NHS-ester, the hydrolysis of NCS is relatively slow.[1] The NCS group remains stable for hours, and therefore reactions in water are relatively common. Isothiocynate groups react with primary amines exclusively, although nucleophiles such as sulfhydryl groups do react, the conjugation is unstable and degrades.[24]

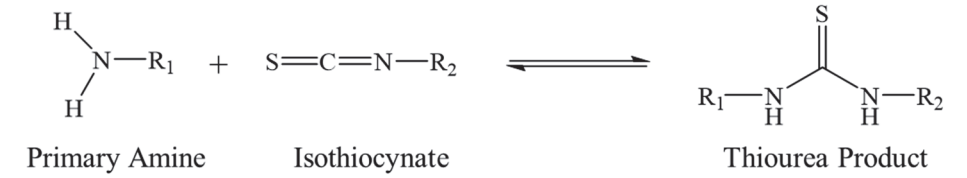

Figure 2.5 General reaction of isothiocynate (NCS) reaction with a primary amine.

Maleimide Reactions

In a maleimide reaction, thiol (thiolate anion) nucleophilically attacks one of the carbons adjacent to the double bond (Figure 2.6).[1] This alkylation reaction with sulfhydryl groups forms stable thioether bonds in aqueous solvents pH 6.5-7.5.[1] The pH of the solution can be crucial in the reaction rate of the maleimide with sulfhydryl. At pH 7, maleimide reactions with sulfhydryls are 1000 times faster than with an amine. As pH increases, some cross-reactivity with amines at higher pH has been shown.[1] Hydrolysis of the maleimide group may occur before coupling which opens the maleimide ring to form maleamic acid, which is no longer reactive.[1] Maleimides are less susceptible to hydrolysis than NHS-esters and become advantageous when using NHS-ester-maleimide heterobifunctional linkers. A relatively fast purification to remove excess cross linker is permitted while maintaining the reactivity of the maleimide groups.

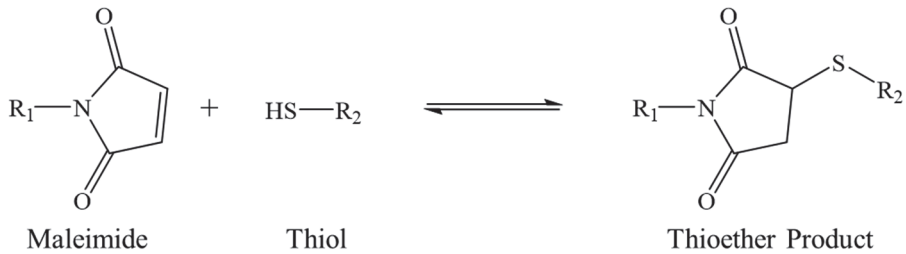

Figure 2.6 General reaction of maleimide with a thiol

Disulfide Reduction Reactions

A simple method of thiol formation is through the reduction of disulfide bonds. There are a multitude of reducing agents that can be used to reduce the disulfide bonds, however, downstream syntheses should be taken into consideration. Since the sulfhydryl groups will be exploited using a maleimide group in subsequent reactions, thiol containing reducing agents should be avoided. Dithiothreitol (DTT) is a common reducing agent in bioconjugation reactions that is water soluble and has similar reactivity to TCEP, however, unreacted DDT has available thiol groups to react. This would require a purification step to remove excess DDT. To avoid unnecessary purifications, TCEP was used for disulfide reduction reactions. A proposed reaction mechanism is shown in Scheme 2.3.

Scheme 2.3 Proposed reaction mechanism of disulfide using TCEP[1]

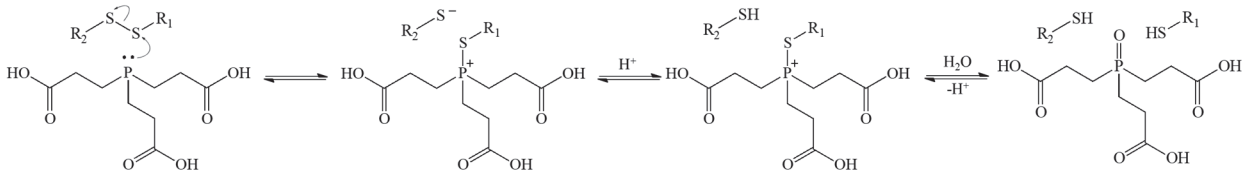

Bromination Reaction

By reacting fluorescein with liquid bromine, the dye eosin Y is produced (Figure 2.7). This reaction generates yields of ≥90%. in ethanol[25] as well as phosphate buffered solution (pH 9)[26] Due to the phenolic groups at 3' and 6' on the xanthene core, which are strong ortho-para activating directors, bromination occurs at positions 2', 4', 5', and 7' (Figure 2.7).[27] Bromination is not likely to occur on the benzoic group due to the carboxylic acid (moderate meta deactivator)[27] at position 2, an isothiocynate group at position 5 (reactive group from FITC), and steric effects from the bulk of the dye.

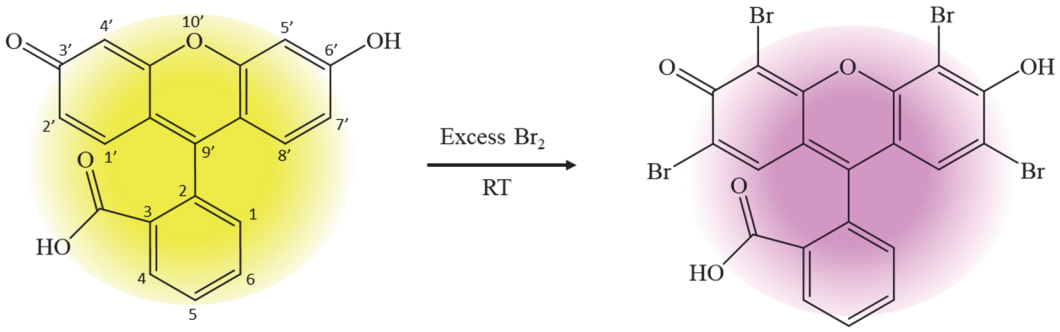

Figure 2.7 Reaction of fluorescein with bromine to produce eosin Y.

Separation Techniques

Separation of the nanoparticles from the reactants is important prior to proceeding with subsequent reactions, characterizing, and sensing. Reactants and side products that are not removed could lead to more side products, inefficient reactions, or misleading analyses. A variety of techniques have been shown to be viable options in the separation of nanoparticles. Many of these techniques are traditionally employed in the isolation of proteins and other biomacromolecules in biochemistry but remain viable options for nanoparticle isolation. Electrophoresis[28,29,30], chromatography[30,31], diafiltration[30-32], centrifugation[30,31,33], flow cytometry[34], and nanoscale lateral displacement arrays[35] are a few of the methods available. Separation methods that do not require an impeding matrix to separate reaction products were thought to be the best

approach to limit any interactions between nanoparticle conjugate and separation methods. Upon review of the aforementioned methods, centrifugation was thought to be the best option as a separation technique due to the high density of silica (1.96 g/cm^3)[36], which allows for easy separation via sedimentation (centrifugation). By centrifuging a reaction, the nanoparticle conjugates are forced to the bottom of the centrifuge tube while the dissolved reactants remain in the supernatant, which can then be decanted.[8] Redispersion and centrifugation with fresh dispersion media serves as a method of washing the nanoparticles and removing remaining reactants. Additionally, centrifugation provides a way to isolate nanoparticle material for drying. Once dry, mass percent recovered from the reaction can be calculated and the nanoparticles can then be redispersed at a set concentration (mg/mL).

Size Determination

A number of methods are available to determine the various properties of nanoparticles.[37] Among them, the most common are transmission electron microscopy (TEM), anisotropy, and dynamic light scattering (DLS). Fundamentally, the three techniques can be divided into two groups: dry and dispersed. TEM, a dry technique, reports particle dimensions defined by the hard edges of the material, which allows for the determination of asymmetrical particles. However, differences in the nanoscale conjugation of silanes or polymers are lost in the TEM image.

TEM uses a beam of electrons transmitted through the sample and measures the interactions of the electrons to form images. Of the three methods, TEM is the best-suited to determine the three dimensional characteristics of particles, such as shape, since the particle is actually viewed (Figure 2.8). Numerous publications have used TEM as a method for measuring nanoparticle size, however, the method falls short when attempting to determine the viability of the nanoparticles when dispersed in solution since most TEM requires a dry sample. Furthermore, TEM cannot differentiate particles that are agglomerated or simply stacked. Experiments that infer single particle dispersion can be carried out through use of sequential dilutions of a dispersion and acquisition of separate TEM images of each dilution. At a certain a dilution, single nanoparticles would begin to appear without other nanoparticles nearby. This would require a considerable amount of time on the TEM, an instrument not currently available at USF.

Fluorescence anisotropy and DLS, both wet techniques, can be used to determine the hydrodynamic (Stokes) diameter (d_H) of a particle, which are dependent on the particle size and the waters of hydration adsorbed to the particle (Figure 2.8, right). The size of a particle measured using a TEM should always be smaller than the size of the same nanoparticle measured in DLS due to these adsorbed molecules and, therefore, the method of size determination should be included when reporting particle sizes. Dimensional characteristics (symmetry) are lost in anisotropy and DLS measurements, and thus the particles are typically assumed to be perfectly spherical.

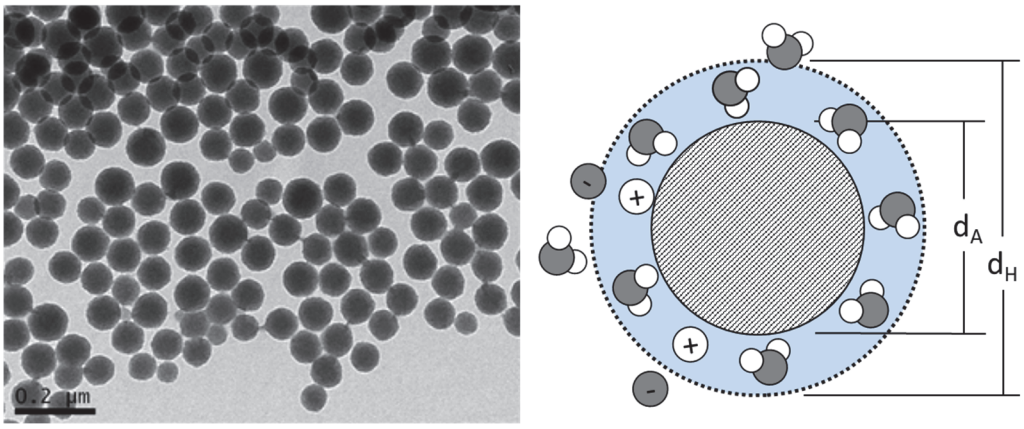

Figure 2.8 TEM image (left) of SNP particles that measure 80 ± 12 nm. Reprinted from the supplemental information of Moore et. al.[2] Diagram of a spherical SNP (right) in which the surface charge is negative when dispersed in water with some electrolytes. The actual diameter (d_A) is always smaller than the hydrodynamic diameter (d_H). The dotted line depicts the slipping plane between the bulk of the suspension medium and the solvent molecules associated with the particle.

A popular technique in biochemistry, fluorescence anisotropy is typically used to measure the interactions between a fluorescently tagged protein and an untagged protein.[38] The technique has also been shown to determine the size of nanoparticles that have a bound dye, either covalently (chemisorbed) or adsorbed (physisorbed) to the surface.[39-42] In general, fluorescence anisotropy excites a population of fluorophores with polarized light and measures the depolarized emission perpendicular to the excitation light. Measuring the intensity of depolarization is dependent on the rotation of the fluorophore in solution and the rotation is based on the size of the particle. The larger the particle, the slower the rotation.

Each technique has advantages and disadvantages, and through the comparison of techniques, conclusions on the most viable option can be made. Arguably, a project would benefit from doing all of the techniques in a true comparison, but due to time constraints, difficulty, and availability, only DLS was pursued here. The following sections are to provide background on the options within the field for future reference.

Dynamic Light Scattering (DLS)

Photon correlation spectroscopy (PCS) or dynamic light scattering (DLS), which is also sometimes referred to as quasi-elastic light scattering (QELS),[43] uses a laser to measure the size of particles in a dispersion medium on the nanometer to micron scale. Nanoparticles move in suspension due to thermal energy, also called Brownian motion, and the DLS uses a laser to measure this motion by monitoring the intensity fluctuations of the light scattered by the nanoparticles.[44] A pattern generated from the detector at an initial time, t_0, is then compared to the pattern at some time after, t_f and the correlation of the two is related to the size of particle. Large particles will move more slowly, resulting in a better correlation of scattering since distance travelled between t_0 and t_f is negligible. Smaller particles move faster and have less pattern correlation between t_0 and t_f. After the correlation function for a particle has been measured, the size distribution can be calculated. Size distribution is based on the intensity of scattered light, and the intensity of light scattered from large particles is much larger than smaller particles.[44] *Note: For a more mathematical description of DLS measurements and calculations to determine sizes of particles please*

refer to Dynamic Light Scattering with Applications to Chemistry, Biology, and Physics[45] *as well as Dynamic Light Scattering: An introduction in 30 minutes.*[46]

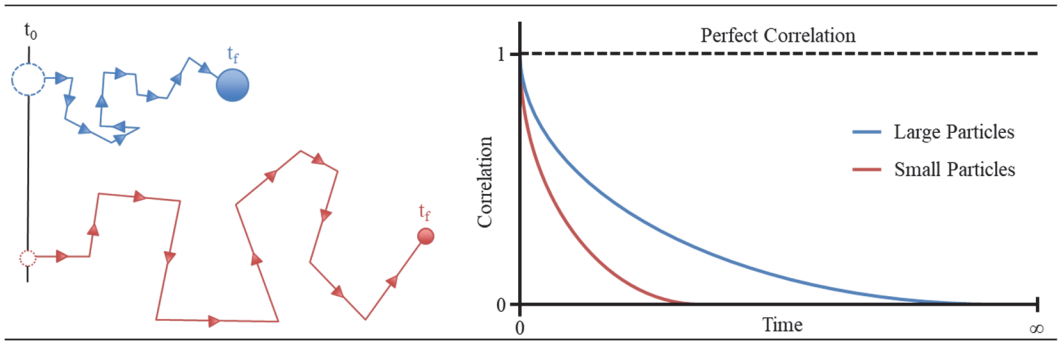

Figure 2.9 The movement of particles is inhibited by random collisions with other particles and solvent molecules. The average distance that a large molecule (blue) travels between collisions is smaller than the distance travelled by small particles (red). This difference translates to the correlation of scattered light from a population of particles. The correlation decay occurs faster for small particles (red) than larger particles (blue) due to the smaller particles moving a greater distance from t_0 to t_f.

Since particle size is determined via Brownian motion of a particle through a medium, size is dependent on a number of factors. The viscosity and ionic strength of the medium in which the particle is dispersed affects size determination by changing the hydrodynamic radius of the particle. As shown in (Figure 2.9), the associated water molecules adsorb to the surface of the particle, thereby hindering the particle's motion, which then increases the measured particle size. By decreasing the viscosity of the medium, solvent molecules flow more easily than if the medium was more viscous. Increasing the ionic strength of the medium decreases the electrical double layer (Figure 2.10), which allows a more pronounced *slipping plane* (dotted line, Figure 2.10 right) across the surface of the particle which then decreases the friction between the particle and the solvent molecules. By increasing the ionic strength to 10 mM or greater, the double layer decreases, resulting in a double layer that is more representative of the actual diameter of the particle. Increasing the ionic strength of the solution also removes any *long-distance* effects (polarization) between particles through the bulk.[44]

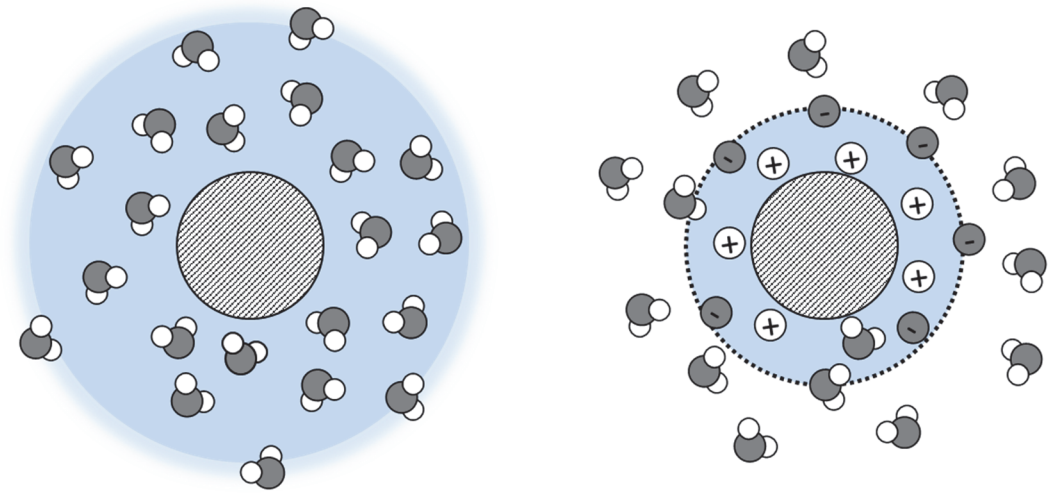

Figure 2.10 A particle suspended in water has a diffuse layer of water molecules loosely adsorbed (left). Increasing the ionic strength of the solution (right) reduces the thickness of the electrical double layer.

Accurate results of size determination via DLS is not only dependent on the viscosity and ionic strength of the medium but also the concentration and size distribution of the particles. A concentrated suspension of nanoparticles can lead to aggregates that mimic the Brownian motion of a larger particle. For example, a 200 nm particle will scatter one million times more light than a 20 nm particle which can result in misleading average diameters since distribution data is measured based on intensity. To account for varying sizes of particles in a dispersion, a polydispersity index is used as a measurement of accuracy. Polydispersity index is defined as

$$PDI = (\frac{\sigma}{d})^2 \qquad \text{Equation 2.2}$$

where $\boldsymbol{\sigma}$ is the square of the standard deviation and d is the mean diameter of the distribution of nanoparticles. Table 2.1 describes the meaning of PDI with respect to the polydispersity of the dispersion and, as shown in Equation 2.2. The lower the PDI, the better the dispersion.

Table 2.1 Polydispersity Index (PDI) and the meaning relative to the colloid being measured.[44]

Polydispersity Index	Comments
< 0.05	Only normally encountered with latex standards or particles made to be monodisperse
< 0.08	Nearly monodisperse sample. Normally, DLS can only give a monomodal distribution within this range
0.08 - 0.7	Mid-range value of PDI. It is the range over which the distribution algorithms best operate over
> 0.7	Indicates a very broad distribution of particle sizes

In cases that require dispersions of multiple sizes, one must be aware of how the distributions are displayed. The difference between *size distributions by intensity, volume, and number* can mislead the

analysis of size distributions based on population. If an equal concentration of 200 nm and 20 nm particles are mixed and sizes determined, the number distribution will result in equal sized peaks of both 200 nm and 20 nm. Volume and intensity distributions however, will result in a thousand and a million times larger peak for the 200 nm particle distribution as compared to the 20 nm distribution peak. This is due to the fact that increase in volume from 20 nm to 200 nm is a thousand fold and the scattering of a 20 nm particle is one millionth of a 200 nm particle (Rayleigh approximation = $I \alpha d^6$).

Size distribution by intensity is the best indicator of size for the instrument used in this work. It is the measure in which the size distribution by volume and number is inferred (size distribution by volume and number can be misleading)[47], and therefore it is crucial to ensure that the suspension in monodispersed.

Surface Analyses

Conjugation with silanes, polymers, and dyes to nanoparticles can change the surface chemistry immensely. Changing the surface chemistry can then alter the dispersion properties of the nanoparticle. Zeta potential is a measurement that can infer long-term stability of dispersions and is dependent on particle size and, more importantly, surface coating. The goal of using zeta potential is to determine the effects of surface conjugation on the relative stability of the colloid.[46] Bare SNP particles have a surface of hydroxyl groups (R-OH) and may be converted to amine groups (R-NH_2) via silane chemistry. The difference in zeta potentials between these two groups is apparent when the zeta potential is monitored over a large pH range (2-10) thereby also providing information on the extent of conjugation with the amine groups.[46]

By incorporating reactive groups on the surface of the SNPs, further reactions through use of bioconjugate techniques can be performed, thereby tuning the surface chemistry to the specifications of an application. Bioconjugation functional groups that are widely used in bioconjugation are hydroxyls (R-OH), carboxylic acids (R-COOH), aldehydes and ketones (RHO and ROR respectively), thiols (R-SH), and primary amines (R-NH_2). Although there are a variety of functional groups, the focus of this project is to use primary amines as the reactive surface groups to simplify the characterization methods by monitoring a single functional group.

Zeta Potential

Using a similar technique as DLS, zeta potential uses light scattering to monitor the motion of suspended nanoparticles, but instead of Brownian motion, zeta potential measures electrophoretic motion.

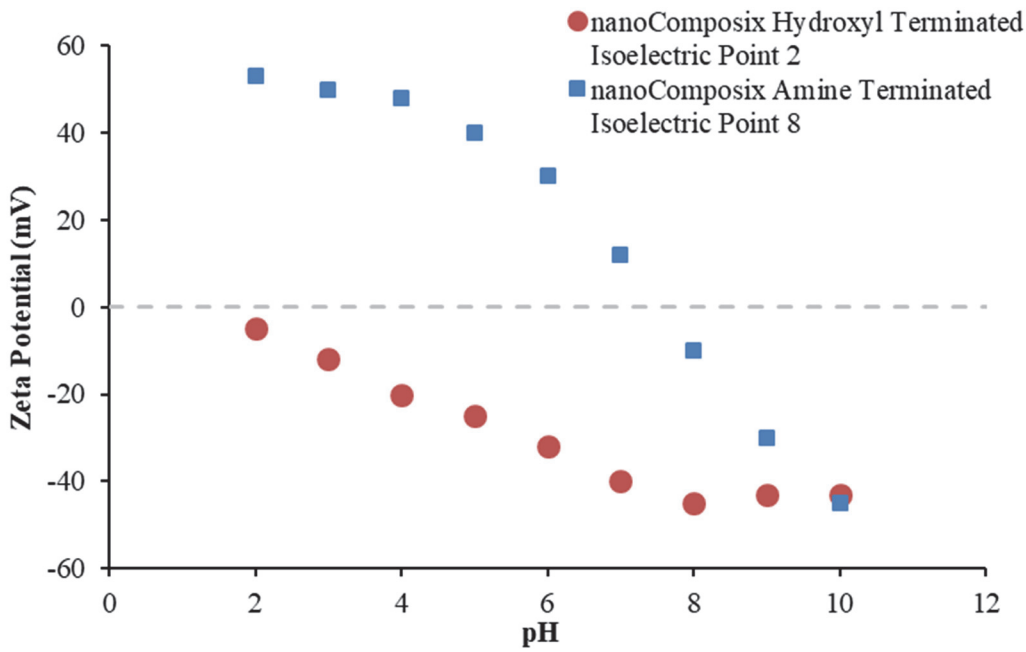

Figure 2.11 Zeta potentials from nanoComposix Hydroxyl terminated and Amine terminated nanoparticles. Reprinted from nanoComposix.[48]

Amine Assays

Monitoring the "apparent" surface amine concentration has a dual purpose. The first is to ensure the surface is coated with enough groups for further conjugation steps and the second is to add charged end groups to ensure the stability of the SNP in dispersion. There was, however, no obligation to ensure reactivity of every amine on the SNP. *Note: There is no guarantee that all surface amines are reactive.* The goal was to monitor relative amine concentrations between materials at different stages of conjugation and determine the number of reaction sites for further conjugation. There are a number of amine assays available, however, only three will be reviewed here, as they were all methods used by the Margerum group in the past. The three assays are ninhrdrin[8,49], nitrobenzaldehyde[50,51], and fluorescamine, all of which are assays named after the active compound used. Each assay uses either spectrophotometry or fluorimetry to detect primary amines.

Ninhydrin

Since discovered by Siegfried Ruhemann in 1910, ninhydrin has been used for a variety of applications and is a well-known amine assay.[52] Ninhydrin has been used for amine determination on amine coated SNPs[22], PAMAM dendrimers[53], as well as the conjugates of PAMAM onto SNPs.[8] The general reaction of ninhydrin with a primary amine can be seen in Figure 2.12.

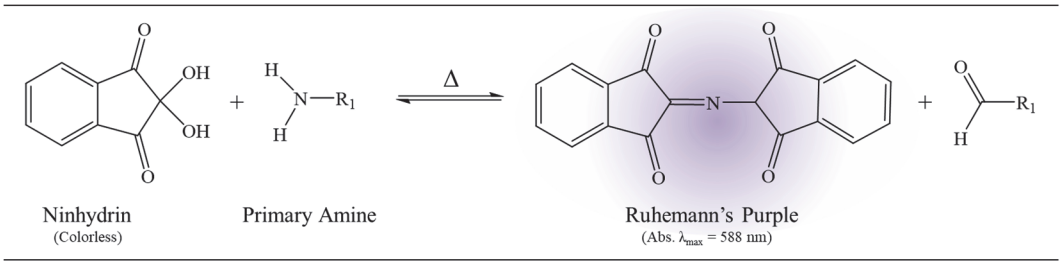

Figure 2.12 General reaction of ninhydrin with a primary amine resulting in a colored product called Ruhemann's Purple. Adapted from Bottom.[54]

Although widely used in amine determination, a number of problems arise when applied to SNP colloidal systems. The ninhydrin assay is a destructive method that requires elevated temperatures (65 °C) and a relatively long reaction period (~35 minutes).[8] By increasing the temperature of the assay, the PAMAM dendrimer may undergo retro-Michael reaction, which initially converts a tertiary amine to secondary and may continue to a primary amine. This would result in artificially inflated amine concentrations that reflect not only the primary amine concentration on the surface of the PAMAM but also the internal amines that only become primary amines when exposed to heat. The Kaiser Test uses a multicomponent system to ensure complete reactions between primary amines and ninhydrin, but the assay becomes convoluted and requires even more non-aqueous environments (n-butanol, phenol, and pyridine) as well as use of potassium cyanide, which is a health hazard. Due to the heterogeneous nature of the assay, post reaction work up requires the removal of SNPs to remove the interfering particles via centrifugation, further lengthening the time to process the material. The assay is a colorimetric type assay that requires the use of absorption techniques, which is less sensitive, thus requiring more material for adequate measurements. Color formation is not always stoichiometric and is dependent on the type of amine being analyzed.[55]

Nitrobenzaldehyde (NBA)

NBA, a heterogeneous assay, has proven useful for determining amines on large substrates such as controlled pore glass (CPG)[51] or on fused silica.[56] The multistep protocol (Figure 2.13), which includes numerous washing steps followed by a hydrolysis of the colorimetric product is well received on macroscopic substrates since rinse and hydrolysis steps can be carried out in a filter (CPG) or merely dipped (fused silica). This, however, becomes far more labor intensive when applied to colloidal systems and would add time to the already excessively long process (3+ h) that is even lengthier than the ninhydrin assay. As with the ninhydrin assay, elevated temperatures are required, and the coupling solution for NBA is non-aqueous.[57,58] Specifically, a 0.8% v/v acetic acid solution in dry methanol is used in washes and reactions.

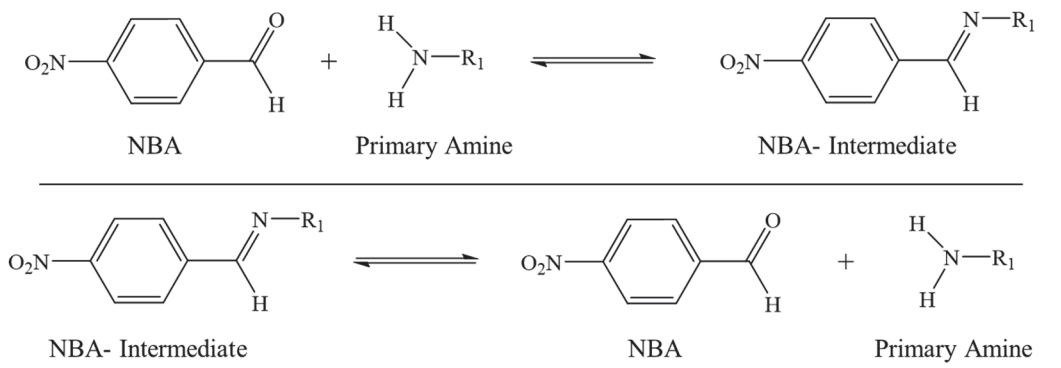

Figure 2.13 Two-step NBA reaction with a primary amine that requires the removal of excess, unreacted NBA.

Fluorescamine

As with the OPA method, the fluorescamine method uses a non-fluorescent precursor (fluorescamine) that reacts with primary amines either free in solution, on a protein, or on nanoparticles[59] to form a fluorescent product (Pyrrolinone) that is quantifiable through fluorimetry (Figure 2.14).

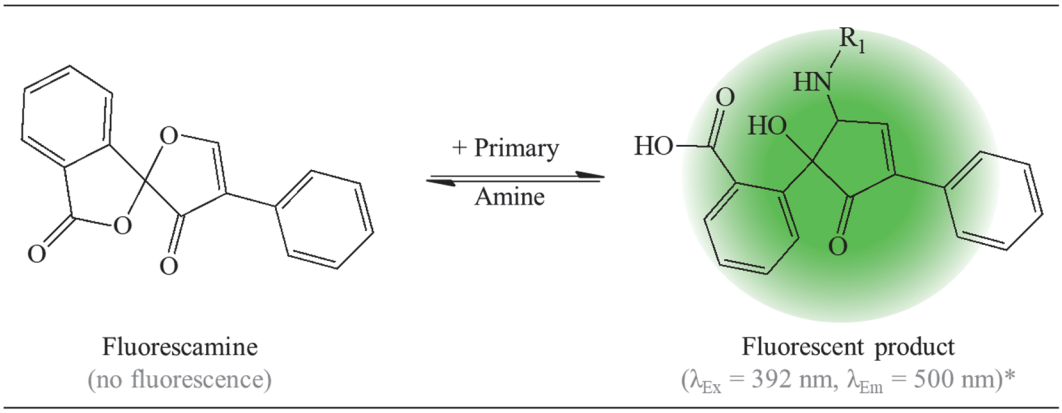

Figure 2.14 Reaction between fluorescamine and primary amine shown generally.

Fluorescamine undergoes hydrolysis in 1-10 sec, whereas aminolysis of fluorescamine occurs within 10-100 ms.[60] Therefore the assay can take place in aqueous solutions, which is ideal for the stability of SNPs in dispersion, since the fluorescamine will react with an amine before hydrolysis (assuming thorough mixing). The aminolysis reaction occurs completely within seconds, and excess fluorescamine is hydrolyzed to a degradation product with nearly no emission at room temperature in the ~500 nm emission range (low background). The fluorescent product is also considered to be stable, at least relative to the OPA method.[59]

Due to water sensitivity, fluorescamine must be prepared in a separate, non-aqueous solvent. No literature precedent was observed to indicate that the non-aqueous solvent must be dry, however wet solvents may degrade some of the fluorescamine prior to assaying. Fresh preparations of fluorescamine should be prepared the day of the assay and used immediately. Another drawback of using fluorescamine is the possibility of reactions with secondary amines that could lead to artificially inflated intensity.[61] The reaction of fluorescamine with amines located in hydrophobic environments within macromolecules may

also lead to artificially inflated emission.[59] Despite some shortcomings, the fluorescamine assay was decidedly more favorable due to the convenience of time, fluorescent product stability, and low background.

Synthetic Hypotheses for this work

The following hypotheses address certain aspects of nanoparticle conjugation that have been problematic. First, the increase in nanoparticle size to about 200 nm will result in lower agglomerations due to solvent effects, to avoid crosslinking byproducts during syntheses, increase the overall curvature of the SNP to increase conjugation on the surface, and shorten the time required for isolation via centrifugation.

Second, conjugate syntheses will be limited to DMSO and water to reduce the number of solvent polarity switches between steps that will limit permanent aggregation (coagulation). Additionally, changes from traditional organic solvents (dioxane) to greener solvents (water) as well as an alternative synthetic approach will not decrease the amine and dye loadings on the new sensor. PAMAM dendrimers will be conjugated to the nanoparticles through CDI chemistry in DMSO to create SNP-Dendrimer conjugates. An SNP-PEG-Dendron conjugate will be synthesized in both DMSO and water to show the feasibility of a water synthesis of a material similar to the SNP-Dendrimer conjugates. A different amine assay will be introduced to reduce the amount of material required for amine assay testing.

Finally, amine assays for the starting material (SNP-Amine), SNP-Dendrimer, and SNP-Dendron will show an increase in amine concentration in the following order: SNP-Amine < SNP-G_3 < SNP-PEG_8-G_{3S} ≤ SNP-G_4. This order should be due to the CDI activated surface of a nanoparticle conjugating more than one amine on a dendrimer and a G_{3S} dendron having the same number of amines as a G_3 dendrimer.

Evidence needed to confirm these hypotheses include testing the? capped intermediate and final materials for concentration of amines on each surface. The capping amine reactive dye (FITC) will be conjugated to all four materials and will reflect the surface amine concentrations of the material. Fluorescence characteristic experiments such as optimizing excitation for maximum emission, emission spectra comparisons, and amine to dye concentrations comparisons will be conducted. Additionally, the SNP-FITC and SNP-G_3-FITC conjugates will be reacted with bromine to change the fluorescein dye to eosin Y. This will not only result in a change of emission properties but will be reflected in the metal ion sensing that will be conducted on all materials (found in Chapter 3 Analyte Sensing).

Experimental

Materials

The following reagents were used directly without further purification. All relevant acronyms used for chemicals are given in the first position of the parenthetic clarifier. Dry DMSO was removed from Sure Seal bottles via syringe and backfilled with N_2 to keep dry. **Pure Solvents:** Dimethyl sulfoxide (DMSO, Sigma-Aldrich, 99.5%, CAS 67-68-5, FW 78.13); Ethanol (EtOH, Sigma-Aldrich, 200 proof, 99.5%, CAS 64-17-5, FW 46.07); Ultra-pure water (18 MΩ H_2O, ELGA PURELAB Option-Q purification system); Methanol (MeOH, VWR Analytical, 99.8%, CAS 67-56-1, FW 32.04); **Buffer:** 4-(2-Hydroxyethyl)-piperazine-1-ethanesulfonic acid (HEPES, Sigma-Aldrich, 99.5% (titration), CAS 7365-45-9, FW 238.30); **Acids/Bases:** Ammonium hydroxide (NH_4OH, Sigma-Aldrich, CAS 1336-21-6, FW 35.05); Hydrochloric acid (HCl, Sigma Aldrich, 37%, CAS 7647-01-0, FW 36.46; Sodium Hydroxide (NaOH, Sigma-Aldrich, 99% (acidimetric), CAS 1310-73-2, FW 40.00); **Silanes:** Tetraethyl-orthosilicate (TEOS, Sigma-Aldrich, 98% (reagent), CAS 78-10-4, FW 208.33); 3-Aminopropyl-triethoxysilane (APTES, Sigma-Aldrich, 99%, CAS 919-30-2, FW 221.37); Trimethoxymethylsilane (MTMS, Sigma-Aldrich, 98%, CAS 1185-55-3; FW 136.22); **Linkers:** 1,1'-Carbonyldiimidazole (CDI, Sigma-Aldrich, 99%, CAS 530-62-1, FW 162.15);

succinimidyl- [(N-(malemidiopropionamido)-octaethyleneglycol]- ester (NHS-PEG$_8$-Mal, Thermo Scientific, N/A, CAS N/A FW 689.71); succinimidyl- [(N-(malemidiopropionamido)-tetracosaethyleneglycol]-ester (NHS-PEG$_{24}$-Mal, Thermo Scientific, N/A, CAS N/A FW 1394.55); **Dendrimers:** PAMAM dendrimer generation 3, ethylene diamine core, amine surface (G_3, Sigma-Aldrich, 20% wt. in MeOH, CAS 153891-46-4, FW 6908.84); PAMAM dendrimer generation 4, ethylene diamine core, amine surface (G_4, Sigma-Aldrich, 10% wt. in MeOH, CAS 163442-67-9, FW 14214.17); PAMAM dendrimer generation 4, cystamine core, amine surface (G_{3SS3}, Andrew Chem Services, 10% wt. in MeOH, CAS N/A, FW 14306.35); **Dyes:** Fluorescein isothiocyanate (FITC, Sigma-Aldrich, 90%, CAS 3326-32-7, FW 389.38); NHS- Tetramethylrhodamine (TAMRA, Thermo Scientific, 96%, CAS 246256-50-8, FW 527.5); **Bromination reagents:** Bromine (Br_2, reagent grade, CAS 7726-95-6, FW 159.81); Sodium thiosulfate pentahydrate ($Na_2S_2O_3$, ≥99.5% CAS 10102-17-7, FW 248.18); **Amine Assays:** 4-Phenylspiro-[furan-2(3H),1-phthalan]-3,3'-dione (fluorescamine, Sigma-Aldrich, 99% (TLC), CAS 38183-12-9, FW 278.26); Phenylspiro-[furan-2(3H),1-phthalan]-3,3'-dione (fluorescamine, AK Scientific, 99% (GC), CAS 38183-12-9, FW 278.26); 1,2,3-Indantrione (ninhydrin, Baker, 99%, CAS 485-47-2, FW 178.15); 1-aminohexane (hexylamine, Sigma-Aldrich, 99%, CAS 111-26-2, FW 101.19); **Reducing Agents:** Tris(2-carboxyethyl)phosphine•HCl (TCEP, Sigma-Aldrich, 98%, CAS 51805-45-9, FW 286.65); **Capping Agents:** Beta-Mercaptoethanol (BME, Sigma-Aldrich, >99%, CAS 60-24-2, FW 78.13); **Nanoparticle Standards (DLS)** LUDOX TMA colloidal silica (TMA, Sigma Aldrich, 34 wt. % suspension in H_2O, no stabilizing counter ion, CAS 7631-86-9, Fw N/A), Silica, nanoparticle dispersion in water triethoxylpropylaminosilane functionalized (Amine SNP, Sigma Aldrich, 30-40 wt. % suspension in H_2O, no stabilizing counter ion, CAS N/A, FW N/A). **Acids/Bases (DLS):** Hydrochloric acid (HCl, Sigma Aldrich, 37%, CAS 7647-01-0, FW 36.46), Sodium Hydroxide (NaOH, Sigma-Aldrich, 99% (acidimetric), CAS 1310-73-2, FW 40.00), **Salts(DLS):** Sodium chloride (NaCl, Sigma-Aldrich, ACS reagent, ≥99%, CAS 7647-14-5, FW 58.44).

Note: When stated as *dry*, the solvent DMSO was used from the anhydrous Sure/Seal^{TM} bottle and was not dried further. No steps were taken to ensure or measure the dryness of the solvent, therefore the word *dry* indicates that the solvent was merely used *as is* from a Sure/Seal^{TM} bottle.

Instrumentation

Centrifuges were used as the main separation technique whereas a vacuum desiccator was used to dry remaining dispersants from the SNPs. A fluorimeter and a Dynamic Light Scattering (DLS) instrument were used to characterize the SNPs after syntheses. Instrumentation is displayed in Table 2.2 with relevant accessories and purposes. *Note: All instrumentation was housed at the University of San Francisco except for the DLS which was housed at St. Cloud State University in Minnesota.*

Table 2.2 Instrumentation used in synthesizing, separating, and characterizing nanoparticle conjugates

Type	Name	Accessories	Purpose
Centrifuge	Eppendorf 5804-R Beckman-Coulter J2-21 Beckman-Coulter Optima TLX Ultracentrifuge	A-4-44 Swinging bucket rotor JA-20 fixed angle roto TLA-110 fixed angle rotor	Isolation of particles from reaction solutions
pH Meter	Vernier Labquest® 2 with a pH Probe	BDH® pH reference standard buffers 4, 7, and 10	Measure pH of buffered solutions
Fluorimeter	Horiba Jobin Yvon Fluoromax-4	Cuvette (1 cm, Quartz)	Fluorescamine (amine) assay, dye loading quantification, and sensing titrations
DLS	Malvern Zetasizer ZS90	Folded Capillary Zeta Cell (Polystyrene) Cuvette (1 cm, polystyrene)	Zeta Potential measurements Nanoparticle size determination
Sonicator	Branson 2210	NA	Disperse nanoparticles
Drying Apparatus	Vacuum Desiccator	Precision DD195 2-stage pump	Drying nanoparticles
Spectrophotometer	Agilent 8453	Cuvette (1 cm, Quartz)	Ninhydrin (amine) assay

Instruments are referenced throughout the following sections either generally or with relevant information such as *centrifugation (centrifuge/rotor, rpm, and duration).*

Syntheses

Preparation of silica nanoparticles

As described in Soto-Cantu et al., two solutions (A and B) were made separately and mixed, although at 1/10th the scale.[22] The ratio of H_2O to TEOS was 2.3, which should produce 200-300 nm silica nanoparticles.[22] Solution A was prepared by adding 28% $NH_4OH_{(aq)}$ (10.0 mL) to ethanol (125 mL), which was stirred (200 rpm) for 20 min. Solution B was prepared by adding TEOS (3.325 mL) to ethanol (16.50 mL) and was then added to solution A all at once. The nanoparticle synthesis was reacted for 20 h (200 rpm, RT, N_2 atm). Observational note: the reaction solution changed from clear to opaque white within the first 2 h, indicating nanoparticle formation. The Eppendorf centrifuge with the A-4-44 swinging bucket was used for 45 min at 4,500 rpm to isolate the silica nanoparticles from the reaction solution. Redispersion of the nanoparticles in ethanol and centrifuging again (4,500 rpm, 45 min) served as a washing step, which was repeated five times. The bare silica nanoparticles were dried in a vacuum desiccator overnight that yielded a white powder (0.87585 g).

Surface Silanization

Silanization of bare SNPs (SNP-OH) was accomplished by the adaptation of the protocol described by Rosu et. al.,[62] where bare SNPs (0.88500 g) were dispersed via sonication (20 min) in ethanol (10 mL) thereby producing a 10% wt. suspension. A 1:1 molar APTES (21.05 µL) and MTMS (12.83 µL) solution was prepared in a separate vial. The 1:1 APTES: MTMS solution (20.0 µL) was added to the SNP dispersion and stirred (1000 rpm, RT, N_2 atm) overnight. Isolation was performed via centrifugation. A total of 15 washes with ethanol were required to ensure that no unreacted APTES remained in the wash supernatants (Ninhydrin Assay). Again the product was dried in a vacuum desiccator overnight and an off-white powder (0.62575 g) was recovered. Ideal surface of the SNP-Amine particles is shown in Figure 2.15.

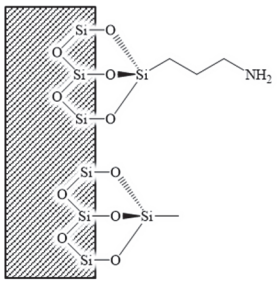

Figure 2.15 Ideal surface of the SNP-Amine conjugate. Although unlikely, the amine and methyl groups are shown here in a 1:1 ratio. Actual ratios between methyl and amine groups were not explored in this work. The figures in the following synthetic sections are also assumed surfaces of the conjugates and are to be used to illustrate the build-up (bottom-up) process of surface conjugation of these materials. The empty space in this figure will be filled in successive figures.

Dendrimer Conjugation

SNP-Amine (100.92 mg) was dispersed in dry DMSO (16 mL) and, in a separate vial, CDI (13.31 mg, 82.1 μmol, 5 times excess to total surface [amine]) was dissolved in dry DMSO (4 mL). The CDI solution was subsequently added dropwise to the SNP-Amine dispersion and stirred (1000 rpm, RT, no N_2 atm) overnight. An aliquot (2mL) was removed from the reaction solution and quenched with H_2O to produce a SNP-COOH set of particles. The remaining reaction mixture was centrifuged (TLA 110, 35,000 rpm, 10 min) to isolated the SNP-CDI particles. Assumed surface of these particles is shown in Figure 2.16, top. Dry DMSO (3 mL) was added to each tube, sonicated until SNP-CDI particles were dispersed (~1 min), and centrifuged again (TLA 110, 35,000 rpm, 10 min). The pellets (SNP-CDI) were dispersed in dry DMSO (2 mL) and half of the volume (16 ml total) was added to a G_3 dendrimer solution and the other to a G_4 dendrimer solution. Each tube was rinsed with dry DMSO (2 mL total) and distributed amongst the two reaction vials (G_3 and G_4).

The G_3 and G_4 dendrimer stock solutions (0.238 mL and 0.979 mL respectively) were diluted with MeOH (diluted to 1 mL) and added to dry DMSO (7 mL). The SNP-CDI dispersion were added to the dendrimer solutions dropwise while stirring and allowed to react (1000 rpm, RT, ambient atm) for 72 h. To limit cross coupling reactions that would lead to agglomerations, the SNP-CDI conjugates were added to the dendrimers.

Isolation of SNP-dendrimer conjugates were performed via centrifugation (TLA 110, 35,000 rpm, 10 min) and washed three times with ethanol (3 mL per tube). Remaining SNP-dendrimer pellets (SNP-G_3 and SNP-G_4) were dried overnight at ambient pressure and a pair of white powders (42.94 mg SNP-G_3 and 39.24 mg SNP-G_4) was recovered.

The aliquot (2 mL) removed from the CDI activation of SNP-Amine reaction solution was quenched with H_2O (2 mL, excess) to produce SNP-COOH *capped* set of particles. *Note: Upon addition of diH2O, the vial became hot (almost too hot to handle) and the solution became cloudy.* The solution was then sonicated, where bubbles were brought to the surface until no bubbles remained and the solution was no longer warm (~1 min). The dispersion was centrifuged (TLA 110, 35,000 rpm, 10 min), washed with ethanol (3 times, 3 mL), and allowed to dry overnight at ambient pressure. The next day, a white powder (8.84 mg) was recovered.

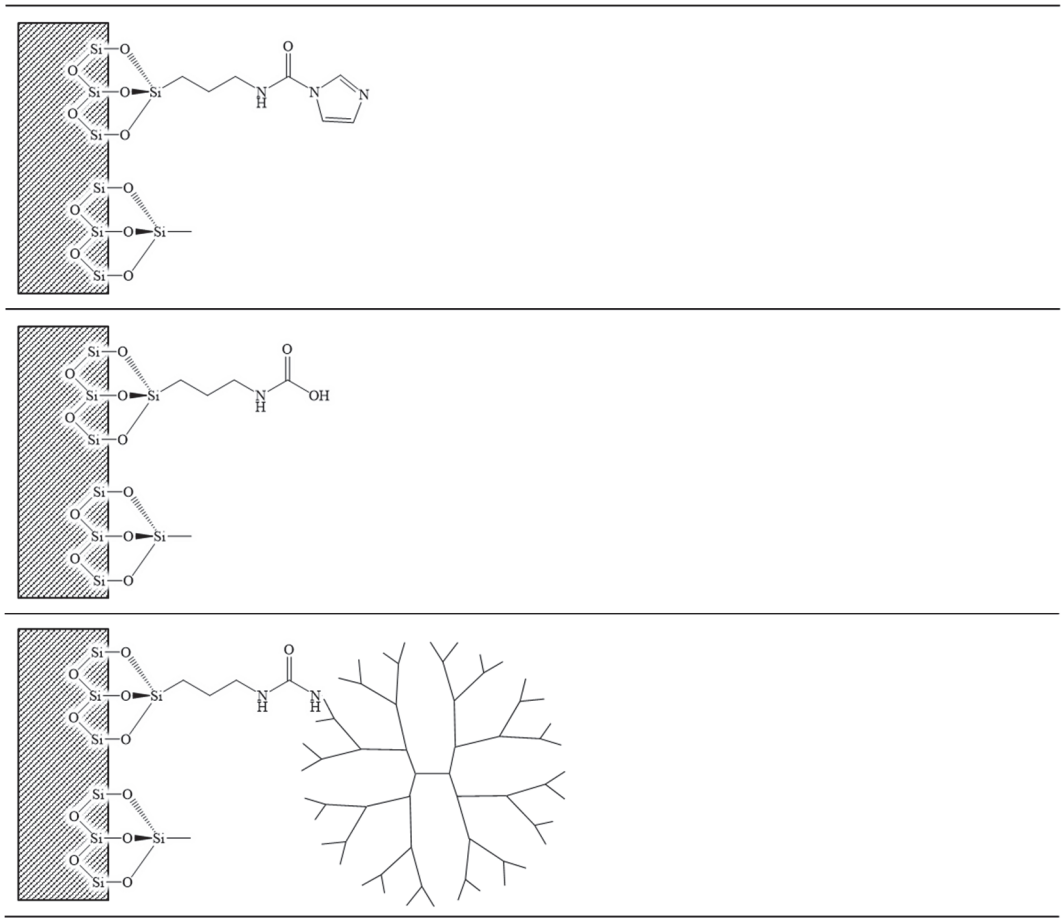

Figure 2.16 Surface of the SNP-CDI conjugate after CDI activation (top) of the amines on the SNP-Amine conjugate. The remaining imidazole was an excellent leaving group for the nucleophilic attack of the primary amines on the surface of the dendrimer. By providing spacers in the form of MTMS, the hope was to prevent adjacent amines from reacting with each other prior to dendrimer addition. Excess CDI was also used to prevent adjacent amines from reacting. SNP-CDI was capped (middle) by reacting H_2O with the imidazole resulting in a carbamic acid functional group denoted as the SNP-COOH conjugate. Surface of the SNP-G_3 conjugate (bottom). SNP-G_4 (not shown) was assumed to be of similar architecture. *Note*: *Due to the reactive nature of the CDI activated surface with amines, the assumption of a single Dendrimer reacting with only a single APTES is very improbable. Please refer to Figure 1.17 or Figure 1.18 for the fine structure of the PAMAM dendrimer.*

Dendron Conjugation

SNP-Amine Dispersion- The SNP-Amine conjugate (40.63 mg) was dispersed in 10 mM HEPES (10 mL, pH 8) and sonicated for 5 min. Sedimentation was occurring over the duration of 5- 10 mins and the dispersion was placed on a stir plate with a stir bar rotating at 1100 rpm, in which the SNPs remained in solution (still opaque white).

PEG Solution – A volume of 0.48 mL of DMSO was added to the vial of 100 mg of NHS-PEG_8-Mal.[63]

PEGylation of SNP-Amine Reaction – A volume of NHS-PEG_8-Mal solution (70 µL, 250 mM) was added to the SNP dispersion and was allowed to react for 30 min. Within the first 10 min, a color change occurred

(opaque eggshell white to an off-white blue color) and agglomerations began to form. The agglomerations were sonicated until dispersed again, and the reaction continued to stir at 1100 rpm (flocculation subsided).

Isolation of the SNP-PEG$_8$-Mal conjugates – The reaction solution of the SNP-PEG$_8$-Mal conjugate (Figure 2.17, top) was divided into 3 centrifuge tubes, isolated via centrifugation (TLA 110, 35,000 rpm, 10 min), and washed three times with HEPES (3 mL, pH 8, 10 mM). The first two centrifuge tubes were redispersed in HEPES (8 mL, pH 8, 10 mM) and used for further conjugation with the G$_{3S}$ dendron. The pellet in the third tube was redispersed in fresh HEPES, and β-mercaptoethanol (4 μL) was added to cap the malemide reactive surface on the PEGylated SNPs (Figure 2.17, middle). The mercaptoethanol capping reaction was also isolated via centrifugation and washed three times with ethanol.

Reduction of PAMAM G$_{3SS3}$ to G$_{3S}$ – A 50 mM TCEP solution was made by dissolving 1.25 mg of TCEP in DMSO (1 mL). G$_{3SS3}$ solution was made by adding DMSO (1 mL) to 0.6 mL of the G$_{3SS3}$ dendrimer (10 wt.% in methanol). A volume of 70 μL of the 250 mM TCEP solution was added to the G$_{3SS3}$ solution and stirred for 2 h (1000 rpm).

Dendron Conjugation - Upon the redispersion of SNP-PEG$_8$-Mal, the G$_{3SS3}$ solution (1.6 mL total) was poured into the dispersion of SNPs. This reaction was stirred (1100 rpm, RT, ambient atm) overnight. The newly synthesized SNP-PEG$_8$-G$_{3S}$ conjugates (Figure 2.17, bottom) were isolated via centrifugation (TLA 110, 35,000 rpm, 10 min), washed three times with ethanol)resulting in a noticeably less dense pellet (Figure 2.18)), and allowed to dry overnight. Prior to drying, the picture in Figure 2.18 was taken to show the difference in *creep* on the centrifuge tube walls. Mass percent recovered of the SNP-PEG$_8$-OH and SNP-PEG$_8$-G$_{3S}$ conjugates were 76% (10.13 mg) and 77% (20.53 mg), respectively.

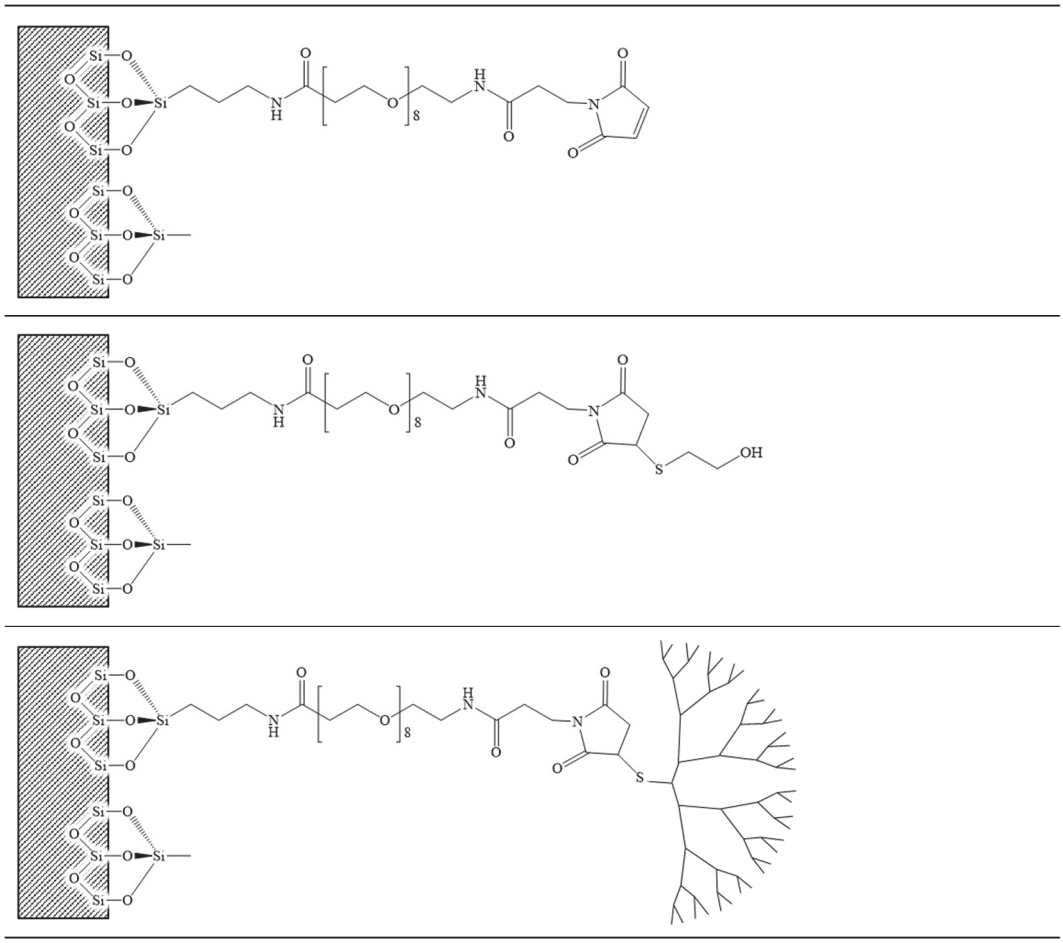

Figure 2.17 Surface of the SNP-PEG$_8$-Mal intermediate conjugate (top) after the reaction between the surface amine of SNP-Amine and the NHS group of NHS-PEG$_8$-Mal. The malemide (Mal) group is not considered reactive with amines and therefore was not considered to react with adjacent amines.[1] By adding beta-mercaptoethanol (BME) to the SNP-PEG$_8$-Mal conjugate (middle), the thiol reacted with the malemide functional group to form the capped conjugate SNP-PEG$_8$-OH. These capped materials were used to indirectly measure the amount of conjugate amines from the SNP-Amine starting material. Reaction with a malemide group on the surface of a SNP-PEG$_8$-Mal conjugate with the thiol of a reduced cystamine dendrimer (dendron) formed the conjugate SNP-PEG$_8$-G$_{3S}$ (bottom). *Please refer to Figure 1.17 or Figure 1.18 for the fine structure of the PAMAM dendrimer, which is nearly the same for the dendron depicted above.*

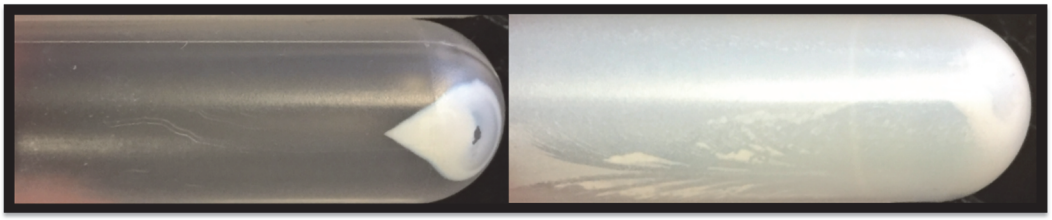

Figure 2.18 Centrifuge tubes of SNP conjugates showing a difference in the centrifugation of the PEGylated SNPs (left) and the PEG-dendron conjugated SNPs (right) after the ethanol washes. Presumably, the dendron SNPs either stick to the Polyallomer tube more than the PEGylated SNPs or the dendron SNPs are more difficult to pellet, again presumably, due to the higher degree of dispersibility in ethanol.

Dye Conjugation and Bromination

The SNP-dendrimer conjugates (Table 2.3) were dispersed in dry DMSO (9 mL each), and ethanol (1 mL) was added to aid in dispersion (10 mL total). FITC (5 mg) was dissolved in dry DMSO (1 mL) and aliquots (50 µL) were delivered to the SNP-dendrimer conjugates. The reactions were stirred (1000 rpm, RT, ambient atm) overnight. The conjugates (Figure 2.19) were centrifuged (TLA 110, 35,000 rpm, 10 min), washed with ethanol (3 mL, 3 times), and dried at ambient pressure overnight.

Table 2.3 FITC conjugate mass percent recovered yields

Conjugate	Mass, mg		Yield, %
	Initial	Final	
SNP-FITC	17.07	14.39	84.30
SNP-G_3-FITC	20.13	15.13	75.16
SNP-G_4-FITC	20.14	18.39	91.31
SNP-PEG_8-G_{3s}-FITC	16.01	13.04	81.45

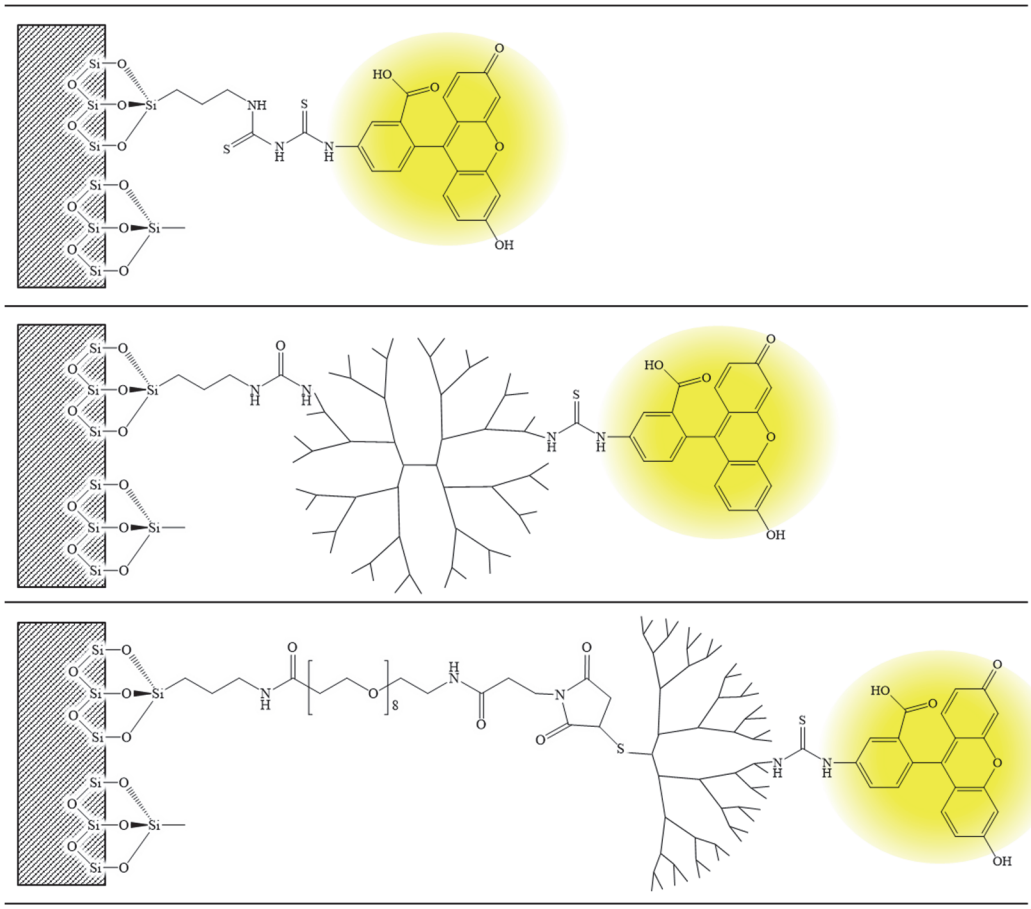

Figure 2.19 The isothiocynate reactive group on the fluorescein dye (FITC) reacted with the surface amines on the SNP-Amine, SNP-G_3, SNP-G_4 (not shown), and SNP-PEG_8-G_{3S} to synthesize the respective FITC conjugates. *Note that a singular dye is shown but the number of dyes per dendrimer or dendron was not determined. More than one per dendrimer is assumed.*

The bromination of FITC (Figure 2.20) after the conjugation of dendrimer and FITC was performed to synthesize eosin Y isothiocynate (EITC) on the surface of SNPs. A mass of SNP-G_3-FITC (9.62 mg) was dispersed in ethanol (3 mL) and a volume of bromine (30 µL) was added dropwise as the solution stirred. The amber solution was capped and allowed to react (600 rpm, RT, ambient atm, 2 h). The change in color of the dispersions after the synthesis were quite apparent (Figure 2.21) The dispersion was isolated via centrifugation (TLA 110, 35,000 rpm, 10 min) and washed with ethanol (3 mL, 3 times). Conjugates were dried at ambient pressure overnight. A pink SNP-G_3-EITC solid 7.99 mg (83 %) was recovered.

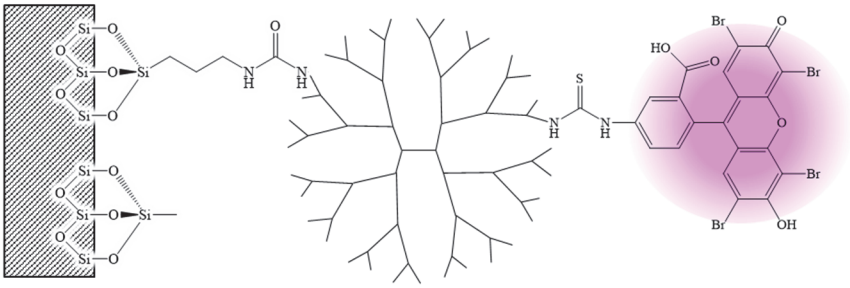

Figure 2.20 With the addition of bromine to the SNP-FITC conjugates, a resulting bromination of FITC on the surface of SNP conjugates produced the dye EITC. *Again, a single dye is shown but more are thought to be conjugated to the surface dendrimers.*

The supernatant and washes were tested for remaining bromide using a saturated solution of sodium thiosulfate (0.5-1 mL per 3 mL wash). The presence of bromide resulted in the precipitation of sodium sulfate, and the amber colored solution turned clear (Reaction 1). *Note: The precipitate was formed due to the solubility of sodium thiosulfate being greater than the solubility of sodium sulfate, which is 70.1 g/100 mL and 13.9 g/100 mL, respectively.*[64]

$$Na_2S_2O_{3(aq)} + 4Br_{2(aq)} + 5H_2O_{(l)} \rightarrow Na_2SO_{4(s)} + H_2SO_{4(aq)} + 8HBr_{(aq)} \qquad \text{Reaction (1)}$$

A similar procedure was carried out on the SNP-FITC (8.23 mg), but half the volume of Br_2 was added (15 µL). A pink/yellow solid was recovered (7.41 mg, 90.0%).

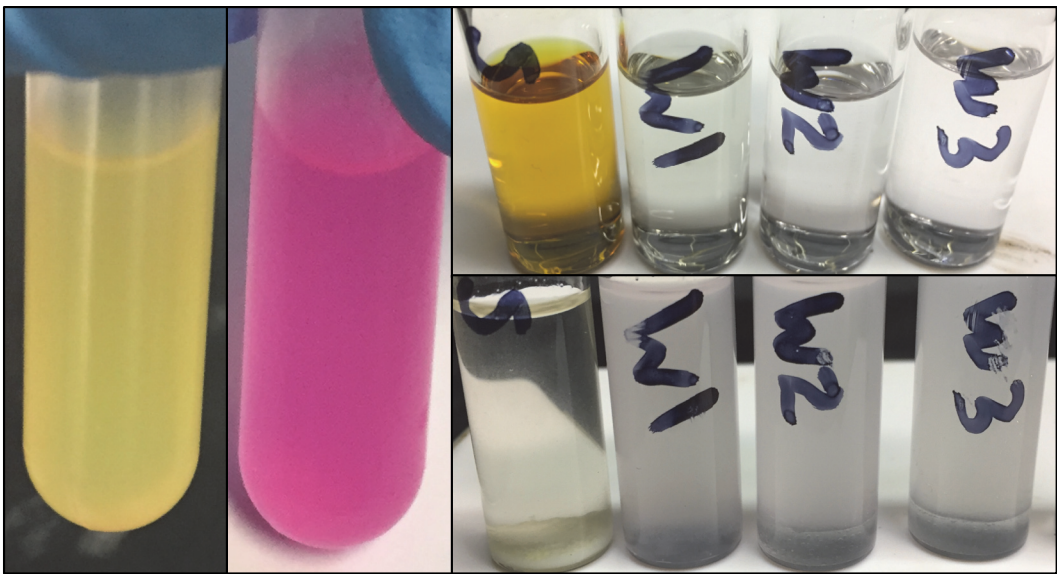

Figure 2.21 Bromination of SNP-G_3-FITC showing the conversion of FITC (left) to eosin Y(middle) in polyallomer centrifuge tubes. Ethanol washes (~3 mL ethanol) were performed and collected (top right). Saturated $Na_2S_2O_3$ solution (1 mL) was added to remove excess Br_2 (bottom right). Precipitate formed only in the supernatant (S) vial, which can be seen in the bottom of vial S.

Characterization

DLS: Size and Zeta Potential

System Suitability with Standards- Silica nanoparticle standards that varied in size coating were tested to ensure that the instrument was working properly and that samples were properly prepared. The nanoparticle standards were sonicated for 5 min then diluted with a NaCl solution (pH 5.37, 10 mM). Dilutions were required to obtain monomodal dispersions, and Table 2.4 from the Zetasizer manual was helpful in obtaining optimal particle concentrations.[44] Salts are often used to dilute the standards and samples to ensure low PDI and small hydrodynamic sphere around the particles. Without salt, the electrical double layer surrounding the particles will have long-distance interactions which can then lead to instability within the colloid and eventual agglomeration.[65] These *long-distance interactions* were thought to cause the greater distribution range within the particle dispersions (Figure 2.22). Counter ions were present in the standards but were extremely low due to the dilutions required to obtain adequate concentrations that allowed size determination. By diluting the samples with 10 mM NaCl, the distribution range narrowed.

Table 2.4 Particle concentration for DLS measurements. *Reprinted from Zetasizer Manual.*

Particle Size	Concentration	
	Minimum	**Maximum**
< 10 nm	0.5 mg/ml (0.005 % mass)	Varies*
10 nm to 100 nm	0.1mg/ml (0.001 % mass)	5% mass**
100 nm to 1 µm	0.01mg/ml (0.0001 % mass)	1% mass**
> 1 µm	0.1mg/ml (0.001 % mass)	1% mass**

*Only limited by the sample material interaction, aggregation, gelation, etc

**assumed density of 1g/cm^3

The averages of the standard nanoparticles (Table 2.5) were relatively close to the quoted sizes. LUDOX® TMA was quoted to be 22 nm, however, the method of size determination was not provided and the method was assumed to be TEM, since the size measured via DLS was 43 nm.[66] The provided Amine SNP literature did mention the size determination as DLS and was confirmed to be less than 50 nm.[67] The PDI of each standard was within the *Mid-range value* (Table 2.1) and was considered suitable. With the data provided in Table 2.5 and the monomodal distributions shown in Figure 2.22, the DLS system was considered suitable to measure experimentally treated particles.

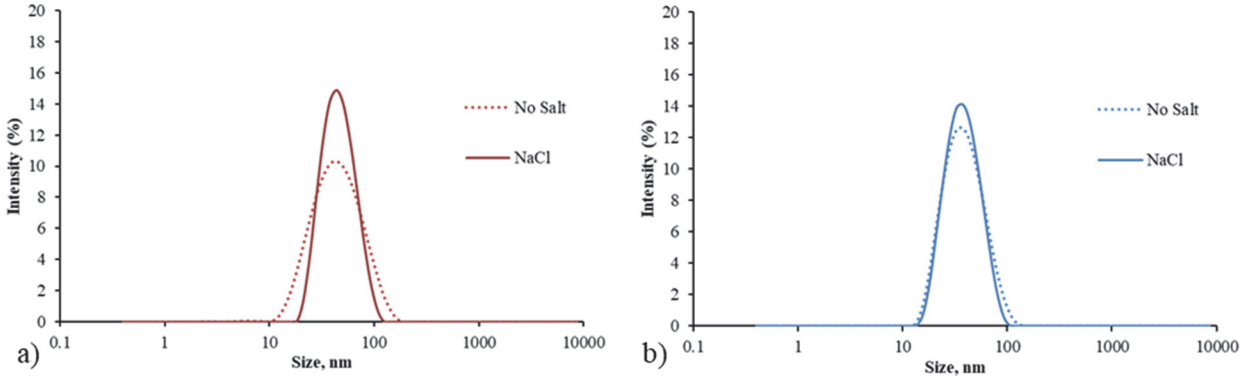

Figure 2.22 Size distributions of the purchased standards LUDOX® TMA (a) and Amine SNP (b) diluted with diH_2O and 10 mM NaCl solution.

Table 2.5 Comparison of dilutions with 10 mM NaCl and dilutions with diH_2O

Sample (w/w %)	Surface	[Final], %	Avg., nm	PDI	Size, nm
LUDOX® TMA (34%)	Hydroxide	0.11	43.4	0.186	22[68]
Amine SNP (30-40%)	Amine	0.10-0.13	34.9	0.180	<50[67]

Standard zeta potential vs. pH curves were made by diluting the SNP standard, LUDOX® TMA, dispersion (to 0.03 wt. %) at a desired pH. This was accomplished by adding an aliquot (100 µL) to a NaCl solution (2.9 mL, pH 2, 10 mM). The dispersion was sonicated again for 5 min and added (1 mL) to the zeta cell. This process was repeated at higher pH (2, 2.96, 3.82, 5.37, 6.13, 7.06, 9.73, and 10.24) until the zeta potential was thought to be sufficiently negative. The Amine SNP standard was also dispersed (to 0.03 wt. %) at a desired pH (2, 2.96, 3.82, 5.37, 6.13, 7.06, 9.73, and 10.24) until the zeta potential was thought to be sufficiently negative. The zeta potential results of these standards were then compared to the zeta potential curves of nanoparticles with similar coatings from an independent manufacturer, nanoComposix (Figure 2.23). The zeta potentials of the LUDOX® TMA and Amine SNP matched the literature values of the respective coatings from the nanoComposix technical information. Some differences in measured and literature zeta potential could be due to individual measurements being taken for the Amine SNP and LUDOX® TMA, whereas the nanoComposix particles were likely one sample that was titrated (option not available for this thesis).

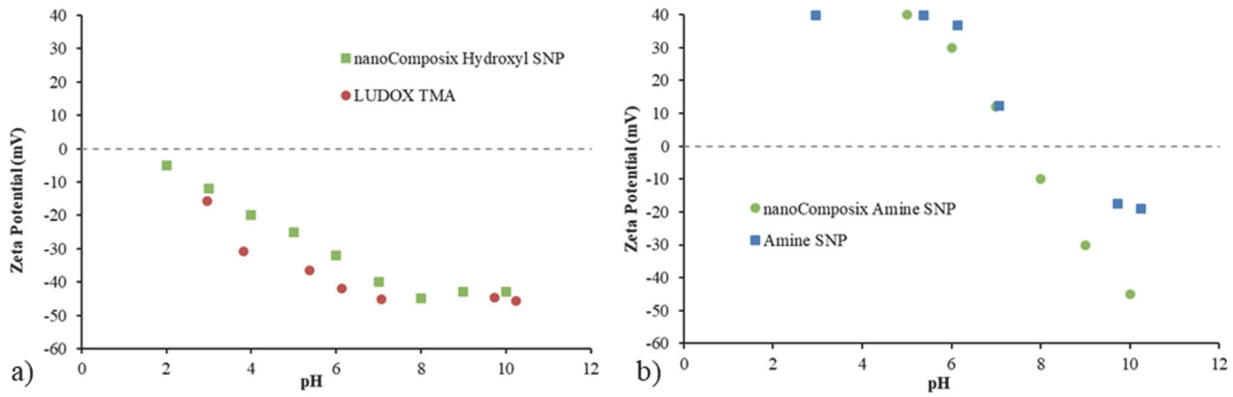

Figure 2.23 Zeta potential measurements of the LUDOX® TMA and Amine SNP standards compared to the literature values.

Experimental - In the size determination experiments, SNP-OH were dispersed (1 mg/mL, NaCl, 10 mM) via sonication until visibly disperse and were diluted to determine the best concentration for size determination (0.055 mg/mL) following Table 2.1. For the zeta potential experiments, SNP-OH were dispersed at a stock concentration (0.33 mg/mL), aliquots were added to NaCl solutions of a particular pH (2, 2.96, 3.82, 5.37, 6.13, 7.06, 9.73, 10.24), and a portion was added to the zeta cell. Acidic solutions were prepared with HCl (1.0 M) whereas basic solutions were prepared with NaOH (1.0 M).

Amine Assay

A HEPES (125 mL, pH 8.33, 10 mM) solution was prepared by dissolving solid HEPES (0.29757 g) into 18 MΩ H_2O (125 mL) and adjusting the pH to 8.33 by adding NaOH (20 drops, 1 M). A hexylamine stock (5 mM) was prepared by adding hexylamine (6.57 µL) to HEPES (10 mL, pH 8.33, 10 mM). A set of five hexylamine standards were made by diluting the following volumes to 5.000 mL: 10, 15, 20, 25, and 30 µL hexylamine, which yielded 0.015, 0.023, 0.030, 0.038, 0.046 µM hexylamine standards solutions. A negative control was used to determine the fluorescence of unreacted fluorescamine. The fluorescamine (1 mg/mL) stock solution was prepared in acetonitrile. The blank (3.000 mL) was placed in the cuvette and the fluorescamine solution (100 µL) was added, mixed, and measured (λ_{Ex} = 392 nm) one minute after mixing. The cuvette was rinsed two times with HEPES (3 mL, pH 8.33, 10 mM) and the emission spectrum was taken of HEPES (3 mL, pH 8.33, 10 mM) to ensure all traces of the previous sample were rinsed away. The remainder of the standards were run in increasing order. A calibration curve was created with the λ_{EmMax} (504 nm) of each concentration after blank subtraction. An expedited version of the assay was developed where the standard concentrations (3 mL each, 10, 15, 20, 25, and 30 µM) were prepared in HEPES (pH 8.00, 10 mM) and reacted with fluorescamine all at once (Figure 2.23), then the emission spectra were taken with no discernable difference observed. This allowed for the assay to be performed in half to a third of the time (30+ min down to 10 min) and was applied to the amine quantification of the nanoparticle conjugates. *Note: Standards and fluorescamine stock solution were prepared fresh and a calibration curve was created each day a nanoparticle conjugate was tested for amines.*

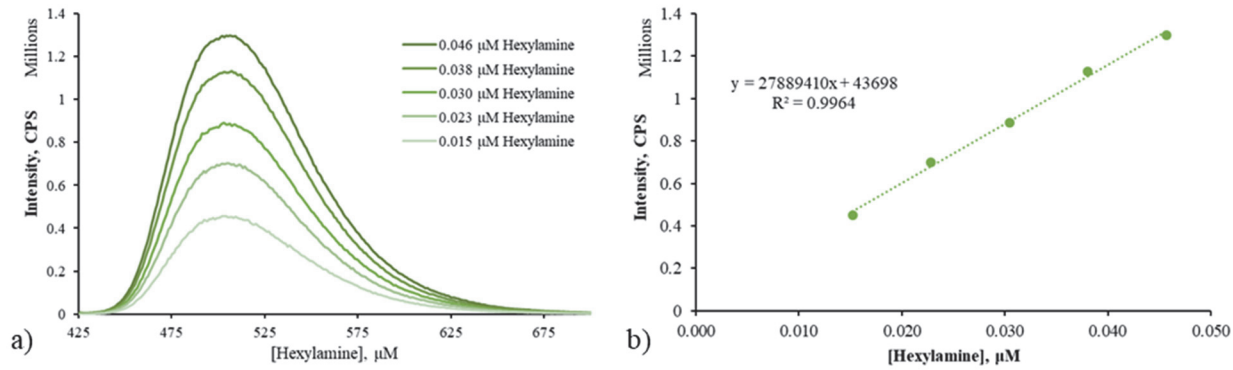

Figure 2.24 Blank corrected emission spectra (a) of fluorescamine reactions with the hexylamine standard which was used to create a calibration curve (b) to calculate the concentration of amines on the surface of nanoparticles.

Fluorescence Characteristics and Dye Loading of FITC

The excitation and emission spectra were studied to determine the optimal excitation and emission wavelengths for the desired application. The approximate excitation wavelength, 500 nm, established using ThermoFisher's Spectra Viewer[69], was first used to determine the wavelength for maximum emission (540 nm). That emission wavelength was used as the emission stop while the excitation spectrum was scanned. Peaks in the excitation scan were then used to monitor and compare emission spectra. The excitation wavelength was chosen (480 nm) based on the emission characteristics of the dye on the conjugates to avoid any scatter effects from the nanoparticle.

A mass of 5.25 mg of FITC dye was dissolved in 1 mL of DMSO. A volume of 1 µL was transferred to 3 mL of a 2:1 ethanol: HEPES (pH 7, 10 mM) solution. Serial dilutions were made until 0.5 million CPS were reached. Of the emission spectra collected, spectra with less than 2.5 million and below (Figure 2.24a) were used to create a calibration curve (Figure 2.24b). *Note: Per the Horiba fluorimeter manual, the detector begins to become saturated at 2.5 million counts per second (CPS) or more and thus loses signal detection linearity.*[70]

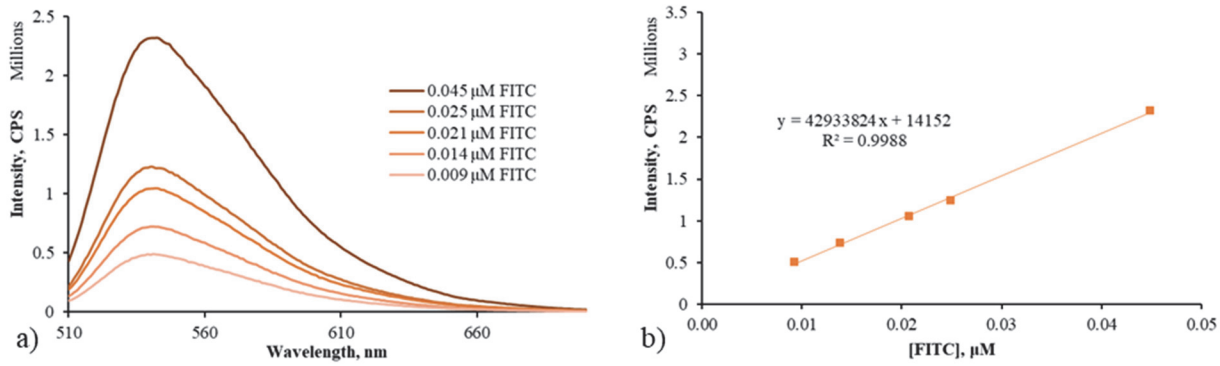

Figure 2.25 Emission spectra of unbound FITC standards (a) used to create a calibration cure (b) from the emissions at 540 nm for dye loading calculations. *Solvent: 2:1 ethanol: HEPES (pH 7, 10 mM); Slit widths: 5 nm; Excitation: 480 nm.*

Results

DLS: Size and Zeta Potential

DLS results (size and zeta) were limited, due to restricted access to the Zetasizer. The following results will not touch on post-conjugation materials beyond the initial amine silanization (SNP-Amine) since access to the instrument was not available. For more robust and reproducible material testing, a DLS would need to become readily available and should be considered a necessity for nanoparticle characterization.

The size of the nanoparticle cores (SNP-OH, bare SNP) were determined to be 246 nm in diameter (Figure 2.26) whereas the SNP-Amine were found to average 342 nm in diameter. The size distributions of the particles were monomodal indicating that the particles were completely dispersed. The polydispersity index (PDI) of the were 0.087 and 0.180 for the SNP-OH, and SNP-Amine particles, respectively. These values fall within the range from Table 2.1 which states that 0.08-0.7 is a *mid-range value of PDI* and *is the range over which the distribution algorithms best operate over*.[44]

Zeta potentials were measured over a pH range of about 2 to 10 (Figure 2.26b) and a best-fit line was applied to a range of pH in which the zeta was changing the most to determine the isoelectric points of the conjugates. The calculated isoelectric point for SNP-OH and SNP-Amine were determined to be 2.7 and 4.4, respectively.

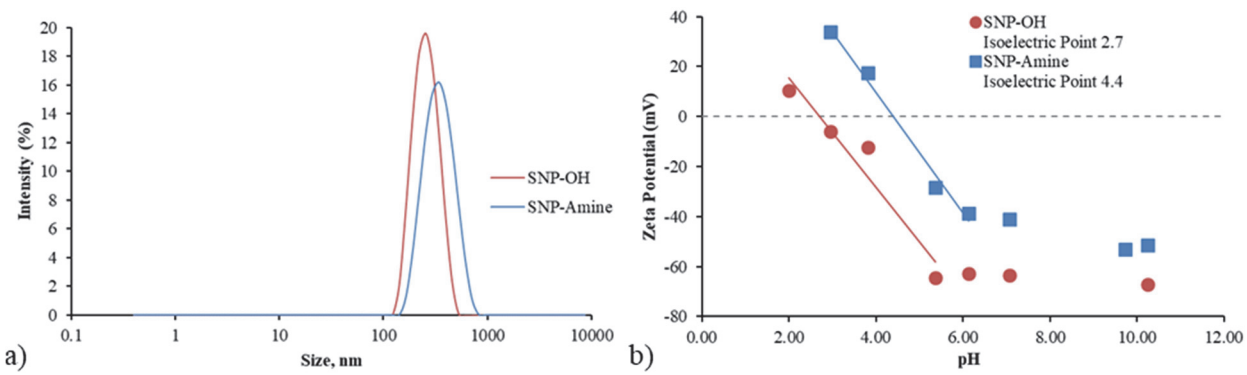

Figure 2.26 Size distribution (a) comparison of SNP-OH and SNP-Amine showing an approximate size of 246 and 342 nm, respectively. Zeta potential titration (b) of SNP-OH and SNP-Amine showing the isoelectric points of both materials.

Amine Assay

All Materials – The fluorescamine assay was used to determine the concentration of amines on all materials (Figure 2.27), made in the steps indicated. Dendrimer and dendron conjugated materials were monitored to determine amine loading which can then infer the concentration of dendrimer or dendrons. Additionally, the conjugation of dendrimers and dendrons were used to increase amine concentration for increased dye loading (next section, Amine conversion to FITC) and better sensing capabilities (Chapter 3 Analyte Sensing). Capped materials were used to monitor the conjugation of CDI and NHS-PEG_8-Mal to SNP-Amine creating SNP-COOH and SNP-PEG-OH respectively. The following description outlines how conjunction efficiency was calculated for the SNP-PEG_8-G_{3S} conjugate. *Note: There were no results for the efficiency of dendrimer conjugations due to the uncontrolled nature of the synthetic design.*

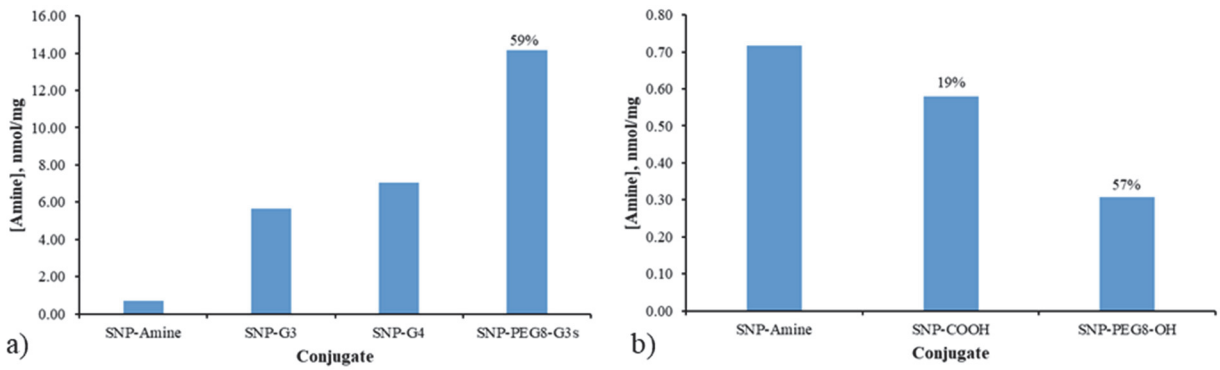

Figure 2.27 Amine densities of conjugates that used SNP-Amine as the original scaffold. (a) Results from the amine assay (a) on bifunctional linker and chelate (dendrimer or dendron) show that all conjugations to SNP-Amine resulted in an increase in amine concentration. (b) Amine densities of the corresponding capped conjugates within the FITC series of SNP coated materials determined via fluorescamine assay showing a decrease in amine density. *Note: the SNP-Amine material was the same value in both (a) and (b).*

Dendron Conjugate - The concentration of conjugated PEG was calculated by the difference in amine density between SNP-Amine and SNP-PEG$_8$-OH, which was equivalent to the PEG loading (Equation 2.3). The concentration of dendron amines was calculated by subtracting the amine concentration remaining on the SNP-PEG$_8$-OH from the amine concentration of the SNP-PEG$_8$-G$_{3S}$ conjugate (Equation 2.4).The number of dendrons was calculated by dividing the dendron amine concentration by the number of amines per dendron (Equation 2.5). Since one dendron conjugates to one PEG, the conjugation efficiency of dendron to PEG was calculated (Equation 2.6). Since the same PEG conjugated material was used in the capping synthesis as in the dendron synthesis, the loadings of PEG should be equal (Equation 2.7).

$$[Amine]_{SNP-Amine} - [Amine]_{SNP-PEG_8-OH} = [PEG_8]_{SNP-PEG_8-OH} \quad \text{Equation 2.3}$$

$$[Amine]_{SNP-PEG_8-G_{3S}} - [Amine]_{SNP-PEG_8-OH} = [Dendron\ Amine]_{SNP-PEG_8-G_{3S}} \quad \text{Equation 2.4}$$

$$\frac{[Dendron\ Amine]_{SNP-PEG_8-G_{3S}}}{32\ Amines\ per\ dendron} = [Dendron]_{SNP-PEG_8-G_{3S}} \quad \text{Equation 2.5}$$

$$\frac{[Dendron]_{SNP-PEG_8-G_{3S}}}{[PEG_8]_{SNP-PEG_8-OH}} = Conjugation\ Efficiency\ (\%) \quad \text{Equation 2.6}$$

$$[PEG_8]_{SNP-PEG_8-OH} = [PEG_8]_{SNP-PEG_8-G_{3S}} \quad \text{Equation 2.7}$$

The percent conversion of SNP-Amine to SNP-PEG$_8$-Mal was 57%, and an overall conversion of SNP-Amine to SNP-PEG$_8$-G$_{3S}$ was 59% (Figure 2.27). The conjugation of the heterobifunctional linker, NHS-PEG$_8$-Mal, lead to the amine concentration to increase 20 times from the original SNP-Amine material.

Dendrimer Conjugates - The percent conversion of SNP-Amine to SNP-COOH through the hydrolysis of the carbomate reactive group from the CDI conjugation was 19% (Figure 2.27b). This means

only 19% of the amines were activated to conjugate either a G_3 or G_4 dendrimer. Even with the low conversion, the amine concentration increased by 8 and 10 times for the SNP-G_3 and SNP-G_4 conjugates, respectively.

Amine conversion to FITC

Amine concentrations were used to determine the amount of FITC to react with the conjugates. A dye loading curve was constructed (Figure 2.25b) and used to determine the concentration of dye on the surface after FITC conjugation. These dye loading results were compared to the amine concentrations to determine the conversion of amine to FITC (Figure 2.28).

Dye loading on the SNP-Amine conjugate was found to be 165% of the amine concentration. This result was thought to be due to either non-specific binding of the dye to the surface of the nanoparticle or the result of dye enhancement due to attachment of the dye being to a rigid scaffold.[36] This effect would not be present in the other conjugates due to solvation of the dendrimer. The SNP-G_3-FITC and SNP-G_4-FITC conjugates had 37% and 32% conversion, respectively, whereas the SNP-PEG_8-G_{3S}-FITC conjugate resulted in a 13% conversion. Overall, conversion was not exceptional and could be mitigated by adding more dye to the reaction.

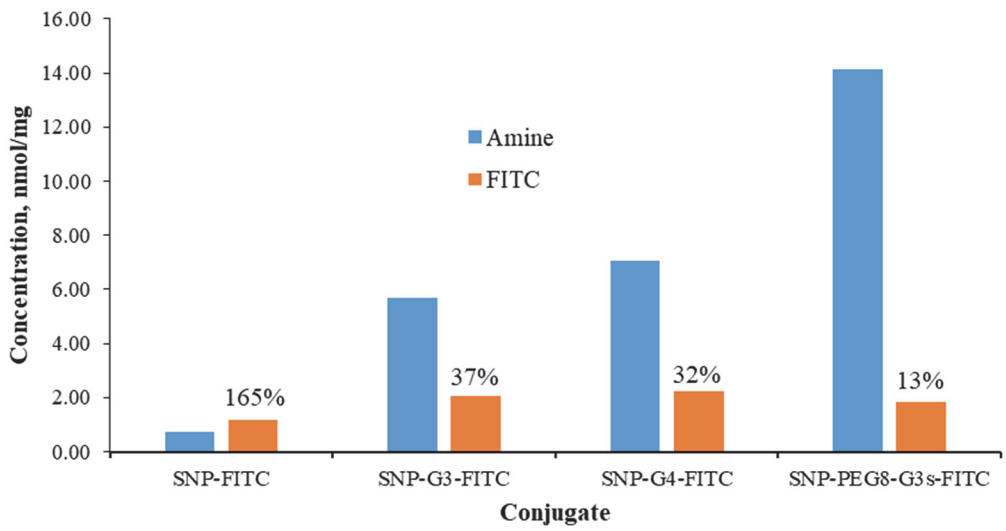

Figure 2.28 Comparison of amine and FITC concentrations of SNP conjugates. Percent conversion of amine to FITC is indicated.

Fluorescence Characteristics of Conjugates

Once the optimal excitation was determined, the emission intensity of the nanoparticle-FITC conjugates were compared to FITC free in solution and the theoretical FITC emissions (Figure 2.29a), which was provided by the ThermoFisher Scientific Spectra Viewer.[69] The emission spectra were normalized to account for the different loadings of FITC on the surface of the nanoparticle conjugates. A bathochromic (red) shift occurred in the free and conjugated dyes as compared to the theoretical maximum? by 40 nm. The theoretical spectrum was likely a FITC simulation in ethanol from ThermoFisher. This redshift has been shown to be a direct result from the solvation of the dye in (solvatochromic effects) in ethanol and ethanol-water mixtures.[71] A goal in the conjugation of dyes is to maintain the same fluorescence character after conjugation. As shown in Figure 2.29a, the emission of the FITC series retained the same

emission maximum (±5 nm) and spectrum shape. Further characterization such as changes in Stokes shift was not determined. Additionally, scattering effects due to macroscopic particles, such as SNPs that are greater in size than the excitation wavelength, present as sharp peaks within the emission band.[36] These sharp peaks were not found in the nanoparticle emission data indicating that the nanoparticles were monodisperse.

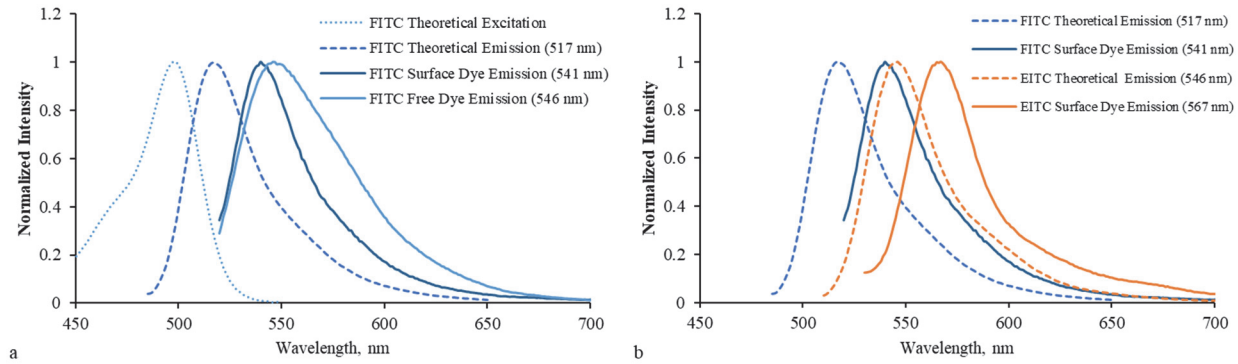

Figure 2.29 Normalized emission spectra comparison between theoretical and free FITC emission with FITC on the surface of nanoparticle conjugates. *Note: Emission maxima are listed in parentheses. Additionally, the emission of all surface dye conjugated to particles had a similar emission spectra and therefore the emission of SNP-PEG$_8$-G$_{3S}$-FITC only is shown here.*

Since a bathochromic shift occurred with the FITC dye, a similar shift should be observed with the EITC dye if the conversion of the dye occurred. The comparison of theoretical emission maxima (Figure 2.29b) show a difference of about 30 nm. As shown in Figure 2.30a, the normalized spectra of SNP-FITC and SNP-EITC differ by 24 nm indicating that the dye was converted. Furthermore, the emission spectrum of SNP-EITC shows very little emission at 543 nm which contributes to the evidence of full dye conversion. Finally, since SNP-EITC was synthesized from the SNP-FITC material, the same number of dyes were present on both conjugates, and when the emission spectra were compared (Figure 2.30b) the total emission of the EITC was a fraction of the SNP-FITC. This is due to the quantum yield of FITC being 0.92[72,73] whereas eosin Y (EITC) has a quantum yield of 0.68.[38]

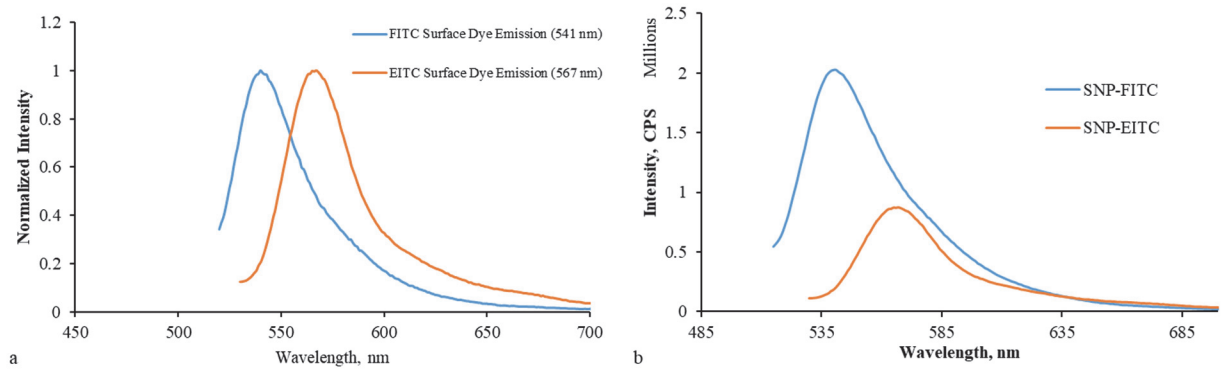

Figure 2.30 Normalized emission spectra (a) comparison of SNP-FITC and SNP-EITC conjugates showing that the emission maximum for SNP-EITC red shifted 26 nm from SNP-FITC. Direct comparison of intensities (b) showed a decrease in emission from SNP-FITC to SNP-EITC. *[SNP] = 0.111 mg/mL; solvent = 2:1 ethanol: HEPES pH 7, 10 mM; excitation =480 nm.*

Discussion

Silica nanoparticles were synthesized according to Soto-Cantu et al. by choosing the approximate size and following the relative concentrations of reactants (water, ethanol, and TEOS) from their preparations. Subsequent building up, using silanization reactions, added functionality to the nanoparticles. Dynamic Light Scattering (DLS) experiments showed that the bare (SNP-OH) particles were about 246 nm in diameter compared to the published value of ~200 nm. The SNP-Amine particles were 342 nm (Figure 2.27a), with a small range of sizes (both monodispersed). The difference in size between the published size and the observed size was likely due to the method of measurement. Soto-Cantu et al. characterized their particles with a TEM, whereas the particles measured here include a sphere of hydration that inflates the nanoparticle size. The increase in size from SNP-OH to SNP-Amine was an indication that the silanization occurred successfully.

Zeta potentials were measured for the two nanoparticles to determine surface characteristics. The SNP-OH particles had similar zeta potentials to the nanoComposix Hydroxyl terminated particles and the isoelectric points were 2.7 and 2.0, respectively (Figure 2.23a and Figure 2.26b). Complete coverage of the SNP surface with amines would have resulted in a zeta potential titration similar to the amine particles from nanoComposix (Figure 2.23b and Figure 2.26b) with an isoelectric point of 8.0. The zeta potential titration of the SNP-Amine particles, however, was closer in comparison to the bare SNPs and the isoelectric point was 4.4 rather than the 8.0 found in the nanoComposix Amine terminated particles (Figure 2.23b). This difference was likely due to the methyl-silane spacer that was used during synthesis. Additionally, an isoelectric point is the pH where particle charge is zero, which would be detrimental to the dispersions used in this work (usually HEPES pH 8) since charged particles repel each other and remain in solution.

The SNP-Amine particles then underwent conjugation reactions to attach chelates for dye attachment and sensing. This process was monitored via amine assay. By conjugating the G_3 and G_4 PAMAM dendrimers, the amine concentrations increased by 8 and 10 times, respectively, as compared to the SNP-Amine starting material (Figure 2.28). This was surprising since only 19% of the amines on the SNP-Amine surface were activated by CDI. Due to the nature of the SNP-PEG$_8$-G$_{3S}$ conjugate synthesis, conjugation efficiency through each step was possible. In total, the conjugation of the G_{3S} dendron to the SNP-Amine was 59% successful and increased the amine concertation by 20 times (Figure 2.28). These results confirmed the hypothesis that amine concentration was in the following order: SNP-Amine < SNP-G_3 < SNP-PEG$_8$-G$_{3S}$ ≤ SNP-G_4. This trend indicated that the use of a more robustly designed synthetic procedure (PEG-Dendron synthesis), that the G_{3S} dendron, which has the equivalent number of amines as a G_3 dendrimer, provides more reaction sites for conjugation than compared to the G_3 dendrimer. Additionally, the G_{3S} conjugate was so successful that the material had approximately the same amine concentration as a G_4 dendrimer even though the G_4 dendrimer has twice as many amines.

In addition, SNP-PEG$_8$-G$_{3S}$ had a higher amine concentration than SNP-G_4 demonstrating that a dendron similar in size and amine concentration to a G_3 could be conjugated to a nanoparticle and produce more surface amines than a G_4 (has double the amines as compared to G_3). As compared to the nanoparticles in Luhrs' thesis, the RITC series had an order of magnitude higher concentration of amines per mass of particles. However, amine densities were at a similar or lower concentration per surface area (Table 2.6). This was likely due to the increase in nanoparticle size in the FITC series. A larger particle has a larger surface area, however, smaller particles have a larger surface area per mass (refer to Nanoparticles as Scaffolds).

Table 2.6 Comparison of amine concentration on nanoparticle conjugates

Conjugate	Amine Density, nmol/mg	Amine Density, amine/ nm^2
SNP_{20}-RITC	16	0.04
SNP_{20}-G_1-RITC	39	0.10
SNP_{20}-G_3-RITC	59	0.15
SNP_{20}-G_4-RITC	113	0.30
SNP_{20}-G_5-RITC	136	0.36
SNP-FITC	0.72	0.10
SNP-G_3-FITC	5.67	0.75
SNP-G_4-FITC	7.07	0.94
SNP-PEG_8-G_{3S}-FITC	14.2	1.88

Dye loading on each conjugate should be amine concentration dependent. This trend was not observed since both dendrimer (G_3 and G_4) materials had nearly the same dye loading (37% and 32% conversion, respectively), and the SNP-PEG_8-G_{3S} conjugate resulted in a mere 13% conversion (Figure 2.29). As dendrimers increase in size so does the likelihood of the terminal amines becoming buried within the dendrimer.[74] In fact, for a G_4 PAMAM dendrimer, only 64% of the peripheral amines are readily reactive.[75] Fluorescamine was able to react with terminal amines in the amine assay, however, the reaction is faster than FITC, and the fluorescamine may be more hydrophobic (hydrophobic pockets are created in larger PAMAM dendrimers).[75] Furthermore, in addition to terminal amines branching inward on the dendrimers, protonated amines were likely the culprit for the 13% conversion SNP-PEG_8-G_{3S}-FITC conjugate. The dendron synthesis was performed at pH 8, and although the FITC conjugation reaction was in DMSO and ethanol, the amines on the dendron likely remained protonated. Cakara et al. showed that approximately half of the terminal amine groups on G_3 and G_4 PAMAM dendrimers were protonated. Protonated amine groups are a well-known culprit of low dye loadings with FITC.[76] The emission characteristics (spectra shape and emission maximum) of FITC did not change due to the conjugations onto the nanoparticle. Other spectroscopic anomalies such as light scattering from the presence of nanoparticles with diameters at or larger than the excitation wavelength were absent. Bathochromic shifts were observed but were due to the dispersion solution and not to scaffold conjugation. This bathochromic shift was also shown to be present in the characterization in the EITC conjugates.

The bromination reaction of FITC to EITC was demonstrated by measuring a shift in emission between the theoretical emissions (Figure 2.30) of the dyes was similar to the shift observed. Additionally, the same number of dyes present on the conjugates led to a much smaller emission intensity of the EITC conjugate. This demonstrates the smaller quantum yield of eosin Y compared to fluorescein. With this evidence, the FITC to EITC reaction was confirmed to be successful.

Conclusions and Future Work

Silica nanoparticles that are monodispersable and approximately 250 nm in diameter were successfully isolated. Furthermore, these particles were monodispersable after the silanization of the surface. Additional work should be carried out at every intermediate step during the synthesis of each sensor *series* to ensure mondispersion remains conserved. Conjugate syntheses of PAMAM dendrimers and dendrons were limited to DMSO and water, which were thought to limit permanent aggregation through observation and fluorescence experiments, however, more work with a DLS would provide more definitive evidence. Greener solvents, such as water, were introduced during the synthesis of the new sensor which did not lead to a decrease in amine concentration on the surface when compared to the traditional

(dendrimer) sensors. Amine concentrations predictively increased based on conjugation reactions on SNP-Amine, however, this increase in amine concentration did not directly translate to higher dye loadings on the conjugates that reflected the amine increase. Selected FITC conjugates were converted through bromination reaction to EITC conjugates that were tested in comparison to the FITC series (Chapter 3).

By changing the amine assay from ninhydrin to fluorescamine, the overall time required to complete the assay went from 30 min or more to less than 10 min. Additionally, less material was required to complete amine assays which reduced the total amount required for each synthesis. This reduction of material needed for post-synthetic testing led to the transition from large scale syntheses that used the Beckman Coulter J2-21 centrifuge (~40 mL syntheses) to the Beckman Coulter Optima TLX centrifuge (~4 mL syntheses) for isolation. The 10x decrease in volume required to be isolated resulted in a decrease in isolation time from about 60 min in the J2-21 centrifuge to about 10 min in the Optima TLX. These improvements in efficiency led to shorter overall synthetic process times for the production of materials for testing. Less time allocated to isolation and testing of materials allows for time allocated to designing, synthesizing, and testing of other materials.

The responsible production of new nanomaterials outlined in the Sustainable Nanomanufacturing and Nanotechnology for Sensors NSI was mostly met in this work due to the conversion of less green reaction solvents from dioxane, ethanol, and DMSO to water for the conjugation of surfaces. Further work is required regarding the scale-up, cost effectiveness, and reliability of these materials, however, the process outlined above was developed to provide a framework in which a multitude of similarly structured materials could be synthesized and tested efficiently.

Future work on these nanoparticle sensors would be to vary the concentrations of reactants more drastically to optimize synthetic procedures. A more thorough investigation of different dendron sizes may lead to sensors that vary in sensitivity. The RITC series has shown that varying the dendrimer generation results in different dynamic ranges for these nanoparticle sensors and that the PAMAM G_4 material had the best (lowest) sensitivity. By utilizing a G_5 cystineamine dendrimer (G_{4SS4}) in the dendron synthesis, a more sensitive copper sensor could be created.

Less nuanced changes would include changing the dendrimer to one listed in Figure 1.17 or to a completely different type of polymer to determine sensitivity to other analytes. Additionally, changing dyes (Figure 1.19) or by merely changing the synthetic step order could give rise to even better sensors.

References

1 Hermanson, G. T. *Bioconjugate Techniques*. 3rd edn, (Academic Press, 2013).

2 Moore, C. J. *et al.* Controlling colloidal stability of silica nanoparticles during bioconjugation reactions with proteins and improving their longer-term stability, handling and storage. *Journal of Materials Chemistry B* **3**, 2043-2055, doi:10.1039/c4tb01915f (2015).

3 Juliano, R. Nanomedicine: is the wave cresting? *Nat Rev Drug Discov* **12**, 171-172, doi:10.1038/nrd3958 (2013).

4 Venditto, V. J. & Szoka, F. C., Jr. Cancer nanomedicines: so many papers and so few drugs! *Adv Drug Deliv Rev* **65**, 80-88, doi:10.1016/j.addr.2012.09.038 (2013).

5 Gerrans, K., Luhrs, A., Feider, C. & Margerum, L. D. Silica nanoparticles functionalized with polyamidoamine (PAMAM) dendrimers as platforms for photoluminescence (PL) sensing of copper and cyanide ions. *J Colloid Interface Sci* **470**, 276-283, doi:10.1016/j.jcis.2016.03.004 (2016).

6 Pham, K. N., Fullston, D. & Sagoe-Crentsil, K. Surface Charge Modification of Nano-Sized Silica Colloid. *Australian Journal of Chemistry* **60**, 662, doi:10.1071/ch07138 (2007).

7 Sun, Y., Zhang, Z. & Wong, C. P. Study on mono-dispersed nano-size silica by surface modification for underfill applications. *J Colloid Interface Sci* **292**, 436-444, doi:10.1016/j.jcis.2005.05.067 (2005).

8 Luhrs, A. *Dendrimer Modified Silica Nanoparticles as Fluorescent Chemosensors for the Detection of Copper and Cyanide Ions*, University of San Francisco, (2016).
9 Arkles, B., Maddox, A., Singh, M., Zazyczny, J. & Matisons, J. Silane Coupling Agents Connecting Across Boundaries. (2014).
10 Iijima, M., Tsukada, M. & Kamiya, H. Effect of particle size on surface modification of silica nanoparticles by using silane coupling agents and their dispersion stability in methylethylketone. *J Colloid Interface Sci* **307**, 418-424, doi:10.1016/j.jcis.2006.11.044 (2007).
11 Winkler, H. C., Suter, M. & Naegeli, H. Critical review of the safety assessment of nano-structured silica additives in food. *J Nanobiotechnology* **14**, 44, doi:10.1186/s12951-016-0189-6 (2016).
12 Korzeniowska, B., Nooney, R., Wencel, D. & McDonagh, C. Silica nanoparticles for cell imaging and intracellular sensing. *Nanotechnology* **24**, 442002, doi:10.1088/0957-4484/24/44/442002 (2013).
13 Kotsuchibashi, Y., Ebara, M. & Narain, R. in *Chemistry of bioconjugates : synthesis, characterization, and biomedical applications* (ed Ravin Narain) 327- (John Wiley & Sons, Inc., 2014).
14 Stober, W., Fink, A. & Bohn, E. Controlled Growth of Monodispersed Silica Spheres in the Micron Sized Range. *Journal of Collodal and Interface Sciences* **26**, doi:10.1016/0021-9797(68)90272-5 (1968).
15 Matsoukas, T. & Gulari, E. Dynamics of growth of silica particles from ammonia-catalyzed hydrolysis of tetra-ethyl-orthosilicate. *Journal of Colloid and Interface Science* **124**, 252-261, doi:10.1016/0021-9797(88)90346-3 (1988).
16 Van Blaaderen, A., Van Geest, J. & Vrij, A. Monodisperse colloidal silica spheres from tetraalkoxysilanes: Particle formation and growth mechanism. *Journal of Colloid and Interface Science* **154**, 481-501, doi:10.1016/0021-9797(92)90163-g (1992).
17 Buckley, A. M. & Greenblatt, M. The Sol-Gel Preparation of Silica Gels. *Journal of Chemical Education* **71**, 599, doi:10.1021/ed071p599 (1994).
18 Bogush, G. H. & Zukoski IV, C. F. Uniform silica particle precipitation: An aggregative growth model. *Journal of Colloid And Interface Science* **142**, 19-34, doi:10.1016/0021-9797(91)90030-C (1991).
19 Carcouet, C. C. *et al.* Nucleation and growth of monodisperse silica nanoparticles. *Nano Lett* **14**, 1433-1438, doi:10.1021/nl404550d (2014).
20 Neville, F., Mohd. Zin, A., Jameson, G. J. & Wanless, E. J. Preparation and Characterization of Colloidal Silica Particles under Mild Conditions. *Journal of Chemical Education* **89**, 940-942, doi:10.1021/ed200684s (2012).
21 Zhang, J. H., Zhan, P., Wang, Z. L., Zhang, W. Y. & Ming, N. B. Preparation of monodisperse silica particles with controllable size and shape. *Journal of Materials Research* **18**, 649-653, doi:10.1557/jmr.2003.0085 (2011).
22 Soto-Cantu, E., Cueto, R., Koch, J. & Russo, P. S. Synthesis and rapid characterization of amine-functionalized silica. *Langmuir* **28**, 5562-5569, doi:10.1021/la204981b (2012).
23 Anderson, G. W. & Paul, R. N,N'-Carbonyldiimidazole, a New Reagent for Peptide Synthesis. *Journal of the American Chemical Society* **80**, 4423-4423, doi:10.1021/ja01549a078 (1958).
24 Podhradský, D., Drobnica, Ľ. & Kristian, P. Reactions of cysteine, its derivatives, glutathione, coenzyme A, and dihydrolipoic acid with isothiocyanates. *Experientia* **35**, 154-155, doi:10.1007/bf01920581 (1979).
25 Wolfson, N. S. *Preparative Organic Chemistry*. 199-200 (1959).
26 Martínez-Utrilla, R., Martín, M. E., Amat-Guerri, F., Sastre, R. & Botija, J. M. New halogenated succinylfluorescein dyes. synthesis and evaluation as singlet oxygen photosensitizers of their free and polymer-bound forms. *Dyes and Pigments* **10**, 47-61, doi:10.1016/0143-7208(89)85039-9 (1989).
27 Klein, D. *Organic Chemistry*. Third edn, (2017).
28 Hanauer, M., Pierrat, S., Zins, I., Lotz, A. & Sonnichsen, C. Separation of nanoparticles by gel electrophoresis according to size and shape. *Nano Lett* **7**, 2881-2885, doi:10.1021/nl071615y (2007).
29 Parak, W. J. *et al.* Conformation of Oligonucleotides Attached to Gold Nanocrystals Probed by Gel Electrophoresis. *Nano Letters* **3**, 33-36, doi:10.1021/nl025888z (2003).
30 Kowalczyk, B., Lagzi, I. & Grzybowski, B. A. Nanoseparations: Strategies for size and/or shape-selective purification of nanoparticles. *Current Opinion in Colloid & Interface Science* **16**, 135-148, doi:10.1016/j.cocis.2011.01.004 (2011).
31 Robertson, J. D. *et al.* Purification of Nanoparticles by Size and Shape. *Sci Rep* **6**, 27494, doi:10.1038/srep27494 (2016).
32 Sweeney, S. F., Woehrle, G. H. & Hutchison, J. E. Rapid purification and size separation of gold nanoparticles via diafiltration. *J Am Chem Soc* **128**, 3190-3197, doi:10.1021/ja0558241 (2006).

33 Akbulut, O. *et al.* Separation of nanoparticles in aqueous multiphase systems through centrifugation. *Nano Lett* **12**, 4060-4064, doi:10.1021/nl301452x (2012).
34 Zucker, R. M., Ortenzio, J. N. & Boyes, W. K. Characterization, detection, and counting of metal nanoparticles using flow cytometry. *Cytometry A* **89**, 169-183, doi:10.1002/cyto.a.22793 (2016).
35 Wunsch, B. H. *et al.* Nanoscale lateral displacement arrays for the separation of exosomes and colloids down to 20 nm. *Nat Nanotechnol* **11**, 936-940, doi:10.1038/nnano.2016.134 (2016).
36 Demchenko, A. P. *Introduction to Fluorescence Sensing*. (Springer, 2009).
37 Mourdikoudis, S., Pallares, R. M. & Thanh, N. T. K. Characterization techniques for nanoparticles: comparison and complementarity upon studying nanoparticle properties. *Nanoscale* **10**, 12871-12934, doi:10.1039/c8nr02278j (2018).
38 Lakowicz, J. R. *Principles of Fluorescence Spectroscopy*. 3rd edn, (Springer, 2006).
39 Time‐Resolved Fluorescence Anisotropy Technical Note TRFT‐2. *Horiba Scientific - Time‐Resolved Fluorescence*.
40 Smith, T. A., Irwanto, M., Haines, D. J., Ghiggino, K. P. & Millar, D. P. Time-resolved fluorescence anisotropy measurements of the adsorption of Rhodamine-B and a labelled polyelectrolyte onto colloidal silica. *Colloid & Polymer Science* **276**, 1032-1037, doi:10.1007/s003960050343 (1998).
41 Apperson, K., Karolin, J., Martin, R. W. & Birch, D. J. S. Nanoparticle metrology standards based on the time-resolved fluorescence anisotropy of silica colloids. *Measurement Science and Technology* **20**, 025310, doi:10.1088/0957-0233/20/2/025310 (2009).
42 Yip, P., Karolin, J. & Birch, D. J. S. Fluorescence anisotropy metrology of electrostatically and covalently labelled silica nanoparticles. *Measurement Science and Technology* **23**, 084003, doi:10.1088/0957-0233/23/8/084003 (2012).
43 Berti, D. & Palazzo, G. *COLLOIDAL FOUNDATIONS OF NANOSCIENCE*. (Elsevier, 2014).
44 *Zetasizer Nano User Manual*. Vol. MAN0485 Issue 1.1 (Malvern, 2013).
45 Berne, B. j. & Pecora, R. *Dynamic Light Scattering with Applications to Chemistry, Biology, and Physics*. (Dover, 2000).
46 Instruments, M. Zeta Potential An introduction in 30 minutes. *Malvern Instruments: Technical Note* **MRK654-01**.
47 NanoComposix. (NanoComposix, 2015).
48 nanoComposix. Charge and Stability of Silica Nanoparticles
49 Sun, Y. *et al.* Quantification of amine functional groups on silica nanoparticles: a multi-method approach. *Nanoscale Advances* **1**, 1598-1607, doi:10.1039/c9na00016j (2019).
50 Dancer, J. *Glass Foundation Chemosensor Synthesis and Functionality Analysis* Master's Thesis thesis, University of San Francisco (2014).
51 Liu, C. *Surface Tethered PAMAM Dendrimers On Controlled Pore Glass As Color Release Sensors For Phosphates* Master's Thesis thesis, Univeristy of San Francisco (2013).
52 Spedding, G. The World's Most Popular Assay? A Review of the Ninhydrin-Based Free Amino Nitrogen Reaction (FAN Assay) Emphasizing the Development of Newer Methods and Conditions for Testing Alcoholic Beverages. *Journal of the American Society of Brewing Chemists* **71**, 83-89, doi:10.1094/asbcj-2013-0411-01 (2018).
53 Luo, D., Haverstick, K., Belcheva, N., Han, E. & Saltzman, W. M. Poly(ethylene glycol)-Conjugated PAMAM Dendrimer for Biocompatible, High-Efficiency DNA Delivery. *Macromolecules* **35**, 3456-3462, doi:10.1021/ma0106346 (2002).
54 Bottom, C. B., Hanna, S. S. & Siehr, D. J. Mechanism of the ninhydrin reaction. *Biochemical Education* **6**, 4-5, doi:10.1016/0307-4412(78)90153-x (1978).
55 Friedman, M. Applications of the ninhydrin reaction for analysis of amino acids, peptides, and proteins to agricultural and biomedical sciences. *J Agric Food Chem* **52**, 385-406, doi:10.1021/jf030490p (2004).
56 Moon, J. H. *et al.* Absolute Surface Density of the Amine Group of the Aminosilylated Thin Layers: Ultraviolet−Visible Spectroscopy, Second Harmonic Generation, and Synchrotron-Radiation Photoelectron Spectroscopy Study. *Langmuir* **13**, 4305-4310, doi:10.1021/la9705118 (1997).
57 Bruce, I. J. & Sen, T. Surface modification of magnetic nanoparticles with alkoxysilanes and their application in magnetic bioseparations. *Langmuir* **21**, 7029-7035, doi:10.1021/la050553t (2005).
58 Moon, J. H., Shin, J. W., Kim, S. Y. & Park, J. W. Formation of Uniform Aminosilane Thin Layers: An Imine Formation To Measure Relative Surface Density of the Amine Group. *Langmuir* **12**, 4621-4624 (1996).

59 Chen, Y. & Zhang, Y. Fluorescent quantification of amino groups on silica nanoparticle surfaces. *Anal Bioanal Chem* **399**, 2503-2509, doi:10.1007/s00216-010-4622-7 (2011).
60 Gore, M. G. *Spectrophotometry and Spectrofluorimetry: A Practical Approach*. 2nd edn, (Oxford University Press, 2000).
61 Nakamura, H. & Tamura, Z. Fluorometric determination of secondary amines based on their reaction with fluorescamine. *Analytical Chemistry* **52**, 2087-2092, doi:10.1021/ac50063a023 (2002).
62 Rosu, C., Gorman, A. J., Cueto, R., Dooley, K. M. & Russo, P. S. Sculpting the internal architecture of fluorescent silica particles via a template-free approach. *J Colloid Interface Sci* **467**, 321-334, doi:10.1016/j.jcis.2016.01.007 (2016).
63 Scientific, T. (Thermo Scientific, 2013).
64 Okorafor, O. C. Solubility and Density Isotherms for the Sodium Sulfate−Water−Methanol System. *Journal of Chemical & Engineering Data* **44**, 488-490, doi:10.1021/je980243v (1999).
65 Farrell, E. & Brousseau, J.-L. Guide for DLS sample preparation *Brookhaven Instruments -Nanoparticle, Protein, & Polymer Characterization*
66 GRACE. LUDOX® Colloidal Silica in Catalyst Applications. (2015).
67 Sigma-Aldrich. Silica, nanoparticle dispersion in water, <50 nm (DLS), triethoxylpropylaminosilane functionalized
68 GRACE. in *Binders for Refractory Fiber Insulation* (W. R. Grace & Co.-Conn., 2017).
69 ThermoFisher. *Spectra Viewer*, <https://www.thermofisher.com/us/en/home/life-science/cell-analysis/labeling-chemistry/fluorescence-spectraviewer.html> (
70 Horiba. *FluoroMax-4 and FluoroMax-4P with USP Operation manual*. Part Number J810005 rev D edn, (Horiba Scientific, 2012).
71 Naderi, F., Farajtabar, A. & Gharib, F. Solvatochromic and preferential solvation of fluorescein in some water-alcoholic mixed solvents. *Journal of Molecular Liquids* **190**, 126-132, doi:10.1016/j.molliq.2013.10.028 (2014).
72 Johnson, I. & Spence, M. T. Z. in *The Molecular Probes Handbook: A Guide to Fluorescent Probes and Labeling Technologies* Ch. 1, (Life Technologies, 2010).
73 Zhang, X. F., Zhang, J. & Liu, L. Fluorescence properties of twenty fluorescein derivatives: lifetime, quantum yield, absorption and emission spectra. *J Fluoresc* **24**, 819-826, doi:10.1007/s10895-014-1356-5 (2014).
74 Frigoli, M., Ouadahi, K. & Larpent, C. A cascade FRET-mediated ratiometric sensor for Cu2+ ions based on dual fluorescent ligand-coated polymer nanoparticles. *Chemistry* **15**, 8319-8330, doi:10.1002/chem.200900475 (2009).
75 Maiti, P. K., Çağın, T., Lin, S.-T. & Goddard, W. A. Effect of Solvent and pH on the Structure of PAMAM Dendrimers. *Macromolecules* **38**, 979-991, doi:10.1021/ma049168l (2005).
76 Johnson, I. & Spence, M. T. Z. in *The Molecular Probes Handbook: A Guide to Fluorescent Probes and Labeling Technologies* Ch. 1, (Life Technologies, 2010).

Chapter 3. Analyte Sensing: Sensitivity of Metal Ion Quenching and QDA with Selected Anions

Introduction to Fluorescence Sensing

As stated previously, the basic requirement for a sensor is for an external stimulus to change the functionality output.[1] For a sensor that uses fluorescence, changes in fluorescence character such as intensity, intensity ratios, anisotropies, time, and phase modulation (Figure 3.1) must occur in response to an analyte.[2] The dynamic or time-dependent methods of fluorescence sensing use the measurement of changes in intensity over time or changes in lifetime (anisotropy and phase modulation) of the fluorescent molecule in response to the analyte.[2] Dynamic fluorescence methods are often complex and require intense analysis whereas static sensing methods (intensity and intensity ratios) are more simple and readily analyzed.[2] Changes in emission intensity, of the dye labelled nanoparticles, were the primary focus of this chapter.

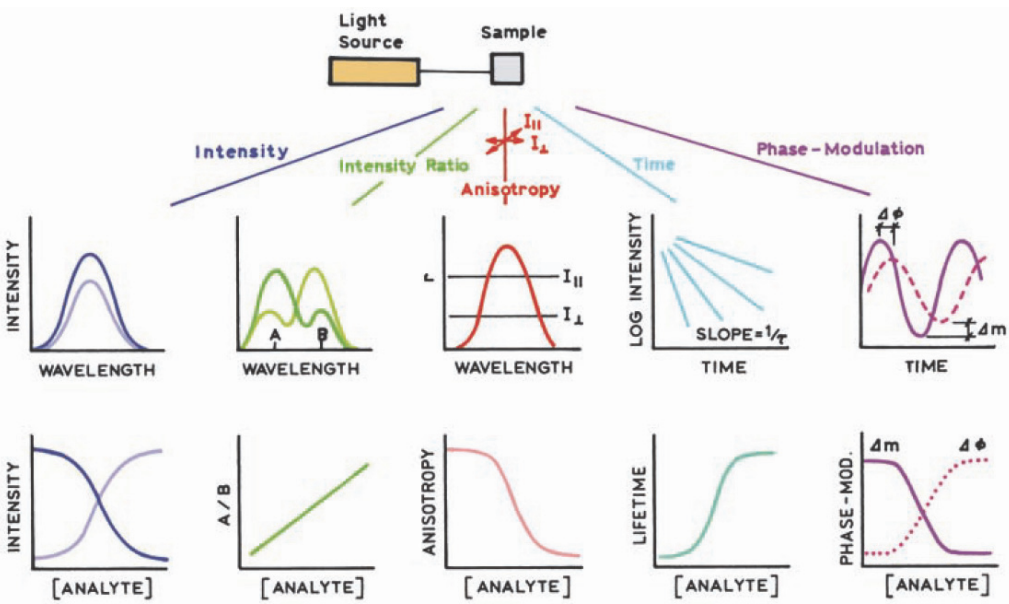

Figure 3.1 Visual representation of the signal changes required for fluorescence sensing. Reprinted.[2]

In general, the emission intensity will yield one of following three results due to the addition of an analyte: increase (enhancement), remain the unchanged due to the sensor lacking sensitivity to the analyte, or decrease (quenching). Copper binding to the thioether-rich moiety of the fluorescein analogs from Figure 1.23 prevents PET from the dye to the ligand which then increases the quantum yield of the dyes, thereby enhancing the emission intensity.[3] Addition of copper to the nanoparticle sensors from Figure 1.12 did not change the emission in the sequestered fluorescein whereas the emission intensity of the external rhodamine dye decreased or quenched.[4]

Quenching Theory

As discussed in Chapter 1, an excited molecule can undergo numerous deactivation processes. The non-radiative deactivation of an excited molecule through the introduction of another molecule is called quenching.[2] A quencher absorbs the excess energy or an electron from the fluorophore through *energy*- or

electron-transfer processes thereby preventing the emission of light.[5] Fluorescence quenching can occur through a variety of different molecular interactions, which include excited state reactions, molecular rearrangements energy transfers, ground-state complex formation, collisional quenching, and static quenching. This chapter will focus on collisional and static quenching. *Note: dynamic and static quenching should not be confused with dynamic and static florescence measurements. Both dynamic and static quenching occur at an equilibrium and therefore are considered a static fluorescence measurement.*

Collisional quenching occurs when the fluorophore is deactivated through momentary contact with the quencher. Fluorophores can also form non-fluorescent complexes with quenchers.[2] These types of quenching are typically referred to as dynamic and static quenching, respectively. As discussed in Chapter 1, if molecule *M* is excited through the absorption of a photon, *hυ*, the excited molecule *M** is formed (Equation 3.1). Without a quencher, excited molecule *M** undergoes radiative decay back to ground state *M* (Equation 3.2).

$$M + h\upsilon \rightarrow M^* \qquad \text{Equation 3.1}$$
$$M^* \rightarrow M + h\upsilon \qquad \text{Equation 3.2}$$

In collisional quenching, with the introduction of a quencher, *Q*, *M** non-radiatively decays to *M* through to the collision with *Q,* (Equation 3.3), which excites *Q* to *Q**. The excited quencher, *Q** then undergoes non-radiative deactivation back to the ground state, *q* (Equation 3.4).

$$M^* + Q \rightarrow M + Q^* \qquad \text{Equation 3.3}$$
$$Q^* \rightarrow Q + \text{heat} \qquad \text{Equation 3.4}$$

Static quenching, however, results in the quencher, *Q*, binding to *M** (Equation 3.5) forming an excited state complex. The excited *M** is deactivated though this binding and the excess energy is localized on the quencher portion of the complex, which then non-radiatively deactivates to the ground state complex *MQ.* A far more likely occurrence in static quenching is the formation of the complex prior to the absorption of the photon (Equation 3.7), however, the outcome is the same.

$$M^* + Q \rightarrow MQ^* \qquad \text{Equation 3.5}$$
$$MQ^* \rightarrow MQ + \text{heat} \qquad \text{Equation 3.6}$$
$$MQ + h\upsilon \rightarrow MQ^* \rightarrow MQ + \text{heat} \qquad \text{Equation 3.7}$$

Since both types of quenching require quencher-fluorophore contact, information about the location of the fluorophore can be determined relative to the quencher.[2] If a fluorophore is buried in an organelle or under the surface of a nanoparticle, a quencher cannot statically or collisionally quench the fluorophore.

Stern-Volmer Equation

Mathematically, collision quenching is described by the Stern-Volmer (SV) equation, shown in Equation 3.8, and a complete derivation of the SV equation can be found in *Principles of Fluorescence Spectroscopy* by Joseph Lakowicz.[2]

$$\frac{F_0}{F} = 1 + k_q \tau_0 [Q] = 1 + K_{SV}[Q] \qquad \text{Equation 3.8}$$

where F_0 is the initial intensity of the fluorophore, F is the intensity upon the introduction of the quencher at concentration Q, k_q is the bimolecular quenching constant, and τ_0 is the lifetime of the fluorophore. The Stern-Volmer constant, K_{SV}, is defined as the product of $k_q\tau_0$ and is referred to as K_D when the quenching is known to be dynamic, otherwise K_{SV} is used.[2] Typically, the F_0/F is plotted against [Q] since the ratio between initial intensity and quenched intensity is expected to be linearly dependent on the concentration of quencher.[2] The intercept of the linear equation is typically 1.0 and the slope of the line is the K_{SV}. This relationship between intensity ratios and the concentration of quencher is linear when there is a single population of readily accessible fluorophores for the quencher to reach. If a population of the fluorophores is not readily available (e.g. buried) to quench, then the SV plot will start to deviate from linearity towards the x-axis resulting in a plateau.

A linear Stern-Volmer plot does not prove collision quenching occurs. Static quenching can result in a linear SV-plot and the easiest method to distinguish between the two quenching types is to increase the temperature and monitor the slope (K_{SV}) of the SV plot.[2] Increasing the temperature for a collisional quencher will result in an increase in the K_{SV} indicating the *efficiency* of the quencher is increased. By increasing the temperature for a static quencher, the slope (K_{SV}) decreases due to weaker binding between fluorophore and quencher thereby lowering the *efficiency* of the quencher. Another method to distinguish between static and collision quenching is by monitoring the absorption spectra of the fluorophore. Ground state complex formation will perturb the absorption spectrum of the fluorophore with a static quencher, whereas the absorption spectrum with remain the same with the addition of a dynamic quencher.[6]

Since the K_{SV} is considered to the measure of quenching efficiency, one can conclude that the relationship between quenching efficiency is directly proportional to the sensitivity of the sensor. That is to say, the more efficient the analyte (quencher) quenches the dye, the less analyte is required to quench, and therefore making the sensor more sensitive to quenching (i.e. the higher K_{SV}, the higher the sensitivity). Comparisons between K_{SV} can be made, however, caution must be employed. Fluorophores may be susceptible to solvent interactions, self-quenching, and fluorophore inaccessibility (the latter two more readily in large systems like nanoparticle or polymer sensors). Additions of quencher concentrations can have a drastic effect on the K_{SV} as well. Incremental additions of quencher are required to ensure subsequent additions do not lead to high influential leverage points[7] within the data that could inflate or deflate the K_{SV} of the sensor.

Quenchers

Table 3.1 provides a list of dyes from *Organic Dyes for Sensing Applications* in Chapter 1 that are quenched by some of the *Chemicals of Interest* from Chapter 2. Organized by the quencher, the list is designed to provide a starting point for the design of a modular quench-fluorescence conjugates of interest. Quenchers, such as zinc, are not shown in Table 3.1, since most zinc sensors are turn-on and are likely far more sensitive and reliable that turn-off sensors.[19] This list, however, is not an exhaustive list and should not be treated as one.

Table 3.1 A list of dyes quenched by the Chemicals of Interest (Chapter 1)

Quencher Ion, M(II) or M(III)	Fluorophore
Arsenic	N/A
Cadmium	N/A
Cesium	Indole[8]
Chromium	N/A
Cobalt	Rhodamine[9], Perylene[10,11], Anthracene[12]
Copper	Cyanine[13], Coumarin[14,15], Anthracene[12], Rhodamine[4], Fluorescein[16]
Iron	Anthracene[12], Erythrosin B[17],
Lead	N/A
Manganese	Anthracene[12]
Mercury	Coumarin[14], Erythrosin B[17],
Molybdenum	N/A
Nickel	Perylene[11]
Silver	Naphthalimide[18], Erythrosin B[17],
Zinc	N/A

Hypotheses of Metal Ions and QDA Sensitivities

Chapter 2 described the synthesis of the FITC series, and the following sections will summarize the sensing characteristics of that series in contrast to individual conjugates as well as past conjugates. Since the RITC series was on very similar set of materials, the quenching character of FITC will be similar to Luhrs' findings in metal sensitivity and dynamic range.[20] The goal was to show similar results on a nanoparticle that was larger and easier to manipulate through synthetic procedures. Specifically, the sensors will show copper-only sensitivity at micromolar concentrations, more precisely, in a range of 0-20 μM. Further exploration of the copper quenched materials will yield sensitivity of the anions EDTA and CN that return the fluorescence of the FITC, thereby creating a QDA sensor for EDTA and CN. By increasing the nanoparticle size and modifying the chelator by attaching a PAMAM dendron via a PEG tether should produce a comparable material to that of Luhrs' particles. Further changes to the material by converting the FITC dye by brominating FITC to create EITC will result in the fluorescence character changing but will remain similar in copper sensitivity.

Materials

The following reagents were used directly without further purification. All relevant acronyms used for chemicals are given in the first position of the parenthetic clarifier. **Solvents:** Ethanol (EtOH, Sigma-Aldrich, 200 proof, 99.5%, CAS 64-17-5, FW 46.07); Ultra-pure water (18 MΩ H_2O, ELGA PURELAB Option-Q purification system); **Buffer:** 4-(2-Hydroxyethyl)-piperazine-1-ethanesulfonic acid (HEPES, Sigma-Aldrich, 99.5% (titration), CAS 7365-45-9, FW 238.30); **Acids:** Nitric Acid (HNO_3, Sigma-Aldrich, ACS reagent 70%, CAS 7697-37-2, FW 63.01); **Bases:** Sodium Hydroxide (NaOH, Sigma-Aldrich, 99% (acidimetric), CAS 1310-73-2, FW 40.00); **Metal Salts:** Copper Nitrate ($Cu(NO_3)_2$, Sigma-Aldrich, ACS reagent 98%, CAS 19004-19-4, FW 232.59); Nickel (II) Nitrate hexahydrate ($Ni(NO_3)_2$, Sigma Aldrich, ≥ 97.0 %, CAS 13478-007-7, FW 290.79); Silver Nitrate ($AgNO_3$, Sigma-Aldrich, ACS reagent, ≥ 99.0%, CAS 7761-88-8, FW 169.87); Zinc Nitrate Hexahydrate ($Zn(NO_3)_2$, Sigma-Aldrich, reagent grade 98%, CAS 10196-18-6, FW 297.49); **Sodium Salts:** Disodium ethylenediaminetetraacetate dihydrate

(Na_2EDTA, EDTA, Baker, 99.7%, CAS 6381-92-6, FW 372.24); Sodium Cyanide (NaCN, Sigma-Aldrich, 97%, CAS 143-33-9, FW 49.01); Sodium Nitrate ($NaNO_3$, Sigma-Aldrich, ACS reagent ≥ 99.0%, CAS 7631-99-4, FW 84.99).

For instrumentation information, please refer to the Instrumentation section of Chapter 2.

Methods

Determination of Quenching Sensitivity via Cation Titrations

All nanoparticle conjugates were dispersed (0.333 mg/mL) in and further diluted with 2:1 ethanol: HEPES (pH7, 10 mM) to obtain an adequate emission signal (between 0.5 and 2 million CPS).[21] Dilutions of SNP conjugates depend on the dispersibility of the material and emission intensity in a particular solvent. A stock $Cu(NO_3)_2$ solution (5 mM, 10 mL) was prepared by dissolving $Cu(NO_3)_2$ in 18 MΩ H_2O (pH 2, HNO_3). Once the correct SNP concentration was determined, the titration of copper began by adding $Cu(NO_3)_2$ (1-10 µL, 5 mM) while monitoring emission intensity. To ensure intensity was quenched maximally, 5-10 min elapsed between the next addition. Some SNP conjugates were too sensitive for the concentration range stated above, which required a dilution (1:10) of the stock $Cu(NO_3)_2$ solution (0.5 mM, 10 mL) and another titration of fresh SNP dispersion. Nitric acid was used as a negative control, which was also used in the comparison between titrated anions (QDA). Comparisons between SNP materials were made by generating Stern-Volmer plots. The slope of the best-fit line is indicative of the efficiency of the metal ion quenching of the material. This process was repeated for all nitrate salt solutions for titration to determine quencher sensitivities.

Quenching Displacement Assay

Once a dynamic range was found for copper, a standard concentration of quencher was added to the particular SNP conjugate. The amount of quencher added was less than the amount required for complete dye quenching to ensure no excess quencher was available to compete with the QDA. A wait time (1-10 mins) was allowed for maximum quenching followed by equivalent additions (1-10µL, 0.1-2 eq.) of EDTA (5 mM, 10mL). Another 10 mins elapsed to allow the system to equilibrate (fluorescence return) and was followed by a second addition of EDTA solution. The titration continued until the fluorescence intensity returned to 100% or the anion concentration was sufficiently concentrated that no measureable effect was observed.

The FITC Series: Results

Sensing via Quenching

Negative Control –The following experiment tested the effects of pH 2 water (nitric acid). This solution was the diluent of analytes, and this it was important to ensure that the diluent did not quench the dye (

Figure 3.2). A slight increase after the addition of 1 µL of pH 2 water was followed by a decrease after the 10 µL addition, implying that changes were due to random noise at 1 µL and dilution at 10 µL (1.96% lower intensity). This indicates that changes in the fluorescence of FITC did not occur due to the more acidic environment.

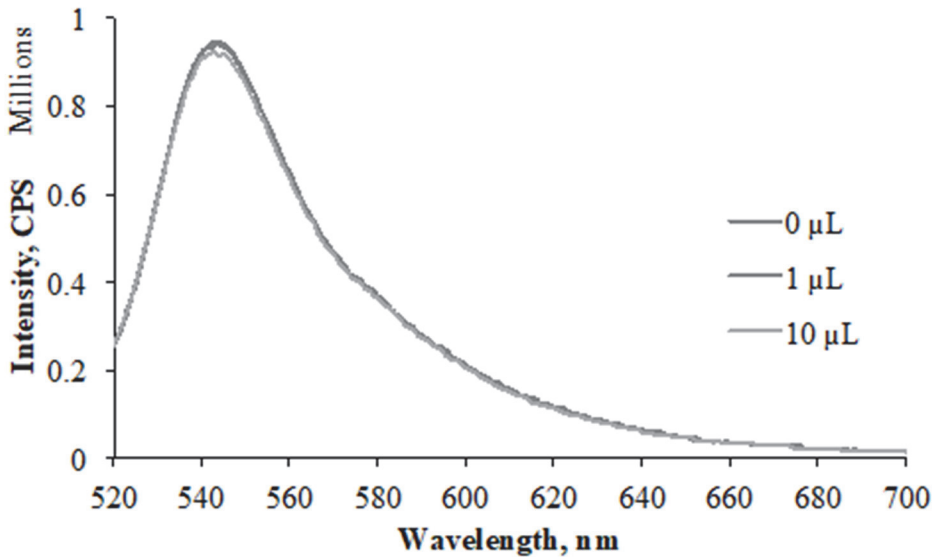

Figure 3.2 Negative control for titrations in the ion sensing of the FITC series. A total volume of 10 µL of water (pH 2, nitric acid) was added to the SNP-G_3-FITC conjugate, and the percent difference between 0 and 10 µL added was calculated to be 1.96%. *[SNP] = 0.030 mg/mL; Solvent = 2:1 ethanol: HEPES pH 7, 10 mM; Excitation = 480 nm.*

Effects of a Sensor Without a Chelate – The following experiment was performed to determine the sensing capability of the dye without the chelate. The effect of dendrimer and dendron chelator on analyte quenching was determined by conjugating the FITC dye directly to the nanoparticle (SNP-FITC conjugate). Addition of copper quenched the emission of the SNP-FITC material (Figure 3.3) but at a much lower percent quenching (40%) and efficiency (K_{SV} = 0.38 x 10^6 M^{-1}) relative to other materials. SNP-FITC showed sensitivity to copper, but the linear dynamic range of the sensor began to taper off at concentrations that approached 1.77 µM, which may indicate that the final titration of copper began to overload the sensor, leading to the saturation of dye quenching (Figure 3.3c). Silver quenching, however, was almost non-existent (Figure 3.3b). After a total concentration of 1.75 µM Ag^+ was achieved, only 10% quenching and an almost flat K_{SV} of 0.045 x 10^6 M^{-1} (Figure 3.3c) resulted after the first addition of silver (0.18 µM). The conclusion was that SNP-FITC conjugate was not sensitive to silver ion.

Effect of Chelate Size and Type – The following experiment was used to determine the effects of sensing with the addition of three chelates: two types of dendrimers and a PEG-Dendrimer. Copper and silver ion quenching of FITC on the SNP-PEG_8-G_{3S}-FITC conjugate (Figure 3.4) was more efficient than the SNP-FITC conjugate. The original PEG-dendron material (hSNP-PEG_8-G_{3S}-FITC) gave a K_{SV} of 1.0 x 10^6 M^{-1} and 0.55 x 10^6 M^{-1}, respectively, for copper and silver ion. At 2 µM of metal ion, FITC emission was quenched by 67% and 50% with copper and silver, respectively. Noisy emission spectra and relatively low coefficient of determination (R^2) was thought to be due to the exceedingly large concentration of particles in solution (0.111 mg/mL) for the SNP-PEG_8-G_{3S}-FITC conjugate. The low loading of FITC dye on this material was likely the culprit. Low dye loading leads to far more particles required to be suspended for adequate signal measurement. More particles then translate to more areas of chelation for the metals but with the same amount of dye ([dye] is directly proportional to emission intensity).

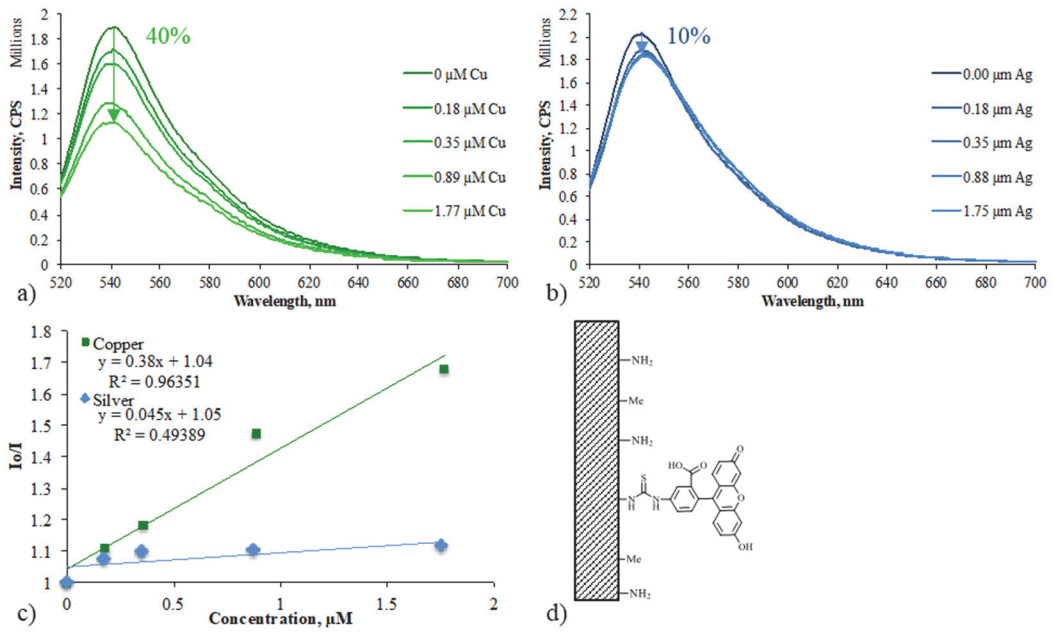

Figure 3.3 Quenching of SNP-FITC when titrated with (a) copper nitrate and (b) silver nitrate resulting in 40% and 10% total quenching, respectively. (c) SV plot of the dye quenching yielded a K_{sv} of 0.38 and 0.045 x 10^6 M^{-1} for copper and silver respectively. (d) Depiction of the SNP-FITC conjugate showing the imagined surface of the nanoparticle. *[SNP] = 0.111 mg/mL; Solvent = 2:1 ethanol: HEPES pH 7, 10 mM; Excitation = 480 nm.*

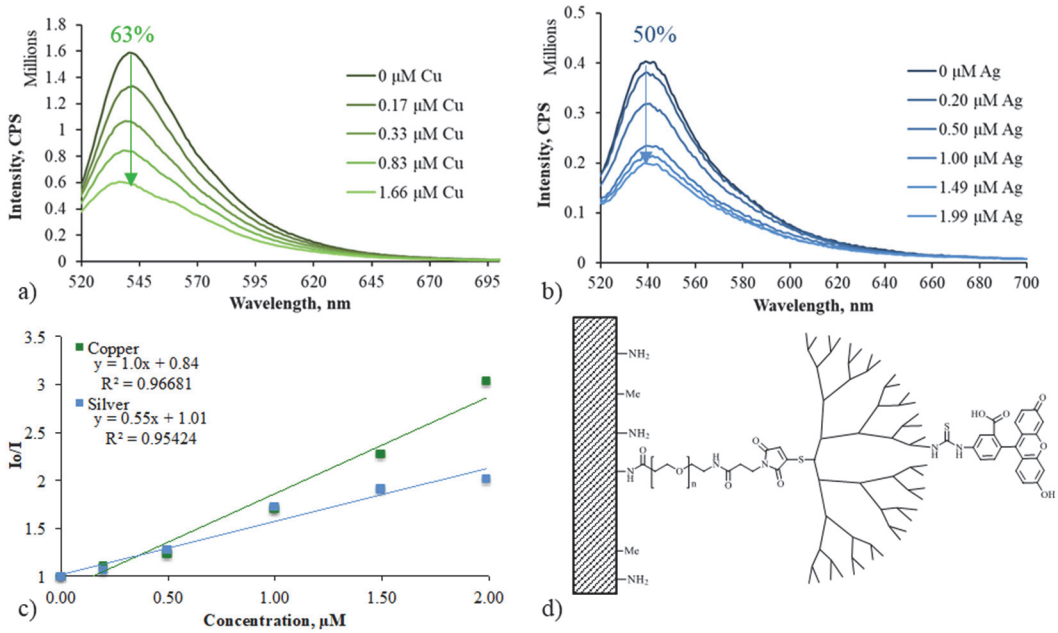

Figure 3.4 Quenching of the SNP-PEG_8-G_{3S}-FITC conjugate when titrated with (a) copper nitrate and (b) silver nitrate resulting in 67% and 50% total quenching respectively. (c) The K_{sv} for copper and silver were calculated to be 1.0 and 0.55 x 10^6 M^{-1}, respectively. (d) Depiction of the SNP-PEG_8-G_{3S}-FITC conjugate showing the imagined surface of the nanoparticle. *[SNP] = 0. 0556 mg/mL for the copper titration, 0.0142 mg/mL for the silver titration; Solvent = 2:1 ethanol: HEPES pH 7, 10 mM; Excitation = 480 nm*

Drastically low concentrations of both copper and silver were required to unearth the dynamic ranges of the SNP-G_3-FITC (Figure 3.5). The titration of 0.10 µM Cu quenched the FITC dye by 34%, while the same concentration of silver quenched the dye by 51%. Further investigation into these titrations showed that the Stern-Volmer quenching of FITC (Figure 3.5c) was linear for both metals. Astonishingly, the K_{SV} calculated were 5.9 x 10^6 M^{-1} and 10.4 x 10^6 M^{-1} for copper and silver, respectively, and therefore SNP-G_3-FITC was a far more efficient sensor than the SNP-PEG_8-G_{3S}-FITC conjugate or the RITC series.

Luhrs showed that the best sensing material produced in the RITC series was the SNP modified with G_4 conjugate. The SNP_{20}-G_4-FITC conjugate seemed to prove even better than the entire RITC series, though statistics determined no significant difference between RITC and FITC on the SNP_{20}-G_4-dye conjugates. However, these results were compelling enough to synthesize and test another SNP-G_4-FITC conjugate (Figure 3.6). Much like the G_3 dendrimer conjugate, the SNP-G_4-FITC material sensed copper and silver through the quenching of FITC but to only 50% and 36% total quenching, respectively. Furthermore, the K_{sv} for this material was found to be 3.4 and 5.4 x 10^6 M^{-1}, respectively, and the R^2 was greater than 0.99, which implied that the concentrations tested were within the dynamic range of the sensor.

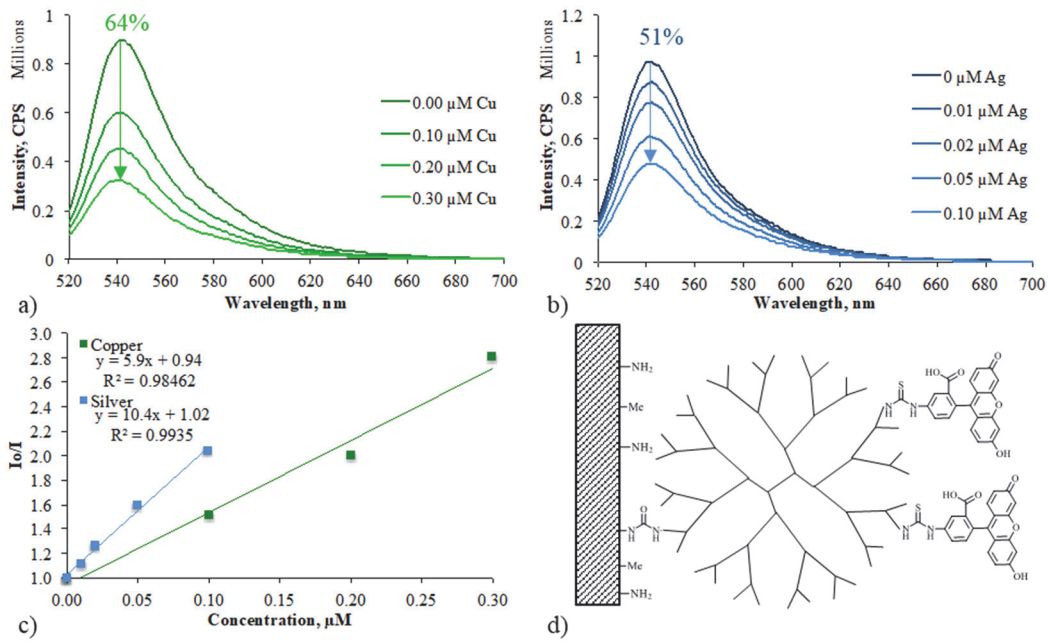

Figure 3.5 Quenching of the SNP-G_3-FITC conjugate when titrated with (a) copper nitrate and (b) silver nitrate resulting in 64% and 51% total quenching respectively. The K_{sv} for copper and silver (c) were calculated to be 5.9 and 10.4 x 10^6 M^{-1}, respectively. (d) Depiction of the SNP-G_3-FITC conjugate showing the imagined surface of the nanoparticle. *[SNP] = 0.030 mg/mL; Solvent = 2:1 ethanol: HEPES pH 7, 10 mM; Excitation = 480 nm.*

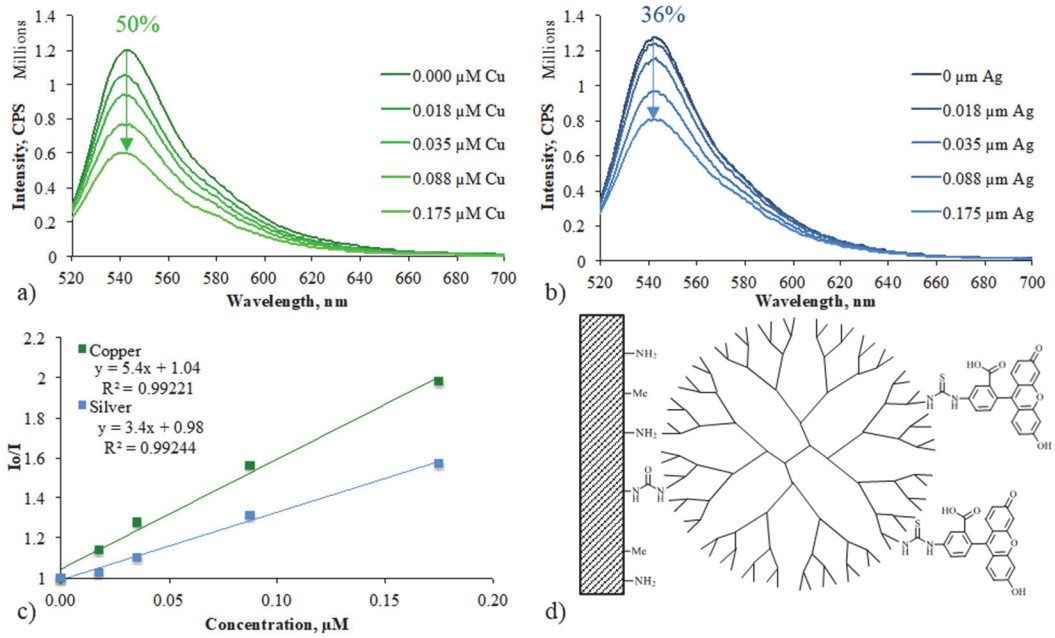

Figure 3.6 Quenching of the SNP-G_4-FITC conjugate when titrated with copper nitrate (a) and silver nitrate (b) resulting in 50% and 36% total quenching respectively. The K_{sv} for copper and silver were calculated to be 5.4 and 3.4 x 10^6 M^{-1} respectively (c). Depiction of the SNP-G_4-FITC conjugate (d) showing the imagined surface of the nanoparticle. *[SNP] = 0.037 mg/mL; Solvent = 2:1 ethanol: HEPES pH 7, 10 mM; Excitation = 480 nm.*

Other cations as quenchers – The following study was performed to determine the sensitivity of the sensors to a few other ions. These experiments were carried out to ensure that the sensors do not quench in the presence of all cations and suggest selectivity towards copper and silver. The sensitivity to additional cations (sodium, nickel and zinc) were compared with the SNP-G_3-FITC and SNP-PEG$_8$-G_{3S}-FITC conjugates (recall that a reduced G_{3SS3} dendron is a G_{3S} dendrimer which is structurally similar to a G_3 dendrimer). Nitrate salt solutions were prepared at a concentration of 2 µM, then screened for quenching by adding 10 µL nitrate salt solutions to the nanoparticle suspensions (similar to the sodium titration). With the baseline subtraction, the quenching of FITC with copper was similar to the hSNP-PEG$_8$-G_{3S}-FITC conjugate for both the PEG-dendron and the dendrimer materials (Figure 3.7). Nickel and zinc gave low quenching efficiency with the FITC dye (similar to the RITC dye in Luhrs' work). Sodium was considered to be a negative control and did not quench significantly. The lack of quenching with sodium ion showed the ability for the use of sodium salts for future QDA experiments. An extremely large difference using silver ion was observed comparing the RITC series and the FITC series. Both dendrimer and PEG-dendron conjugates showed significant emission quenching (52% and 50%, respectively) when silver nitrate added. Based on these results, the next endeavor was to determine the dynamic ranges and K_{SV} of these materials with the two Group 11 elements (Cu and Ag).

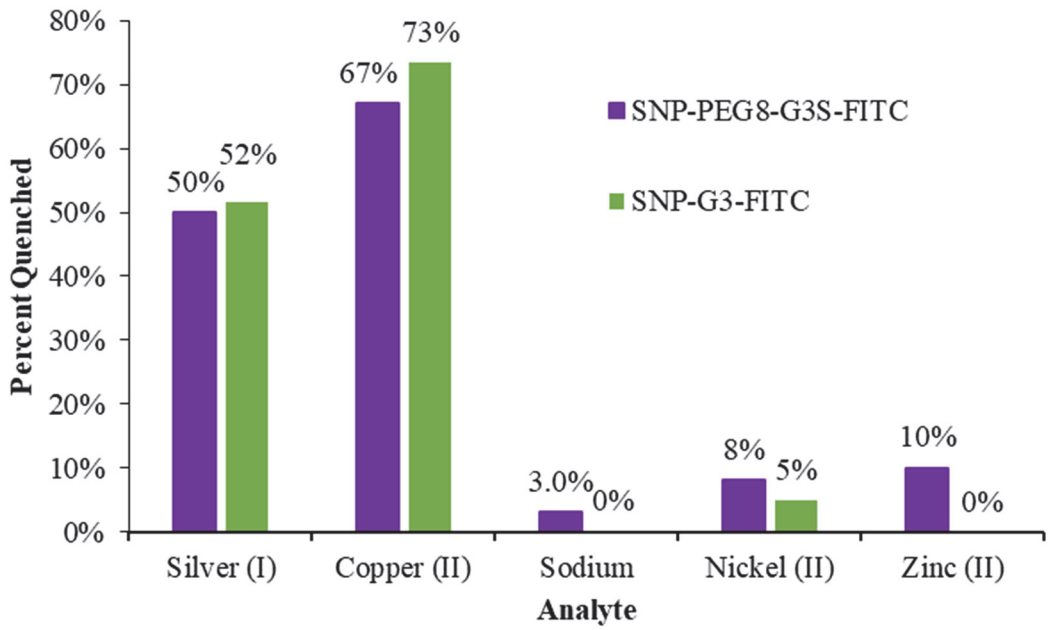

Figure 3.7 General titrations of selected metal salts at 2 µM (10 µL total). [SNP-G_3-FITC] = 0.030 mg/mL and [SNP-PEG_8-G_{3S}-FITC] = 0. 0556 mg/mL; Solvent = 2:1 ethanol: HEPES pH 7, 10 mM; Excitation = 480 nm.

Sensing with EITC – The goal of the following experiment was to determine the effects of in situ synthesis of EITC via FITC bromination and to test the hypothesis that changing the dye will change the sensitivity of the sensor (in situ synthesis ensured dye loading was exactly the same between FITC and EITC conjugates). A newly synthesized SNP-EITC conjugate (no dendrimer) suspension (Figure 3.8), required 52.61 µM Cu to quench the dye by 22% and resulted in a K_{SV} = 0.0052 x 10^6 M^{-1} which was a significant increase of copper required to quench as compared to the SNP-FITC conjugate (recall that the SNP-EITC conjugate was synthesized directly from SNP-FITC). As shown in Figure 3.3, SNP-FITC was sensitive between 0-2 µM Cu and quenched by 40%, which was a 30-fold decrease in sensitivity, and quenching was reduced by half by simply brominating the FITC dye on the surface of the nanoparticles. In stark contrast, addition of 20 µM Ag to the SNP-EITC conjugates showed a similar lack of change in emission intensity (decreased by 1.4%) as the negative control (decreased by 1.9%) indicating that no quenching had occurred.

Further investigation into the EITC series showed increased in sensitivity with the SNP-G_3-EITC conjugate when compared to SNP-EITC and provided more evidence that chelates, such as dendrimers, can increase sensor sensitivity for certain analytes. SNP-G_3-EITC was quenched by 33% with a concentration of 3.54 µM Cu and yielded a K_{SV} of 0.26 x 10^6 M^{-1}. Total quenching increased by 11% from SNP -EITC to SNP-G_3-EITC, however, the quenching resulted from a 93% reduction in Cu concentration. Similar to the SNP-EITC conjugate, silver titration of SNP-G_3-EITC yielded in poor quenching results with nearly 20 µM Ag and less than 5% quenching. SNP-G_3-EITC followed a similar trend that was shown with the SNP-ETIC conjugate when compared to the FITC series counterpart. The SNP-G_3-EITC required a 10-fold increase in copper concentration to yield about half of the quenching found with SNP-G_3-FITC.

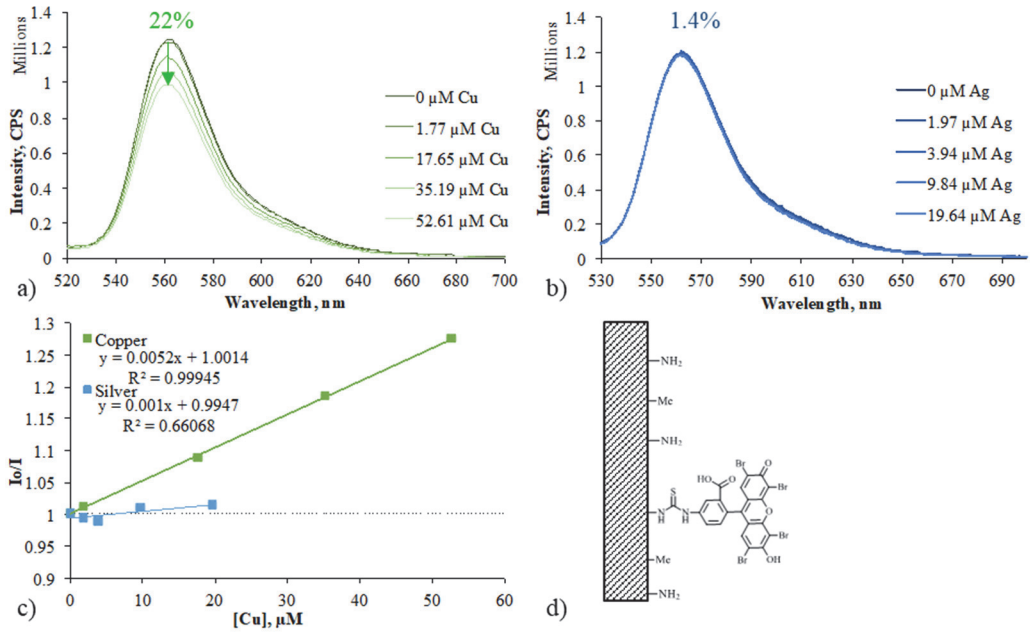

Figure 3.8 Quenching of the SNP-EITC conjugate when titrated with copper nitrate (a) resulting in 22% total quenching. The titration of silver nitrate (b) resulted in a 1.4% change in emission. The K_{sv} for copper was calculated to be 0.0052 x 10^6 M^{-1} whereas the K_{SV} was considered to be zero for the silver due to the low correlation (R^2 = 0.66) of the SV-plot (c). Depiction of the SNP-EITC conjugate (d) showing the imagined surface of the nanoparticle. *[SNP] = 0.111 mg/mL; Solvent = 2:1 ethanol: HEPES pH 7, 10 mM; Excitation =480 nm.*

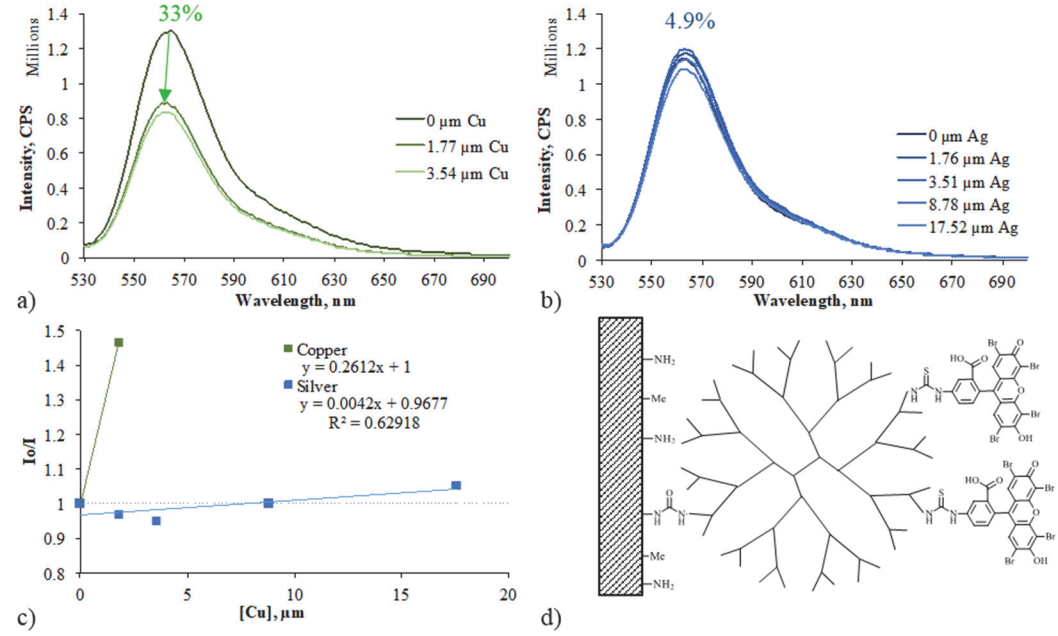

Figure 3.9 Quenching of the SNP-G_3-EITC conjugate when titrated with copper nitrate (a) resulting in 33% total quenching. The titration of silver nitrate (b) resulted in a 4.9% change in emission. The K_{sv} for copper was calculated to be 0.26 x 10^6 M^{-1} whereas the K_{SV} for silver was considered to be zero due to the low correlation (R^2 = 0.63) of the SV-plot (c). Depiction of the SNP-EITC conjugate

(d) showing the imagined surface of the nanoparticle. *[SNP] = 0.0666 mg/mL; Solvent = 2:1 ethanol: HEPES pH 7, 10 mM; Excitation =480 nm.*

Quenching Displacement Assay of the Copper Quenched Dendron Conjugate

The following experiment was used to determine the sensing capability of copper-quenched SNP-PEG_8-G_{3S}-FITC via QDA to detected anionic analytes. Luhrs showed with the RITC series that the addition of EDTA and cyanide resulted in increases in fluroescence emission, thereby creating EDTA and cynaide turn-on sensors. A QDA was performed with EDTA and cyanide that resulted in the partial emission return of SNP-PEG_8-G_{3S}-FITC. Emission return with EDTA was found to total 95% of the original emission at approximately two equivalents of EDTA per copper. Cyanide was less successful and returned 68% at approximately four equivalents of copper.

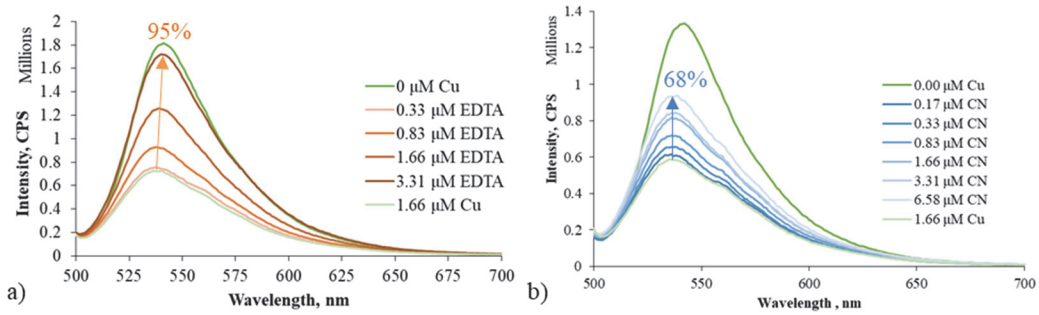

Figure 3.10 Emission return of the copper quenched conjugate SNP-PEG_8-G_{3S}-FITC upon the addition of (a) EDTA and (b) cyanide (CN). The two green emission spectra show the initial and final emission before (0 µM Cu) and after quenching (1.66 µM Cu). *[SNP] = 0.0556 mg/mL; Solvent = 2:1 ethanol: HEPES pH 7, 10 mM; Excitation = 480 nm.*

Discussion

The FITC nanoparticle series were synthesized to compare the effects of copper and silver quenching on conjugates without a dendrimer/dendron chelate, with a varying dendrimer chelate size on the surface, and changing the dye characteristics (on the surface, in situ). The SNP-G_3-FITC conjugate was selected in a negative control test (

Figure 3.2) to show that the 10 µL volume titration additions would not alter the responses of the sensors. The additions used pH 2 water adjusted with nitric acid since the metal ion salts were prepared in the same solutions. The resulting emission intensity decreased by only 2%, indicating that the majority of the quenching in the metal ion studies was due to the metals and not by the addition of the acidic diluent.

The direct attachment of FITC to the nanoparticle (SNP-FITC conjugate) resulted in an effective sensor for copper, but not for silver (Figure 3.3). The linear dynamic range for copper was 0.18 – 1.77 µM giving a K_{sv} of 0.38 x 10^6 M^{-1} with total quenching at 40% for 1.77 µM. This conjugate was comparable to the SNP_{20}-G_3-RITC material and indicated that, for copper, a dendrimer or dendron chelate may not be needed when FITC is used for the sensing dye. Chelates may be required for silver detection since the SNP-FITC conjugate was not sensitive to silver.

Addition of dendrimer/dendron chelates in the conjugates aided in sensing of both copper and silver ions (Figure 3.4, Figure 3.5, and Figure 3.6) with similar total quenching of 50-60% of varying concentrations ranging from 0.1 – 2 µM. The SNP-PEG_8-G_{3S}-FITC conjugate results were similar to that of the original dendron conjugate hSNP-PEG_8-G_{3S}-FITC. Astonishingly, SNP-G_3-FITC conjugate yielded better sensitivity to copper and silver at concentrations of 0.10 – 0.30 µM Cu and 0.01 – 0.10 µM Ag, with K_{SV} of 5.9 and 10.4 x 10^6 M^{-1}, respectively, than compared to the other conjugates in the series. We

concluded that the G_3 dendrimer was the superior chelator for copper and silver ions. For comparison, the G_4 dendrimer conjugate possessing more binding sites, SNP-G_4-FITC, had comparable results for copper quenching with a dynamic range of 0.018 – 0.175 μM Cu and a K_{SV} of 5.4 x 10^6 M^{-1}. Table 3.5 shows the comparisons of the FITC series with the RITC series. An interpretation was that an increase of bound dendrimer/nanoparticle size may have increased the efficiency of copper quenching (K_{SV}). *Note: More comparisons between the FITC series and RITC series work are shown in* Table 3.2 *below.* More binding sites and/or larger nanoparticles may increase the sensitivity of the sensor, however, direct comparison of the materials in the RITC series and materials found here should be made with caution. Synthetic and sensing methods were quite different, and a more systematic approach to comparing the differences in nanoparticle size, dendrimer or dendron generations, and dyes should be addressed in the future.

Preliminary sensing with the EITC conjugates yielded a lower sensitivity in copper which increased the linear dynamic ranges from sub-micromolar to micromolar (Table 3.2). Although the EITC conjugates showed significantly lower copper ion sensitivity, the conversion from FITC to EITC eliminated the sensors sensitivity to silver ion, which may have applications in samples that contain both copper and silver ions. The total quenching was about half of the quenching found in the FITC series which may limit the resolution of the EITC series.

The use of sodium nitrate in the *Other cations as quenchers* experiment showed that the use of sodium salts did not significantly affect the emission of the FITC dye. The QDAs yielded promising results for EDTA and cyanide sensing at μM concentrations for copper quenched-SNP-FITC conjugates. When compared to the RITC series, the water based synthesis of the FITC series was not as efficient in QDA[20], requiring the same or more equivalents to return the fluorescence signal.

Table 3.2 Comparison of the RITC, FITC, EITC series for copper sensing

Conjugate	Dynamic Range, μM	Copper K_{SV}, 1x10^6 M^{-1}	Quenched, %
SNP_{20}-G_1-RITC	-	0.61	-
SNP_{20}-G_3-RITC	1 - 2	0.36	40 - 45
SNP_{20}-G_4-RITC	0.25 - 1.5	1.1	60
SNP_{20}-G_5-RITC	-	0.55	-
SNP_{20}-G_4-FITC	0.25 - 1.5	1.4	60
SNP-FITC	0.18 - 1.77	0.38	40
SNP-G_3-FITC	0.02 - 0.30	5.9	64
SNP-G_4-FITC	0.02 - 0.18	5.4	50
SNP-PEG_8-G_{3S}-FITC	0.10 – 1.99	1.0	67
SNP-EITC	1.77 – 35.2	0.0052	22
SNP-G3-EITC	1.77-3.54	0.26	33

In comparison to this work, a nanoparticle sensor using similar components was constructed and found to yield far more sensitive results than presented here. Qiao et al. demonstrated that fluorescent polyethyleneimine (PEI) core-silica shell FITC nanoparticles were sensitive to copper at 0.1 – 90.0 nM with near 100% quenching and a K_{SV} of 4.3 × 10^8 M^{-1}.[22] PEI is a cross-linked polymer very similar in structure to PAMAM and nearly identical to the PPI dendrimer shown in Figure 1.17. The major difference in the results provided here and the Qiao et al. conjugates was the orientation of the components. By encapsulating PEI dendrimer in a silica shell, the core became isolated from the environment of the solution, and etching of the silica shell allowed FTIC access to the core to react with the primary amines on the surface of the PEI dendrimer.[22] Once in solution, copper was free to migrate into the nanoparticle through the pores made

by etching the silica shell and quench the dye. Increased emission intensity from the dye, due to limited degrees of freedom for the encapsulated dye and chelate, was likely a strong factor in the sensitivity at low concentrations. Additionally, the surface of the nanoparticle remained charged and readily suspended in aqueous environments.

Conclusions

The dendrimer conjugates outlined in this section were found to have better metal sensitivity than those of Luhrs' work with the RITC series.[20] Sources for the increased sensitivity were hard to pinpoint due to the drastic changes in methodology that occurred between the two studies (RITC dye conjugates need testing on larger nanoparticles for a better comparison). The dynamic range, albeit at higher concentrations, was wider for RITC series which is better for determination of copper in environmental samples. The goal of the new conjugates descried here was to show sensor sensitivity up to 20 μM Cu; instead, the maximum concentration for the entire FITC series was 2 μM Cu. Additionally, the RITC series was only sensitive towards copper. Although silver does not readily dissolve in water and the addition of chloride ion should effectively remove silver ions in environmental samples prior to titrations, the RITC series was more selective for copper, indicating less interference from non-analytes species.

In the QDA experiments, EDTA and cyanide were titrated with the dendron-FITC conjugate and compared to the RITC series. EDTA was similarly effective at returning the emission of FITC as in the FITC and RITC conjugates of Luhrs' work. Cyanide was not as effective as compared to the RITC series (Table 3.2). Upwards of 8 equivalents of cyanide and 30 min of equilibration were required for the 97% emission return in the hSNP-PEG$_8$-G$_{3S}$-FITC conjugate as compare to the 2 equivalents and 90-100% return in the RITC series. Although not as effective for cyanide as the RITC series, the preliminary hSNP-PEG$_8$-G$_{3S}$-FITC conjugate remains a likely candidate for a QDA sensor for both cyanide and EDTA. By expanding on Luhrs' work[20], the goal of this project was to increase nanoparticle size, change the chelator by attaching a PAMAM dendron via a PEG tether, and change the synthetic approaches to use more green solvents while producing comparable materials to that of Luhrs' particles.

The results presented here provide evidence that the above goals were met, and future work with these materials will show more promising results and applications. Overall, the materials shown in Table 3.5 were considered effective sensors for copper and are well below the threshold of 1.3 mg/L (20.5 μM) Maximum Contaminant Level for drinking water.[23] The sensors in Table 3.2 could be used in the sensing of copper in drinking water sources and, since the concentration of copper found in the body (Table 1.4) ranges from 10 – 50 μM[24], biological samples from humans. Further optimization would be required before true environmental samples could be tested, but the sensors have proven to be sensitive at well below the level needed for drinking water and human tissue copper concentration determination.

Future Work

In future work, a comparison of the effects of dye on materials of similar composition and the influence of size (as with the FITC and RITC series) would be required. Each batch of material SNP-dendrimer/dendron would need to be split and reacted with each dye to keep the scaffold and chelates constant. Additionally, FITC and RITC concentrations on the conjugates would need to be equal if adequate comparisons were to be made.

If these comparable conjugates were made, more robust testing could be performed to refine the sensor properties of each type of sensor. The following subsections outline short descriptions on how to approach such refinement:

Accuracy: Accuracy assessments of could be performed with NIST copper standards with results of the fluorescent nanoparticle sensors compared to the atomic absorption (AA) spectra of the same NIST standard.

Precision: Performing multiple accuracy measurements with the sensors and the AA will provide precision comparisons.

Error: From the accuracy and precision data, the error in the sensor measurements will be found.

Noise: Noise will not only be found in the fluctuations in the instrument and the emission of the dyes but compounded by the stability of the colloid dispersion. By taking multiple measurements of each concentration, the noise should be determined.

Resolution: See dynamic range

Sensitivity: See dynamic range

Dynamic range: More refined and possibly different additions of analyte (Cu) concentration should be added to determine the incremental changes (sensitivity) over wider concentrations of analyte. By keeping the titration volumes constant, variations due to volume change will not have an effect on results, and changes to concentration of those volumes would allow for a more refined dynamic range. Incremental additions of very dilute analyte would provide the resolution of the analyte and the same incremental additions of concentrated analyte would yield the upper bounds of the dynamic range (Figure 3.11).

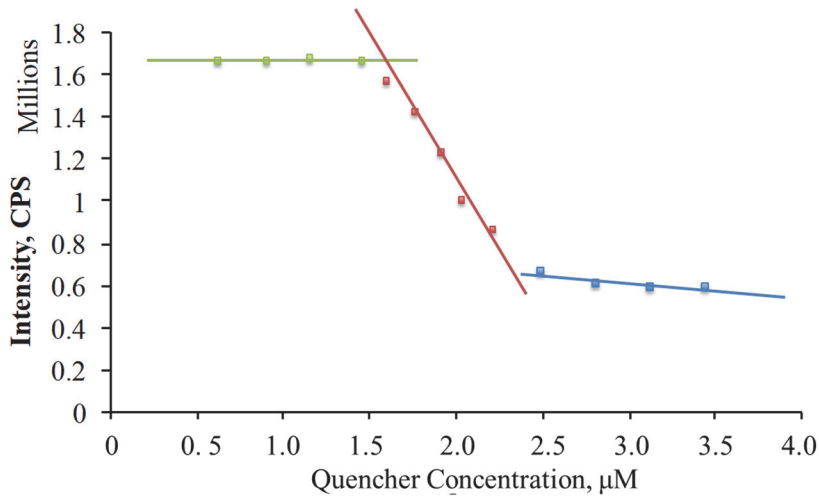

Figure 3.11 Refined dynamic range determination via traditional titration where small volumes of dilute quencher are added to the sensing material. The lower part of the dynamic range could be found through the intersections of the best-fit line of green and red, whereas the intersection of red and blue best-fit lines results in the upper limits of the dynamic range. (This may prove difficult due to colloidal instabilities or long equilibration times.)

Selectivity: Individual titrations of a variety of metal ions at concentrations below, within, and above the dynamic range of the analyte (Cu). Further titration studies including addition of the analyte (Cu) at concentrations within the dynamic range followed by the addition of possible interfering (non-analytes) ions or molecules. This would likely be a general investigation since experimental matrices would likely need to be tested as a control prior to use in the field. `

Stability: Perform stability studies through repeated drying and dispersing samples for a period of time, then perform analyte (Cu) titrations to determine the stability of the conjugate.

Drift: Similar to stability, after a titration is performed, a period of time would pass and the emission would be measured again.

Response time: Incremental spectra would be taken at specified time at the various concentrations of the dynamic range to determine the response time, otherwise known as the time required for the system to equilibrate and provide a steady/ unchanging signal response.

Following the establishment of a set of sensor characteristics, more single dye conjugates could be produced using different dendrimers/dendrons/branched polymers and other dye types[25] (Figure 1.19) that eventually lead to a library of materials to match analyte to sensor materials. Double dye conjugates could also be produced similar to the example in Figure 1.12. Additionally, all materials produced could then be tested for anion testing through QDA analyses.

Alternatively, an increase in intensity emission (enhancement) would be a preferred method of sensing an analyte, especially with a nanoparticle sensor. Nanoparticle dispersions are sensitive to dissolved solutes which can disrupt the suspension, initiate nanoparticle coagulation, and eventually lead to the nanoparticles falling out of suspension entirely. Analysis of results from a sensor designed based on quenching may lead to a false positive if the addition of an analyte coagulates the nanoparticles, thereby removing them from solution. The response would still give a "quenched" emission spectrum. However, analysis of an enhanced emission sensor that was susceptible to analyte addition would easily show that a decrease in emission would be due to dispersion instability. Synthesis of sensors that incorporate dyes[3] similar to ones described in Figure 1.23 would be quenched though PET until a metal ion is added.

References

1 Kalantar-zadeh, K. & Fry, B. *Nanotechnology-Enabled Sensors*. (Springer, 2008).

2 Lakowicz, J. R. *Principles of Fluorescence Spectroscopy*. 3rd edn, (Springer, 2006).

3 Jia, S., Ramos-Torres, K. M., Kolemen, S., Ackerman, C. M. & Chang, C. J. Tuning the Color Palette of Fluorescent Copper Sensors through Systematic Heteroatom Substitution at Rhodol Cores. *ACS Chem Biol*, doi:10.1021/acschembio.7b00748 (2017).

4 Zong, C., Ai, K., Zhang, G., Li, H. & Lu, L. Dual-emission fluorescent silica nanoparticle-based probe for ultrasensitive detection of Cu2+. *Analytical Chemistry* **83**, 3126-3132, doi:10.1021/ac2001324 (2011).

5 Balzani, V., Ceroni, P. & Juris, A. *Photochemistry and Photophysics: Concepts, Research, Applications*. (Wiley-VCH, 2014).

6 Mark, S. S., Sandhyarani, N., Zhu, C., Campagnolo, C. & Batt, C. A. Dendrimer-functionalized self-assembled monolayers as a surface plasmon resonance sensor surface. *Langmuir* **20**, 6808-6817, doi:10.1021/la0495276 (2004).

7 Goodson, D. Z. *Mathematical Methods for Physical and Analytical Chemistry*. (J. WILEY, 2011).

8 Fonseca, M. M., Scofano, H. M., Carvalho-Alves, P. C., Barrabin, H. & Mignaco, J. A. Conformational Changes of the Nucleotide Site of the Plasma Membrane Ca2+-ATPase Probed by Fluorescence Quenching†. *Biochemistry* **41**, 7483-7489, doi:10.1021/bi015783v (2002).

9 Morris, S. J., Bradley, D. & Blumenthal, R. The use of cobalt ions as a collisional quencher to probe surface charge and stability of fluorescently labeled bilayer vesicles. *Biochimica et Biophysica Acta (BBA) - Biomembranes* **818**, 365-372, doi:10.1016/0005-2736(85)90011-2 (1985).

10 Salthammer, T., Dreeskamp, H., Birch, D. J. S. & Imhof, R. E. Fluorescence quenching of perylene by Co2+ ions via energy transfer in viscous and non-viscous media. *Journal of Photochemistry and Photobiology A: Chemistry* **55**, 53-62, doi:10.1016/1010-6030(90)80018-s (1990).

11 Holmes, A. S., Suhling, K. & Birch, D. J. S. Fluorescence quenching by metal ions in lipid bilayers. *Biophysical Chemistry* **48**, 193-204, doi:10.1016/0301-4622(93)85010-f (1993).

12 Chang, J. H., Choi, Y. M. & Shin, Y.-K. A Significant Fluorescence Quenching of Anthrylaminobenzocrown Ethers by Paramagnetic Metal Cations. *Bull. Korean Chem. Soc.* **22** (2001).

13 Wang, H.-H., Xue, L., Fang, Z.-J., Li, G.-P. & Jiang, H. A colorimetric and fluorescent chemosensor for copper ions in aqueous media and its application in living cells. *New Journal of Chemistry* **34**, 1239, doi:10.1039/c0nj00168f (2010).

14 Yang, Y., Wang, Y. & Peng, Y. A bifunctional, colorimetric and fluorescent probe for recognition of Cu2+ and Hg2+ and its application in molecular logic gate. *Science China Chemistry* **57**, 289-295, doi:10.1007/s11426-013-4999-1 (2013).

15 Pathak, S. *et al.* Synthesis of 4-hydroxyindole fused isocoumarin derivatives and their fluorescence "Turn-off" sensing of Cu(ii) and Fe(iii) ions. *RSC Advances* **5**, 17308-17318, doi:10.1039/c5ra01060h (2015).

16 Seo, S. *et al.* Fluorescein-Functionalized Silica Nanoparticles as a Selective Fluorogenic Chemosensor for Cu2+ in Living Cells. *Eur. J. Inorg. Chem.*, doi:10.1002/ejic.200901039 (2010).

17 Wang, M., Meng, G. & Huang, Q. Iodeosin-based fluorescent and colorimetric sensing for Ag+, Hg2+, Fe3+, and further for halide ions in aqueous solution. *RSC Adv.* **4**, 8055-8058, doi:10.1039/c3ra47928e (2014).

18 Dodangeh, M., Gharanjig, K. & Arami, M. A novel Ag(+) cation sensor based on polyamidoamine dendrimer modified with 1,8-naphthalimide derivatives. *Spectrochim Acta A Mol Biomol Spectrosc* **154**, 207-214, doi:10.1016/j.saa.2015.09.031 (2016).

19 Carter, K. P., Young, A. M. & Palmer, A. E. Fluorescent sensors for measuring metal ions in living systems. *Chem Rev* **114**, 4564-4601, doi:10.1021/cr400546e (2014).
20 Luhrs, A. *Dendrimer Modified Silica Nanoparticles as Fluorescent Chemosensors for the Detection of Copper and Cyanide Ions*, University of San Francisco, (2016).
21 Horiba. *FluoroMax-4 and FluoroMax-4P with USP Operation manual*. Part Number J810005 rev D edn, (Horiba Scientific, 2012).
22 Qiao, Y. & Zheng, X. Highly sensitive detection of copper ions by densely grafting fluorescein inside polyethyleneimine core-silica shell nanoparticles. *Analyst* **140**, 8186-8193, doi:10.1039/c5an01880c (2015).
23 EPA. in *National Primary Drinking Water Regulations for Lead and Copper: Short-Term Regulatory Revisions and Clarifications* 57781-57820 (Office of the Federal Register, National Archives and Records Administration, 2008).
24 Lech, T. & Sadlik, J. K. Copper concentration in body tissues and fluids in normal subjects of southern Poland. *Biol Trace Elem Res* **118**, 10-15, doi:10.1007/s12011-007-0014-z (2007).
25 Johnson, I. & Spence, M. T. Z. in *The Molecular Probes Handbook: A Guide to Fluorescent Probes and Labeling Technologies* Ch. 1, (Life Technologies, 2010).

Chapter 4. Dye Doped Conjugates: Synthesis and Preliminary Characterization

Introduction

One of the biggest limitations of the colloidal turn-off sensors from the previous chapters was the inability to determine causation of diminishing fluorescence intensity. Turn-off sensors rely on the decrease in dye intensity as the concentration of analyte increases. FITC, however, is a dye that is easily photobleached[1], and colloids can struggle to remain in solution, and both phenomena can mimic the quenching of a turn-off colloidal sensor. Incorporation of dyes into the silica matrix, called dye doped silica nanoparticles (ddSNPs, Figure 4.1) could address these issues. ddSNPs have a variety of applications similar to those of SNPs with surface dyes, which include bioimaging[2], biosensing[3], and ratiometric sensing.[4,5] Benefits of a ddSNP are (1) increased emission of the internal dye when incorporated (likely due to lack of solvent effects)[6], (2) significantly decreased photobleaching and degradation of the internal dye, and (3) ability/ flexibility to allow the dye-doped particle a self-calibrated sensor in which the changing intensity of the external (sensing) dye is ratiometrically compared to the unchanging internal dye.[5]

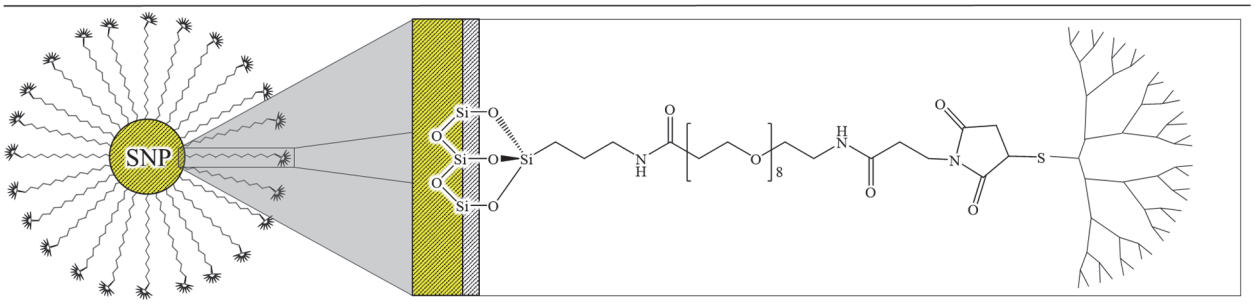

Figure 4.1 Cored view of the conjugated surface of a dye doped silica nanoparticle with a silane, heterobifunctional PEG, and cystamine dendron. Additions of TEOS were added to create a shell of silica effectively burying the FITC dye. *Note that the nanoparticles are spherical, considerably larger than the conjugated coating, and that this view is not to scale. Similar figures will be used to illustrate steps in syntheses in this chapter and to aid in clarification as to which conjugated material is being addressed later in the thesis.*

Due to the inherent instability of nanoparticle dispersions, additions of analytes or incomplete dispersion can lead to the nanoparticles aggregating and falling out of solution, which may skew the results of a quenching sensor. By internalizing a dye, the response of both sensing and internal dyes can be monitored and should provide conclusive results of colloid stability as the analyte is being added. Additionally, the use of an internal calibration dye would allow for more controlled comparisons across experiments for a set of materials, assuming all ddSNP cores have a similar dye loading. Moreover, refinement of more accurate nanoparticle concentrations can be achieved to aid in more accurate characterization (amine assay) and quenching assay results.

In order for this self-calibration to function properly, the internal dye cannot be affected by the external environment of the nanoparticle or by the surface of the nanoparticle. The goal of this work was to incorporate a dye within the nanoparticle that would remain unchanged with an analyte present, whereas a second dye of different emission character is conjugated to the surface and is quenched linearly with the addition of analyte. This goal was to incorporate FITC into the core of the nanoparticle without FITC being accessible to the dispersion environment or FRET. Successively adding TEOS to the reaction mixture during synthesis creates an outer silica shell that does not have FITC (depicted in Figure 4.1). Chelates

would then be conjugated to the surface, similarly to the surfaces of pervious materials (Chapter 2) followed by a sensing dye similar to the rhodamine isothiocynate (RITC) dye of Luhrs' thesis in the form of tetramethylrhodamine (TAMRA) (Figure 4.2).

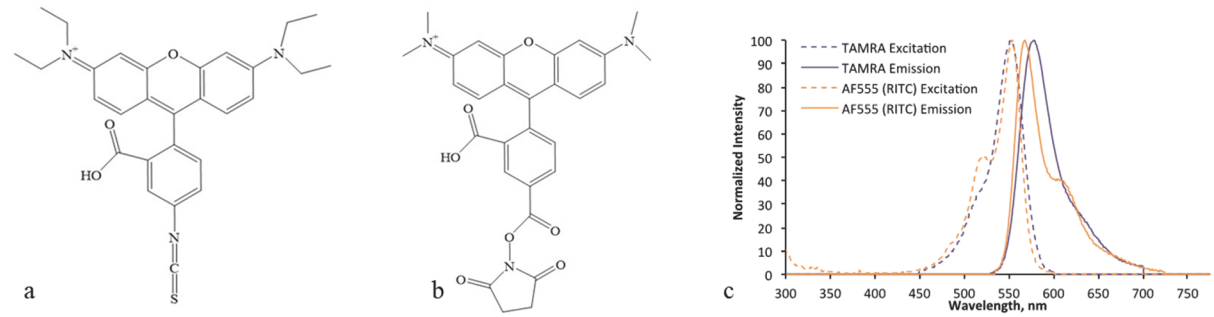

Figure 4.2 Comparison of RITC (a) and TAMRA (b) depicting the small differences in structure which results in a nearly identical theoretical excitation and emission spectra (c).[7]

FITC and RITC are well known Förster Resonance Energy Transfer (FRET) pairs[1] that, when in close proximity (≤ 10 nm), transfer energy from the donor (FITC) to the acceptor (RITC). FRET, therefore, should be apparent between FITC and TAMRA since RITC and TAMRA are related in structure and fluorescence character (Figure 4.2). If the TEOS shell and polymer (PEG-dendron or dendrimer) conjugation did not separate the two dyes, FRET would occur. Experimentally, the excitation of the FITC dye results in the emission of the TAMRA dye if the dyes are not in direct contact but are less than 10 nm apart. FRET between the internalized dye (FITC) and the external dye (TAMRA) would change the sensing characteristics of the sensor from a self-calibrated sensor to more of a turn-on sensor with regards to the emission of FITC. Additionally, the occurrence of FRET between dyes may provide useful information relative to the surface conjugation character of the sensor in terms of coating depth. Furthermore, other dye combinations can be utilized that can follow the procedures outlined below to create sensing ddSNP conjugates that do not FRET.

FRET Theory

FRET is widely used in a variety of sub-disciplines within biology and chemistry as a nanoscopic ruler to measure distances between molecules.[8] FRET is a dipole-dipole interaction between two fluorophores within a short proximity (≤ 10 nm). Additionally, the emission of one fluorophore (donor) must have spectral overlap with the excitation of the other (acceptor).[5,8] Upon absorption of a photon (abridged Equation 1.1 giving Equation 4.1) the donor (D) enters an excited state, and the energy is the transferred to the acceptor (A) non-radiatively (Equation 4.2), which then excites the acceptor. The excited acceptor then emits a photon corresponding to the emission character of the acceptor (Equation 4.3).

$$D + h\upsilon \rightarrow D^* \qquad where\ E = h\nu = \frac{hc}{\lambda} \qquad \text{Equation 4.1}$$

$$D^* + A \rightarrow D + A^* \qquad \text{Equation 4.2}$$

$$A^* \rightarrow A + h\upsilon \qquad \text{Equation 4.3}$$

To better visualize the transfer of energy, refer to Figure 4.3. The excitation of a surface-bound fluorescamine molecule by a photon of adequate energy (λ_{Ex} = 392 nm) will result in the emission of a redshifted photon (λ_{Em} = 505 nm), which was the basis of the fluorescamine assay of Chapter 2. Some energy can be transferred via FRET to a dye that is in close proximity and has an excitation that spectrally overlaps with the emission of fluorescamine, such as FITC. FITC then radiatively decays by emitting a photon (λ_{Em} = 531 nm). *Note: Each of the dyes are bound to R_1 and must be relatively stationary for FRET to occur.*[8]

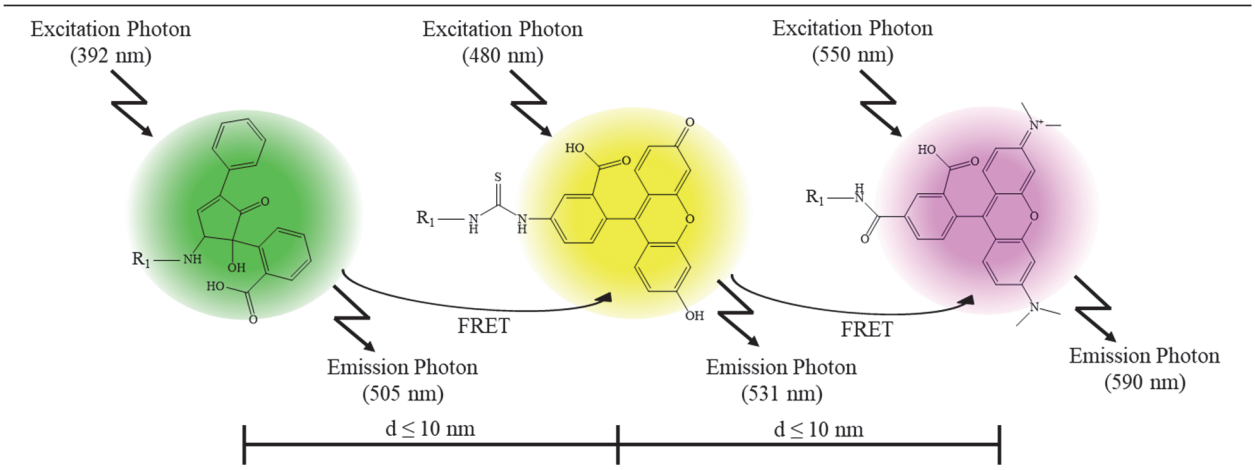

Figure 4.3 Depiction of FRET between the dyes used in this chapter, fluorescamine, FITC, and TAMRA. *Note: This depiction may infer the transfer of energy from fluorescamine to TAMRA through FITC. While this may be possible, this was not the intent of the figure.*

The efficiency, *e*, of the transfer from donor to acceptor can be monitored experimentally by the following equation:[5]

$$e = 1 - \frac{F_{DA}}{F_D} \qquad \text{Equation 4.4}$$

where F_{DA} and F_D are the donor emission intensities with and without acceptor present, respectively. By this definition, the donor concentrations for both measurements must be known in order to be normalized.[5] Time-resolved measurements may be used to find *e* without knowing the concentration of the donor, or the intensity measurement F_D can be taken prior to the addition of the acceptor.[5] FRET efficiency, however, is not linearly dependent on distance.

Figure 4.4 shows that the efficiency of a FRET pair forms a sigmoidal curve where the efficiency remains near 100% until $0.5R_0$ and sharply decreases to 50% by R_0. At $1.5R_0$, the efficiency is under 10%, and when the distance increases to $2R_0$, the efficiency is nearly zero. As described by Hildebrandt, the distances between $0.5R_0$ and $1.5R_0$ are the most sensitive to measurements using FRET.[9]

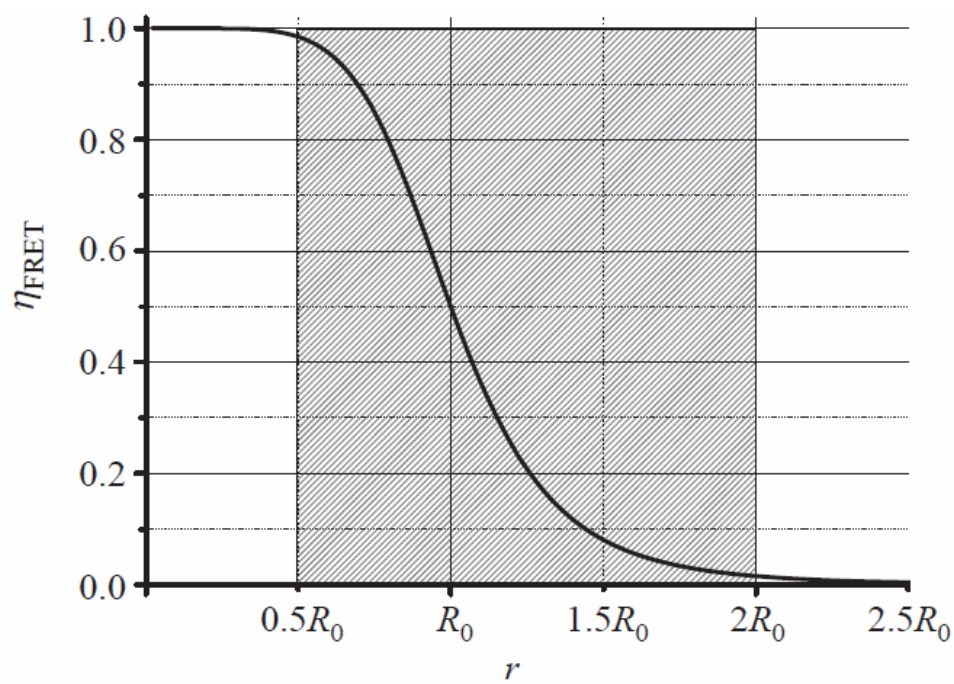

Figure 4.4 FRET efficiency (ηFRET) as a function of D–A distance (r). The r^{-6} distance dependence leads to a strong sensitivity of ηFRET to r in the distance region of about $0.5R_0$–$2.0R_0$ (gray background area). Figure reprinted from Hildebrandt.[9]

Efficiency, *e*, can also be calculated via the Förster distance, R_0, which is the distance between donor and acceptor whose efficiency is 50%, and by the actual distance between dyes, *r*.[8]

$$e = \frac{R_0^6}{R_0^6 - r^6} \qquad \text{Equation 4.5}$$

The Förster distance, R_0, is calculated via[8]

$$R_0^6 = \frac{9000(ln10)k^2 Q_D}{128\pi^5 N n^4} * J(\lambda) \qquad \text{Equation 4.6}$$

where k^2 is a factor that describes the orientation of transition dipoles of the donor and acceptor in space (typically assumed to be 2/3), Q_D is the quantum yield of the donor (without acceptor), *N* is Avogadro's number, *n* is the refractive index of the medium (1.3647 for a 2:1 ethanol: water mixture), and *J(λ)* is the integral overlap of the donor excitation spectrum and the acceptor emission spectrum. A visual depiction of the spectral overlap integrals for fluorescamine (donor) and FITC (acceptor) as well as FITC (donor) and TAMRA (acceptor) are shown in Figure 4.5. Equation 4.6 can be reduced to the following equation by combining constants which are experimentally known.[8]

$$R_0^6 = 0.211(k^2 n^{-4} Q_D J(\lambda))^{1/6} \qquad \text{Equation 4.7}$$

The integral overlap, *J(λ),* of the donor excitation spectrum and the acceptor emission spectrum can be calculated using *a|e UV-Vis-IR Spectral Software*.[10]

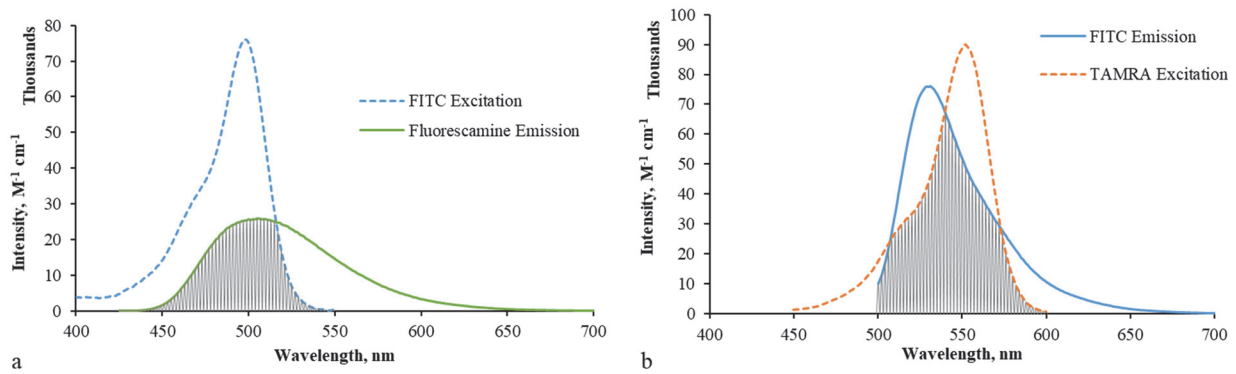

Figure 4.5 Overlays of the fluorescamine emission and FITC excitation spectra (a) and the FITC excitation and TAMRA emission spectra depicting the integral overlap, *J(λ)*, as a shaded region. *Note: Intensity is in units of molar absorptivity ($M^{-1}cm^{-1}$) to aid in the calculation of the Förster distance, R_0 (accomplished by multiplying normalized spectra by the respective molar absorptivities).*

By calculating the Förster distance, R_0, using Equation 4.7 the actual distance between dyes, *r*, can be determined by rearranging Equation 4.5 and monitoring the efficiency of FRET via fluorescence characterization studies.

Synthetic Hypotheses

First, using the synthesis outlined Nyffenegger[11], a dispersible dye-doped (FITC) nanoparticle will be synthesized and measured by visual confirmation that dispersion occurred. Second, by applying extra TEOS to the surface of the ddSNPs, the FITC dye will be sufficiently encapsulated and will be measured by the bromination reaction that converts FITC to EITC. Third, with the added scaffolding (APTES and chelates), FRET will be prevented between surface and dopant dyes. If FRET is observed, the addition of a new, longer PEG linker (NHS-PEG_{24}-Mal) would extend the distance between dyes to prevent FRET. Fourth, by following similar synthetic procedures as outlined in Chapter 2, similar amine and dye loadings will be found on the surface of the dye ddSNPs (ddSNP-Amine < ddSNP-G_3 < ddSNP-PEG_8-G_{3S} ≤ ddSNP-G_4 ≤ ddSNP-PEG_{24}-G_{3S}) and will be measured via fluorescamine assay.

Materials

The following reagents were used directly without further purification. All relevant acronyms used for chemicals are given in the first position of the parenthetic clarifier. **Pure Solvents:** Ethanol (EtOH, Sigma-Aldrich, 200 proof, 99.5%, CAS 64-17-5, FW 46.07); Ultra-pure water (18 MΩ H_2O, ELGA PURELAB Option-Q purification system); **Buffer:** 4-(2-Hydroxyethyl)-piperazine-1-ethanesulfonic acid (HEPES, Sigma-Aldrich, 99.5% (titration), CAS 7365-45-9, FW 238.30); **Acids/Bases:** Ammonium hydroxide (NH_4OH, Sigma-Aldrich, CAS 1336-21-6, FW 35.05); **Silanes:** Tetraethyl-orthosilicate (TEOS, Sigma-Aldrich, 98% (reagent), CAS 78-10-4, FW 208.33); 3-Aminopropyl-triethoxysilane (APTES, Sigma-Aldrich, 99%, CAS 919-30-2, FW 221.37); **Linkers:** succinimidyl- [(N-(malemidiopropionamido)-octaethyleneglycol]- ester (NHS-PEG8-Mal, succinimidyl- [(N-(malemidiopropionamido)-tetracosaethyleneglycol]-ester (NHS-PEG24-Mal, Thermo Scientific, N/A, CAS N/A FW 1394.55); **Dendrimer:** PAMAM dendrimer generation 4, cystamine core, amine surface (G_{3SS3}, Andrew Chem Services, 10% wt. in MeOH, CAS N/A, FW 14306.35); **Dyes:** Fluorescein isothiocyanate (FITC, Sigma-Aldrich, 90%, CAS 3326-32-7, FW 389.38); **Bromination reagents:** Bromine (Br_2, Sigma-Aldrich,

reagent grade, CAS 7726-95-6, FW 159.81); Sodium thiosulfate pentahydrate ($Na_2S_2O_3$, Sigma-Aldrich, ≥99.5% CAS 10102-17-7, FW 248.18); **Reducing Agents:** Tris(2-carboxyethyl) phosphine• HCl (TCEP, Sigma-Aldrich, 98%, CAS 51805-45-9, FW 286.65); **Capping Agents:** Beta-Mercaptoethanol (BME, Sigma-Aldrich, >99%, CAS 60-24-2, FW 78.13).

Methods

Syntheses

Preparation of FITC-Silane

A FITC-silane reaction was performed to covalently bond the FITC dye to APTES, which was then added to a SNP synthesis.[11] The FITC-silane was synthesized by dissolving FITC (4.18 mg) in ethanol (10 mL) followed by an aliquot of APTES (1.972 µL). The reaction occurred over the course of two days (42 °C, N_2 atm) while covered in aluminum foil. No purification was performed prior to addition to SNP synthesis.

FITC dye-doped silica nanoparticles (ddSNP)

An ammonium hydroxide solution was prepared by adding NH_4OH (54.48 g) to ethanol (250 g) producing a ~28% solution. TEOS (990 µL) was added to the 28% NH_4OH solution, stirred (600 rpm, RT, N_2 atm, 50 min), and was followed by the addition of the FITC-silane reaction solution. After 8 min, a TEOS (99 µL) addition was made and aliquots added every 8 min until 20 additions were made, after which the reaction was covered with aluminum foil and allowed to stir (600 rpm, RT, N_2 atm) overnight. The newly synthesized ddSNPs were isolated via centrifugation using the JA-21 (15,000 rpm, 1 hour), washed three times with ethanol, and dried in a vacuum desiccator overnight. A bright yellow solid ddSNP (0.85568 g) was recovered.

Amine and methyl silanization

The ddSNPs (0.79939 g) were dispersed in ethanol (20 mL, in order to minimize flocculation, a probable cause of low APTES silanization). The same 1:1 solution of APTES to MTMS was prepared and that solution (20.0 µL) was added to the ddSNP dispersion of ddSNPs. The reaction was stirred (1000 rpm, RT, ambient atm) overnight. The resulting ddSNP-Amine nanoparticles were isolated via centrifugation (TLA 110, 35,000 rpm, 10 min) and washed three times with ethanol. A bright yellow solid (0.76478 g) was obtained after drying. The fluorescamine assay, however, showed little to no amines on the surface. The same particles were redispersed, and the silane coating was attempted again. The second silanization performed used the redispersed ddSNP (0.76378 g) in ethanol (10 mL), where no flocculation was observed after 4-5 min of sonication. A new solution of 1:1 of APTES to MTMS was made by adding APTES (100.0 µL) to MTMS (60.0 µL), then the mixture (100.0 µL) was added to the dispersion. The reaction was stirred (1000 rpm, RT, ambient atm) overnight. The resulting ddSNP-Amine nanoparticles were isolated via centrifugation (TLA 110 at 35,000 rpm for 10 min) and washed three times with ethanol, and a less bright yellow solid (0.71643 g) was recovered. All reactions were at ambient temperatures and covered with aluminum foil to protect the FITC dopant.

Dendrimer Conjugation

A mass of 101.22 mg ddSNP-Amine were each dispersed in 7 mL dry DMSO, and 1.0 mL of 12.5 mg/mL CDI in dry DMSO was added dropwise. This reaction was stirred overnight at RT. The dispersion was centrifuged (TLA-110 rotor, 35,000 rpm, 10 min) and redispersed in dry DMSO and transferred to new

scintillation vials. The 8 mL ddSNP-CDI dispersion was split in two, where the first had 0.75 mL 10% w/w G_4 dendrimer solution in methanol and the other had 0.25 mL 20% w/w G_3 dendrimer (plus an additional 0.5 mL methanol to keep methanol concentration consistent). Reactions were stirred at RT for 2 days. The resulting conjugates were then washed 3 times with 3 mL ethanol each. Drying of nanoparticle conjugates occurred overnight, and the percent yields of each conjugate are shown in Table 4.1.

Table 4.1 Yields for Dendrimer conjugated ddSNPs

Sample	Mass, mg		Yield, %
	Initial	Final	
ddSNP-G_3	50.61	45.10	89.11
ddSNP-G_4	50.61	44.58	88.09

Dendron Conjugation

The ddSNP-Amine (122.52 mg, 4.08 mg/mL) were added to HEPES (30 mL, pH 8, 10 mM), which dispersed completely in about 1 min. The dispersion was split between two 20 mL scintillation vials (15 mL each) and NHS-PEG$_8$-Mal (150 µL, 250 mM) was added to the first vial, while NHS-PEG$_{24}$-Mal (150 µL, 250 mM) was added to the other and stirred (1050 rpm, RT, ambient atm) for 4 h. A TCEP solution was made (2 mL, 50 mM) in HEPES (pH 8, 10 mM) and was mixed with G_{3SS3} dendrimer (2 mL) and reacted for 2 h (1050 rpm, RT, ambient atm). A small volume of each SNP-PEG-Mal dispersion (2.5 mL) was removed from each reaction to synthesize capped conjugates, which will be described in the Capping section. The dendron reduction solution (2 mL) was added to each of the remaining dispersion solutions and allowed to react overnight (1000 rpm, RT, ambient atm). The newly synthesized ddSNP-PEG$_8$-G_{3S} and ddSNP-PEG$_{24}$-G_{3S} conjugates were isolated via centrifugation (TLA 110, 35,000 rpm, 10 min), washed three times with ethanol, and allowed to dry overnight where yellow powders (34.66 mg and 33.20 mg respectively) were recovered.

Capping of ddSNP-PEGn-Mal conjugates with BME

BME capped conjugates were created for each PEG length by adding mercaptoethanol (3 µL) to HEPES (1.000 mL, pH 8, 10 mM). After the washing of SNP-PEG conjugates with HEPES (pH 8, 10 mM, 3 times, 3 mL), the SNP conjugates were redispersed and two aliquots (2.5 mL each) were removed. Half of the BME solution was delivered to the SNP-PEG$_8$-Mal dispersion while the other half was delivered to the SNP-PEG$_{24}$-Mal dispersion. *Please refer to* Figure 2.17 *for a graphical representation of the assumed particle surface after capping.*

NHS-TAMRA with ddSNPs

The ddSNP conjugates (**Error! Reference source not found.**) were suspended in HEPES (7.5 mL, pH 8, 10 mM) and sonicated for less than 1 minute. A NHS-TAMRA solution (11 mg/mL) was made in dry DMSO and was added (0.5 mL) to each dispersion. The reaction was stirred (1000 rpm, RT, ambient atm) overnight while covered with aluminum foil. The resulting conjugates were isolated via centrifugation (TLA-110 rotor, 35,000 rpm, 10 min) and washed with aliquots of ethanol (3 mL) until no decrease in TAMRA was shown in the supernatant (as monitored using a handheld 405 nm laser). Several rinses of the reaction vial and particles resulted in 2 rinses and 4 washes. The ddSNP-TAMRA conjugates were dried at

ambient pressure overnight and varying pink particles (Figure 4.11) were recovered (masses given in **Error! Reference source not found.**)

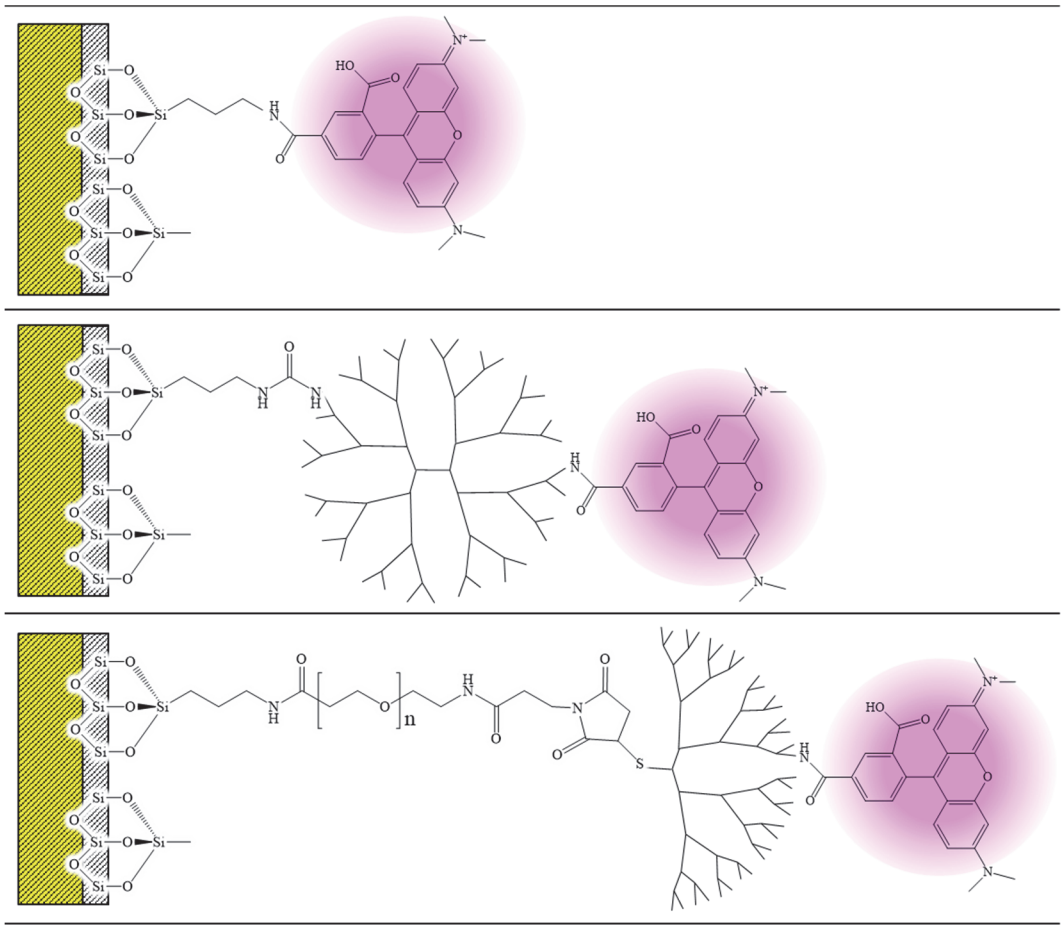

Figure 4.6 By reacting a malemide group on the surface of a ddSNP-PEG$_8$-Mal conjugate with the thiol of a reduced cystamine dendrimer (dendron), the conjugate ddSNP-PEG$_8$-G$_{3S}$ was synthesized. Similarly, the ddSNP-PEG$_{24}$-G$_{3S}$ was synthesized. *Please refer to* Figure 1.18 *for the fine structure of the PAMAM dendrimer, which is nearly the same for the dendron depicted above.*

Characterization

FITC Emission Character and Bromination Assay

The ddSNPs were dispersed and diluted to the concentration of 5.55 µg/mL in 2:1 ethanol: HEPES (pH 7, 10 mM) to yield an acceptable emission intensity (ex. 480 nm). This emission spectrum was compared to the spectra of unbound (free) FITC, surface bound FITC from the FITC series of Chapter 2, and theoretical FITC emissions to determine if the fluorescence character of the FITC dye was conserved through the process of nanoparticle formation.

The bromination assay was performed in similar fashion as the bromination reaction in Chapter 2 on the surface bound FITC. The goal was to show the dye doping of the FITC within the silica was not readily available to react or coordinate and thus not turn the material pink. A mass of ddSNP-Amine (10.70 mg) was dispersed in ethanol (3 mL) and the reaction (2 h, 600 rpm, RT, ambient atm) was cover with aluminum foil to prevent photobleaching. The ddSNPs were isolated form the reaction supernatant via centrifugation (TLA 110, 35,000 rpm, 10 min) and washed (3 times, ethanol). A yellow solid (8.45 mg,

78.97%) was recovered. The washes were quenched with a saturated solution of sodium thiosulfate (0.5-1 mL per wash). The sodium thiosulfate quench also provided information on the viability of each wash by resulting in a precipitate at the bottom of the vial.

Fluorescamine Assay

The fluorescamine assay was performed according to the procedure given in Chapter 2. The nanoparticle conjugate samples (prior to TAMRA conjugation) were prepared in the same solvent, HEPES (pH 8.33, 10 mM), at concentrations (0.111 mg/mL) that were diluted until sample signal intensity (500,000 to 1 million CPS) was within the calibration.

Fluorescence Characteristics and Dye Loading of TAMRA

A mass of 5.3 mg of TAMRA dye was dissolved in 1 mL of DMSO. A volume of 1 µL TAMRA solutions was transferred to 3 mL of a 2:1 ethanol: HEPES (pH 7, 10 mM) solution. The initial concentration saturated the fluorimeter detector and therefore serial dilutions were performed until a final concentration of about 1 nM was achieved. As in the FITC calibration curve (Figure 2.24a), the concentration saturated the fluorimeter detector and therefore serial dilutions were performed until 0.5 million CPS were reached (Figure 4.7a). Of the emission spectra collected, spectra with 2.5 million CPS and below were used to create a calibration curve (Figure 4.7b) due to fluorimeter limitations.[12] Emission spectra for the dye loading of TAMRA on conjugates were completed at 9.0 µg/mL dispersed in 2:1 ethanol: HEPES (pH 7, 10 mM).

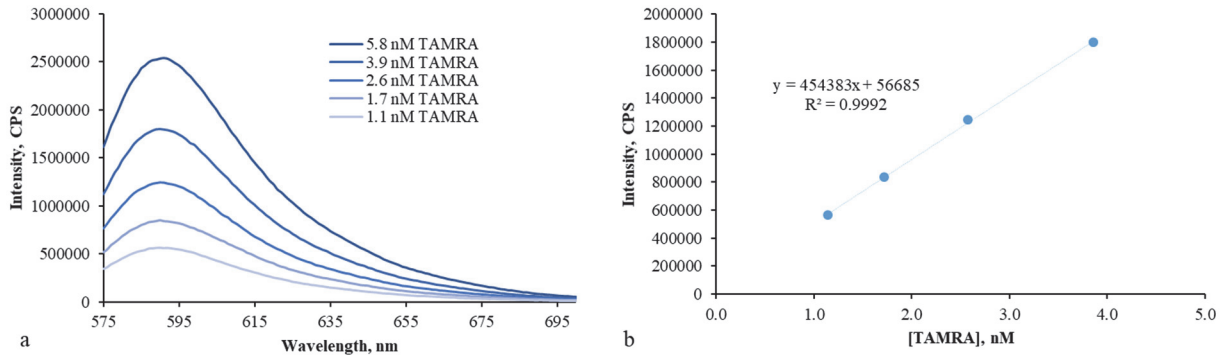

Figure 4.7 Emission spectra (a) and curve (b) of unbound TAMRA. Emissions at 592 nm were used for dye loading calibration and calculations. *Solvent: 2:1* ethanol*: HEPES (pH 7, 10 mM); Slit widths: 5 nm; Excitation: 543 nm.*

Results

The dye doped nanoparticles were synthesized and characterized as in Chapter 2. Unfortunately, the size of the dye-doped particles could not be determined due to limited access to the DLS. Characterization of the ddSNP materials included the bromination reaction, amine assays, and fluorescence character determination throughout the synthesis.

FITC Fluorescence and Encapsulation

The FITC emission spectrum of ddSNP was normalized and plotted with the emission spectra of other FITC materials (Figure 4.8) to show that the FITC fluorescence was mostly unchanged apart from the changes in emission maxima, which was indicative of environmental changes around the dye (less polar = blue shift, Figure 4.8, blue arrow). *Note: Refer to Solvent and Environmental Effects section for more information.*

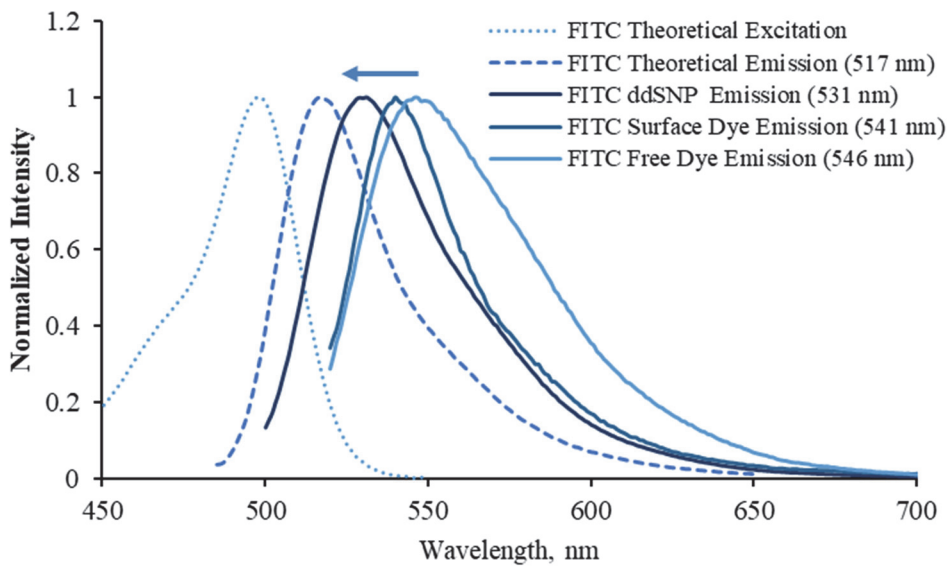

Figure 4.8 Normalized data of FITC theoretical excitation and emission spectra with experimental data of FITC imbedded in the nanoparticle (ddSNP), FITC on the surface of a nanoparticle, and FITC free in solution. *Note: FITC ddSNP emission was added to Figure 2.29 to show the blueshift relative to other emissions.*

To ensure the FITC dyes were entirely encapsulated in the silica of the nanoparticle, bromine was added. The color of the ddSNPs after the addition of Br_2 remained yellow, indicating no FITC dyes were converted to EITC. Further investigation was performed to confirm encapsulation through the dispersion and monitoring of the emission spectra of the ddSNPs before and after bromination (Figure 4.9a). The majority of the FITC dyes were not converted, as shown in Figure 4.9a, however, an emission increase near 565 nm (indicated by the orange arrow) shows that FITC dyes near the surface may have been brominated, however, not significantly (<8%). This result was thought to indicate that the FITC dye was sufficiently buried within the nanoparticle such that addition of analytes would not affect the emission of FITC (quench).

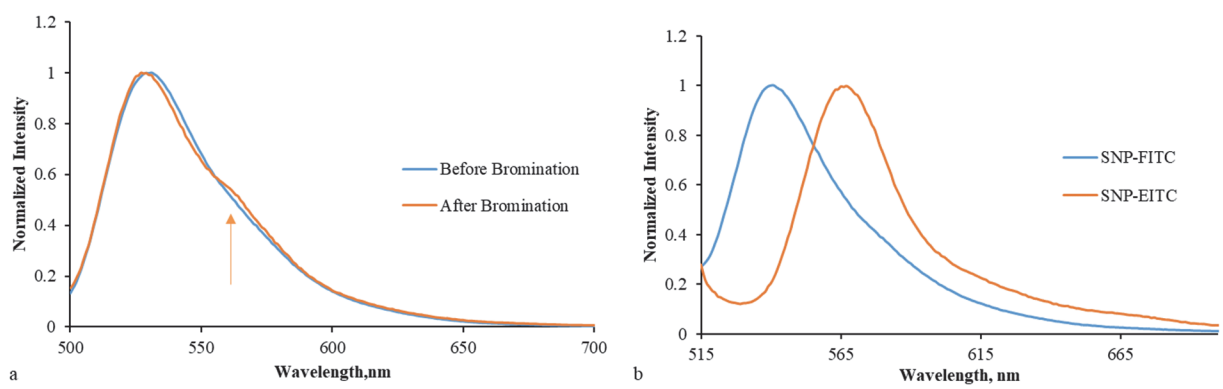

Figure 4.9 Normalized emission spectra (a) of ddSNP-Amine before (blue) and after (orange) the bromination reaction indicating little to no FITC dyes were converted to EITC. Normalized comparison (b) of SNP-FITC and SNP-ETIC showing the difference in emission maxima at 541 and 567 nm, respectively.

Amine Assay

An amine assay was performed using fluorescamine before the conjugation of TAMRA. During this assay, FITC can act as a FRET acceptor for fluorescamine emission after aminolysis. For simplicity, the FRET between FITC and fluorescamine was assumed to be 100% efficient, and the FITC emission peak was added to the fluorescamine emission peak in order to determine an amine concentration. *Note: The efficiency between FITC and fluorescamine, however, cannot be 100% due to non-radiative decay and was likely significantly lower indicating that the amine concentrations were higher than observed.* Concentrations of amines (Figure 4.10) fit the general trend that was shown in the FITC series (Chapter 2), increasing between dendrimer generations and increasing or equal from dendrimer to dendron, in spite of adding the emission of two peaks together. Also, the order of magnitude of amine concentration was similar between SNP and ddSNP conjugates. Amine concentrations from the capped dendron materials (SNP-CDI intermediates were not capped) when compared to the amine concentrations of the dendron materials show conflicting results. The lower concentration of amines in a capped material should indicate a more successful PEGylation reaction, which then should lead to a higher concntration of amines in the dendron material. This inverse relationship, however, did not occur (Figure 4.10) and may be due to error in the assumptions made about the fluorescamine-FITC FRET.

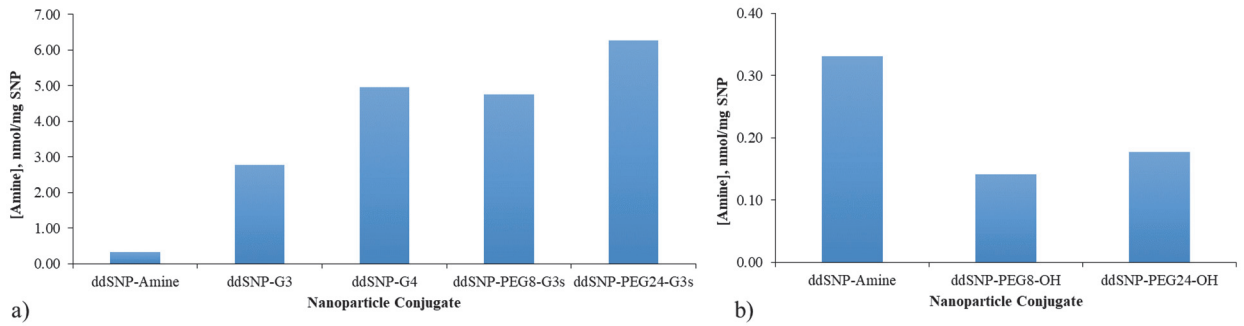

Figure 4.10 Fluorescamine assay results (a) comparing the ddSNP-Amine starting material with the dendrimer and PEG-dendron conjugates. The ddSNP-Amine starting material was also compared to the capped ddSNP-PEG materials (b) showing that there were less available amines on the ddSNPs that were reacted with PEG_8 than PEG_{24}.

Characterization of Conjugated TAMRA

TAMRA was conjugated to all the ddSNP conjugates to yield a pink to dark purple solid (all synthesis resulted in a >90 % yield, Figure 4.11). The color trend was thought to be indicative of dye loading (darker means higher loading) and upon investigation, this trend was generally confirmed (Figure 4.12). The pink ddSNP-T conjugate was found to have the lowest emission followed by the more purple ddSNP-G_3-T conjugate. Overall, the trend of TAMRA concentrations, relative to conjugate, matched the trend of amine concentrations (Figure 4.10), although at much lower concentrations. The G_4 and dendron conjugates were indistinguishable by color alone and, as shown in Figure 4.12, emission spectra and dye loadings were quite close for each material. Percent conversion of amines to dyes (Figure 4.12b) were quite low and only reached above 10% for the ddSNP-T material.

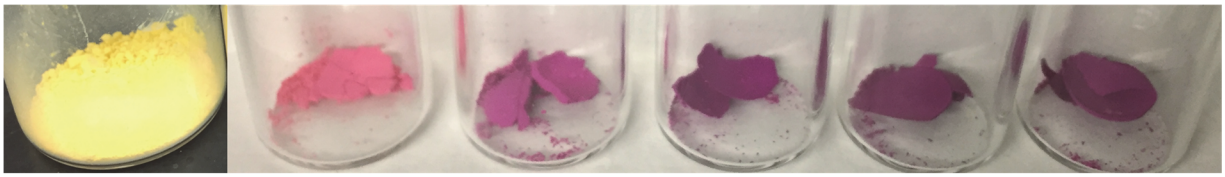

Figure 4.11 Dried nanoparticle conjugates showing the color change from the ddSNP-Amine starting material to the pink and purple powders post-TAMRA dye conjugation.

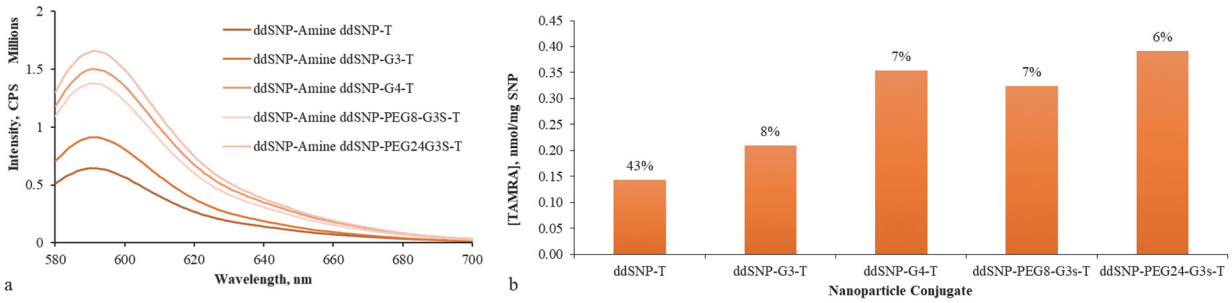

Figure 4.12 TAMRA emission spectra (a) showing the relative loading of TAMRA on the surfaces of the ddSNP conjugates. Calculated loadings (b) of TAMRA based on the dye loading calibration with percentages above the bars show the amount of amines converted to TAMRA based on the fluorescamine assay in Figure 4.10. *Note: TAMRA concentrations were so low that plotting TAMRA concentration with amine concentration would have inhibited any trends shown by the TAMRA concentration data.*

FRET

Evidence that FRET occurred between the fluorescamine donor (D) and the FITC acceptor (A) is shown in the normalized overlay of spectra of the individual dyes and the conjugate on which the assay was being performed (Figure 4.13a). The blue shift in the fluorescamine emission on the surface of the particle compared to the emission of fluorescamine from the calibration curve (~15 nm) was likely due to the more rigid nanoparticle (lack of solvent effects).[8] This shift was shown with FITC in different local environments (Figure 4.8), although the shift was less drastic. Futher evidence of FRET occuring among the conjugate materials during the fluorescamine assay was shown in the spectral overlay of all materials (Figure 4.13b). As the conjugates progress through syntheses from the ddSNP-Amine starting material to the dendrimer or PEGylated dendron materials, the relative emission of FITC (acceptor) decreases while the emission of the fluorescamine (donor) increases (orange arrows, Figure 4.13b). This trend is indicative of the assumed surface morphology progression laid out in Figure 4.6 (without TAMRA dyes of course), where reactive surface amines would be gradually distanced from the FITC-imbedded silica core. As descibed in the FRET Theory section, the efficiency of the energy transfer decreases as the two dyes diverge from one another (Figure 4.4).

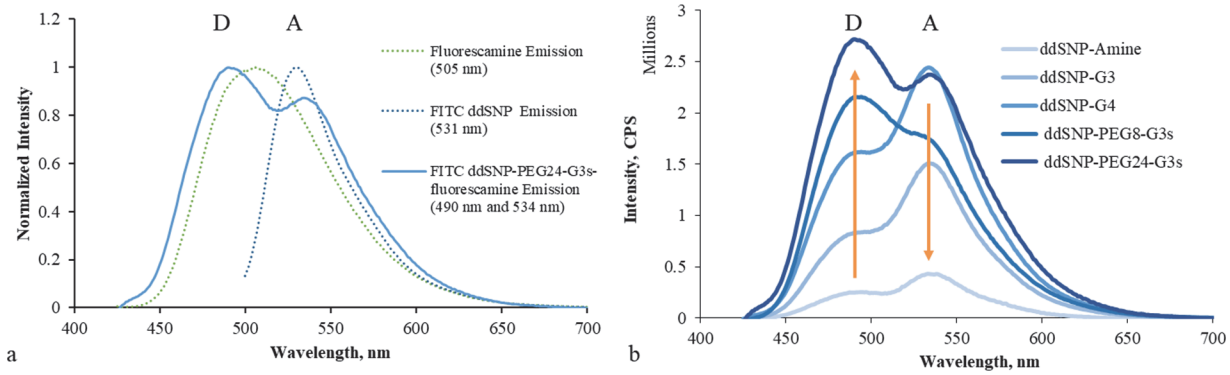

Figure 4.13 Normalized emission spectra overlay (a) of fluorescamine, ddSNPs (FITC), and the ddSNP-PEG_{24}-G_{3S} conjugate that was reacted with fluorescamine showing similar peak maxima. Raw fluorescamine assay spectra (b) showing FRET between fluorescamine and FITC on each conjugate. The orange arrows indicate the change in maxima as the distance between the core and the fluorescamine becomes larger.

With the aid of ale UV-Vis-IR Spectral Software, the spectra from Figure 4.5 were uploaded and the integral overlap, *J(λ)*, was calculated for the FRET pairs.[10] The calculated R_0 values of the fluorescamine-FITC and FITC-TAMRA FRET pairs were 4.3 nm and 6.3 nm, respectively. The efficiency was calculated differently in the case of fluorescamine-FITC FRET due to the acceptor being present prior to addition of the donor. The emission intensity was monitored at the acceptor wavelength with and without the donor and the following equation was applied:

$$e = \frac{F_{DA}}{F_{DA} + F_D} \qquad \text{Equation 4.8}$$

Using a table of approximate conjugate lengths (Table 4.2), the calculated distance using FRET from the fluorescamine-FITC and the FITC-TAMRA data were compared to the theoretical distances (

In general, the addition of longer conjugates to the surface of the ddSNPs resulted in a lower efficiency and therefore a longer measured distance with both FRET systems. Disagreements between theoretical and experimental values are likely due to the unknown thickness of the TEOS shell and the dynamic nature of polymers in solution. The TEOS shell, according to the data, was between 4 and 5 nm. Measured distances between FRET pairs may be shorter than theoretical since the theoretical distances were determined by the fully extended polymers without consideration to the distortions that occur within solution. Dendrimers have been shown to become oblate when attached to a surface[16] and the PEG polymers are not likely to remain fully extended as depicted in Figure 4.6.

Differences between the two methods of measurement are likely due to the method of calculation (Equation 4.8*) and low efficiency between fluorescamine-FITC FRET pair. The spectral data of the fluorescamine-FITC FRET (Figure 4.13b) shows a change in maximum emission from FITC in the amine and dendrimer materials to fluorescamine in the dendron materials. This indicates that there was a change in efficiency from above 50% in the amine and dendrimer materials to below 50% in the dendron materials, demonstrating an increase in distance from the surface of the ddSNP as the conjugates get longer.

Table 4.3). *Note: The theoretical distance does not take the thickness of the TEOS shell that was applied to the ddSNP core.*

Table 4.2 Conjugate unit lengths

Conjugation Unit	Length, nm	References
APTES	0.7-0.8	13
CDI	~ 0	14
PEG_8-Mal	3.925	14
PEG_{24}-Mal	9.52	14
G_3 Dendrimer*	3.1	15
G_4 dendrimer*	4.2	15
G_{3S} dendron**	2.1	-

*DLS Measurements
**Estimate

In general, the addition of longer conjugates to the surface of the ddSNPs resulted in a lower efficiency and therefore a longer measured distance with both FRET systems. Disagreements between theoretical and experimental values are likely due to the unknown thickness of the TEOS shell and the dynamic nature of polymers in solution. The TEOS shell, according to the data, was between 4 and 5 nm. Measured distances between FRET pairs may be shorter than theoretical since the theoretical distances were determined by the fully extended polymers without consideration to the distortions that occur within solution. Dendrimers have been shown to become oblate when attached to a surface[16] and the PEG polymers are not likely to remain fully extended as depicted in Figure 4.6.

Differences between the two methods of measurement are likely due to the method of calculation (Equation 4.8*) and low efficiency between fluorescamine-FITC FRET pair. The spectral data of the fluorescamine-FITC FRET (Figure 4.13b) shows a change in maximum emission from FITC in the amine and dendrimer materials to fluorescamine in the dendron materials. This indicates that there was a change in efficiency from above 50% in the amine and dendrimer materials to below 50% in the dendron materials, demonstrating an increase in distance from the surface of the ddSNP as the conjugates get longer.

Table 4.3 Comparison of FRET results of distances between dyes (r)

Conjugate	r (nm)		
	fluorescamine-FITC	FITC-TAMRA	Theoretical
ddSNP-Amine	3.9	5.8	1.0
ddSNP-G_3	4.4	6.8	3.1
ddSNP-G_4	5.1	8.4	4.2
ddSNP-PEG_8-G_{3S}	5.4	8.5	6.0
ddSNP-PEG_{24}-G_{3S}	5.5	9.3	11.6

Discussion and Conclusion

Dye-doped silica nanoparticles (ddSNPs) were successfully synthesized with a shell of TEOS that prevented the conversion of FITC to EITC via the bromination reaction. Unfortunately, the TEOS shell was not thick enough to prevent FRET from occurring between FITC-TAMRA and separate results indicate fluorescamine-FITC FRET occurred during the fluorescamine assay. The results of the FRET studies were used to experimentally determine the distances from the external dyes (fluorescamine and TAMRA) to the

internal FITC dye. The results from the FRET experiments confirmed a trend in increased polymer length that were hypothesized from the addition of individual polymers in Table 4.2. This showed that the addition of dendrimers to the ddSNPs increased the distance between amine and the surface. The distance was then extended by the conjugation of PEG-dendrons. The PEG_{24}-G_{3S} conjugation was not long enough to prevent FRET from occurring, but both PEG-dendron materials were found to be lower than 50% FRET efficiency indicating that a longer PEG could push the amine (and dye) further from the surface. The results show us a more structured view of what the actual surface looks like since SEM is far too insensitive to provide thin film structure on the surface of a nanoparticle.

The fluorescamine assay, albeit with some experimental difficulty, followed the hypothesized trend of amine concentration ddSNP-Amine < ddSNP-G_3 < ddSNP-PEG_8-G_{3S} ≤ ddSNP-G_4 ≤ ddSNP-PEG_{24}-G_{3S}. This trend implied that the use of a more robustly designed synthetic procedure (selective synthesis using heterobifunctional linkers rather than homobifuntional linkers) with a G_{3S} dendron, which has the equivalent number of amines as a G_3 dendrimer, provides more amine reaction sites for conjugation than the PAMAM dendrimer counterpart. Additionally, the dendron conjugate was more comparable to a higher dendrimer conjugate (ddSNP-G_4) with regards to amine concentration.

Future Work

The current materials utilizing TAMRA as the sensing dye could be tested with a battery of metal ion titrations to determine selectivity and sensitivity for quenching. One hypothesis is that copper would have similar results to the RITC series of Luhrs' thesis work, but would be a turn-on sensor rather than a turn-off sensor. Hypothetically, two scenarios could result. The first is that this type of dual sensor would function by the metal ion quenching of TAMRA emission which, in turn, would no longer result in FRET with FITC. The effect would be the turning on of the FITC emission as a function of increasing metal ion addition as shown in Figure 4.14a. This would be dependent on the excitation character of the TAMRA dye when bound to the metal ion analyte. The second scenario arises if the TAMRA is merely quenched but the excitation does not change, and thus the FITC dye emission would remain constant creating a ratiometric sensor (Figure 4.14b). Further testing would include the QDA assessments using anions.

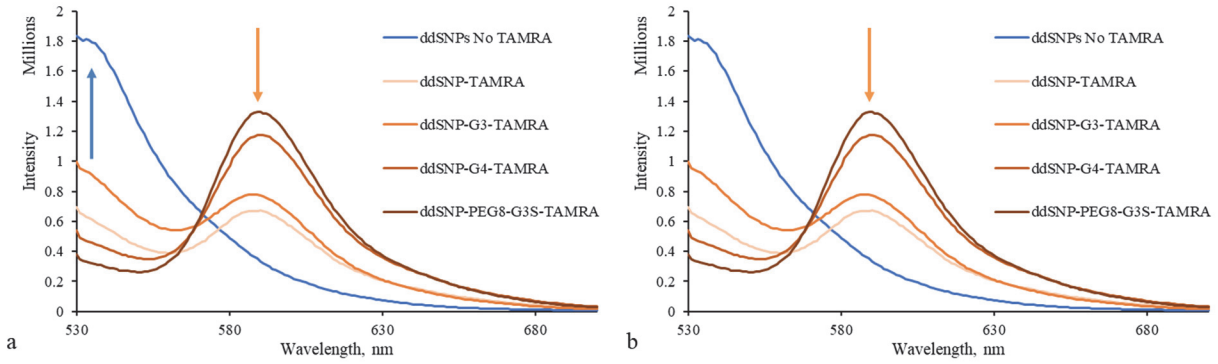

Figure 4.14 Excitation of ddSNPs with (orange) and without (blue) TAMRA conjugated showing the hypothetical sensing scenarios of enhancement through quenching (a) and simple quenching (b). *[ddSNP]* = 0.018 mg/mL; *Solvent* =2:1 ethanol: HEPES (pH 7, 10 mM); *Excitation = 500 nm*

Other, more drastic materials could also be explored. Numerous variations of the ddSNP materials could be synthesized to study the effects of dopant concentration (FITC), silica shell thickness (TEOS), and

the exchange of dopant and sensing dyes. Overall, the testing of TAMRA on SNP materials may also generate some interesting results since RITC and TAMRA are very close structurally.

References

1 Johnson, I. & Spence, M. T. Z. in *The Molecular Probes Handbook: A Guide to Fluorescent Probes and Labeling Technologies* Ch. 1, (Life Technologies, 2010).

2 Bae, S. W., Tan, W. & Hong, J. I. Fluorescent dye-doped silica nanoparticles: new tools for bioapplications. *Chem Commun (Camb)* **48**, 2270-2282, doi:10.1039/c2cc16306c (2012).

3 Knopp, D., Tang, D. & Niessner, R. Review: bioanalytical applications of biomolecule-functionalized nanometer-sized doped silica particles. *Anal Chim Acta* **647**, 14-30, doi:10.1016/j.aca.2009.05.037 (2009).

4 Frigoli, M., Ouadahi, K. & Larpent, C. A cascade FRET-mediated ratiometric sensor for Cu2+ ions based on dual fluorescent ligand-coated polymer nanoparticles. *Chemistry* **15**, 8319-8330, doi:10.1002/chem.200900475 (2009).

5 Demchenko, A. P. *Introduction to Fluorescence Sensing*. (Springer, 2009).

6 Canton, G., Riccò, R., Marinello, F., Carmignato, S. & Enrichi, F. Modified Stöber synthesis of highly luminescent dye-doped silica nanoparticles. *Journal of Nanoparticle Research* **13**, 4349-4356, doi:10.1007/s11051-011-0382-3 (2011).

7 ThermoFisher. *Spectra Viewer*

8 Lakowicz, J. R. *Principles of Fluorescence Spectroscopy*. 3rd edn, (Springer, 2006).

9 Hildebrandt, N. in *FRET – Förster Resonance Energy TransferFrom Theory to Applications* (eds Igor Medintz & Niko Hildebrandt) (Wley, 2014).

10 Preus, S. *a|e UV-Vis-IR Spectral Software 1.2 FluorTools* www.fluortools.com, (2015).

11 Nyffenegger, R., Quellet, C. & Ricka, J. Synthesis of Fluorescent, Monodisperse, Colloidal Silica Particles. *Journal of Colloid and Interface Science* **159**, 150-157, doi:10.1006/jcis.1993.1306 (1993).

12 Horiba. *FluoroMax-4 and FluoroMax-4P with USP Operation manual*. Part Number J810005 rev D edn, (Horiba Scientific, 2012).

13 Rong, G. & Weiss, S. M. *Influence of Biomolecule Size on Performance of Nanostructured Sensing Devices*. Vol. 6769 676909-4.

14 Hermanson, G. T. *Bioconjugate Techniques*. 3rd edn, (Academic Press, 2013).

15 Dobrovolskaia, M. A. *et al.* Nanoparticle size and surface charge determine effects of PAMAM dendrimers on human platelets in vitro. *Mol Pharm* **9**, 382-393, doi:10.1021/mp200463e (2012).

16 Mecke, A., Lee, I., Baker, J. R., Jr., Holl, M. M. & Orr, B. G. Deformability of poly(amidoamine) dendrimers. *Eur Phys J E Soft Matter* **14**, 7-16, doi:10.1140/epje/i2003-10087-5 (2004).